Information Content of Halo Displays for Remote Sensing of Ice Crystal Properties

Linda Forster

München 2017

Information Content of Halo Displays for Remote Sensing of Ice Crystal Properties

Linda Forster

Dissertation
an der Fakultät für Physik
der Ludwig–Maximilians–Universität
München

vorgelegt von
Linda Forster
aus Starnberg

München, Oktober 2017

Erstgutachter: Prof. Dr. Bernhard Mayer
Zweitgutachter: Prof. Dr. Markus Rapp
Datum der Abgabe: 27.10.2017
Datum der mündlichen Prüfung: 19.12.2017

Zusammenfassung

Zirren bestehen aus kleinen asphärischen Eiskristallen, die solare Strahlung reflektieren und thermische Strahlung absorbieren und emittieren. Abhängig davon welcher Effekt dominiert, haben Zirren einen kühlenden oder erwärmenden Effekt auf Erdatmosphäre und -boden. Eiskristalle können, je nach Umgebungstemperatur und relativer Feuchtigkeit, zu unterschiedlichen Größen und Formen anwachsen. Mögliche Eiskristallformen variieren von einfachen hexagonalen Säulen und Plättchen bis hin zu komplexen Formen wie Aggregaten und Dendriten. Fehlende Kenntnis der Eiskristallform verursacht große Unsicherheiten bei der Fernerkundung der optischen und mikrophysikalischen Eigenschaften von Zirren. Jede Information über Eiskristallformen ist deshalb nützlich, um Fernerkundungsmethoden von Eiswolken zu verbessern und um den Effekt von Eiswolken auf das Strahlungsbudget und damit auf das Klima besser zu quantifizieren.

Ziel dieser Arbeit ist es zu untersuchen, ob Beobachtungen von Haloerscheinungen Informationen liefern können, um die Komplexität der Eiskristalleigenschaften einzugrenzen. Zu diesen Eigenschaften zählen die Eiskristallgröße, -form, -rauigkeit, und -orientierung. Haloerscheinungen entstehen durch Brechung und Reflexion von Licht an verschiedenen Eiskristallformen mit unterschiedlicher Orientierung und können deshalb wichtige Informationen über diese Eigenschaften liefern. Der häufig sichtbare 22° Halo und der seltene 46° Halo entstehen beide durch zufällig orientierte hexagonale Prismen. Die Berührungsbögen zum 22° Halo entstehen durch orientierte Säulen. Nebensonnen hingegen treten bei Lichtbrechung an orientierten Eiskristallplättchen auf. Die optischen Erscheinungen können mit Hilfe von Strahlungstransportmodellen quantitativ simuliert werden, die für zufällig orientierte Teilchen etabliert sind. Um die Simulation orientierter Teilchen zu ermöglichen, wurde der Ray-Tracing-Algorithmus CrystalTrace entwickelt und in das Monte Carlo Modell MYSTIC implementiert.

Im Rahmen dieser Arbeit wurde zur kontinuierlichen Beobachtung von Haloerscheinungen das wetterfeste Kamerasystem HaloCam auf der Messplattform des Meteorologischen Instituts München aufgebaut und vollständig charakterisiert. Zusammen mit dem neu entwickelten Halo-Erkennungsalgorithmus HaloForest liefert HaloCam einen konsistenten Datensatz von Halobeobachtungen. Zwischen Januar 2014 und Juni 2016 detektierte HaloForest 22° Halos in 2% der Beobachtungszeit. Mittels gleichzeitig gesammelter Ceilometerdaten konnte abgeleitet werden, dass etwa 25% der Eiswolken einen sichtbaren 22° Halo erzeugten.

Das Ableitungsverfahren RICO wurde entwickelt, um Eiskristallgröße, -form sowie den Anteil glatter und rauer Kristalle aus kalibrierten Strahldichtemessungen von 22° Halos zu bestimmen. Die Analyse von HaloCam-Beobachtungen von September 2015 bis November 2016 ergab effektive Eiskristallradien von etwa 20 µm im Mittel, wobei mehr als 90% der Radien kleiner als 40 µm waren. Innerhalb der Messunsicherheit konnten die Beobachtungen von 22° Halos durch plättchenförmige, hohle und massive säulenförmige Kristalle mit einem Anteil glatter Kristalle von jeweils 80%, 60% und 30% reproduziert werden. Die optischen Eigenschaften von Eiskristallplättchen ergaben die beste Übereinstimmung mit den Messungen im Bereich des 22° Halos, gefolgt von Eiskristallsäulen und Aggregaten von Säulen. Die in dieser Arbeit verwendeten Streueigenschaften von Eiskristallplättchen erzeugen einen deutlichen 46° Halo zusätzlich zum 22° Halo für Effektivradien bis etwa 50 µm. Da die ausgewerteten HaloCam-Beobachtungen ausschließlich 22° Halos ohne 46° Halo zeigten, müssen Plättchen als repräsentative Eiskristallform ausgeschlossen werden. Folglich wird dieser Datensatz am besten durch säulenförmige Eiskristalle repräsentiert.

Während der ML-CIRRUS Messkampagne konnte ein einzigartiger Datensatz aufgenommen werden, welcher HaloCam Beobachtungen mit in-situ Messungen des Forschungsflugzeugs HALO kombiniert. Dieser Datensatz enthält Beobachtungen von komplexen Haloerscheinungen, die durch orientierte Kristalle erzeugt wurden. Mit CrystalTrace wurde eine Methode demonstriert, die es erlaubt den Anteil orientierter Kristalle aus Beobachtungen von Nebensonnen und

Berührungsbögen zu bestimmen.

Die vorliegende Arbeit zeigt, dass Haloerscheinungen wertvolle Informationen über Eiskristallform, -rauigkeit, -größe und -orientierung enthalten und führt erstmals eine systematische Untersuchung dieser Eigenschaften durch. Zusammen mit dem neu entwickelten automatischen Halo-Erkennungsalgorithmus HaloForest liefert HaloCam einen konsistenten Datensatz von Langzeit-Halobeobachtungen. Kombiniert mit dem Ableitungsverfahren RICO und CrystalTrace tragen diese Beobachtungen zu einem verbesserten Verständnis von Eiskristalleigenschaften bei.

Abstract

Cirrus clouds consist of small non-spherical ice crystals, which scatter solar radiation and absorb and emit thermal infrared radiation. Depending on which of the effects dominates, these clouds have either a cooling or a warming effect on the earth's atmosphere and surface. Ice crystals can grow to different sizes and shapes depending on the temperature and relative humidity of their environment. Potential shapes range from hexagonal columns and plates to complex ice crystal aggregates and dendrites. Inadequate knowledge about ice crystal shape results in large uncertainties in retrievals of ice crystal optical and microphysical properties. Any information about ice crystal shape is therefore valuable to improve ice cloud remote sensing and to better quantify effects on the radiation budget and thus on climate.

This thesis aims at investigating the information content of halo displays regarding ice crystal properties, which comprise ice crystal size, shape, surface roughness, and orientation in cirrus clouds. Halo displays form by refraction and reflection of light by ice crystals with different shapes and orientations and could therefore provide important information about these properties. The frequently observed 22° halo and the rare 46° halo are both formed by randomly oriented hexagonal crystals. Upper and lower tangent arcs are caused by oriented ice crystal columns and sundogs emerge from light refracted by oriented ice crystal plates. The optical displays can be simulated quantitatively using radiative transport models, which are well established for the simulation of randomly oriented crystals. To allow simulation of oriented crystals, the raytracing algorithm CrystalTrace was developed and implemented into the Monte Carlo model MYSTIC.

Within the scope of this work the weather-proof camera system HaloCam was designed and installed on the rooftop platform of the Meteorological Institute Munich to allow for continuous observation of halo displays. Together with the newly developed automated halo detection algorithm HaloForest, HaloCam provides a consistent dataset of halo observations. Between January 2014 and June 2016 HaloForest detected 22° halos 2% of the time. Using co-located ceilometer data, it was estimated that about 25% of the cirrus clouds produced a visible 22° halo.

The RICO retrieval was developed to estimate ice crystal size, shape and the fraction of smooth and rough ice crystals from calibrated radiance measurements of 22° halos in combination with radiative transfer simulations. Analyzing HaloCam data between September 2015 and November 2016 with RICO revealed effective ice crystal radii of about 20 µm on average, with more than 90% of the radii being smaller than 40 µm. Within the measurement uncertainty, the 22° halo observations can be reproduced with plate-like, hollow, and columnar crystals with a smooth crystal fraction of about 80%, 60%, and 30%, respectively. The optical properties of ice crystal plates were found to best match the HaloCam observations in the region of the 22° halo, followed by solid columns and aggregates of columns. The scattering properties of the ice crystal plates used in this study, produce a pronounced 46° halo in addition to the 22° halo for effective radii up to about 50 µm. Since the evaluated HaloCam observations showed only 22° halos without visible 46° halo, plates must be excluded as representative ice crystal shape. Therefore, solid columns and aggregates of columns are the best matching habits for this dataset.

During the ML-CIRRUS campaign a unique dataset was collected combining HaloCam observations with in-situ measurements of the research aircraft HALO. This dataset contains observations of complex halo displays formed by oriented ice crystals. Using CrystalTrace, a method was presented to retrieve the fraction of oriented ice crystals from observations of sundogs and upper tangent arcs.

This study demonstrates that halo displays contain valuable information about ice crystal properties such as size, shape, roughness, and orientation and performs for the first time a systematic investigation. Operating HaloCam in combination with HaloForest provides a consistent dataset of long-term halo observations. In synergy with the RICO retrieval and CrystalTrace, these observations contribute to an improved understanding of ice crystal properties.

Contents

Zusammenfassung **v**

Abstract **vii**

1 Introduction **1**

2 Theory **5**
2.1 Ice crystals and cirrus clouds . . . 5
2.1.1 Formation of cirrus clouds . . . 5
2.1.2 Formation and growth of ice crystals . . . 6
2.1.3 Ice crystal shape . . . 8
2.1.4 Cirrus microphysical properties . . . 11
2.2 Radiation and atmospheric radiative transfer . . . 12
2.2.1 Radiative properties and physical description . . . 12
2.2.2 Radiative transfer equation . . . 14
2.2.3 Light scattering by atmospheric particles . . . 15
2.3 Halo displays . . . 19
2.3.1 Reflection and refraction laws . . . 20
2.3.2 Formation of halo displays . . . 21

3 Methods **27**
3.1 Radiative transfer simulations . . . 27
3.1.1 MYSTIC . . . 27
3.1.2 DISORT . . . 29
3.2 Optical properties . . . 30
3.2.1 Aerosol optical properties . . . 30
3.2.2 Ice crystal optical properties . . . 30
3.3 Information content of the 22° and 46° halo . . . 36
3.3.1 Single scattering regime . . . 36
3.3.2 Multiple scattering regime . . . 39
3.4 specMACS – the cloud and sky hyperspectral imaging spectrometer . . . 43
3.5 HaloCam – an automated sun-tracking halo observation system . . . 47
3.5.1 System description . . . 47
3.5.2 Geometric calibration . . . 51
3.5.3 Radiometric characterization . . . 52
3.6 HaloForest – an automated halo detection algorithm . . . 62
3.6.1 Image processing and feature extraction . . . 62
3.6.2 Setup and training of HaloForest . . . 64
3.7 RICO – Retrieval of ice crystal properties . . . 67

3.7.1 Ice crystal shape and roughness models . . . 67
3.7.2 Sensitivity studies . . . 68
3.7.3 Ancillary data . . . 75
3.8 CrystalTrace – a raytracing algorithm for oriented ice crystals . . . 80

4 Results **85**
4.1 Halo display statistics . . . 85
4.1.1 Halo display statistics during ACCEPT . . . 85
4.1.2 Long-term halo statistics in Munich . . . 87
4.2 Retrieval of ice crystal properties . . . 90
4.2.1 Case study of 24 March 2015 . . . 90
4.2.2 Case study of 22 September 2015 . . . 98
4.2.3 Application to long-term HaloCam observations . . . 102
4.3 Considerations on ice crystal orientation . . . 111
4.3.1 Observation of oriented ice crystals during ML-CIRRUS . . . 111
4.3.2 Information content of sundogs . . . 115
4.3.3 Information content of upper tangent arcs . . . 118

5 Discussion **121**

6 Summary and Conclusions **125**

7 Outlook **129**

A Appendix **131**
A.1 Decision trees and random forest classifier . . . 131
A.1.1 Decision trees . . . 131
A.1.2 Random forest classifier implementation . . . 132
A.2 Projection of the 22° halo . . . 133

Bibliography **135**

Acknowledgements **149**

Chapter 1

Introduction

Cirrus clouds cover about 30% of the globe (Wylie and Menzel, 1999, Stubenrauch et al., 2006) and play an important role in the earth's energy budget. These clouds consist of small non-spherical ice crystals, which scatter solar radiation and absorb and emit thermal infrared radiation. Depending on which of the effects dominates, cirrus clouds have either a cooling or a warming effect on the earth's atmosphere and surface. The amount of transmitted and reflected light is governed by the ice crystal radiative properties, which in turn depend crucially on shape, surface roughness and orientation (e.g. Liou (1986), Wielicki et al. (1995), Wendisch et al. (2007), Yi et al. (2013)).

Ice crystals can grow to different shapes depending on the temperature and relative humidity of their environment. Potential shapes include hexagonal columns and plates as well as complex shapes such as bullet rosettes, aggregates of crystals and dendrites (Bailey and Hallett, 2004, 2009). Their sizes range from less than 10 micrometers up to a few millimeters (Baran, 2012). Ice crystals often have roughened surfaces, hollow structures, included air bubbles and other inhomogeneities which can significantly affect their scattering characteristics (Tape, 1994, Schmitt and Heymsfield, 2007, Neshyba et al., 2013, Ulanowski et al., 2014, Tang et al., 2017).

For a given ice water content ice clouds may have a net warming or cooling effect, depending on the ice crystal size and shape (Stephens et al., 1990). Furthermore, wrong assumptions regarding the ice crystal shape can result in significant errors in retrievals of optical thickness and cloud microphysical properties using satellite-based shortwave infrared measurements (Mishchenko et al., 1996, Baran et al., 1999, Yang et al., 2015, Holz et al., 2016). The uncertainty in the cirrus optical thickness and the ice crystal effective radius was estimated to more than 50% and 20%, respectively, by Key et al. (2002), Eichler et al. (2009) and Zinner et al. (2016). Ice crystal orientation also has significant effects on the global radiative budget, as pointed out by Noel and Sassen (2005). Better knowledge of ice crystal shape, surface roughness, and orientation is therefore essential to improve estimates of the radiative forcing of cirrus clouds as well as satellite retrievals of cirrus optical and microphysical properties (e.g. Yang et al. (2015), Liou and Yang (2016)).

Over the past decades the natural distribution of ice crystal shape has been investigated by laboratory studies (Magono and Lee, 1966, Bailey and Hallett, 2004, 2009) and in situ measurements (Weickmann, 1947, Heymsfield and Platt, 1984, Field et al., 2005, Heymsfield et al., 2013). Although these methods have been providing more and more detailed information about ice crystal size and shape under various nucleation and growth conditions, they suffer from certain limitations. The nucleation technique used in laboratory studies, for example, can influence the shape of the growing ice crystals and lead to biased results (e.g. Bailey and Hallett (2012)). In situ observations by aircraft probes are spatially limited. Furthermore, due to the high speed of the aircraft, shattering of larger complex ice crystals at the inlets of the in situ probes is an issue which might cause an artificially increased fraction of small particles (Baran (2012) and

references therein).

Therefore, satellite-based methods have been investigated in recent years to retrieve information about ice crystal shape with large spatial and temporal coverage. Retrievals of ice crystal habit from multi-angular satellite measurements were pioneered by Baran et al. (1998, 1999) using radiance measurements at two different viewing angles from the Along Track Scanning Radiometer (ATSR-2). McFarlane and Marchand (2008) present a retrieval using measurements from MISR (Multi-angle Imaging Spectroradiometer) and MODIS (Moderate resolution imaging system) reflectances based on optical properties of single ice crystal habits. Multi-angular polarized reflectances from the Polarization and Directionality of Earth Reflectance (POLDER) have been used to infer information about ice crystal shape (e.g. Descloitres et al. (1998), Chepfer et al. (2001), Baran and Labonnote (2006), Sun et al. (2006) and van Diedenhoven et al. (2012)). However, these studies mainly focused on optically thick cirrus. Ice crystal shapes in thin cirrus clouds were investigated by Wang et al. (2014) and Holz et al. (2016) using a combination of active and passive remote sensing instruments with co-located MODIS and CALIOP (Cloud Aerosol Lidar with Orthogonal Polarization) observations. The majority of studies implies that ice crystals with roughened surface represent the observations better than crystals with smooth faces (Liu et al., 2014, Holz et al., 2016).

In addition to spectral information or polarization signals, another source of information about ice crystal properties is the spatial distribution of refracted and reflected light in the sky, caused by the details of ice crystal scattering characteristics. These scattering features, commonly known as halo displays, can be observed as bright and colorful circles and arcs in the vicinity of the sun. Halo displays are produced by hexagonal ice crystals with smooth faces via refraction and reflection of light. The formation of halo displays has already been described by Wegener (1925) and by a number of later publications (Greenler (1980), Minnaert (1993) and Tape (1994)). Figure 1.1 illustrates the most frequent halo displays: the 22° halo (top left) is formed by randomly oriented hexagonal ice crystals and appears as a bright ring around the sun at a scattering angle of about 22°. The 22° parhelia, commonly called sundogs, are caused by light refracted by horizontally oriented hexagonal plates. The top right image in Fig. 1.1 shows a bright sundog on the right side of the sun. Upper and lower tangent arcs, which are produced by oriented ice crystal columns, are presented on the lower left in Fig. 1.1. Their shape depends on the solar elevation. For small solar elevations the upper and lower tangent arcs are separated. They merge for larger solar elevations to form an elliptical ring around the 22° halo, as depicted on the lower right image in Fig. 1.1. The merged tangent arcs are called circumscribed halo. As the sun approaches the zenith, the initially elliptical circumscribed halo becomes more and more spherical until it is almost indistinguishable from the 22° halo. Halos are not only beautiful optical displays but also contain valuable information about ice particle size, shape and orientation (Lynch and Schwartz, 1985, Sassen et al., 1994, van Diedenhoven, 2014, Flatau and Draine, 2014). van Diedenhoven (2014) showed that the brightness contrast of the 22° halo in ice crystal scattering phase functions is related to the aspect ratio and surface roughness of the crystals. Quantitative analysis of the frequency of occurrence as well as brightness contrast of halo displays can therefore help determine ice crystal shape, surface roughness and orientation in cirrus clouds.

Probably the first reported photometric measurements of halo displays were performed by Lynch and Schwartz (1985), who took a photo of a 22° halo around the moon with a Kodak film camera. After digitizing the photo, the relative brightness and width of the 22° halo were analyzed and possible ice crystal sizes and shapes were discussed based on theoretical considerations. In the 1990s, many halo observations have been collected by amateur observing networks (Pekkola, 1991, Verschure, 1998), which is work-intensive and requires substantial personnel. To the author's

Figure 1.1: *Examples of halo displays observed at the Meteorological Institute of the LMU in Munich. The sun is blocked by a black circular shade to avoid stray light and saturation of the camera sensor. Top left:* 22° *halo. Top right: right-hand* 22° *parhelia or sundog. Bottom left: faint* 22° *halo with upper and lower tangent arc. Bottom right:* 22° *halo with circumscribed halo.*

knowledge, the largest dataset so far has been collected by the German "Arbeitskreis Meteore e.V. Sektion Halobeobachtungen" (AKM, `https://www.meteoros.de`). The community was founded in 1990 and consists of a network of about 80 volunteers who collect halo observations on a monthly basis throughout Germany, Austria, Romania and the UK. Since 1986 more than 150 000 observations of halo displays have been reported. AKM collects information about the halo type and its duration, the type of cloud producing the halo display, the weather situation during the observation (frontal system, precipitation) and more. An extensive long-term observation study of high-level clouds and halo displays was performed by Sassen et al. (2003b), who evaluated a ∼10 year record of halo observations, accompanied by polarization lidar measurements at the Facility for Atmospheric Remote Sensing (FARS) in Salt Lake City, Utah. This study is also based on visually collected halo observations. A fisheye camera, which took pictures every 20 min, was used in this study in combination with field notes and extra photographs to monitor optical displays.

So far, halo displays were investigated regarding ice crystal properties only qualitatively in single case studies. Long-term studies have focused primarily on the frequency of halo displays with high personnel effort. Ice crystal orientation and macrophysical properties of the cirrus clouds, such as height and temperature, were investigated (Sassen et al., 2003b). To the author's knowledge, no systematic analysis of halo observations regarding ice crystal properties, such as ice crystal size, shape and surface roughness, exists to date.

This thesis aims to investigate the information content of halo displays regarding ice crystal properties, which comprise ice crystal size, shape, surface roughness, and orientation in cirrus clouds.

This endeavor was approached with the following strategy:

- The information content of halo displays has to be investigated via a systematic analysis of ice crystal properties under single and multiple scattering conditions.
- In order to investigate ice crystal orientation, a method has to be developed to allow radiative transfer simulations of oriented ice crystals.
- To test the information content under realistic conditions, a retrieval needs to be developed and applied to observations of halo displays.
- For a final assessment of the developed retrieval, it should be applied to long-term observations, which can be achieved by an automated observation and data evaluation method.

To perform automated halo observations, the weather-proof camera system HaloCam was designed featuring a sun-tracking mount and a wide-angle lens, providing images with high temporal and spatial resolution. This thesis presents, to the author's knowledge, the first automated, continuous and long-term camera observations of halo displays. Together with HaloForest, a newly developed automated detection algorithm for halo displays, the HaloCam system provides consistent long-term observations of halo displays. Both the HaloCam camera system and the halo detection algorithm are described in Forster et al. (2017). Furthermore, this is, to the author's knowledge, the first study using calibrated radiance observations of 22° halos to systematically investigate the ice crystal optical and microphysical properties of the halo-producing cirrus clouds with radiative transfer models. To allow simulation of oriented crystals, the raytracing algorithm CrystalTrace was developed and implemented into the Monte Carlo model MYSTIC (Mayer, 2009), which is part of the radiative transfer library libRadtran (Mayer and Kylling, 2005). This combination of CrystalTrace and MYSTIC allows radiative transfer simulation of oriented ice crystals accounting for multiple scattering and interaction with aerosol and surface albedo.

Following a brief overview over the underlying theoretical concepts and equations in Chapter 2, methods developed and used in this thesis will be presented in Chapter 3. First, ice crystal single scattering properties are investigated and suitable parameters are determined to retrieve information about ice crystal microphysical properties. All presented tools and methods were developed within this work with exception of the radiative transfer library libRadtran with the MYSTIC and DISORT solvers, the ice crystal optical property database and the specMACS instrument. Chapter 4 presents statistics of halo displays obtained during the ACCEPT campaign. Long-term HaloCam observations of 22° halos in Munich were evaluated with the automated halo detection algorithm HaloForest. Using calibrated radiance measurements, the RICO retrieval of ice crystal properties is applied to specMACS observations for two case studies and to long-term HaloCam observations. With CrystalTrace a method is proposed to retrieve the fraction of oriented ice crystals from observations of upper tangent arcs and sundogs together with 22° halos. The findings of this thesis are discussed and compared to previous results in Chapter 5. Key findings and conclusions are summarized in Chapter 6 and ideas for future applications of HaloCam are provided in Chapter 7.

Chapter 2

Theory

This chapter provides the theoretical basis for this work which focuses on the remote sensing of cirrus clouds and halo displays. Halo displays are produced by refraction and reflection of light by ice crystals. The formation of ice crystals and cirrus clouds, which are a prerequisite for the formation of halo displays, are described in the first section of the theory chapter. The second section presents the basic radiative laws used in this study including the radiative transfer equation. The optical properties of molecules, aerosol and ice crystals necessary for radiative transfer simulations are described. Combining the radiative with the ice crystal microphysical principles, the final section of this chapter explains the formation of halo displays.

2.1 Ice crystals and cirrus clouds

The following sections provide a description of the formation of cirrus clouds which consist primarily of ice crystals. The description of their macro- and microphysical properties mainly follows Rogers and Yau (1996), Wallace and Hobbs (2006), Lynch et al. (2002), Lamb and Verlinde (2011), and Liou and Yang (2016).

2.1.1 Formation of cirrus clouds

Clouds in the atmosphere form when the air becomes supersaturated with respect to liquid or ice water and water vapor condenses. The most frequent way of reaching a state of supersaturation is the rise of an air parcel accompanied by adiabatic cooling. In the upper troposphere where the temperatures are well below 0 °C, ice clouds form. This study focuses on the properties of thin high-level ice clouds, which are separated by the WMO (World Meteorological Organization, 2017) into three types according to their morphology: cirrus, cirrocumulus and cirrostratus. Cirrus clouds are composed of ice crystals and have a transparent and wispy, sometimes feather- or veil-like, appearance against the blue sky. They typically occur at altitudes greater than 6 km and consist entirely of ice crystals for temperatures less than about −38 °C (Wylie and Menzel, 1999, Baran, 2012, Guignard et al., 2012). A typical example of a cirrus cloud is displayed in Fig. 2.1.

As described in Liou and Yang (2016) cirrus clouds mainly form by synoptic-scale disturbances such as jet streams, closed upper-levels lows, frontal overriding, etc. with relatively weak mean vertical lifting rates. Cirrus clouds usually develop from top to lower levels but they can also be generated by strong thunderstorm updrafts producing anvil-cirrus. Other formation mechanisms are orographic processes and the rapid cooling of aircraft exhausts, which forms condensation trails, short contrails. Persistent contrails and contrail cirrus, which also consist of ice crystals, were recently added to the International Cloud Atlas of the World Meteorological Organization.

Figure 2.1: *Example of a cirrus cloud from World Meteorological Organization (2017).*

Contrails are called cirrus homogenitus, since they are formed as a consequence of human activity. Contrail cirrus occurs when persistent contrails spread out over time by strong upper-level winds and transform to more natural-looking cirrus clouds. These clouds are called cirrus homomutatus. Ice clouds also form in the middle atmosphere: the polar stratospheric ice clouds, called nacreous or mother-of-pearl clouds, form between 20 km to 30 km at high latitudes in the winter stratosphere. Polar mesospheric clouds, called noctilucent clouds, form in about 82 km in the summer mesosphere when the lowest temperatures occur (e.g. Baumgarten et al. (2008)).

Having outlined the macrophysical formation of cirrus clouds, their microphysics will be described in the following in terms of the formation and growth of ice crystals.

2.1.2 Formation and growth of ice crystals

Water can exist in three thermodynamic states: vapor, liquid, and ice. Essentially all ice in the Earth's biosphere is ice *Ih*, the hexagonal crystal form of ordinary ice. Stable down to $-200\,°C$ it has a density of $0.917\,g\,cm^{-3}$ (Liou and Yang, 2016). In rare cases the structure of ice can exhibit dodecagonal, bullet pyramidal and pyramidal shape. The majority of ice crystals owe their hexagonal (six-fold) shape to the hexagonal molecular symmetry within the crystal. Ice crystals in the atmosphere can form either by homogeneous or heterogeneous nucleation. Homogeneous freezing or sublimation occurs when water molecules produce a stable ice-like structure by statistical fluctuations which can serve as ice nuclei. However, extremely high supersaturation is required for homogeneous freezing which rarely occurs in the atmosphere. At temperatures slightly below $0\,°C$, supersaturation of more than a factor of 20 with respect to ice is necessary for homogeneous nucleation. Liou and Yang (2016) state that droplets smaller than $5\,\mu m$ freeze homogeneously only at temperatures of $-40\,°C$ or lower.

In the atmosphere clouds at a temperature of $-15\,°C$ already contain a significant amount of ice crystals. These ice crystals are formed by heterogeneous nucleation. Ice crystals form either by contact freezing or deposition on most materials. The required supersaturation and supercooling for contact freezing or deposition, i.e. heterogeneous nucleation, is significantly smaller than for homogeneous nucleation. Supersaturation in conjunction with supercooling as well as the material properties influence the probability of heterogeneous nucleation. Common materials for ice nuclei are clay materials, especially kaolinite, bacteria, and meteoric material. The concentration of ice nuclei, which are necessary for heterogeneous nucleation, is decreasing with height. Thus, supercooled water droplets at $-15\,°C$ and below are not uncommon, whereas for temperatures lower than $-35\,°C$ supercooled water clouds are rarely found (e.g. Hogan et al.

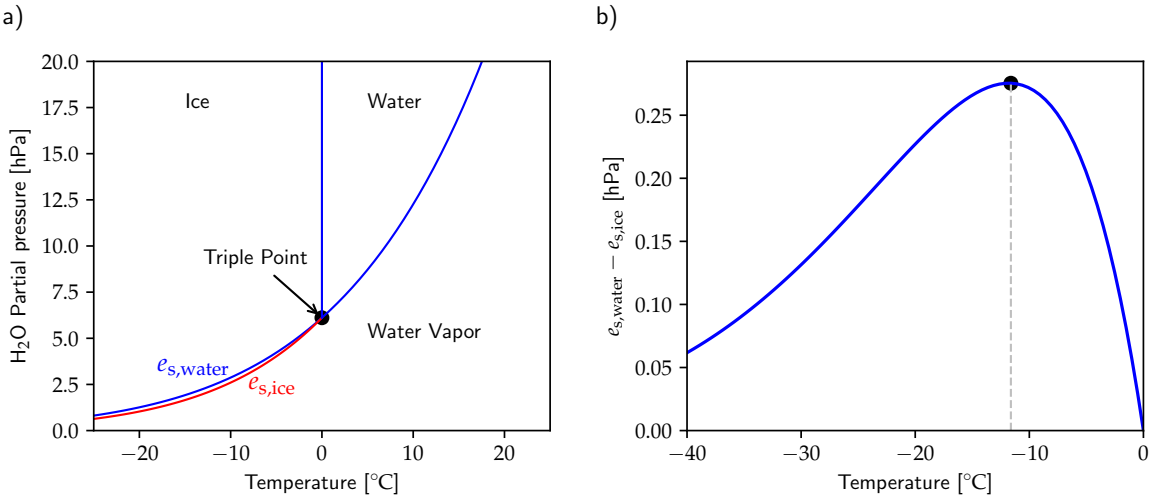

Figure 2.2: *(a) Phase diagram of water illustrating the saturation vapor pressure as a function of temperature for the ice, water and vapor phase of the water molecules. The triple point is indicated by a black dot. The red and blue lines below 0 °C represent the saturation vapor pressure over ice and water, respectively. (b) Difference between the saturation vapor pressure of water and ice as a function of temperature with a maximum at about −12 °C. Calculations based on the equations in Sonntag (1990).*

(2004) and Hu et al. (2010)). Secondary ice crystals can be produced by shattering of ice crystals when they collide with large graupel particles. Another formation mechanism for secondary ice crystals is splintering of freezing water droplets.

The mass increase of a growing ice particle is governed by the diffusion process. How the saturation vapor pressure e_s changes with temperature T is described by the Clausius-Clapeyron equation

$$\frac{de_s}{dT} = \frac{\mathcal{L}_v \, e_s}{R_v \, T^2} \, , \tag{2.1}$$

with the specific latent heat $\mathcal{L}_v$ for water or ice, respectively, and R_v the specific gas constant for water vapor. Its integrated form gives the exponential increase of the saturation vapor pressure with temperature:

$$\frac{e_s(T)}{e_0} = \exp\left[\frac{\mathcal{L}_v}{R_v}\left(\frac{1}{T_0} - \frac{1}{T}\right)\right] \, , \tag{2.2}$$

where $e_0 (= 6.11\,\text{hPa})$ is the value at the triple point with a temperature of $T_0 (= 273.15\,\text{K})$ at which vapor, liquid, and ice phase can coexist (black dot in Fig. 2.2a). The saturation vapor pressure over ice (red curve in Fig. 2.2a) is smaller than over supercooled water (blue curve in Fig. 2.2a) at the same temperature due to the different latent heat at the transition. With help of the time-dependent second-order diffusion equation

$$\frac{\partial n}{\partial t} = \mathcal{D} \, \nabla^2 \, n \tag{2.3}$$

the concentration of molecules n can be described at any point in the water vapor field with the molecular diffusion coefficient $\mathcal{D}$. Under the assumption that the system is in equilibrium and imposing boundary conditions at the positions of the ice particle ($\rho_v(s)$) and ambient air ($\rho_v(\infty)$), the growth equation for an ice crystal can be described by

$$\frac{dm}{dt} = 4\pi \, C \, \mathcal{D} \, [\rho_v(\infty) - \rho_v(s)] \, , \tag{2.4}$$

where $\rho_v(\infty)$ denotes the vapor density of the ambient air and $\rho_v(s)$ at the ice crystal surface. The non-sphericity of ice crystals is accounted for by the parameter C which depends on the size and shape of the ice crystal. While for a spherical particle $C = r$, a circular disk of radius r is parameterized by $C = 2r/\pi$ which can be used as an approximation for ice crystal plates. The shape of needles can be approximated by prolate spheroids. The saturation ratio with respect to ice S_{ice} is defined by

$$S_{ice} = e/e_{s,ice}\,, \tag{2.5}$$

with the water vapor pressure of the ambient air e and the saturation pressure over ice $e_{s,ice}$. Using the Clausius-Clapeyron equation and Eq. (2.5), an analytical expression can be derived for the ice crystal growth:

$$\frac{dm}{dt} = \frac{4\pi\, C\,(S_{ice} - 1)}{(f_k + f_{\mathcal{D}})}\,, \tag{2.6}$$

where

$$f_k = \mathcal{L}^2/(K\, R_v\, T^2) \text{ and } f_{\mathcal{D}} = R_v\, T/(\mathcal{D}\, e_{s,ice})\,, \tag{2.7}$$

with ambient temperature T, thermal conductivity K and latent heat $\mathcal{L}$. The growth rate is a function of temperature and inversely proportional to pressure. In a cloud containing supercooled water droplets the air is saturated with respect to liquid water and therefore supersaturated with respect to ice (cf. Fig. 2.2a). Supersaturation ranges from 10 % at −10 °C to 21 % at −20 °C (Wallace and Hobbs, 2006). This allows ice particles to grow by sublimation from the vapor phase at the expense of the water droplets, which is called Wegener-Bergeron-Findeisen process (Wegener, 1926, Bergeron, 1935, Findeisen, 1938). Liou and Yang (2016) state that the growth rate of ice crystals via this process reaches its maximum at a temperature of about −12 °C, as shown in Fig. 2.2b. A contribution to the different morphology of ice and water clouds is the lower equilibrium vapor pressure over ice compared to water at the same temperature (cf. Fig. 2.2). This enables ice particles to survive longer in the non-saturated air surrounding the cloud producing the feather-like appearance of ice clouds as well as fallstreaks or virgae (Wallace and Hobbs, 2006).

Ice crystals are formed by diffusion of water vapor and grow further by accretion, which consists of collision and coalescence. Growth by collision is determined by the ice crystal fall speed. For ice crystal aggregation the collection efficiency strongly depends on the ice crystal shape, since dendrites are more likely to stick together than compact particles. Moreover, it is favored by warmer temperatures, particularly above about −5 °C where ice surfaces become sticky. In a mixed phase cloud ice particles grow by riming which describes the process of an ice crystal capturing supercooled water droplets which subsequently freeze upon it. Particle shapes range from rimed needles, columns, plates, to stellars which will finally loose their shape and turn into graupel particles.

2.1.3 Ice crystal shape

Ice crystals have a common shape with a six-fold (hexagonal) symmetry which can be realized in a range of different axis ratios. Simple hexagonal crystals have two basal faces and six prism faces as shown in Fig. 2.3. The hexagonal axes a_1, a_2, a_3, and c in Fig. 2.3 define the orientation of the crystal lattice. Growing ice crystals exhibit non-spherical shapes due to non-uniform deposition coefficients which affect the growth rates across the crystal surface. Their specific shape depends on temperature and ice supersaturation (e.g. Magono and Lee (1966)). Ice crystal shapes can be separated into plates and columns, which are called primary habits and provide a first-order category for the classification of ice crystal shapes (Lamb and Verlinde, 2011). The formation of these primary ice crystal habits is mainly determined by the ambient temperature

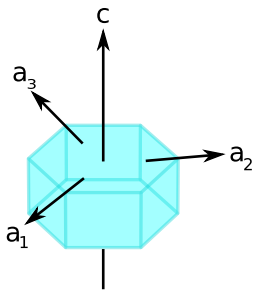

Figure 2.3: *Ice crystal geometry. Following the definition in Liou and Yang (2016) the c-axis is perpendicular to the base and top faces of the ice crystal. The three a_i-axes are defined perpendicular to the c-axis and coincide with the intersections of two neighboring crystal side faces.*

(cf. Fig. 2.4). Bailey and Hallett (2009) present a comprehensive ice crystal habit diagram based on both laboratory studies and field observations using the Cloud Particle Imager (CPI) as shown in Fig. 2.4. They report plate-like shapes from −20 °C to −40 °C and columnar shapes from −40 °C to −70 °C. With increasing supersaturation the ice crystal shapes become more and more complex. At temperatures below −20 °C mostly polycrystalline particles occurred. Between −10 °C to −20 °C a variety of plate types, crystals with sector-like branches, fern-like, ordinary dendritic, and stellar crystals as well as hexagonal plates were observed. For temperatures between −20 °C to −40 °C, hollow columns, hollow bullet rosettes and aggregates occur. Bailey and Hallett (2009) stated that most ice crystals are defective and irregular in shape to varying degrees. They also found that most individual crystals are complex, irregular, and imperfect including single crystals such as plates and columns. It was also pointed out that very small ice crystals growing at low ice supersaturation are mainly compact faceted polycrystals, not spheroids, as suggested in previous publications (Bailey and Hallett, 2009). The spatial distribution of water vapor and temperature is modified by the primary crystal habit and influences the shape of the further growing ice crystal. Primary habits such as columns, plates and dendrites are modified when the ice crystals grow or move around in the cloud according to temperature and saturation. For example plates can develop peripheral dendritic structure which forms sector stars or columns can grow plates on their ends and turn into capped columns.

Ice crystal sizes in cirrus clouds span values from a few to thousands of microns. Figure 2.5 shows the definition of the ice crystal dimensions for columnar (a) and plate-like crystals (b). The length of the c-axis is referred to by L, while the maximum diameter of the ice crystal top and base faces is denoted by $2a$. For certain ice crystal types the length L and diameter $2a$ are related which was found in laboratory and field observations (Auer and Veal, 1970, Heymsfield, 1972). From these observations Mitchell and Arnott (1994) derived the following empirical relationship for columns:

$$2a = 0.7000\, L^{1.0} \qquad \text{for } L \leq 100\,\mu\text{m}\,, \tag{2.8}$$

$$2a = 0.0696\, L^{0.5} \qquad \text{for } L > 100\,\mu\text{m}\,. \tag{2.9}$$

In synoptically generated cirrus, typical for the mid-latitudes, the ice crystal size tends to increase with cloud depth (Lynch et al., 2002, Baran, 2012). Ice production occurs in the topmost layer, called nucleation layer, which is supersaturated with respect to ice and contains small, single ice crystals. While sedimenting into the deeper cloud layers, the ice crystals can grow from tens of microns up to several cm in size (Heymsfield and Miloshevich, 2003). Growth is mainly due to deposition of water vapor and aggregation. At the cirrus cloud base sublimation takes place due to the dry air below and leads to rounded crystal edges.

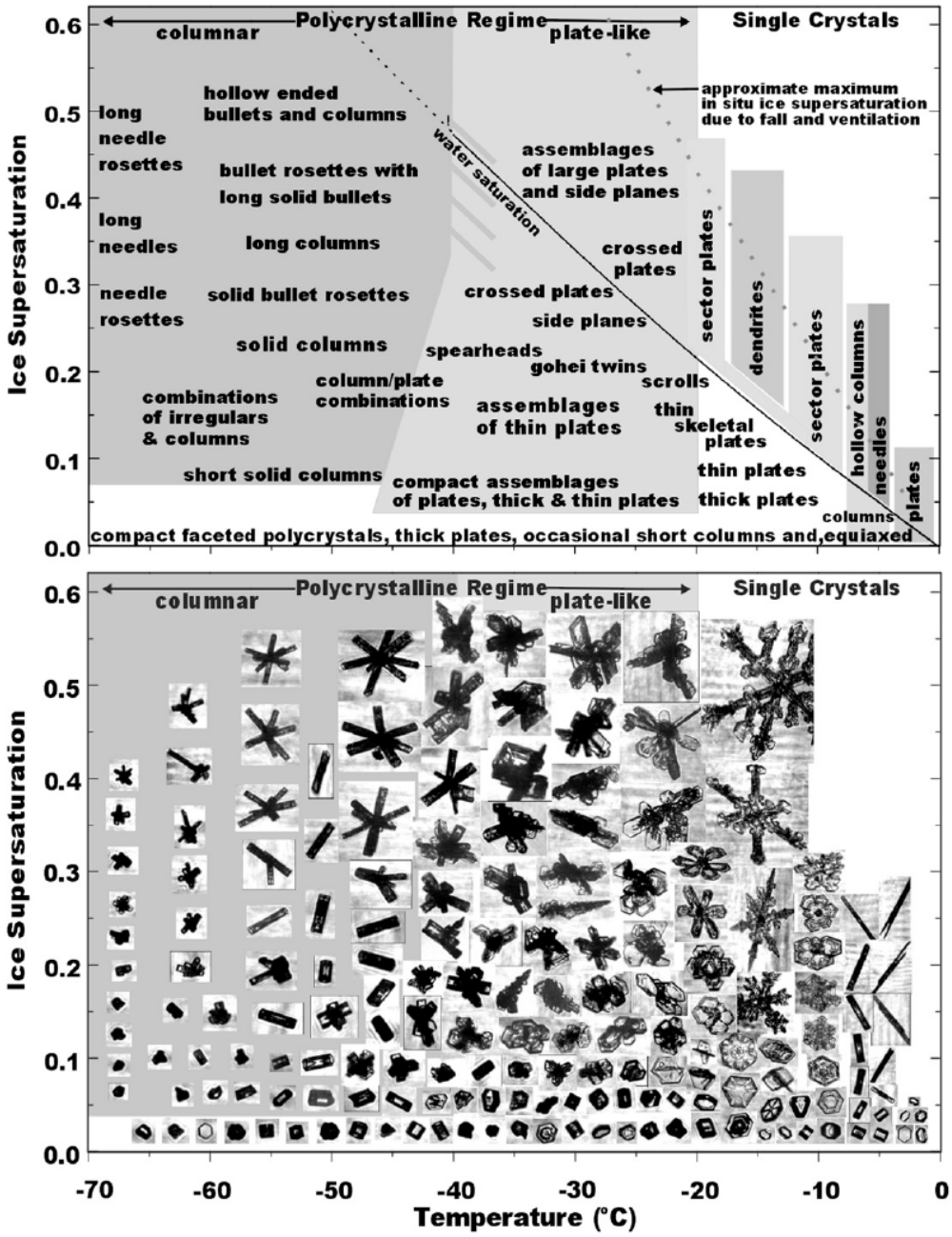

Figure 2.4: *Ice crystal morphology as a function of temperature and supersaturation (Bailey and Hallett, 2009).* ©*American Meteorological Society. Used with permission.*

Larger ice crystals tend to take preferred orientations while falling. Jayaweera and Mason (1965) found that cylinders tend to fall with their long axes horizontal in a viscous fluid if the ratio of diameter ($2a$) to the maximum dimension (L) is less than 1, i.e. $2a < L$. Ono (1969) observed freely falling columnar and plate crystals in natural ice clouds. The author confirmed that columnar crystals are oriented with a horizontal c-axis, whereas plates are oriented with a vertical c-axis while falling. Platt (1978) performed lidar backscatter measurements and found predominantly plate-shaped ice crystals which were oriented horizontally in cirrus clouds at approximately $-15\,°\mathrm{C}$.

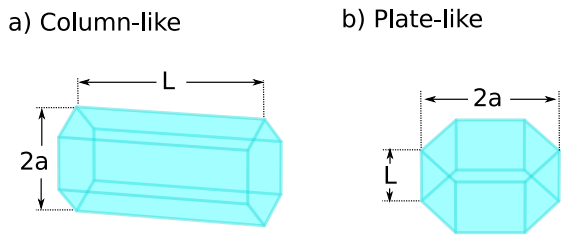

Figure 2.5: *Definition of ice crystal dimensions. The length of the c-axis is denoted by L. The maximum diameter of the ice crystal top and base is defined by $2a$.*

2.1.4 Cirrus microphysical properties

Depending on the excess of water vapor and temperature the ice crystals grow to slightly different sizes within a certain cloud volume. This ensemble of ice crystals can be described by a size distribution, relating the particle size with the number concentration. The size of single ice crystals is usually measured by their maximum dimension D, which corresponds to the length of the c-axis L for columns and the diameter $2a$ for plates for example. The size distribution of ice crystals is most commonly parameterized by a gamma distribution (Heymsfield et al., 2013)

$$N(D) = N_0 \, D^{\mu} \, \exp\left(-\lambda D\right), \tag{2.10}$$

with the particle maximum dimension D, the intercept N_0, the dispersion μ and the slope λ. According to Heymsfield et al. (2013) μ typically takes values between about 0 and 2, whereas λ ranges between about $10\,\mathrm{cm}^{-1}$ to $100\,\mathrm{cm}^{-1}$ for stratiform clouds and temperatures between $0\,^{\circ}\mathrm{C}$ to $-50\,^{\circ}\mathrm{C}$. With increasing temperature the particle size distribution broadens and the dispersion μ decreases. Assuming a certain particle size distribution N, the total projected area per unit volume of air A_{tot} and total volume of ice per unit volume of air V_{tot} are determined by

$$A_{\mathrm{tot}} = \int_{\mathrm{D_{min}}}^{\mathrm{D_{max}}} A(D)\, N(D)\, dD\,, \tag{2.11}$$

and

$$V_{\mathrm{tot}} = \int_{\mathrm{D_{min}}}^{\mathrm{D_{max}}} V(D)\, N(D)\, dD\,, \tag{2.12}$$

where D_{min} and D_{max} denote the lower and upper boundary of the maximum dimension, N is the number concentration and $A(D)$ and $V(D)$ are the projected area and volume of a specific particle with maximum dimension D. The ice water content (IWC) is defined by

$$\mathrm{IWC} = \rho_{\mathrm{ice}} \int_{D_{\mathrm{min}}}^{D_{\mathrm{max}}} V(D)\, N(D)\, dD = \rho_{\mathrm{ice}}\, V_{\mathrm{tot}}\,, \tag{2.13}$$

with $\rho_{\mathrm{ice}} = 0.917\,\mathrm{g\,cm}^{-3}$. As discussed by McFarquhar and Heymsfield (1998) there are different ways to define the effective radius r_{eff}. Throughout this study the definition

$$r_{\mathrm{eff}} = \frac{3}{4}\,\frac{V_{\mathrm{tot}}}{A_{\mathrm{tot}}} \tag{2.14}$$

will be used. In general, the particle size distribution evolves from cloud top to cloud base: ice crystal size increases and ice crystal shapes become increasingly more complex toward the cloud base (Baran (2012) and references therein).

2.2 Radiation and atmospheric radiative transfer

In order to provide a basic understanding of ground-based remote sensing of halo displays, this section gives an overview over the characteristics of light and basic radiation laws, as well as interactions of light with atmospheric constituents. Finally, these interactions are brought together in the radiative transfer equation, which describes the emission, absorption and scattering of photons traveling through the atmosphere.

2.2.1 Radiative properties and physical description

Solar and thermal spectrum

Table 2.1: *Classification of electromagnetic radiation for the solar and thermal spectrum according to Thomas and Stamnes (1999).*

Subregion	Range	Description
X rays	$\lambda < 10\,\mathrm{nm}$	Gamma radiation
UV	$10\,\mathrm{nm} < \lambda < 400\,\mathrm{nm}$	Ultra violet light
VIS	$400\,\mathrm{nm} < \lambda < 700\,\mathrm{nm}$	Visible light
Near IR	$0.7\,\mu\mathrm{m} < \lambda < 3.5\,\mu\mathrm{m}$	Near infrared light
Thermal IR	$3.5\,\mu\mathrm{m} < \lambda < 100\,\mu\mathrm{m}$	Thermal infrared light

Table 2.1 describes the classification of the electromagnetic spectrum into specific regimes, where the wavelength of the radiation λ is defined by

$$\lambda = \frac{c}{\nu} = \frac{2\pi c}{\omega}\,, \tag{2.15}$$

with the speed of light c measured in $[\mathrm{m\,s^{-1}}]$ and the (angular) frequency ν (ω) in $[\mathrm{s^{-1}}]$ with $\omega = 2\pi\nu$. For remote sensing applications it is convenient to separate the spectrum of the light into two main regimes: the solar and the thermal spectrum with the transition at a wavelength of about 3.5 µm according to Thomas and Stamnes (1999). This study focuses on the solar spectrum and more precisely on the visible spectral range between 400 nm and 700 nm.

Radiative quantities

A beam of radiation is commonly described by its radiant energy Q with units [J]. The radiant energy per unit time dt is called radiant flux Φ, which is calculated by $\Phi = \frac{\mathrm{dQ}}{\mathrm{dt}}$ with the unit [W]. Throughout this study two radiative quantities are commonly used, the spectral irradiance E and the spectral radiance L:

$$E = \frac{\mathrm{dQ}}{\mathrm{dA}\;\mathrm{d}\lambda\,\mathrm{dt}} \qquad [\mathrm{W\,m^{-2}\,nm^{-1}}] \tag{2.16}$$

$$L = \frac{\mathrm{dQ}}{\mathrm{dA}\;\mathrm{d}\Omega\;\mathrm{d}\lambda\,\mathrm{dt}} \qquad [\mathrm{W\,m^{-2}\,nm^{-1}\,sr^{-1}}] \tag{2.17}$$

The spectral irradiance E is defined as the variation of the radiating energy dQ by unit area dA, time dt and wavelength dλ. Note, that in this definition the unit area dA is perpendicular to

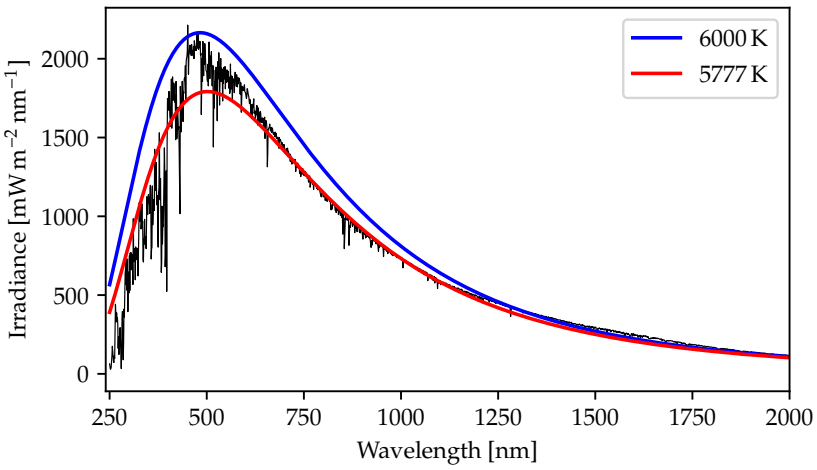

Figure 2.6: *Spectrum of the solar radiation at the top of the atmosphere (black) based on data from Kurucz (1992). The blue and red curves represent the emitted irradiance from an ideal blackbody at* 6000 K *and* 5777 K*, respectively.*

the incident direction. The spectral radiance L additionally takes into account the direction of the incident radiation as an element of the unit solid angle $\mathrm{d}\Omega$. Subsequently, an introduction to some fundamental radiative laws is provided following primarily Thomas and Stamnes (1999) and Zinth and Zinth (2005).

Basic radiative laws

The solar spectrum, measured at the top of the atmosphere, is very similar to the radiation spectrum of a blackbody with a temperature of 5778 K (Thomas and Stamnes, 1999). **Planck's radiation law** describes the spectral radiance of a blackbody as a function of its temperature

$$B_{\mathrm{Planck}}(\lambda, T) = \frac{2hc^2}{\lambda^5} \left[\exp\left(\frac{hc}{\lambda k_{\mathrm{B}} T} \right) - 1 \right]^{-1} , \tag{2.18}$$

with Planck's constant h, the speed of light in vacuum c and Boltzmann's constant k_{B}. The red and blue curves in Fig. 2.6 result from Eq. (2.18) integrated over the half space, which yields the irradiance. Integrating Planck's radiation law in addition over the wavelength gives the irradiance as a function of the blackbody temperature, known as **Stefan-Boltzmann's law**

$$E_{\mathrm{Planck}}(T) = \pi \cdot \int_0^\infty B_{\mathrm{Planck}}(\lambda, T)\, d\lambda = \sigma_{\mathrm{B}}\, T^4 , \tag{2.19}$$

where $\sigma_{\mathrm{B}} = 2\pi^5 k_{\mathrm{B}}^4 / 15 h^3 c^2$ is called Stefan-Boltzmann's constant.

Bouguer-Lambert-Beer's law describes the attenuation of the radiance dL along the path length ds through an extincting substance of concentration n

$$dL = -L \cdot n \cdot \sigma_{\mathrm{ext}}\, ds , \tag{2.20}$$

with the extinction cross section σ_{ext}. The extinction cross section is the sum of the absorption and the scattering cross section

$$\sigma_{\mathrm{ext}} = \sigma_{\mathrm{abs}} + \sigma_{\mathrm{sca}} . \tag{2.21}$$

The optical thickness along a tilted path of light s' is defined by

$$\tau_\mathrm{s} = \int_0^s k_\mathrm{ext}(s')\, ds' \,, \tag{2.22}$$

with the extinction coefficient

$$k_\mathrm{ext} = n \cdot \sigma_\mathrm{ext} \,. \tag{2.23}$$

Solving the integral over ds in Eq. (2.20) results in the integrated form of Bouguer-Lambert-Beer's law:

$$L(s) = L(0) \cdot \exp(-\tau_\mathrm{s}) \,. \tag{2.24}$$

In a plane-parallel atmosphere the extinction coefficient k_ext is only a function of height z. For such a plane-parallel atmosphere the optical thickness τ is defined by the integral of the extinction coefficient k_ext along the vertical direction

$$\tau = \int_0^z k_\mathrm{ext}(z')\, dz' \,, \tag{2.25}$$

or $d\tau = -k_\mathrm{ext}\, dz$ using the differential notation.
A path element ds tilted by an angle θ with respect to dz can be calculated by $ds = dz/\cos\theta = dz/\mu$ with $\mu < 0$ for upward and $\mu > 0$ for downward directed radiances. Using

$$\tau = \int_s^\infty k_\mathrm{ext}(s') \cdot \cos\,\theta\, ds' = \cos\,\theta \cdot \tau_\mathrm{s} = \tau_\mathrm{s} \cdot \mu \,, \tag{2.26}$$

the integrated form of Bouguer-Lambert-Beer's law in a plane-parallel atmosphere yields

$$L(\tau) = L(0) \cdot \exp(-\tau/\mu) \,, \tag{2.27}$$

with $\mu > 0$ and the extraterrestrial radiance at the top of the atmosphere $L(0)$ at $\tau = 0$.

2.2.2 Radiative transfer equation

One major focus of this study is the transfer of light through the atmosphere and its interaction with atmospheric components such as clouds, molecules and aerosol particles. These processes are described by the radiative transfer equation, which was first formulated by Chandrasekhar (1960). Following Zdunkowski et al. (2007) the radiative transfer equation in a three-dimensional medium can be expressed as

$$\mathbf{\Omega} \cdot \nabla L = -k_\mathrm{ext} L + \frac{k_\mathrm{sca}}{4\pi} \int_{4\pi} \mathcal{P}(\mathbf{\Omega}' \cdot \mathbf{\Omega})\, L(\mathbf{\Omega}')\, d\mathbf{\Omega}' + k_\mathrm{abs} J^\mathrm{e} \,, \tag{2.28}$$

with the spectral radiance L, the extinction coefficient, which is the sum of the scattering and absorption coefficients, $k_\mathrm{ext} = k_\mathrm{sca} + k_\mathrm{abs}$, the scattering phase function $\mathcal{P}$, the solid angle Ω and the source term J^e. The radiative transfer equation in plane-parallel (one-dimensional) geometry yields

$$\mu \frac{d}{d\tau} L(\tau,\mu,\phi) = \overbrace{L(\tau,\mu,\phi)}^{(1)} - \overbrace{\frac{\omega_0}{4\pi} \int_0^{2\pi} \int_{-1}^{1} \mathcal{P}(\cos\Theta)\, L(\tau,\mu',\phi') d\mu' d\phi'}^{(2)} - \overbrace{(1-\omega_0) B_\mathrm{Planck}(T)}^{(3)} \,, \tag{2.29}$$

using $\mathbf{\Omega} \cdot \nabla L = dL/ds$ and $k_\mathrm{ext}\, ds = k_\mathrm{ext}\, dz/\mu = -d\tau/\mu$ with $\mu = \cos\theta$. The term $\cos\Theta = \mathbf{\Omega}' \cdot \mathbf{\Omega}$ is the cosine of the scattering angle Θ, which is a function of $\theta', \phi', \theta, \phi$. The four angles denote

the zenith and azimuth angle of the incoming direction (θ', ϕ') and the scattered direction (θ, ϕ). $B_{\text{Planck}}(T)$ is the Planckian emission (cf. Eq. (2.18)). Further variables in the radiative transfer equation are: the single-scattering albedo $\omega_0 = k_{\text{sca}}/k_{\text{ext}}$, the optical thickness τ.

In the following, the individual parts of the radiative transfer equation will be explained: Together with the left hand side of Eq. (2.29),

- (1) represents the reduction of radiation due to extinction by atmospheric constituents according to Bouguer-Lambert-Beer's law (Eq. (2.27)),
- (2) characterizes the scattering of the radiation from the direction (θ', ϕ') into the new direction (θ, ϕ), which is determined by the scattering phase function,
- (3) is the contribution of thermal emission to the radiation from the volume element along the propagation direction of the photons following Planck's law (Eq. (2.18)). This study focuses on the visible part of the solar spectrum between 400 nm and 800 nm. In this spectral range the single-scattering albedo $\omega_0 \approx 1$ for ice crystals (Liou and Yang, 2016) and thus, the thermal emission is negligible.

2.2.3 Light scattering by atmospheric particles

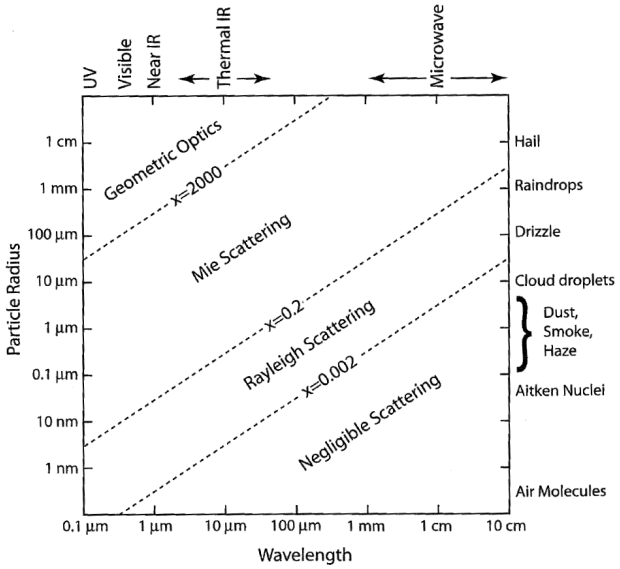

Figure 2.7: *Relationship between particle size, radiation wavelength and scattering behavior for atmospheric particles. Diagonal dashed lines represent rough boundaries between scattering regimes (Petty, 2006).*

The method to describe and calculate the optical properties of scattering particles in the atmosphere depends crucially on the relationship between the size of the particle and the wavelength of the radiation, which is expressed by the size parameter χ:

$$\chi = \frac{2\pi r}{\lambda}\,, \tag{2.30}$$

with wavelength λ and particle radius r. For non-spherical particles different definitions of the size parameter exist in the literature (Um et al., 2015). Throughout this thesis the size parameter of ice crystals is defined by

$$\chi = \frac{\pi D}{\lambda}\,. \tag{2.31}$$

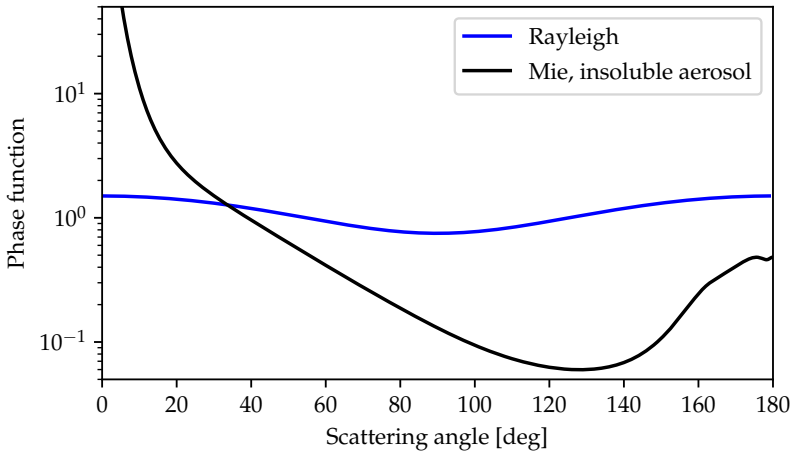

Figure 2.8: *Scattering phase functions for Rayleigh scattering (blue) and Lorentz-Mie theory for an insoluble aerosol (black) at a wavelength of* 550 nm.

As depicted in Fig. 2.7 there are basically three main scattering regimes:

1. Rayleigh or molecular scattering (Strutt (1871), $\chi \ll 1$)
2. Lorentz-Mie theory (Mie (1908), $\chi \approx 1$, only valid for spherical particles)
3. Geometric optics ($\chi \gg 1$)

Molecular and aerosol optical properties

For ground-based remote sensing of cirrus clouds, molecular and aerosol optical properties have to be considered and will briefly be explained in the following. For very small particles in the atmosphere, like molecules, with radii much smaller than the wavelength in the visible spectrum ($r \ll \lambda$), the size parameter $\chi \ll 1$ and Rayleigh scattering can be applied (cf. Fig. 2.7). Named after Lord Rayleigh, who explained 1871 successfully the color and polarization of skylight. The phase function for Rayleigh scattering is defined as

$$\mathcal{P}(\cos\Theta) = \frac{3}{4}(1 + \cos^2\Theta) \tag{2.32}$$

and depicted in Fig. 2.8 with a blue line. The scattering probability is equally maximal in the forward and backward direction and decreases towards its minimum at a scattering angle of $\Theta = 90°$.

A measure for the relative strength of forward scattering is given by the asymmetry factor, which is the first moment of the scattering phase function. The asymmetry factor can be calculated by

$$g = \frac{1}{2}\int_{-1}^{1} \mathcal{P}(\cos\Theta)\,\cos\Theta\; d\cos\Theta\,, \tag{2.33}$$

where $\mathcal{P}(\Theta)$ is the normalized phase function. For Rayleigh scattering $g = 0$, which is equivalent to symmetric scattering. For complete forward or backward scattering the asymmetry factors are $g = 1$ and $g = -1$, respectively. The scattering cross section for Rayleigh scattering is inversely proportional to the 4th power of the wavelength λ (Thomas and Stamnes, 1999):

$$\sigma_{\text{sca}} \propto 1/\lambda^4\,. \tag{2.34}$$

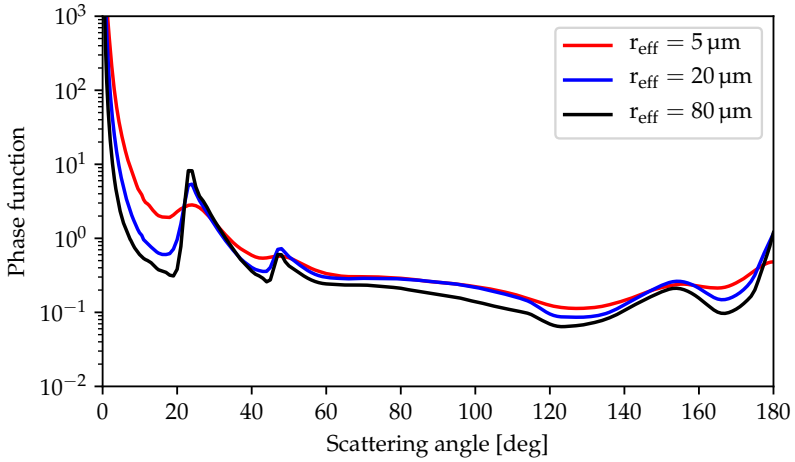

Figure 2.9: *Ice crystal phase functions of smooth solid columns for effective radii of 5 (red), 20 (blue), and* 80 µm *(black) and a wavelength of* 550 nm *from the database of Yang et al. (2013). The* 22° *and* 46° *halo at the respective scattering angles are a geometric optics phenomenon and thus become more pronounced for larger ice crystals.*

Equation (2.34) explains for example why the sky appears blue: the scattering cross section strongly increases for smaller wavelengths. Blue light ($\lambda = 420\,\text{nm}$) is scattered 10 times stronger than red light at 720 nm. During dusk and dawn, light travels much longer distances through the atmosphere, and only the longer wavelengths of the solar radiation reach the observer causing the reddish light of the rising or setting sun. In the Mie regime (cf. Fig. 2.7) the size parameter χ is close to 1. Small aerosol particles have size parameters of $\chi \sim 1$ and a pronounced forward scattering compared to molecules, as shown in Fig. 2.8 by the black line for an insoluble aerosol at $\lambda = 550\,\text{nm}$. In this case the asymmetry factor takes values $g > 0$.

Ice crystal optical properties

Mie theory is only applicable to spherical particles, thus different methods have to be used to calculate the optical properties of non-spherical ice crystals. Liou and Yang (2016) give detailed explanations of available methods for different size parameters, such as the Finite-Difference Time Domain (FDTD) method, the T-matrix method or the Discrete Dipole Approximation. For ice crystals much larger than the wavelength with size parameters $\chi \gg 1$, scattering is predominantly in the forward direction and the geometric optics principles can be applied. Figure 2.9 shows three phase functions of solid ice crystal columns with smooth surface, which are averaged over size distributions with effective radii of $r_{\text{eff}} = 5\,\mu\text{m}$ (red), $r_{\text{eff}} = 20\,\mu\text{m}$ (blue), and $r_{\text{eff}} = 80\,\mu\text{m}$ (black) at a wavelength of 550 nm. The phase functions exhibit a pronounced forward scattering peak and show the 22° and 46° halo at the respective scattering angles. For a given wavelength, the size parameter increases for larger effective radii and the halo peaks become more pronounced. Like rainbows, halo displays are a geometric optics phenomenon. Thus, the optical properties of large ice crystals can be calculated using the geometric optics approximation. According to Liou and Yang (2016), the scattering phase function of an ensemble of non-spherical ice particles of the same size and random orientation can be expressed by

$$\mathcal{P}(\Theta) = \frac{1}{2\pi\sigma_{\text{sca}}} \int_0^{2\pi} \int_0^{\pi/2} \mathcal{P}'(\alpha', \gamma')\sigma'_{\text{sca}}(\alpha', \gamma') \sin\alpha' d\alpha' d\gamma' \,, \tag{2.35}$$

where α' and γ' are the orientation angles relative to the direction of the incident light beam and $\mathcal{P}'$ is the scattering phase function for a single particle. For randomly oriented particles the scattering phase function depends solely on the scattering angle Θ. Integrated over the scattering angle Θ and the azimuth angle ϕ, the phase function is normalized to unity:

$$\int_0^{2\pi} \int_0^{\pi} \frac{\mathcal{P}(\Theta)}{4\pi} \sin\Theta \, d\Theta d\phi = 1 \,. \tag{2.36}$$

For horizontally oriented ice crystals (cf. Section 2.1.3) the scattering phase function can be written as

$$\mathcal{P}(\alpha, \gamma; \mu', \phi'; \mu, \phi) = \mathcal{P}(\alpha', \gamma'; \cos\Theta, \Delta\phi) \,, \tag{2.37}$$

with $\Delta\phi = \phi - \phi'$. The phase function depends on the directions of the incident (α', γ') and the scattered beams (α, γ) as well as the orientation of the non-spherical ice crystal. The extinction and scattering cross-sections σ_{ext} and σ_{sca}, however, depend only on the direction of the incident light and the ice crystal orientation.

For a symmetric hexagonal ice crystal two orientation angles can be defined with respect to the direction of incident light: α the complement of the zenith angle and β the angle projected on the x-y plane relative to the incident beam. The surface area of the ice crystal basal face is $3\sqrt{3}D^2/8$ and $D\,L$ for the prism faces. The cross-sectional area for the basal plane of the ice crystal mapped along the light beam is $3\sqrt{3}D^2/8 \sin\alpha$. For the prism plane the cross-sectional area also depends on the angle of the light beam relative to the six prime planes, which should be maximum for $\beta = \pi/6$. This yields $DL \cos\alpha \cos(\pi/6 - \beta)$. Thus, the geometric cross-section for the entire hexagonal crystal can be written as

$$G(\alpha, \beta) = \frac{3\sqrt{3}}{8} D^2 \sin\alpha + DL \cos\alpha \cos(\pi/6 - \beta) \,. \tag{2.38}$$

To obtain the average cross-section for randomly oriented ice crystals the previous equation is integrated over α and β:

$$\overline{G} = \frac{6}{\pi} \int_0^{\pi/6} \int_0^{\pi/2} G(\alpha, \beta) \cos\alpha \, d\alpha d\beta = \frac{3}{4}(\sqrt{3}D^2/4 + DL) \,. \tag{2.39}$$

The surface of a hexagonal ice crystal is $S = 3(\sqrt{3}D^2/4 + DL)$. The extinction efficiency is defined as $Q_{\text{ext}} = \sigma_{\text{ext}}/G$ and approaches 2 in the geometric optics approximation, which is called the optical extinction theorem. In the geometric optics limit the extinction cross-section is $\sigma_{\text{ext}} = 2\overline{G} = S/2$. Thus the average geometric cross-section for randomly oriented hexagonal ice crystals (plates, columns) yields $\overline{G} = S/4$ and

$$\overline{G} = \frac{\sigma_{\text{ext}}}{2} = \frac{S}{4} \,. \tag{2.40}$$

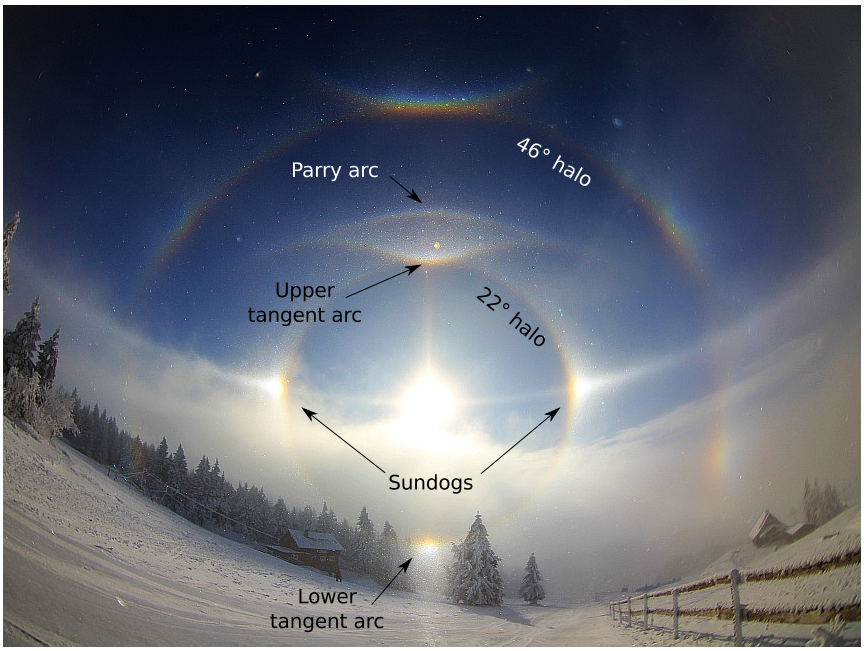

Figure 2.10: *Halo phenomenon in ice fog photographed by Wolfgang Hinz in Neklid, Czech Republic, 30 January 2014. Among other halo displays, the 22° halo, both sundogs, the upper and lower tangent arcs as well as the rare Parry arc and 46° halo are visible. ©Wolfgang Hinz. Used with permission.*

2.3 Halo displays

This section describes the formation of halo displays, which are produced by refraction and reflection of light by ice crystals suspended in the atmosphere. According to the World Meteorological Organization (2017) halo displays are a group of optical phenomena in the form of rings, arcs, pillars or bright spots, which are classified as photometeors. In general, a photometeor is an optical phenomenon caused by reflection, refraction, diffraction or interference of light from the sun or moon. Figure 2.10 shows a halo phenomenon formed by hexagonal crystals in ice fog. If 5 or more halo displays are visible simultaneously, the optical displays together are called halo phenomenon, according to AKM ("Arbeitskreis Meteore e.V. Sektion Halobeobachtungen", `http://meteoros.de`). While the 22° and 46° halo are produced by randomly oriented hexagonal crystals, the upper and lower tangent arcs are formed by oriented ice crystal columns with horizontal c-axis. The Parry arc is produced by oriented columns with horizontal orientation as for the tangent arcs, but in addition the crystals have a fixed orientation around their c-axis. These crystals have only a random orientation around the zenith and are called Parry oriented. The Parry arc is named after W. E. Parry who first described this type of halo display between 1819 and 1820 (e.g. (Pernter and Exner, 1910, Tricker, 1970, Greenler, 1980)). Sundogs are caused by oriented ice crystal plates with vertical c-axis. According to AKM, 22° halos can be observed on 80 to 120 days per year, sundogs on 60 to 80 days per year, and upper tangent arcs on 20 to 30 days per year. These three halo displays can be spotted most frequently, whereas the 46° halo appears only on 4 to 10 days and the Parry arc on 2 to 6 days per year. The formation of these halo displays will be explained in the following using the basic radiative laws in the geometric optics approximation.

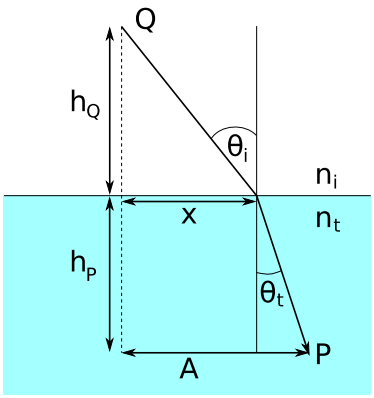

Figure 2.11: *Schematic drawing of the light path geometry for refraction at a boundary. Here, the light propagates from the source Q to the point of observation P with the incident angle θ_i and the angle of refraction θ_t. The refractive indices of the two media are denoted with n_i and n_t.*

2.3.1 Reflection and refraction laws

The refraction and reflection of light by ice crystals depends mainly on the refractive index, which is primarily a function of the wavelength. The temperature dependence of the refractive index is negligible for $\lambda < 20\,\mu\mathrm{m}$ (Liou and Yang, 2016). The refractive index n is defined by the ratio of the speed of light c_0 in vacuum to that in the medium

$$n(\lambda) = c_0/c(\lambda) \approx \sqrt{\epsilon} \tag{2.41}$$

and can be expressed with the permittivity ϵ for frequencies in a small spectral range and far apart from resonance frequencies. The refractive index consists of a real part n_Re and an imaginary part n_Im

$$n = n_\mathrm{Re} - i\, n_\mathrm{Im}\,. \tag{2.42}$$

While the real part describes refraction, absorption is determined by the imaginary part of the refractive index. For wavelengths in the visible spectral range, the real refractive index takes values of $n_\mathrm{Re} \approx 1.31$, whereas the imaginary part is small with $n_\mathrm{Re} < 2 \times 10^{-7}$ (Warren and Brandt, 2008). The propagation of light in inhomogeneous media can be described using Fermat's Principle in the geometric optics approximation. Fermat's Principle states that light propagates such that the optical path W on the traveled path S_0 is maximum or minimum compared to neighboring paths S_i. The optical path W is defined as

$$W(S) = \int_{S(Q->P)} n(\vec{x})\, dS \tag{2.43}$$

for light propagating from the source Q to the point of observation P through the medium with the refractive index n, which depends on the location $\vec{x}$. For the light path which exhibits an extreme value, the condition

$$\left(\frac{dW(S)}{dS}\right)_{S_0} = 0 \tag{2.44}$$

has to be fulfilled. **Snell's law** can be derived using Eq. (2.44). Figure 2.11 shows schematically the geometry of a refracted light path. The refractive index of the medium of the incident light n_i is smaller than the refractive index of the medium of the transmitted light n_t. Using the

Pythagorean theorem, the optical path W can be calculated from P to Q.

$$W = n_\mathrm{i}\sqrt{h_Q^2 + x^2} + n_\mathrm{t}\sqrt{h_P^2 + (A-x)^2}\,. \tag{2.45}$$

With $dW/dx = 0$ we obtain

$$\frac{dW}{dx} = n_\mathrm{i}\frac{x}{\sqrt{h_Q^2 + x^2}} - n_\mathrm{t}\frac{A-x}{\sqrt{h_P^2 + (A-x)^2}} = 0 \tag{2.46}$$

and finally **Snell's law**

$$n_\mathrm{i}\,\sin\theta_\mathrm{i} = n_\mathrm{t}\,\sin\theta_\mathrm{t}\,. \tag{2.47}$$

Snell's law describes the relation between the angle of incidence θ_i in a medium with refractive index n_i and the angle of refraction θ_t in a medium with refractive index n_t.

To calculate the intensity of the reflected and transmitted light, the electric fields have to be decomposed into their components parallel and perpendicular to the plane of incidence, denoted by $E_{r\parallel}$ and $E_{r\perp}$. Applying the respective continuity conditions yields the reflection coefficients of the field components parallel ($\vec{r_\parallel}$) and perpendicular ($\vec{r_\perp}$) relative to the plane of incidence, called **Fresnel Equations**:

$$\vec{r_\perp} = \frac{E_{r\perp}}{E_{i\perp}} = -\frac{\sin(\theta_\mathrm{i}-\theta_\mathrm{t})}{\sin(\theta_\mathrm{i}+\theta_\mathrm{t})}\,, \tag{2.48}$$

$$\vec{r_\parallel} = \frac{E_{r\parallel}}{E_{i\parallel}} = \frac{\tan(\theta_\mathrm{i}-\theta_\mathrm{t})}{\tan(\theta_\mathrm{i}+\theta_\mathrm{t})}\,. \tag{2.49}$$

2.3.2 Formation of halo displays

According to the long-term observations of Sassen et al. (2003b) and AKM, the most frequently observed halo displays are the 22° halo, sundogs, and upper and lower tangent arcs. The scattering geometry of 22° halos and sundogs can be calculated with simple analytic equations and will be explained in the following. Although rarely observed, the formation of the 46° halo will be explained together with the 22° halo due to the similarity of the raypaths forming the two halo types.

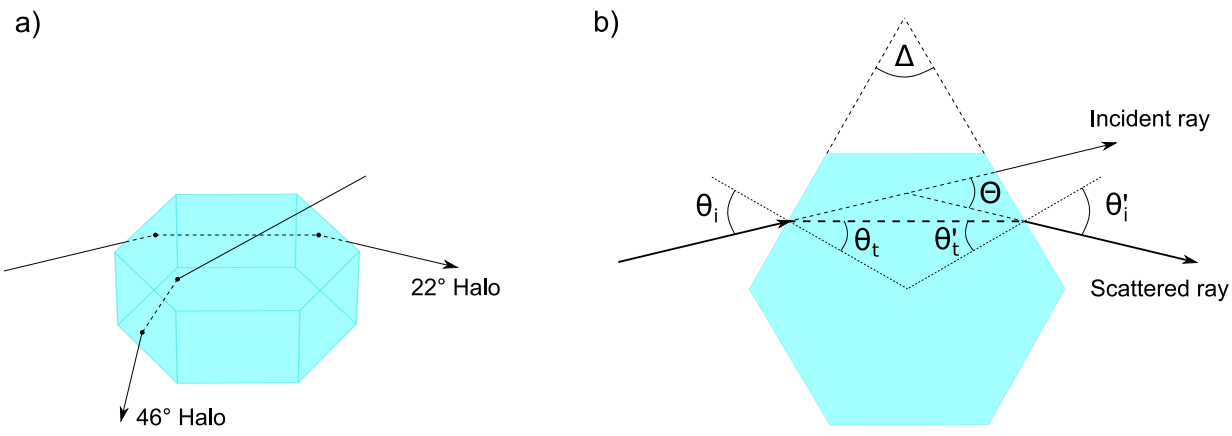

Figure 2.12: *Ray paths of the 22° and 46° halo through an ice crystal with prism angle Δ, defined by the incident angles θ_i, angles of refraction θ_t, and the resulting scattering angle Θ.*

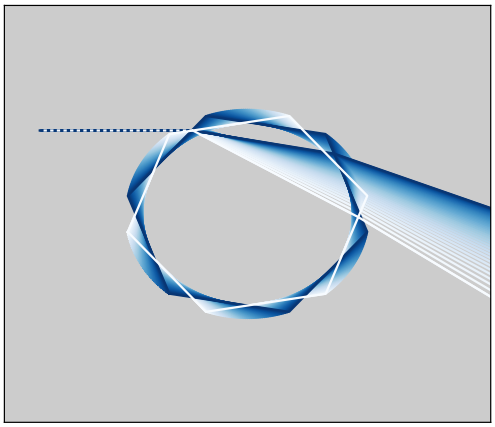

Figure 2.13: *Schematic plot of 22° halo raypaths for different incident angles, realized by different rotation angles of the ice crystal. The hexagons are rotated anti-clockwise with the initial position represented in white and the final position in dark blue. The calculations were performed using Eq. (2.51) for a wavelength of 500 nm. The color of crystal and raypath is changing from white to blue for decreasing scattering angles. The raypath and hexagon corresponding to the minimum scattering angle of 22.1° are represented in dark blue.*

The 22° and 46° halo

The scattering phase functions in Fig. 2.9 feature both the 22° and 46° halo, which are formed by two refractions by randomly oriented hexagonal prisms, as depicted in Fig. 2.12a. Examples of a 22° halo and 46° halo are presented in Fig. 2.10. While the formation of the 22° halo requires refraction through two side faces of the hexagon enclosing an angle of 60°, the 46° halo forms by refraction through a base and a side face with a wedge angle of 90°. The scattering angle Θ of a light ray refracted by a prism with opening angle Δ, can be written as

$$\Theta = (\theta_\mathrm{i} - \theta_\mathrm{t}) + (\theta'_\mathrm{i} - \theta'_\mathrm{t}) = 2\theta'_\mathrm{i} - \Delta\,. \tag{2.50}$$

Using Snell's law (Eq. (2.47)) and assuming $n_\mathrm{i} = 1$ for the refractive index of air, the scattering angle can be calculated as a function of the incident angle θ_i for a given prism wedge angle Δ:

$$\Theta = \theta_\mathrm{i} - \Delta + \arcsin\left(\sin\Delta\sqrt{n^2 - \sin^2\theta_\mathrm{i}} - \sin\theta_\mathrm{i}\ \cos\Delta\right)\,, \tag{2.51}$$

with the refractive index of ice $n = n_\mathrm{t}$. Figure 2.13 shows a schematic plot of the raypaths from Fig. 2.12b for different incident angles, which are realized here by rotating the hexagon relative to the incident direction. Hexagon and raypath are displayed using a color gradient from white to blue for decreasing scattering angles. For a symmetric raypath through the prism, i.e. for $\theta_\mathrm{i} = \theta'_\mathrm{t}$, the scattering angle Θ reaches a minimum $\Theta = \Theta_\mathrm{min}$. Using $\Theta_\mathrm{min} = 2\theta_\mathrm{i} - \Delta$, Eq. (2.51) becomes

$$\Theta_\mathrm{min} = 2\arcsin\left(n\ \sin\left(\frac{\Delta}{2}\right)\right) - \Delta\,, \tag{2.52}$$

or

$$n = \frac{\sin\left(\frac{\Theta_\mathrm{min}+\Delta}{2}\right)}{\sin\left(\frac{\Delta}{2}\right)}\,. \tag{2.53}$$

The dark blue raypath and hexagon in Fig. 2.13 correspond to the minimum scattering angle of 22.1° at a wavelength of 500 nm. The scattering angles for a 60° and 90° prism are presented in Fig. 2.14 as a function of the incident angle for 400 nm (blue) and 800 nm (red). The incident angle is varied between 15° and 90°, perpendicular to the crystal face. For the 60° prism the minimum

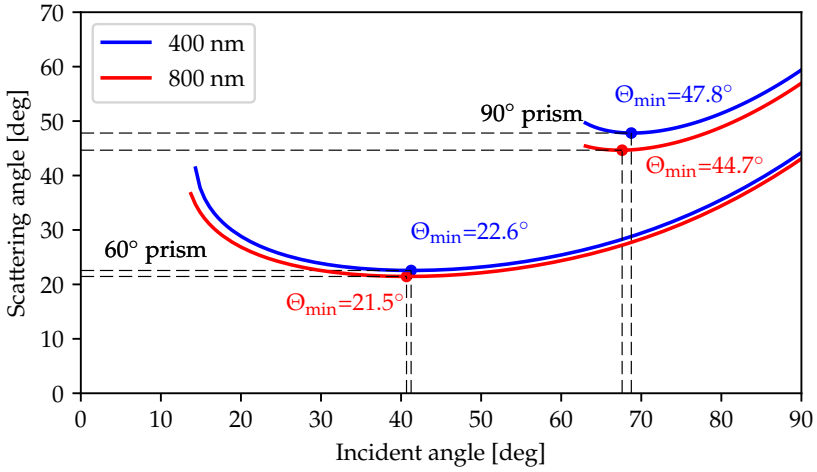

Figure 2.14: *Scattering angle as a function of the incident angle for a 60° and 90° prism using the refractive index of ice for wavelengths of 400 nm (blue) and 800 nm (red). The calculations were performed using Eq. (2.51). Red and blue dots indicate the minimum scattering angles.*

scattering angles result in 21.5° for 800 nm and 22.6° for 400 nm which are the theoretical values for the 22° halo. Since the refractive index of ice is smaller for larger wavelengths, the minimum scattering angle for 800 nm is smaller than for 400 nm, which explains the reddish inner edge of the 22° halo. Minimum scattering angles of 47.8° (400 nm) and 44.7° (800 nm) are found for the 90° prism and represent the 46° halo. The flat minimum of the scattering angles calculated for the 22° halo in Fig. 2.14 implies a bunching of rays close to the minimum scattering angle, which is also illustrated in Fig. 2.13. This is the reason for the sharp inner edge of the 22° halo, as visible in Fig. 2.10.

The 22° parhelia or sundogs

Another frequently observed halo type are the parhelia of the 22° halo, which are commonly called sundogs (cf. Fig. 2.10). Sundogs form by refraction through two crystal side faces of horizontally oriented ice crystal plates (i.e. with vertical *c*-axis). This halo type is not visible in the phase functions in Fig. 2.9 since they assume randomly oriented ice crystals. The raypath responsible for the formation of sundogs can be calculated analytically which was already presented by Wegener

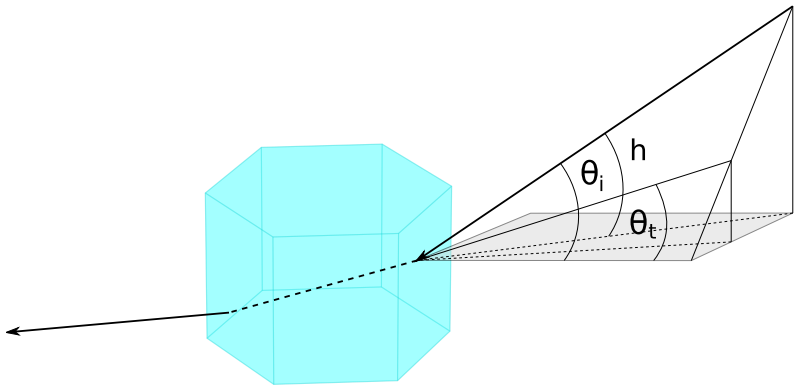

Figure 2.15: *Geometry of a skew ray producing a sundog in an ice crystal plate. The solar elevation angle is denoted with h. The incident and transmitted angles are indicated by θ_i and θ_t, respectively.*

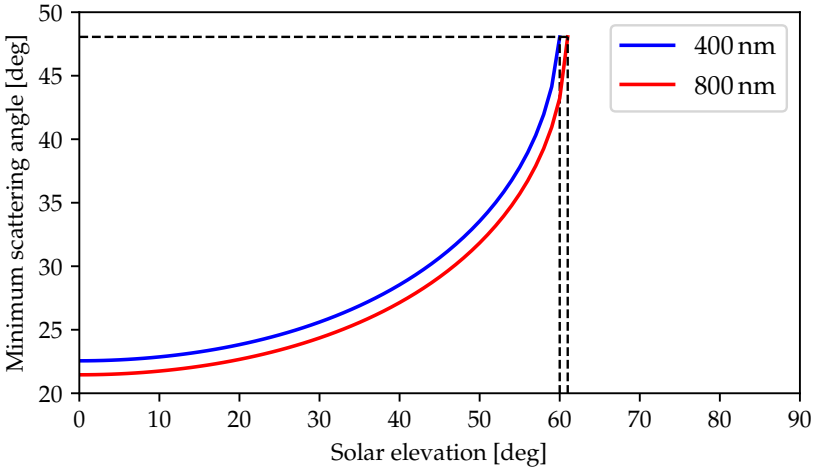

Figure 2.16: *Minimum scattering angle of the 22° parhelia or sundogs Θ'_{min} as a function of the solar elevation h for a wavelength of 400 nm and 800 nm. For a solar elevation of 0° the raypath is the same as for the 22° halo resulting in the same scattering angles as in Fig. 2.14: 22.6° and 21.5° for 400 nm and 800 nm, respectively. For solar elevations larger than about 60° ($\Theta'_{\text{min}} \approx 48°$) Eq. (2.56) cannot be solved and sundogs cannot form.*

(1925) and Minnaert (1937). Similar as for the 22° halo, the rays are refracted through two crystal side faces as illustrated in Fig. 2.15. However, the raypaths are skewed due to the tilted plane of incidence relative to the crystal c-axis, which depends on the solar elevation angle h. Only for a solar elevation of 0°, i.e. at sunrise or sunset, the plane of incidence is perpendicular to the c-axis and the raypath for sundogs is the same as for the 22° halo. For larger solar elevations the light rays cannot follow the path of minimum deviation since the scattering plane is not perpendicular to the c-axis as shown in Fig. 2.15. An equation for the minimum scattering angle of the sundogs can be derived as outlined in Minnaert (1993):

$$\Theta'_{\text{min}} = 2 \arcsin\left(\sqrt{\frac{n^2 - \sin^2 h}{1 - \sin^2 h}}\, \sin\frac{\Delta}{2}\right) - \Delta\,, \tag{2.54}$$

where h is the solar elevation. Δ is the opening angle of the prism, which is 60° in the case of sundogs. Introducing an "effective refractive index"

$$n' = \sqrt{\frac{n^2 - \sin^2 h}{1 - \sin^2 h}} \tag{2.55}$$

the minimum scattering angle for sundogs can be written similar to Eq. (2.52)

$$\Theta'_{\text{min}} = 2 \arcsin\left(n'\, \sin\frac{\Delta}{2}\right) - \Delta\,, \tag{2.56}$$

with the effective refractive index n' which is increasing with solar elevation. Figure 2.16 shows the minimum scattering angle Θ'_{min} as a function of the solar elevation h. For a solar elevation of $h = 0°$ sundogs and 22° halo are located at the same scattering angle. As the solar elevation increases, the sundogs move further away from the 22° halo to larger scattering angles and their brightness decreases as shown in Fig. 2.17. Due to the geometry of the raypath, there is an upper limit of the solar elevation at which the formation of sundogs is possible. For $h > 60°$ the arcsin

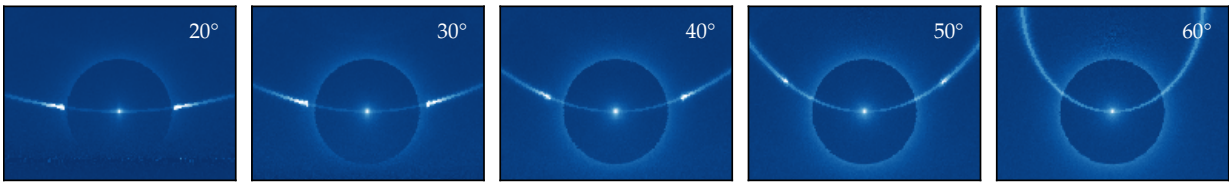

Figure 2.17: *Sundogs for increasing solar elevations, calculated with CrystalTrace (see Section 3.8).*

in Eq. (2.56) is not defined as its argument takes values > 1. According to Minnaert (1993), no sundogs have been reported for solar elevations larger than 40°. The minimum scattering angles increase with wavelength causing a reddish inner edge and blueish outer edge of the sundogs, similar to the 22° halo. The scattering angle difference between 400 nm and 800 nm is about 1.1° at a solar elevation of 0° and increases to $> 2°$ for a solar elevation larger than 55°.

The upper and lower tangent arcs and the circumscribed halo

Upper and lower tangent arcs form by ice oriented crystal columns with their c-axis horizontal. Light is refracted through two crystal side faces, similar as for the 22° halo and the sundogs. These arcs are located tangential to the 22° halo (cf. Fig. 2.10). The shape of the upper and lower tangent arc depends strongly on the solar elevation, as illustrated in Fig. 2.18 using raytracing simulations. For small solar elevations up to about 30° the upper and lower tangent arcs are separated. As the solar elevation further decreases, the wings of the upper/lower tangent arc are bending more and more upwards/downwards from the 22° halo. For solar elevations larger than about 30° the upper and lower tangent arcs merge to form the circumscribed halo. For high solar elevations the circumscribed halo approaches the 22° halo until the two halos merge for the sun at the zenith. More details about the calculation on the formation and raypaths of tangent arcs and circumscribed halos will be presented in Sections 3.8 and 4.3.

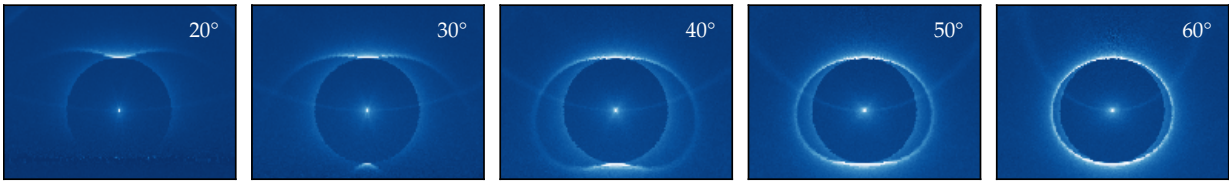

Figure 2.18: *Upper and lower tangent arc merging into circumscribed halo for increasing solar elevations, calculated with CrystalTrace (see Section 3.8).*

Chapter 3

Methods

Sections 3.3.2, 3.5.1, 3.5.2 and 3.6 were partly published in Forster et al. (2017):
Forster, L., M. Seefeldner, M. Wiegner, and B. Mayer, 2017: Ice crystal characterization in cirrus clouds: a sun-tracking camera system and automated detection algorithm for halo displays. *Atmospheric Measurement Techniques*, **10 (7)**, 2499–2516, 10.5194/amt-10-2499-2017.

3.1 Radiative transfer simulations

Radiative transfer simulations were performed using the *libRadtran* radiative transfer package (Mayer and Kylling, 2005, Emde et al., 2016). This library provides different solvers for the radiative transfer equation. *libRadtran* allows for an accurate simulation of Rayleigh scattering, molecular absorption, aerosols, surface albedo, and water and ice clouds. The DISORT and MYSTIC solvers were used for the radiative transfer simulations in this study and will be explained in the following.

3.1.1 MYSTIC

MYSTIC (Emde and Mayer, 2007, Mayer, 2009, Emde et al., 2011, Buras et al., 2011), which stands for "Monte Carlo code for the physically correct tracing of photons in cloudy atmospheres", was used in this study for radiative transfer simulations in the vicinity of the sun with a realistic representation of the sunshape, which was implemented by Reinhardt et al. (2014). Furthermore, MYSTIC was extended with the ray-tracing algorithm CrystalTrace to perform radiative transfer simulations of oriented ice crystals, which will be explained in Section 3.8.

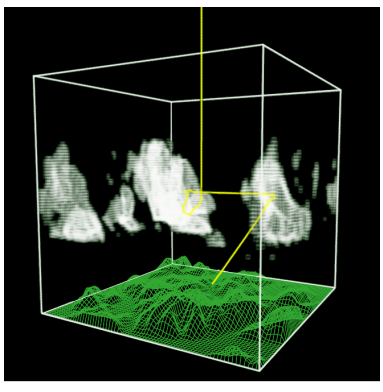

Figure 3.1: *Online visualization of a MYSTIC simulation (Mayer, 2009).*

The principle of the Monte Carlo solver MYSTIC is the tracing of individual photons through the atmosphere. Sampling a large number of photons allows for an accurate simulation of radiances and irradiances and their interaction with inhomogeneous clouds, surface albedo, BRDF[1], and topography without explicit knowledge of the radiative transfer equation. The model domain consists of

[1]The "Bi-Directional Reflectance Function" is a 4D function, describing the reflection of light from an opaque surface (Mayer, 2009)

a one-dimensional (1D) grid, on which the concentrations of molecules and aerosols are defined, and a three-dimensional (3D) grid for the cloud cells. A visualized example of a MYSTIC simulation is shown in Fig. 3.1. This procedure is outlined in the following for the solar spectrum, i.e. assuming the sun as photon source which is quantified by the extraterrestrial solar irradiance. In MYSTIC, photons are defined by a location and direction in 3D space and are assigned with a weight w_a, which equals 1 at the source. With the sun as source, the photon's initial direction is defined by the solar zenith angle θ_0 and azimuth angle ϕ_0. The photons are traced through the atmosphere from one scattering event to the next one. The photon's free path length to the next scattering event is sampled according to the probability density function (PDF)

$$P_\mathrm{s} = \exp\left(-\int_0^s k_\mathrm{sca}\, ds'\right) \tag{3.1}$$

with the total scattering coefficient $k_\mathrm{sca} = \sum_{i=1}^{N} k_\mathrm{sca,i}$, which is the sum of the scattering coefficients $k_\mathrm{sca,i}$ for N interacting particles and molecules. The decision, which interaction takes place is made by drawing a random number $r \in [0, 1)$. The photon interacts with the jth particle type if the random number fulfills the condition

$$\frac{\sum_{i=1}^{j-1} k_\mathrm{sca,i}}{k_\mathrm{sca}} < r \leq \frac{\sum_{i=1}^{j} k_\mathrm{sca,i}}{k_\mathrm{sca}}\ . \tag{3.2}$$

For sampling the scattering direction the phase function is used as PDF for the scattering angle and a random number between 0 and 2π for the azimuth angle. Since loosing photons is computationally inefficient, absorption is treated implicitly by reducing the photon's weight w_a according to Bouguer-Lambert-Beer's law (Eq. (2.24)).

$$w_\mathrm{a} = \exp\left(-\int k_\mathrm{abs}\, ds\right). \tag{3.3}$$

Here, ds is the element of the photon path s and k_abs is the total absorption coefficient including molecules, aerosols, water and ice clouds. Photons absorbed by the earth's surface are scattered and weighted with either the Lambertian albedo or the BRDF, depending on the set up. In case a photon exits the sides of the domain, periodic boundary conditions ensure that it re-enters the domain from the opposite side. The path of the photon terminates if it hits the detector or exits the atmosphere at the top. The preceding description of the photon tracing was based on the

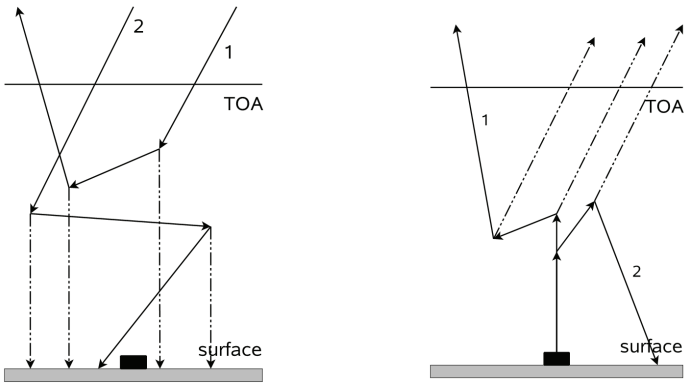

(a) *Forward tracing* **(b)** *Backward tracing*

Figure 3.2: *MYSTIC forward (a) and backward tracing mode (b), from Mayer (2009). The solid lines represent the photon path, while the dashed lines indicate the local estimate in the direction of the source at each scattering event. TOA stands for top of atmosphere.*

forward method which traces photons from their source to their final points. In contrast to the forward tracing method, it is also possible to trace the photons backward from the final point to the source of the radiation (Emde and Mayer, 2007). Both methods are illustrated in Fig. 3.2. The backward tracing method is based on the Helmholtz reciprocity principle, which states that the path of light from A to B is reversible (von Helmholtz and König, 1896). For the simulation of radiances measured by remote sensing instruments with a small field of view (FOV), backward tracing is a very powerful method to save computational time since only a very small amount of the photons started in the beginning are finally detected by the sensor (cf. Fig. 3.2). For backward tracing, the probability that a photon is scattered towards the source is calculated at every scattering event. To obtain a better sampling statistic, the photon follows the direct path to the source at each scattering event weighted by the probability for the respective scattering angle, which is given by the scattering phase function. This method is called *local estimate* (Davis et al., 1985, Kunkel and Weinman, 1976) and is illustrated by the dashed lines in Fig. 3.2. For the radiative transfer simulations in clouds, the extremely efficient Variance Reduction "Optimal Options" Method vroom (Buras et al., 2011) was used. This method enables radiance calculations without the need to truncate the forward peak of the scattering phase functions.

3.1.2 DISORT

DISORT stands for "discrete ordinate technique" and was developed by Stamnes et al. (1988) to calculate the angular variation of the radiance. This 1D solver treats the atmosphere as a number of homogeneous, plane-parallel layers. The single terms of the radiative transfer equation can be represented by Fourier and Legendre moments and the integral over the scattering phase function can be approximated by a sum over discrete angles. This differential equation system can be solved to calculate the radiance at $2n$ "discrete ordinates" or "streams". One advantage of the DISORT solver is that the solution of the radiative transfer equation can be derived in a completely explicit form. The computational effort for each individual layer is independent of its optical thickness. Furthermore, the method is accurate enough to perform benchmark calculations. DISORT is used in this study to calculate the radiance distribution in the angular region of the 22° halo with 16 streams, which is the default value for radiances in *libRadtran*. These simulations could also be performed with the MYSTIC solver but with much higher computational effort. Since cirrus clouds, especially during the presence of halo displays, are rather homogeneous, 3D effects are negligible in this case and the radiative transfer simulations can be performed with the DISORT solver. Another advantage of DISORT is the noise-free result. Figure 3.3 shows the result of a radiative transfer simulation using DISORT (red) in comparison with MYSTIC (blue) for a horizontal slice through the 22° halo at a wavelength of 550 nm. The simulations were performed at a solar zenith angle of $\theta_0 = 50°$ in the almucantar plane, i.e. for a constant viewing zenith angle $\theta = \theta_0$. While MYSTIC accounts for the finite opening angle of the sun with 0.5°, DISORT assumes the sun as point source. The difference between the simulations performed with DISORT and MYSTIC is small and amounts to about $(1.4 \pm 2.3)\,\%$ for a cirrus cloud with optical thickness COT = 0.5, consisting of smooth solid columns with $r_{\text{eff}} = 80\,\mu\text{m}$.

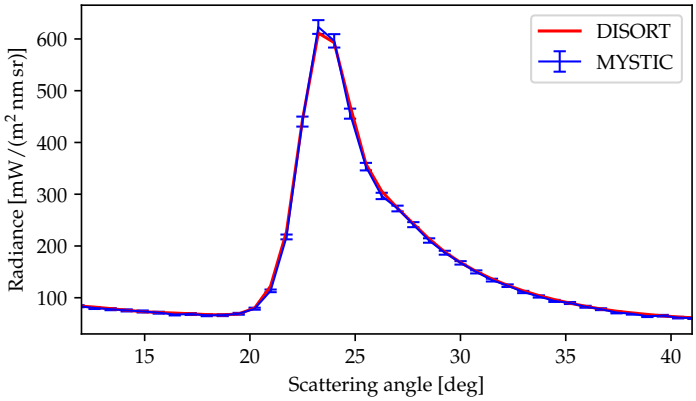

Figure 3.3: *Radiative transfer simulations of a horizontal slice through the 22° halo using DISORT (red line) and MYSTIC (blue line). The simulations were performed at a solar zenith angle of $\theta_0 = 50°$ in the almucantar plane, i.e. for a constant viewing zenith angle $\theta = \theta_0$. The cirrus cloud consists of smooth solid columns with an effective radius of $r_{\text{eff}} = 80\,\mu\text{m}$ and an optical thickness of 0.5. The simulation was performed for a wavelength of 550 nm. The MYSTIC simulations were performed for 1×10^4 photons and the blue error bars represent the 2σ confidence interval. While MYSTIC accounts for the finite opening angle of the sun with 0.5°, DISORT assumes the sun as point source.*

3.2 Optical properties

3.2.1 Aerosol optical properties

Throughout this study aerosol optical properties from the OPAC database are used, which are described in Hess et al. (1998). Figure 3.4 shows radiative transfer simulations with DISORT using 4 different aerosol types of the OPAC database: continental clean, average, polluted, and urban represented by the turquoise, blue, red and black curve, respectively. The optical properties consist of different concentrations of insoluble and water-soluble aerosol, soot and sulfate aerosol. Their concentrations vary with height and the differences between the aerosol types is confined to the lowest level between the surface and 1 km height. The continental clean aerosol type does not contain soot in the lowest level. For the continental average, polluted and urban aerosol type the concentrations of the insoluble, water-soluble and soot component increase slightly in this order. If not stated otherwise, the continental average aerosol type is used throughout this study.

3.2.2 Ice crystal optical properties

Two different parameterizations of ice crystal optical properties were used in this study. The first is based on the database of Yang et al. (2013) who use different methods to calculate the single scattering properties for different particle sizes. The second database of optical properties is compiled using the raytracing technique, which will be further explained in Section 3.8, and calculated with the freely available code presented by Macke et al. (1996). The optical properties of these two parameterizations will be described in the following.

Optical properties based on Yang et al. (2013)

Based on the Amsterdam Discrete Dipole Approximation (ADDA) and Improved Geometric Optics Method (IGOM), Yang et al. (2013) provide an extensive database of ice crystal optical properties for 11 different habits assuming random orientation. The database covers a wavelength range between 0.2 µm to 100 µm, maximum diameters from 2 µm to 10 000 µm and three roughness

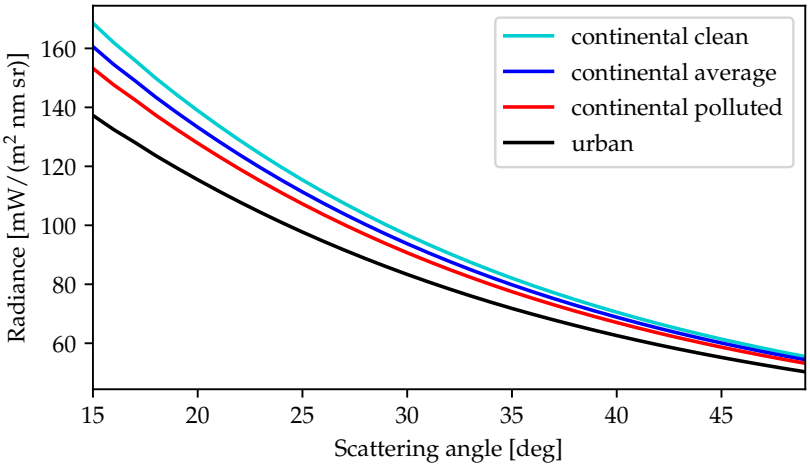

Figure 3.4: *Radiative transfer simulations with DISORT using the continental clean (turquoise), continental average (blue), continental polluted (red) and urban (black) aerosol type from the OPAC database. An aerosol optical thickness of 0.1 was chosen at a wavelength of* 500 nm. *The simulations were performed for a solar zenith angle of* $\theta_0 = 45°$ *in the almucantar plane, i.e. for a constant viewing zenith angle of* $\theta = \theta_0$.

levels for the ice crystal surface (smooth, moderately and severely roughened). The database contains optical properties for solid and hollow columns, aggregated columns consisting of 8 elements, plates and aggregates of plates with 5 and 10 elements, droxtals and solid and hollow bullet rosettes. Prolate and oblate spheroids are not used in this study. The optical properties for single ice crystals were averaged over gamma size distributions with $N_0 = 1$ and $\mu = 1$ in Eq. (2.10) as explained in the appendix of Emde et al. (2016). According to Heymsfield and Miloshevich (2003) these values are a reasonable assumption for mid-latitude cirrus clouds. With $N_0 = 1$ and $\mu = 1$ the gamma distribution simplifies to an exponential distribution

$$N(D) = D \ \exp\left(-\lambda D\right), \tag{3.4}$$

with the ice crystal maximum dimension D. The slope λ was chosen such that the size distribution results in prescribed effective radii between $r_{\text{eff}} = 5\,\mu\text{m}$ to $90\,\mu\text{m}$. Based on these size distributions the bulk optical properties were calculated according to Eq. (2.14). Henceforth, these optical properties will be referred to as YANG. Figure 3.5 shows scattering phase functions for each of the 9 habits organized in four panels for columnar, hollow and plate-like crystals and droxtals. These ice crystal groups favor the formation of similar halo types: solid columns, aggregates of columns with 8 elements and solid bullet rosettes form both a 22° and 46° halo, whereas the 22° halo is much more pronounced than the 46° halo. A special feature of the solid bullet rosette's phase function is a small peak at a scattering angle of about 10°. Crystals with hollow ends, such as hollow columns and hollow bullet rosettes exhibit a 22° halo but cannot produce a 46° halo since they lack the 90° prism between the crystal base and side faces. For the phase functions of plate-shaped crystals the 46° halo is almost as pronounced as the 22° halo. Surface roughness is parameterized similar to the approach by Cox and Munk (1954) who defined the roughness conditions of the sea surface. A normal distribution of the slope of the ice crystal surface is defined by

$$P(Z_\text{x}, Z_\text{y}) = \frac{1}{\sigma^2_\text{rough}\pi} \exp\left(-\frac{Z_\text{x}^2 + Z_\text{y}^2}{\sigma^2_\text{rough}}\right), \tag{3.5}$$

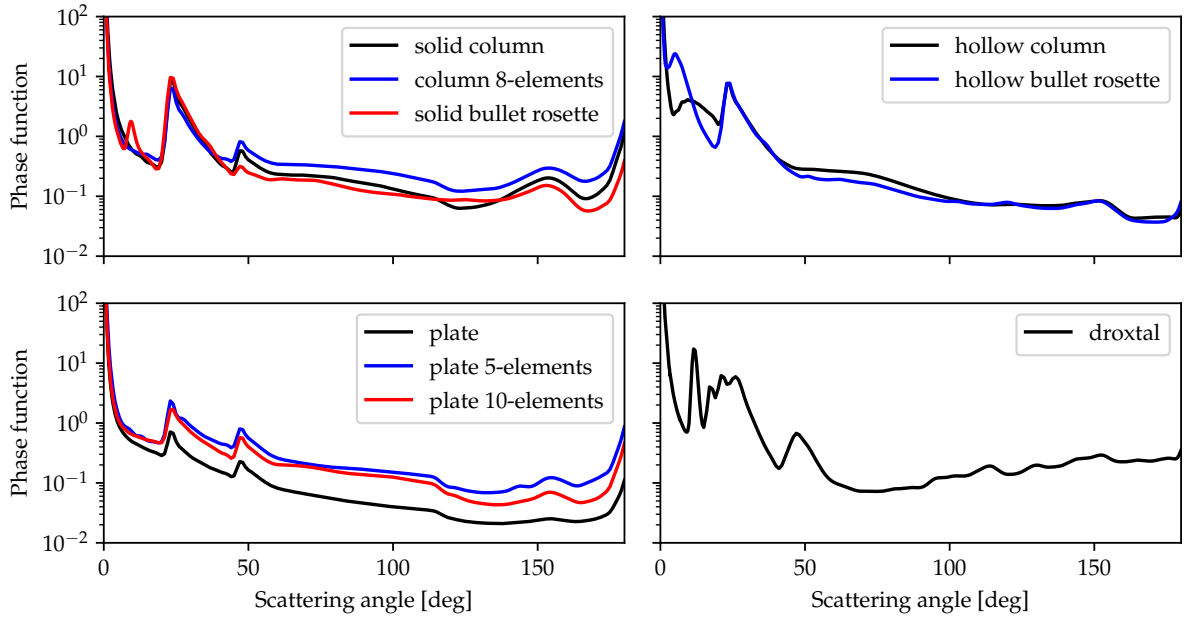

Figure 3.5: *Phase functions for 9 different ice crystal habits with smooth surface displayed for a wavelength of* 550 nm *and an effective radius of* $r_{\text{eff}} = 90\,\mu\text{m}$ *from the database of Yang et al. (2013). The phase functions are grouped for columnar crystals with solid (upper left) and hollow ends (upper right), plate-like (lower left) ice crystals and droxtals (lower right).*

with Z_{x} and Z_{y} representing the slope variations of the crystal's surface along the two orthogonal directions x and y. The parameter σ_{rough} is a measure of the degree of surface roughness and represents crystals with increased surface roughness for larger values. The optical properties of Yang et al. (2013) are provided for ice crystals with smooth ($\sigma_{\text{rough}} \to 0$), moderately roughened ($\sigma_{\text{rough}} = 0.03$) and severely roughened surface ($\sigma_{\text{rough}} = 0.5$). The effect of surface roughness is displayed in Fig. 3.6 for solid columns with $r_{\text{eff}} = 90\,\mu\text{m}$ and a wavelength of 550 nm. While for smooth crystals both the 22° and the 46° halo are visible (blue curve), increasing the surface roughness of the ice crystals causes the halo features to fade. For moderately rough ice crystals, indicated by the red curve, the 46° halo already disappears, while the brighter 22° halo is still visible. Both halo features are completely smoothed out for severely roughened ice crystals, represented by the black curve.

Figure 3.7 displays the parameterization of the aspect ratio for plates and columns which is used in Yang et al. (2013) based on the the findings of Arnott et al. (1994), Auer and Veal (1970), Yang et al. (2003) and Zhang et al. (2004). The aspect ratio in Fig. 3.7 is defined by $\text{AR}_{\text{yang}} = 2a/L$ as in Yang et al. (2013)[2]. The maximum dimension of the ice crystal D is equal to the length of the c-axis L by definition. For crystal maximum dimensions up to 100 µm the solid columns have a constant aspect ratio of $\text{AR}_{\text{yang}} = 0.7$ which is decreasing for larger crystals with $6.96\sqrt{L}$. Thus, solid columns become more elongated with increasing size. The opposite holds for ice crystal plates. Starting from compact particles ($\text{AR}_{\text{yang}} = 1$) for radii of the basal face $a \leq 2\,\mu\text{m}$, the basal faces of the plates grow faster than their side faces resulting in very thin and wide plates.

[2]Note that except for Fig. 3.7 the aspect ratio throughout this work is defined by the inverse, i.e. $\text{AR} = L/(2a) = 1/\text{AR}_{\text{yang}}$.

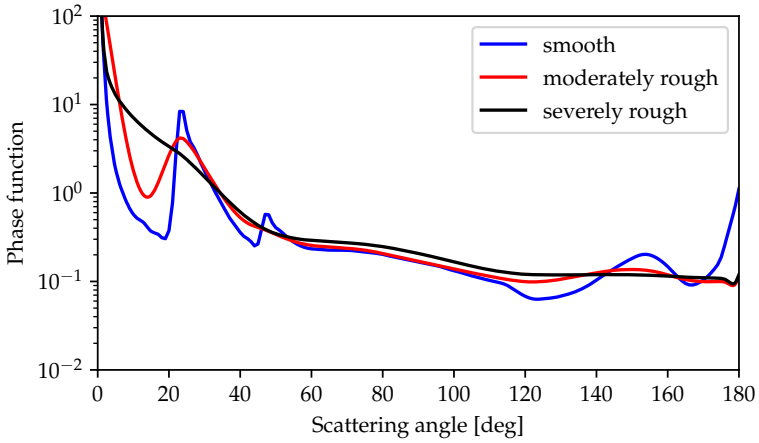

Figure 3.6: *Phase functions for solid columns compared for three different levels of surface roughness: smooth (blue), moderately (red), and severely (black) roughened for an effective radius of* 90 µm *and a wavelength of* 550 nm.

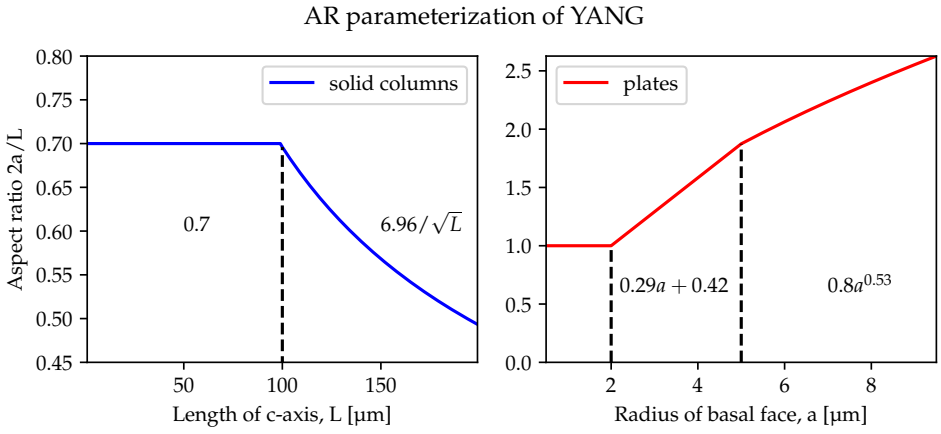

Figure 3.7: *Parameterization of the ice crystal aspect ratio of the Yang et al. (2013) optical properties for solid columns (blue) on the left and plates (red) on the right. The definition of the aspect ratio here follows Yang et al. (2013).*

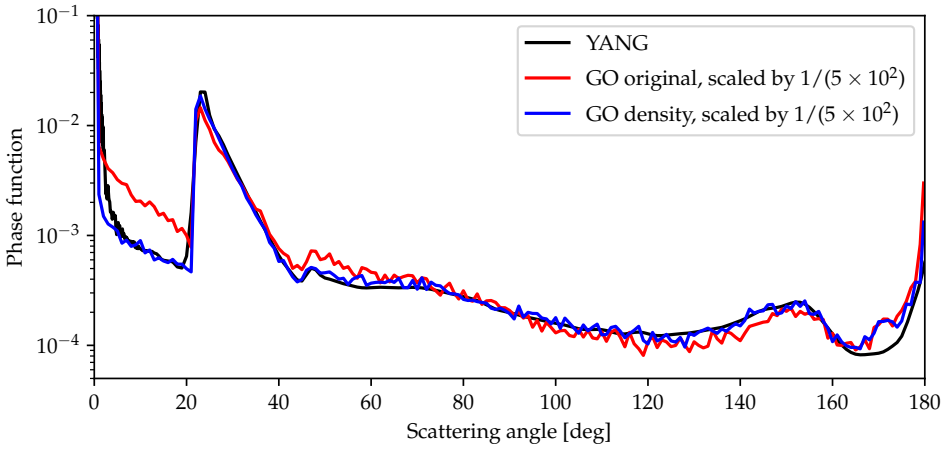

Figure 3.8: *Phase functions calculated with the raytracing code described in Macke et al. (1996) based on the original version (red) and the corrected version using the photon density instead of a fixed photon number (blue). As a reference, the phase function of the YANG database (black) is shown for the same wavelength of* 550 nm *and the same ice crystal: a single smooth ice crystal column with aspect ratio* AR = 14.4 *and maximum dimension* D = 1 × 10⁴ µm.

Optical properties based on raytracing calculations

The second parameterization of ice crystal optical properties used in this study is based on the freely available raytracing code described in Macke et al. (1996). Since this parameterization is based on the geometric optics approximation, it will be referred to as GO in the following. It is important to note that, except for Fig. 3.7, throughout this study the ice crystal aspect ratio (AR) is defined by the length of the side faces L divided by the diameter of the hexagonal base $2a$

$$\mathrm{AR} = L/2a\,, \tag{3.6}$$

with AR < 1 for plates and AR > 1 for columns. This definition will be used in the following for both the YANG and the GO optical properties.

Figure 3.8 shows the scattering phase functions calculated with the GO raytracing code in comparison with the phase function of the YANG database at a wavelength of 500 nm for the same columnar ice crystal with AR = 14.4 and a maximum dimension of D = 1 × 10⁴ µm. The red curve represents the phase function calculated using the original raytracing code as described in Macke et al. (1996). In comparison with the phase function of the YANG database (black curve), GO shows significantly larger values for scattering angles inside the 22° halo for an identical ice crystal size and aspect ratio. For compact ice crystals, however, the GO and YANG scattering phase functions are in good agreement (not shown). For growing columns and plates with aspect ratios increasingly deviating from 1, the difference between the GO and YANG phase functions is increasing for smaller scattering angles. The reason for this behavior of the GO raytracing code was identified by Konoshonkin et al. (2016): "incident rays are emitted from a rectangular bounded the particle projection. With a change of particle orientation, the area of the rectangular is variable. This area variation must be taken into account." In correspondence with A. Macke the bug was fixed by providing the photon density as a constant instead of the number of photons to trace. For every orientation of the crystal the number of photons is calculated from the photon density multiplied by the area of the bounding rectangle of the projected ice crystal. The blue line in Fig. 3.8 shows the result of the corrected GO code using a constant photon density as input parameter. Compared with the YANG phase function of the same ice crystal size and

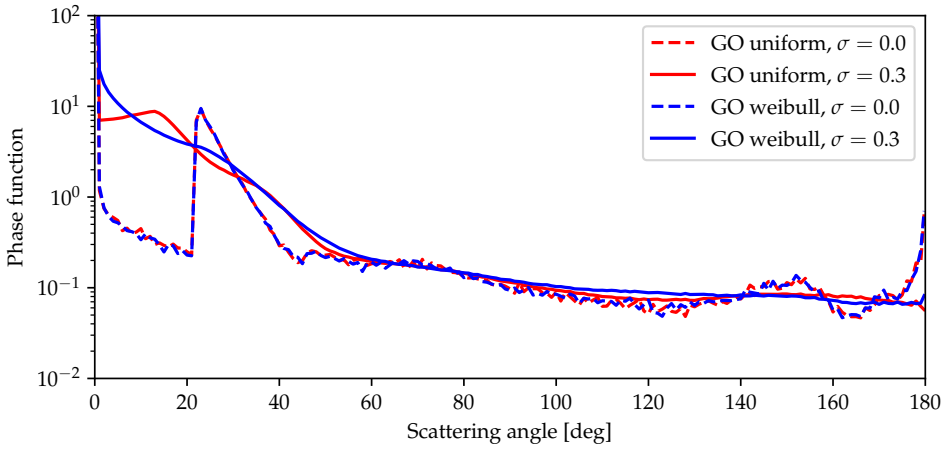

Figure 3.9: *Phase functions calculated with the corrected GO raytracing code compared for a different parameterization of surface roughness at a wavelength of* 550 nm. *The parameterization described in Macke et al. (1996) assumes a uniform distribution, which is represented by the red lines. The parameterization based on a Weibull distribution with* $\eta = 0.75$ *is indicated by the blue lines. A single ice crystal column with maximum dimension* $\mathrm{D} = 1 \times 10^4$ µm *and aspect ratio* $\mathrm{AR} = 14.4$ *was chosen with a smooth surface (*$\sigma_{\mathrm{rough}} = 0$*, dashed lines) and a roughened surface (*$\sigma_{\mathrm{rough}} = 0.3$*, solid lines).*

shape, which is depicted in black, and the phase functions agree well.

The raytracing code described in Macke et al. (1996) models surface roughness by introducing random distortions of the crystal's surface normal following a uniform distribution. This leads to a random distortion of the outgoing ray after a reflection or refraction event. Neshyba et al. (2013) measured single ice crystals in natural conditions during the South Pole Ice Crystal Experiment with the polar nephelometer instrument (Gayet et al., 1997, 1998) and compared the angular scattering intensities with simulations using the GO raytracing code. They found better agreement with the observations when assuming a Weibull distribution instead of the uniform roughness model. Thus, the GO code was modified for this study by replacing the uniform by a Weibull distribution as described in Geogdzhayev and van Diedenhoven (2016). For this new roughness model, the cosine of the zenith tilt angle $\tilde{\mu}$ is calculated by

$$\tilde{\mu} = 1/\left[1 + \sigma_{\mathrm{rough}}^2(-\ln t)^{1/\eta}\right]^{1/2}. \tag{3.7}$$

Here, t is a random number uniformly distributed in the interval [0,1) and the roughness value σ_{rough} determines the height of the distribution. For the parameter governing the shape of the distribution η a value of 0.75 was chosen which Neshyba et al. (2013) found to best match their observations. Geogdzhayev and van Diedenhoven (2016) found that the phase functions calculated with $\eta = 0.75$ produce asymmetry factors comparable to the model based on a uniform distribution for different roughness levels. Figure 3.9 illustrates the effect of a Weibull instead of a uniform distribution on the phase function for the same ice crystal geometry as in Fig. 3.8 (solid column) and a wavelength of 550 nm. For smooth crystals (dashed lines) there is no difference between the phase functions since $\tilde{\mu} = 1$ for $\sigma_{\mathrm{rough}} = 0$. For a roughness value of $\sigma_{\mathrm{rough}} = 0.3$ it is clearly visible that the phase function based on a uniform distribution features an artificial plateau at a scattering angle of about 19°. Performing the calculations with an underlying Weibull distribution with $\eta = 0.75$ yields a smooth phase function without 22° halo.

The raytracing code allows to perform simulations with different ice crystal aspect ratios, ranging from thin plates ($\mathrm{AR} < 1$) over compact crystals ($\mathrm{AR} = 1$) to long columns ($\mathrm{AR} > 1$)

with surface roughness parameters from $\sigma_{\text{rough}} = 0$ (smooth) to $\sigma_{\text{rough}} = 0.7$ (rough). Roughness parameters are limited to values $\sigma_{\text{rough}} \leq 0.7$ as the code does not handle the shadowing and re-entry effects correctly, which occur for highly tilted facets (Geogdzhayev and van Diedenhoven, 2016). It is further possible to perform simulations for different wavelengths associated with different refractive indices, which have to be provided as input parameter.

In the subsequent section the information content of the ice crystal phase functions regarding ice crystal microphysical and optical properties will be analyzed using the features of the 22° and 46° halo.

3.3 Information content of the 22° and 46° halo

Halo displays can be analyzed regarding three features: the angular position of the halo, its brightness contrast relative to the background, and the angular width of the halo. The angular position of the halo can help identify the type of halo display. For example, Eq. (2.52) can be used to calculate the angular position of the brightness peak of the 22° halo and Eq. (2.56) for sundogs. The angular position depends on the refractive index and thus the wavelength and provides basic information about ice crystal geometry in terms of the prism angle and the orientation. In the following sections the brightness contrast and the angular width of the halo will be investigated regarding their information content about ice crystal properties. Exploiting the fact that halo displays are single scattering phenomena, these features will be analyzed using ice crystal scattering phase functions. Subsequently, the effect of multiple scattering on the brightness contrast and angular width and thus on the information content of the 22° halo will be investigated.

3.3.1 Single scattering regime

The halo ratio

The brightness contrast of the 22° and 46° halo in the scattering phase function can be measured by the halo ratio (HR), which was used in previous publications for the analysis of scattering phase functions (Gayet et al., 2011, Shcherbakov, 2013, van Diedenhoven, 2014). Here, the HR is calculated by

$$\text{HR} = \mathcal{P}(\Theta_{\text{max}})/\mathcal{P}(\Theta_{\text{min}})\,, \tag{3.8}$$

with $\Theta_{\text{max}} = 23°$ and $\Theta_{\text{min}} = 21°$ for the 22° halo and $\Theta_{\text{max}} = 47°$ and $\Theta_{\text{min}} = 45°$ for the 46° halo at 500 nm. The effect of the ice crystal aspect ratio on the halo ratio of the 22° and 46° halo is demonstrated in Fig. 3.10 with a fixed ice crystal equivalent radius of 320 µm. The equivalent radius r_{eq} is the radius of a sphere with a projected area equivalent to the projected area of the ice crystal, assuming random orientation. The HR of the 22° halo increases from thin plates (AR < 1) over compact crystals (AR $= 1$) to long ice crystal columns (AR > 1). This behavior can be explained by the ice crystal geometry changing with the AR. The raypath of the 22° halo passes through two side faces as shown in Fig. 2.12a. For an increasing area of the side faces compared to the basal faces these raypaths are favored and the 22° halo becomes more pronounced. The 46° HR exhibits a maximum for compact crystals with ARs slightly larger than 1 and decreases for thin plates and long columns. Recalling the raypath of the 46° halo from Fig. 2.12a explains this relationship. The probability of a path passing through one base and one side face of the crystal is maximum for a particle with equal areas of the side and basal face. For a compact particle ($2a = L$), the hexagonal basal faces have a slightly larger geometric cross section than the side faces (cf. Eq. (2.39)). Thus, the ice crystal has to be slightly elongated to achieve equal cross sections of the side and basal faces and thus the maximum probability for

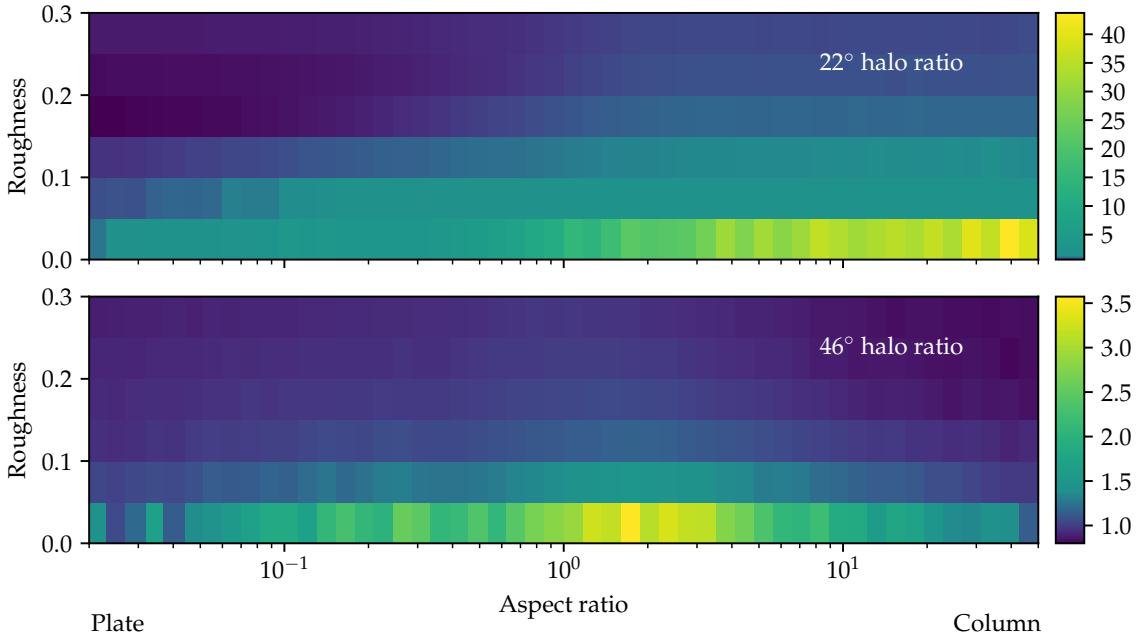

Figure 3.10: *22° (top) and 46° halo ratio (bottom) as a function of the ice crystal aspect ratio and surface roughness, calculated with the fixed version of the GO raytracing code. The ice crystal aspect ratios range from 0.02 (plate) over 1 (compact particle) to 50 (column) and surface roughness values increase from* $\sigma_{\text{rough}} = 0$ *(smooth) to* $\sigma_{\text{rough}} = 0.3$ *(rough). An equivalent radius of* $r_{\text{eq}} = 320\,\mu\text{m}$ *and a wavelength of* 500 nm *was chosen.*

the raypath of the 46° halo. For increasing surface roughness of the ice crystals both the 22° and the 46° HR are decreasing. It can be concluded that the HR contains information about the aspect ratio of the ice crystal. The 22° HR, however, exhibits an ambiguity for smooth plates and rough columns which can result in the same HR. In other words, smooth plates can produce an equally bright 22° halo as rough columns. The presence of a 46° halo indicates smooth compact ice crystals, as shown in Fig. 3.10.

The asymmetry factor as a function of the ice crystal aspect ratio is displayed in Fig. 3.11 for an equivalent radius $r_{\text{eq}} = 320\,\mu\text{m}$. The distribution of the asymmetry factor appears u-shaped

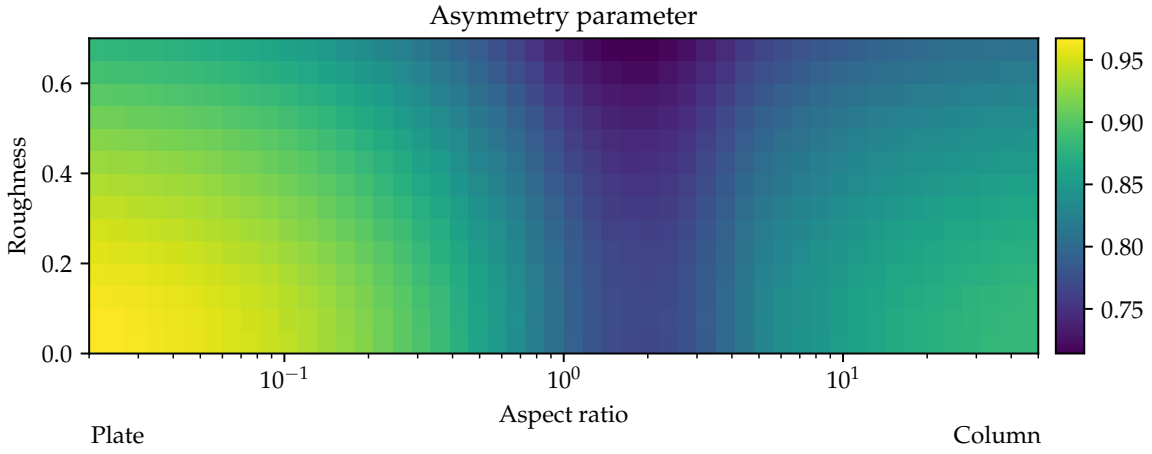

Figure 3.11: *Asymmetry factor as a function of ice crystal aspect ratio and surface roughness for the same parameter range and wavelength as Fig. 3.10.*

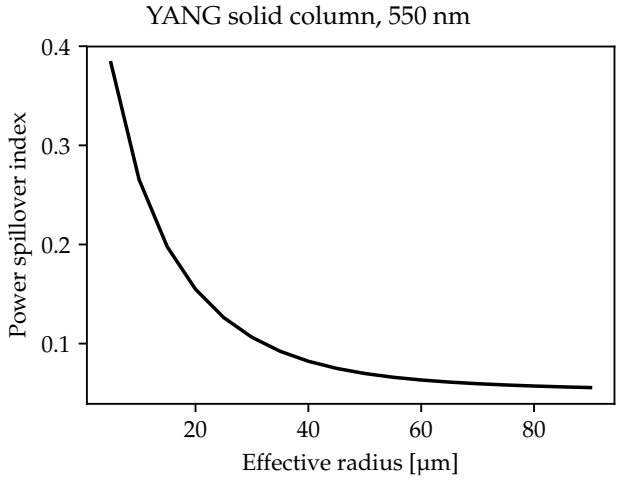

Figure 3.12: *Power spillover index of the 22° halo as a function of the effective ice crystal radius calculated using phase functions of solid columns (YANG) at a wavelength of 550 nm.*

with a minimum asymmetry factor of about 0.7 for columns with an AR slightly larger than 1. The largest asymmetry factors occur for thin plates with values larger than 0.95. However, the asymmetry factors are skewed towards ice crystal plates with larger values for thin plates than for long columns. Figure 3.10 shows that the 22° HR is ambiguous for smooth plates and rough columns. Thus, measurements of the HR can only be used to constrain the asymmetry factor if this ambiguity is resolved. This is the case for very large values of the 22° HR, which can only be achieved for smooth columns with large ARs.

The width of the 22° halo

Another source of information about ice crystal properties is the angular width of the 22° halo, which seems to be determined by the size of the ice crystals, as shown in Fig. 2.9. Flatau and Draine (2014) introduce the so-called "power spillover index" Ψ as a measure of the amount of light scattered into the "shadow region" inside the 22° halo. The authors suggest that this parameter may be used for constraining the ice crystal size. Figure 3.12 shows the power spillover index for effective radii ranging from 5 to 90 µm at a wavelength of 500 nm using phase functions of the YANG database. Here, the power spillover index is calculated by

$$\Psi = \frac{\int_{19^\circ}^{\Theta_{\min}} (\mathcal{P}(\Theta)/d\Theta) d\Theta}{\int_{19^\circ}^{25^\circ} (\mathcal{P}(\Theta)/d\Theta) d\Theta}\,, \tag{3.9}$$

with $\Theta_{\min}$ the scattering angle of the 22° halo peak, which is determined using Eq. (2.52) and amounts to 22.1° for 500 nm. Similar to the findings of Flatau and Draine (2014), the spillover index strongly decreases with increasing effective radius. Thus, for larger ice crystal sizes the amount of light scattered into the shadow region at scattering angles smaller than the 22° halo peak decreases.

This section demonstrates that the 22° halo peak of the ice crystal phase functions contains valuable information about ice crystal shape (i.e. aspect ratio) and surface roughness, as well as particle size. The HR, which depends on the brightness contrast of the 22° halo peak, is sensitive to ice crystal aspect ratio and surface roughness, whereas the spillover index is mainly determined by the size of the ice crystals. In the subsequent section, the information content of the 22° halo will be investigated under multiple scattering conditions in a realistic atmosphere.

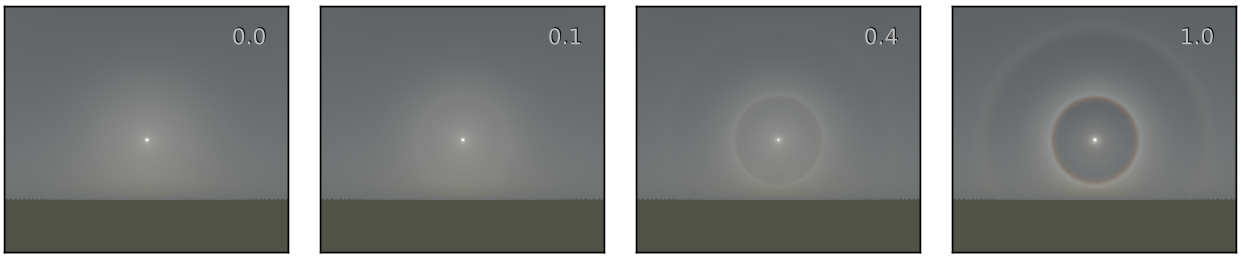

Figure 3.13: *Sky radiance simulations with libRadtran (Mayer and Kylling, 2005) using the DISORT solver for a solar zenith angle of 60°, a viewing azimuth angle range of 0° to 160° and for viewing zenith angles from 10° to 110°. The simulations were performed for a spectral range of 380 nm to 780 nm (5 nm steps), weighted with the spectral sensitivity of the human eye. A homogeneous cirrus cloud layer with optical thickness of 1 was assumed. Solid column ice crystal optical properties of Yang et al. (2013) with an effective radius of 80 µm were used. Aerosol scattering was not considered. The four panels show radiative transfer simulations with different fractions of smooth solid columns ranging from 0% to 100%, as indicated by the labels. A background of severely roughened solid columns is assumed with fractions changing from 100% to 0%, accordingly.*

3.3.2 Multiple scattering regime

This section discusses the influence of multiple scattering on the visibility and brightness contrast of halo displays, using the frequently observed 22° halo as example.

The 22° halo ratio

The effect of varying cloud optical thickness on the visibility of halo displays has already been investigated by Hess (1996), Kokhanovsky (2008), Gedzelman and Vollmer (2008) and Gedzelman (2008) using radiative transfer simulations. Kokhanovsky (2008) performed simulations of the brightness contrast of the 22° halo as a function of the cirrus optical thickness using the radiative transfer model SCIATRAN neglecting molecular and aerosol scattering. The results show a linear decrease of the halo contrast with increasing optical thickness. Gedzelman (2008) and Gedzelman and Vollmer (2008) used the model HALOSKY for radiative transfer simulations of 22° halos with varying cloud optical thickness. HALOSKY considers single scattering by air molecules, aerosol particles and cloud particles assuming homogeneous, plane-parallel atmospheric layers. Multiple scattering is calculated only within the cloud by a Monte Carlo subroutine. Gedzelman and Vollmer (2008) show results for radiance simulations of the 22° halo in the principal plane below and above the sun. They found that the radiance at the bottom of the 22° halo reaches a maximum value for a smaller cirrus optical thickness (COT ≈ 0.25) than the radiance at the top of the cloud (COT ≈ 0.63). Hess (1996) found that the a 22° halo is visible if the COT is larger than the Rayleigh and aerosol optical thickness (AOT) together and depends on the solar zenith angle (SZA).

In this work, radiative transfer simulations were performed using the *libRadtran* radiative transfer package and the DISORT solver, which were explained in Section 3.1. Radiative transfer simulations of a cirrus cloud were performed assuming a homogeneous ice cloud layer with optical thickness 1 (at 550 nm) located at a height between 10 km and 11 km. Figure 3.13 shows simulations using different fractions of smooth solid columns (0%, 10%, 40%, 100%) and assuming a background of severely roughened solid columns. All ice crystals have an effective radius of 80 µm. The optical properties were chosen from the database of Yang et al. (2013). The sun is located at a zenith angle of 60°. Sky radiance was calculated for an angular range between 0° and 160° in

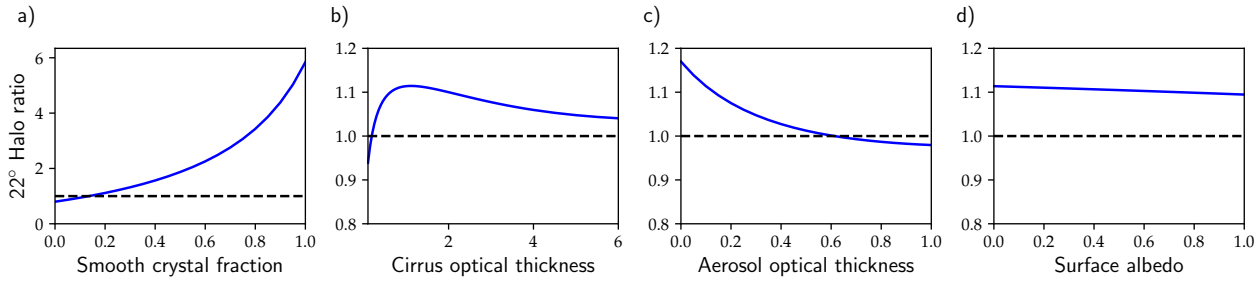

Figure 3.14: *Sensitivity studies of the* 22° *halo ratio at* 550 nm *(as defined in Eq. (3.47)) as a function of the smooth crystal fraction (SCF) (a), cirrus optical thickness (b), aerosol optical thickness (c), and surface albedo (d). The radiative transfer simulations were performed with libRadtran and the DISORT solver for an ice cloud between* 10 km *and* 11 km *using the same optical properties as in Fig. 3.13 for a solar zenith angle of* 60°*. The default parameters, i.e. if not varied, are 20% smooth solid columns,* AOT = 0.2, COT = 1.0, *and* albedo = 0.0*. The dashed black line indicates* HR = 1*, which marks the threshold for the visibility of a halo display.*

the azimuth direction and 10° to 110° in the zenith direction (i.e. from 10° off-zenith to 20° below the horizon), which corresponds to the field of view of a wide-angle camera. The simulations were performed for a spectral range of 380 nm to 780 nm (5 nm steps) and the results were weighted with the spectral sensitivity of the human eye according to CIE 1986, as implemented in specrend (http://www.fourmilab.ch/documents/specrend/).

Aerosol scattering was not considered and a spectral surface albedo of grass was chosen (Feister and Grewe, 1995). For 0% (first panel of Fig. 3.13) all ice crystals are rough and thus no 22° or 46° halo is visible. For a fraction of 10% smooth crystals the 22° halo starts to form which is in agreement with the findings of van Diedenhoven (2014). The 46° halo becomes visible for a fraction of 40% smooth crystals. For 100% smooth crystals both 22° and 46° halo reach a maximum brightness contrast for the respective cirrus optical thickness.

Figure 3.14 depicts the sensitivity of the 22° halo brightness contrast, represented by the halo ratio as a function of the smooth ice crystal fraction (a), the cirrus optical thickness (b), the aerosol optical thickness (c) and the surface albedo (d) for a wavelength of 550 nm. As in Fig. 3.13 an SZA of 60° was chosen and the ice cloud was defined at a height between 10 km and 11 km. The halo ratio was determined in the principal plane above the sun. The dashed lines indicate a halo ratio of 1, which was defined as threshold for the visibility of halo displays. Figure 3.14a shows clearly that for SCF $>$ 10% the halo ratio exceeds 1 and the 22° halo is visible. Figure 3.14b illustrates how the HR is determined by the optical thickness of the cirrus cloud (COT) itself. A maximum value for COT $\sim$ 1 can be observed. For a very thin cirrus, Rayleigh and aerosol scattering become dominant, resulting in a small HR. The HR approaches its maximum value only when COT is larger than the optical thickness of the background (here Rayleigh and aerosol). For large COT, multiple scattering reduces the contrast of the 22° halo feature and the HR decreases, similar to the findings of Kokhanovsky (2008). However, as Gedzelman and Vollmer (2008) point out, the 22° halo peak might still be visible up to an optical thickness of $\sim$ 5 due to the pronounced maximum in the scattering phase function. An increasing AOT causes a decrease of the HR, which is displayed in Fig. 3.14c. For a typical value of AOT = 0.2 the HR is reduced by $\sim$ 10% compared to an aerosol free atmosphere. A higher surface albedo causes longer photon paths through the atmosphere and thus a higher chance of multiple scattering (Fig. 3.14d). Reflected photons therefore cause a higher "background" brightness which leads to a weaker brightness contrast of the halo display.

In general, the effect of the surface albedo on the HR is small compared to the effect of AOT or COT. Halo displays are a geometric optics phenomenon, which means that they emerge only

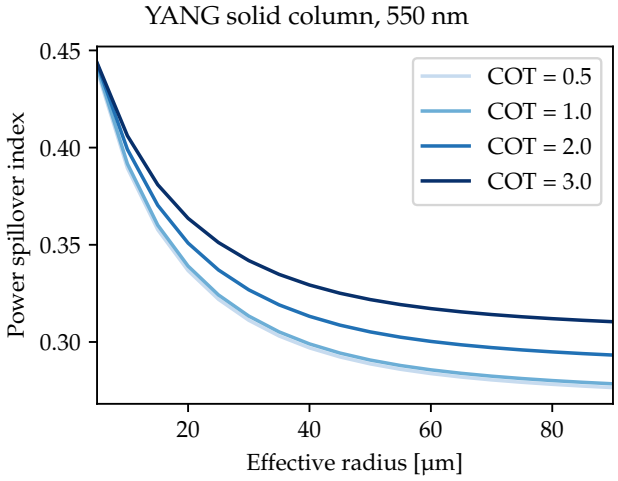

Figure 3.15: *Power spillover index of the 22° halo as a function of the effective ice crystal radius for solid columns (YANG) and a wavelength of* 550 nm *calculated using radiative transfer simulations with DISORT for different cirrus optical thickness (COT) values.*

when the particle size is much larger than the wavelength (Fraser, 1979, Mishchenko and Macke, 1999, Garrett et al., 2007, Flatau and Draine, 2014) which also depends on the aspect ratio of the crystals (Um et al., 2015). The solar zenith angle affects the 22° halo brightness contrast indirectly by increasing the optical path length through the atmosphere for large SZAs and thus increasing the amount of multiple scattering (not shown). This effect is the same for different viewing zenith angles which explains why the 22° halo is always brightest at the top (directly above the sun) and faintest below the sun.

The power spillover index and FWHM

The power spillover index, which was defined in Section 3.3.1, proved useful as an estimate of the ice crystal size for scattering phase functions. For halo observations under multiple scattering conditions in a real atmosphere, however, the power spillover index is sensitive to the COT. As shown in Fig. 3.15, increasing the COT has a similar effect on the power spillover index as decreasing the effective radius. Flatau and Draine (2014) further suggest that the full width at half maximum (FWHM) of the 22° halo peak could be used as a measure of its angular width. To determine the FWHM of a 22° halo in the atmosphere a method was developed to correct the radiance distribution for multiple scattering and to fit a Gaussian distribution to the 22° halo peak. The method is visualized in Fig. 3.16. Figure 3.16a shows the radiance distribution of a 22° halo formed by solid columns with an effective radius of 20 µm and a SCF of 30%. The blue curve represents the fit of the background brightness distribution which is produced by multiple scattering. The fit function for the background is defined by

$$L_{\text{background}} = l_1 \exp(l_2\,\Theta) + l_3 \cos(\Theta) + l_4\,\Theta + l_5\ , \tag{3.10}$$

with the scattering angle Θ and the 5 fit coefficients l_1 to l_5. For the background fit scattering angles $\Theta \leq 19°$ and $35° \leq \Theta \leq 45°$ were considered. The region of the 22° halo, which is masked out for this fit, is displayed with gray shading in Fig. 3.16a. In a next step the background $L_{\text{background}}$ was subtracted from the radiance distribution for the whole scattering angle range which results in the black curve in Fig. 3.16b. Finally, a Gaussian distribution was fitted to the background-corrected curve which is illustrated in Fig. 3.16b by the red curve. For the Gaussian

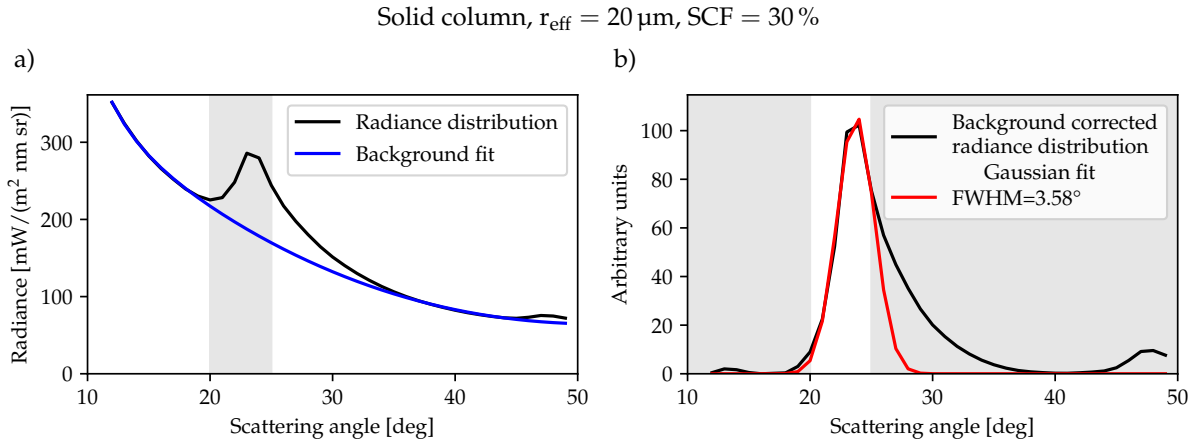

Figure 3.16: *Estimation of the FWHM of the 22° halo under multiple scattering conditions. (a) Radiance distribution across the 22° halo (black) and the background fit (blue). (b) Background-corrected radiance distribution (black) and the Gaussian fit (red). The background fit was performed for scattering angles $\Theta \leq 19°$ and $35° \leq \Theta \leq 45°$ and the Gaussian fit was performed for $20° \leq \Theta \leq 25°$. The scattering angle regions, which are not considered for the fit, are represented in gray. The original radiance distribution (black) was simulated with libRadtran using the DISORT solver for solid ice crystal columns with $r_{eff} = 20\,\mu m$ and a smooth crystal fraction of 30% at a wavelength of 550 nm.*

distribution the following fit function was used

$$L_{\text{gauss}} = l_0 \exp\left(\frac{(\Theta - \mu_\Theta)^2}{2\sigma_\Theta^2}\right) , \tag{3.11}$$

with the amplitude l_0, the expectation value μ_Θ, and the standard deviation σ_Θ as fit coefficients. The fit of the Gaussian distribution was performed using the background-corrected radiance distribution in the scattering angle range $20° \leq \Theta \leq 25°$. The scattering angle region outside the 22° halo, which is represented with a gray shading in Fig. 3.16b, is not used for this fit. It revealed that mainly the inner edge of the 22° halo peak is sensitive to the ice crystal size, which is also visible in the scattering phase function Fig. 2.9. The FWHM of the 22° halo is then calculated by

$$\text{FWHM} = 2\sqrt{2\log 2} \cdot \sigma \, . \tag{3.12}$$

Figure 3.17a shows the FWHM of the 22° halo for different ice crystal effective radii ranging from 5 µm to 90 µm and for a COT of 0.5 (red), 1.0 (blue), and 3.0 (black). The sensitivity of the FWHM to variations of the COT is negligible, as depicted in Fig. 3.17a. This is in contrast to the 22° HR, which strongly depends on the COT (cf. Section 3.3.2). Figure 3.17b shows the FWHM for different ice crystal habits and SCFs ranging between 10% and 100%. All habits were considered except for droxtals, which do not produce a 22° halo. This figure demonstrates that ice crystal shape and surface roughness slightly influence the FWHM. However, this effect is still smaller than the sensitivity of the FWHM to the ice crystal effective radius.

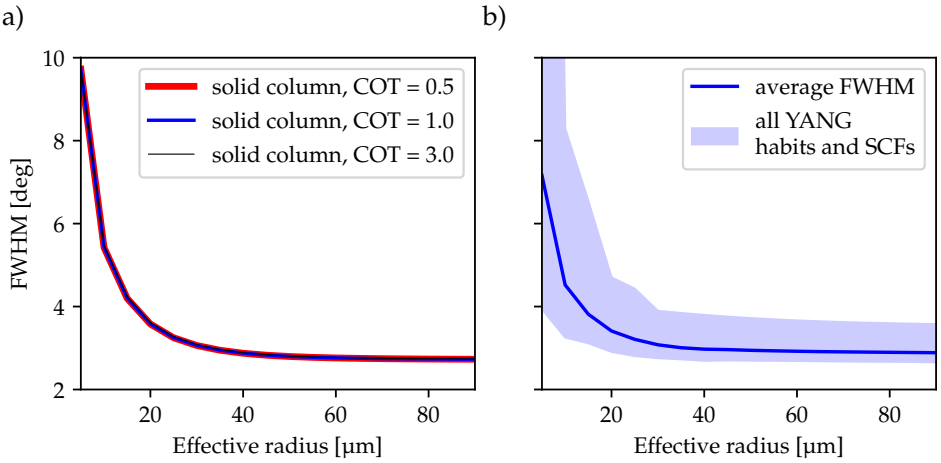

Figure 3.17: *Sensitivity tests of the 22° halo FWHM to (a) COT and (b) ice crystal habit and smooth crystal fraction (SCF). Panel (a) demonstrates that the sensitivity of the FWHM to variations of the COT is negligible. The blue curve in (b) shows the mean FWHM and the light blue shading represents the minimum and maximum FWHM values for the respective ice crystal effective radius for all ice crystal habits except droxtals and SCFs ranging between 10% and 100%.*

3.4 specMACS – the cloud and sky hyperspectral imaging spectrometer

Measurements of halo displays were performed with the multipurpose hyperspectral cloud and sky imaging spectrometer specMACS which is part of the Munich Aerosol Cloud Scanner (MACS). The characterization and calibration of specMACS is described in detail in Ewald et al. (2015). Designed to measure solar radiation transmitted and reflected by clouds and aerosol, specMACS covers a wavelength range between 400 nm and 2500 nm with a spectral bandwidth between 2.5 nm and 12.0 nm. The instrument consists of two cameras, the VNIR (visible near-infrared) spectrometer with a wavelength range of 400 nm to 1000 nm, and the SWIR (shortwave infrared) spectrometer with a wavelength range of 1000 nm to 2500 nm. A scanning strategy was implemented to cover the angular region of the complete 22° halo as well as both sundogs. Figure 3.18 displays specMACS measurements of a 22° halo, which deviates slightly from the circular shape due to the representation in an azimuth-elevation grid. The scan starts above the sun and is performed horizontally at 3 different elevations across spatial line, i.e. with the camera line sensor oriented vertically. To avoid stray light and saturation of the sensor the shutter of the camera was closed when the scattering angle between sun and camera was smaller than 10°. specMACS is equipped with shielding baffles to protect the detector from stray light. Scanning across spatial line, the baffles ensure that stray light can be assumed negligible for scattering angles larger than about 10° (personal communication with F. Ewald and T. Kölling).

The measurement error was calculated as described in Ewald et al. (2015) with some corrections and modifications (personal communication with T. Kölling) which are presented in the following. The signal S, which is measured in digital numbers (DN), consists of the radiometric signal S_0, the dark signal S_{dark} and the temporal noise $\mathcal{N}$

$$S = S_0 + S_{\mathrm{dark}} + \mathcal{N}\,. \tag{3.13}$$

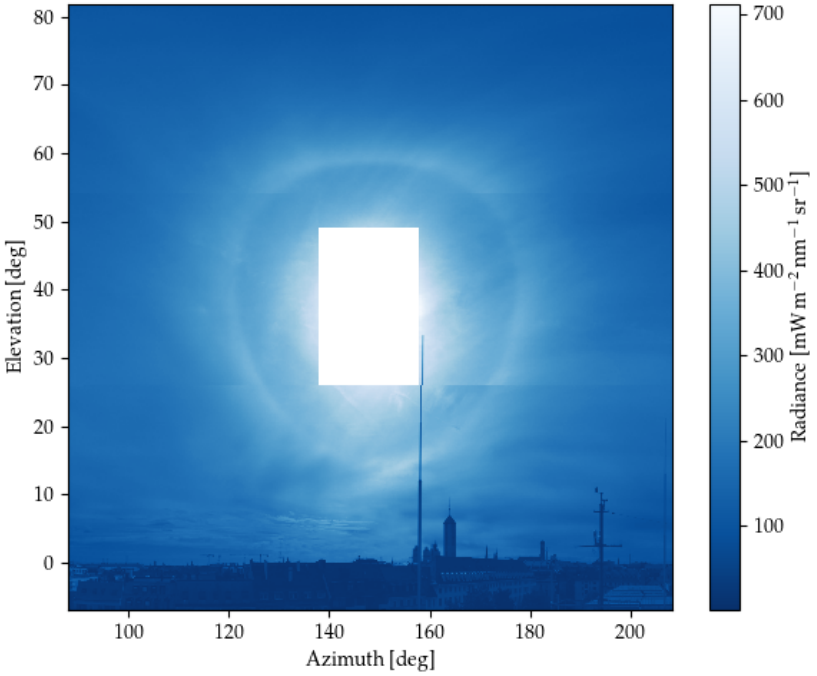

Figure 3.18: *specMACS scan of a 22° halo from 22 September 2015 showing the radiance in* $\mathrm{mW\,m^{-2}\,nm^{-1}\,sr^{-1}}$ *for a wavelength of* 550 nm. *Note that the 22° halo deviates from a circular shape due to the representation in an azimuth-elevation grid.*

The noise $\mathcal{N}$ consists of the shot noise $\mathcal{N}_{\mathrm{shot}}$, the dark noise $\mathcal{N}_{\mathrm{dc}}$ and the read noise $\mathcal{N}_{\mathrm{read}}$ with a joint standard deviation of

$$\sigma_{\mathcal{N}} = \sqrt{\sigma^2_{\mathrm{shot}} + \sigma^2_{\mathrm{dc}} + \sigma^2_{\mathrm{read}}}\,. \tag{3.14}$$

The SWIR noise standard deviation $\sigma_{\mathcal{N}}$ can be represented by a Poisson distribution and is parameterized by

$$\sigma_{\mathcal{N},\mathrm{SWIR}} = \sqrt{0.015\,S_0 + 4.77^2}\,, \tag{3.15}$$

between 0 and 12000 DN. For larger values $\sigma_{\mathcal{N},\mathrm{SWIR}}$ shows a linear dependence with $k^2 = 0.015$ [DN] until saturation is reached

$$\sigma_{\mathcal{N},\mathrm{SWIR}} = \sqrt{0.015\,S_0}\,. \tag{3.16}$$

The VNIR noise standard deviation can be modeled by

$$\sigma_{\mathcal{N},\mathrm{VNIR}} = \sqrt{-4.98e^{-6}\,S_0^2 + 5.22e^{-2}\,S_0 + 24.5}\,, \tag{3.17}$$

which accounts for the non-linearity of the signal noise for large signals (cf. Fig. 13 in Ewald et al. (2015)). The dark signal uncertainty is interpolated between the dark signal before and after the measurement

$$\sigma_{\mathrm{dark}}(t_0) = \sqrt{\sigma^2_{\mathrm{dark}}(t_{0-})\,(1-w)^2 + \sigma^2_{\mathrm{dark}}(t_{0+})\,w^2}\,, \tag{3.18}$$

where $\sigma_{\mathrm{dark}}(t_{0\mp})$ results from the standard deviation $\sigma_{\mathrm{dark}}(t_{\mp 1})$ of the dark signal average at $t_{\mp 1}$ in combination with an upper estimate of the dark signal drift $\Delta\overline{S_{\mathrm{dark}}}$ projected forward/backward

from $t_{\mp 1}$ to t_0:

$$\begin{aligned}\sigma^2_{\mathrm{dark}}(t_{0,-}) &= \sigma^2_{\mathrm{dark}}(t_{-1}) + 1/2\,(\Delta\overline{S_{\mathrm{dark}}}(t_0 - t_{-1}))^2\,,\\ \sigma^2_{\mathrm{dark}}(t_{0,+}) &= \sigma^2_{\mathrm{dark}}(t_{+1}) + 1/2\,(\Delta\overline{S_{\mathrm{dark}}}(t_{+1} - t_0))^2\,.\end{aligned} \tag{3.19}$$

Since $\Delta\overline{S_{\mathrm{dark}}}$ can not be treated as Gaussian error, the 2σ percentile of σ_{dark} is used to combine the errors. The normalized signal accounting for the photo response nonlinearity can be modeled by

$$s_n = \frac{\sqrt{4\gamma(S - S_{\mathrm{dark}}) + 1} - 1}{2\gamma(t_{set} + t_{ofs})}\,, \tag{3.20}$$

with $\gamma_{\mathrm{VNIR}} = (-2.3 \pm 0.3) \times 10^{-5}$ DN^{-1} and $t_{\mathrm{ofs,VNIR}} = (-0.001 \pm 0.010)$ ms and $\gamma_{\mathrm{SWIR}} = 0$ DN^{-1} and $t_{\mathrm{ofs,SWIR}} = (0.055 \pm 0.001)$ ms. The remaining uncertainty of the sensor's nonlinearity is estimated by

$$\sigma_{\mathrm{nonlin}} = \frac{1}{2}\,\frac{s_{\mathrm{n,max}} - s_{\mathrm{n,min}}}{s_{\mathrm{n,mean}}} \cdot S_0\,. \tag{3.21}$$

In addition, the signal measured by the optical components can be polarization sensitive. This is accounted for by

$$\sigma_{\mathrm{pol}} = \frac{1}{2}\,\frac{1 + p_{\mathrm{tot}}}{1 - p_{\mathrm{tot}}} p_{\mathrm{tot}}\,, \tag{3.22}$$

where $p_{\mathrm{tot}} = P \cdot p_{\mathrm{max}}$ with the sensor polarization sensitivity P and the maximum radiance polarization p_{max}. The sensor polarimetric response is composed of a polarization insensitive part O and a polarization sensitive part with partial response $2A$. Then, the polarization sensitivity P is

$$P = \frac{A}{A + O} \cdot 100\%\,. \tag{3.23}$$

For a linear sensor the normalized signal s_{n} scales linearly with the radiance L

$$s_{\mathrm{n}} = R\,L\,, \tag{3.24}$$

with the radiometric response R. For an unknown degree of polarization $p > 0$ the error of the measured normalized signal s_{n} relative to the normalized polarization insensitive signal $s^{\mathrm{P}}_{\mathrm{n}}$ is defined by $\Delta s^{\mathrm{P}}_{\mathrm{n}} = |s_{\mathrm{n}} - s^{\mathrm{P}}_{\mathrm{n}}|$.

Following Ewald et al. (2015), the total error of the photoelectric signal S_0 is calculated by

$$2\sigma_{\mathrm{S_0}} = 2\sqrt{\sigma^2_{\mathrm{dark}} + \sigma^2_{\mathcal{N}}}\,. \tag{3.25}$$

Then, the error of the normalized signal s_{n} is composed of the relative errors of the photoelectric signal $\sigma_{\mathrm{S_0}}$, the non-linearity error σ_{nonlin} and the polarization error $\Delta s^{\mathrm{P}}_{\mathrm{n}}$

$$\frac{2\sigma_{\mathrm{s_n}}}{s_{\mathrm{n}}} = \sqrt{\left(\frac{2\sigma_{\mathrm{S_0}}}{S_0}\right)^2 + \left(\frac{2\sigma_{\mathrm{nonlin}}}{s_{\mathrm{n}}}\right)^2 + \left(\frac{\Delta s^{\mathrm{P}}_{\mathrm{n}}}{s^{\mathrm{P}}_{\mathrm{n}}}\right)^2}\,, \tag{3.26}$$

where $s^{\mathrm{P}}_{\mathrm{n}}$ is the polarization dependent normalized photoelectric signal. Finally, the total error of the measured radiance L is calculated by

$$\frac{2\sigma_{\mathrm{L}}}{L} = \sqrt{\left(\frac{2\sigma_{\mathrm{s_n}}}{s_{\mathrm{n}}}\right)^2 + \left(\frac{2\sigma_{\mathrm{R}}}{R}\right)^2}\,. \tag{3.27}$$

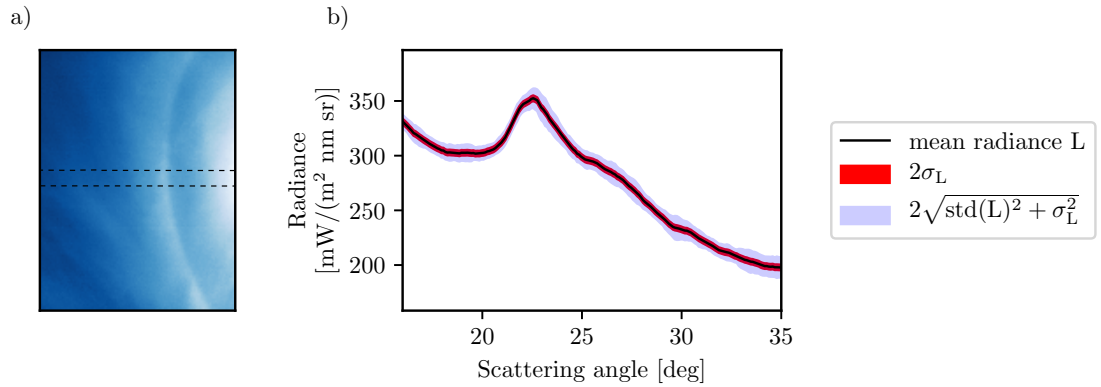

Figure 3.19: *(a) specMACS scan across the left side of the 22° halo on 22 September 2015, 9:38 UTC displayed at a wavelength of 550 nm. The black dashed lines indicate the region centered around the almucantar plane with an angular width of 2°. (b) Radiance distribution across the 22° halo as a function of the scattering angle obtained by averaging the radiance over the 2° bins with a resolution of 0.1°. The blue shaded region around the mean radiance represents the the measurement error (red shading) σ_L combined with the standard deviation of the radiance averaged over the region marked in (a). Both values are provided within a 2σ confidence interval.*

To extract radiance distributions across the 22° halo, the specMACS measurements were binned over a certain interval of the elevation angle and averaged. Figure 3.19 shows an example of a specMACS scan of a 22° halo. The left part of the picture highlights the angular region which is used to calculate the angular dependence of the radiance across the halo. In this case a bin width of 2° was chosen in the elevation angle, centered around the solar elevation, i.e. in the almucantar plane. To obtain the radiance distribution shown in the right panel of Figure 3.19, the data was interpolated to a scattering angle grid with 0.1° resolution ranging from 10° to 35° and averaged over the angular bins. The averaged radiance distribution across the 22° halo L is represented by the black line in Fig. 3.19b. The red shaded region around the mean radiance displays the measurement error $2\sigma_L$. The total error of the measurement uncertainty and the variability of the radiance within the masked angular region is represented by the blue shaded area in Fig. 3.19b and was obtained by Gaussian error propagation assuming the measurements of the individual pixels are independent.

3.5 HaloCam – an automated sun-tracking halo observation system

3.5.1 System description

To automatically collect halo observations, the sun-tracking camera system HaloCam was developed and installed on the rooftop platform of the Meteorological Institute Munich (MIM) at Ludwig-Maximilians University (LMU). HaloCam consists of two weather-proof, wide-angle

Figure 3.20: *HaloCam setup with different wide-angle cameras: HaloCam$_{JPG}$ represents the Mobotix S14D camera which consists of one camera body and two lenses with* 4 mm *focal length. One lens is centered relative to the sun, the other lens is pointing to the zenith and is not used for this study. This camera records pictures only in the compressed JPEG format. HaloCam$_{RAW}$ represents the Allied Vision Manta G-235 C camera with a Kowa wide-angle lens with* 6 mm *focal length and provides the uncompressed "raw" signal measured at the sensor.*

cameras which are mounted on a sun-tracking system shown in Fig. 3.20. Detailed specifications are provided in Table 3.1. HaloCam$_{JPG}$ (Mobotix S14D) is a light-weight modular camera with an RGB CMOS sensor of 1/2" size and two lenses with the same specifications: each lens has a focal length of 4 mm and provides a horizontal and vertical field of view (FOV) of 90° and 67°, respectively. As visible in Fig. 3.20, one lens is pointing to the sun, the other one to the zenith. In this study only the sun-centered lens is used and is, together with the camera body, referred to as HaloCam$_{JPG}$. This very robust and easy-to-operate camera records images in the compressed JPEG format, hence the notation HaloCam$_{JPG}$. The large temperature range from −30 °C to 60 °C allows HaloCam$_{JPG}$ to be operated all year without external heating or cooling. However, due to on-chip post-processing and JPEG compression the images cannot be used for a quantitative analysis.

For this purpose, HaloCam$_{RAW}$ was additionally installed which provides the "raw", i.e. unprocessed and un-compressed, signal from the sensor. HaloCam$_{RAW}$, which is shown in Fig. 3.21, consists of an Allied Vision Manta G-235C camera and a Kowa LM6HC wide-angle lens with 6 mm focal length. The camera features a Sony IMX174 CMOS sensor with 1936×1216 squared pixels, which uses a Bayer color filter array (CFA, Bayer (1975)) for spectral measurements (cf. Table 3.1). The color information is captured by the sensor via so-called primary color (RGB) filters, which are located over the individual pixels and arranged in a Bayer mosaic pattern. For HaloCam$_{RAW}$ the Bayer pattern starts with a red pixel (Allied Vision Technologies GmbH, 2015) and a Bayer demosaicing algorithm (Allied Vision proprietary) is used to determine a red, green and blue value for each pixel. For this study, HaloCam$_{RAW}$ is used in the raw-mode, i.e. the

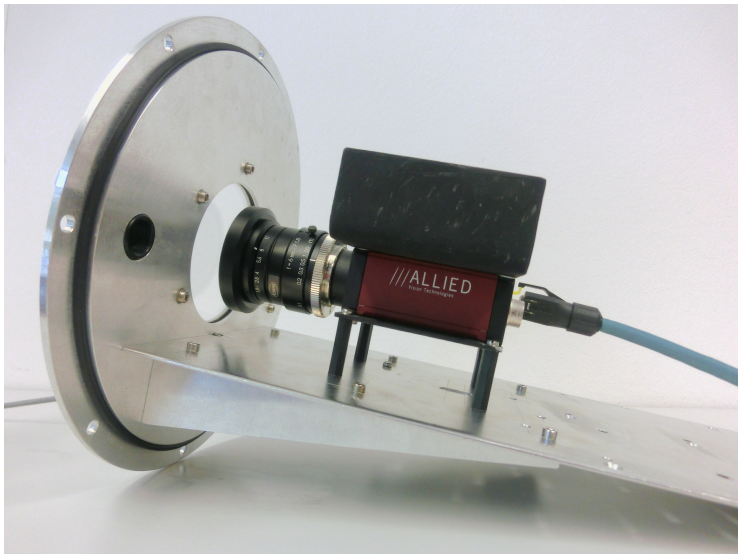

Figure 3.21: *Interior of HaloCam$_{\mathrm{RAW}}$'s weather-proof casing. HaloCam$_{\mathrm{RAW}}$ consists of an Allied Vision Manta G-235C camera with a Kowa lens of* 6 mm *focal length. The camera is fixed on a drawer, which is attached to the circular front lid of the cylindric weather-proof casing shown in Fig. 3.20. A metal sheet is attached on the top of the camera body with a thermal compound to support the cooling of the camera. For the window of the camera casing, a Heliopan UV-filter with anti-reflection coating was used. The PoE (Power over Ethernet) cable is guided inside the camera casing via a water-proof connecting plug through the lid just below the window (cf. Fig. 3.20).*

signal measured by the camera sensor is directly used without (color) processing. This provides monochrome images with superimposed Bayer checkerboard pattern as shown in Fig. 3.22. A schematic illustration of the Bayer CFA layout with the red (R), blue (B) and two green (G1, G2) channels is displayed as a magnified detail of Fig. 3.22.

Since HaloCam$_{\mathrm{RAW}}$ itself is not protected, a weather-proof aluminum casing was built at MIM (cf. Fig. 3.20). The casing has a cylindric shape and the camera is fixed on a drawer which is attached to the circular front lid as shown in Fig. 3.21. An anti-reflection coated UV-filter (Heliopan GmbH) is used as a window for the casing. The PoE (Power over Ethernet) cable is guided inside the casing through the circular lid just below the window via a water-proof connecting plug visible in Fig. 3.20. Both HaloCam cameras are operated in an automatic exposure mode. For HaloCam$_{\mathrm{JPG}}$ the image region used to determine the optimum exposure time is confined to the region where the 22° halo occurs, which ensures that the pixels around the 22° halo are not saturated. HaloCam$_{\mathrm{RAW}}$ measures the histogram of the current image to adjust the exposure time of the next image so that bright areas are not saturated. An upper limit for the exposure time of 50 ms is imposed since the automatic exposure for HaloCam$_{\mathrm{RAW}}$ occasionally escalates to very large values resulting in overexposed images. In the following, the term HaloCam refers to the camera system including the sun-tracking mount and both cameras, whereas the terms HaloCam$_{\mathrm{JPG}}$ and HaloCam$_{\mathrm{RAW}}$ will be used for the specific camera.

Using a sun-tracking mount is ideal for the automated observation of halo displays and later image processing since it automatically aligns the center of the camera with the sun. This implies that all recorded halo displays are centered on the images. With this setup a small circular shade fixed in front of the camera is sufficient to protect the lens from direct solar radiation and to avoid overexposed pixels and stray light (cf. Fig. 3.20). The mount features two stepper motors with gear boxes for adjustment of the azimuth and elevation angles, as described in Seefeldner et al. (2004), with an incremental positioning of 2.16 arcmin per step. The positioning of the mount is performed by passively tracking the sun: an algorithm calculates the current

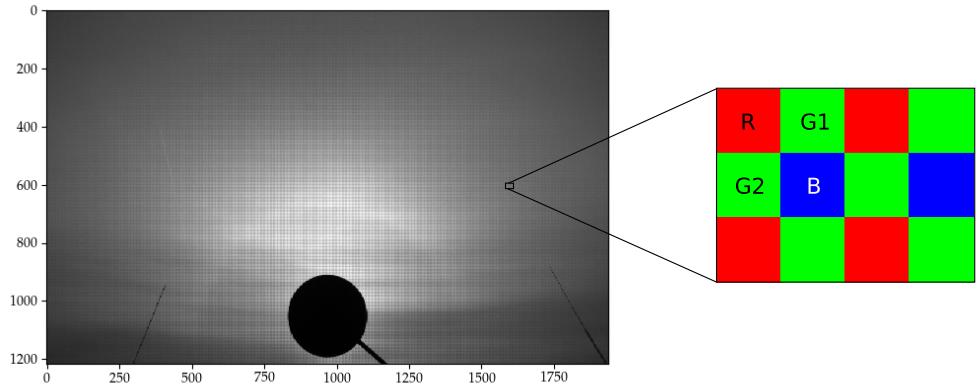

Figure 3.22: *HaloCam$_{\mathrm{RAW}}$ image as detected by the sensor. The image exhibits the superimposed checkerboard pattern of the Bayer color filter array (CFA, Bayer (1975)) which is shown schematically on the right for the red (R), the 2 green (G1, G2), and the blue (B) channels.*

position of the sun which is converted to incremental motor steps. The pointing accuracy of the mount can be roughly estimated to about $\pm 0.5°$ (2σ confidence interval), which will be explained in more detail in Section 3.6.1. Every 10 s HaloCam's position relative to the sun is updated and a picture is recorded. The camera FOV and the sensor resolution were chosen to optimize the trade-off between a large coverage of the sky with high spatial resolution and low image distortion. HaloCam$_{\mathrm{JPG}}$ allows observation of the 22° halo, sundogs, upper and lower tangent arc and circumscribed halo, which are the most frequently observed halo displays according to Sassen et al. (2003b) and the results of AKM.

HaloCam observations aim at gaining a better understanding of the relationship between halo displays and typical ice crystal properties in cirrus clouds. Hence, the observations are limited to the most frequent halo displays without loosing relevant information about ice crystal shape and orientation while achieving a high spatial and temporal resolution of the selected scene. Since the presence or absence of the rare 46° halo might add information (cf. Section 3.3) HaloCam$_{\mathrm{RAW}}$ was tilted upward by 26° compared to HaloCam$_{\mathrm{JPG}}$ to observe the upper part of both the 22° and 46° halo.

The HaloCam system was installed in September 2013 on the rooftop platform of MIM (LMU) in Munich with HaloCam$_{\mathrm{JPG}}$ only and was extended in September 2015 by HaloCam$_{\mathrm{RAW}}$. On the rooftop platform additional measurements are performed operationally by a MIRA-35 cloud radar (Görsdorf et al., 2015), a CHM15kx ceilometer (Wiegner et al., 2014) and a sun photometer, which is part of the part of the AERONET (Aerosol Robotic Network) network (Holben et al., 1998), as well as with the institute's own sun photometer SSARA (Sun–Sky Automatic Radiometer, Toledano et al. (2009, 2011)). HaloCam observations could ideally complement these measurements to retrieve information about ice crystal properties.

Table 3.1: *HaloCam specifications*

Camera system	**HaloCam**$_{\text{JPG}}$	**HaloCam**$_{\text{RAW}}$
Lens	Mobotix L22	Kowa LM6HC
Focal length	4 mm (22 mm)	6 mm
Aperture	F2.0	F1.8 - F16.0 (manual)
Horizontal field of view[3]	93°	87°
Vertical field of view[4]	70°	65°
Camera	Mobotix S14D flexmount	Allied Vision, Manta G-235C
Interface	IEEE 802.3af (PoE)	IEEE 802.3af (PoE)
Protection class	IP65	None
Operating (ambient) temperature	−30 °C to 60 °C	5 °C to 45 °C
Sensor	1/2“ CMOS, RGB	1/1.2“ CMOS, RGB Sony IMX174LQJ
Maximum bit depth	8 bit	12 bit
Sensor resolution	3 MPixel	2.4 MPixel
Sensor pixels	2048×1536	1936×1216
Shutter type	not specified	global shutter
Image formats	JPEG (8 bit)	Bayer (8 or 12 bit) Mono (8 or 12 bit) RGB (8 bit), YUV
Measures $w \times h \times d$	115 × 130 × 33 mm	86.4 × 44 × 29 mm
Weight (camera body + lens)	444 g + 2×159 g	200 g + 215 g

[3]The horizontal and vertical FOV for both camera systems are the result of the geometric calibration in Section 3.5.2.

[4]See footnote 3.

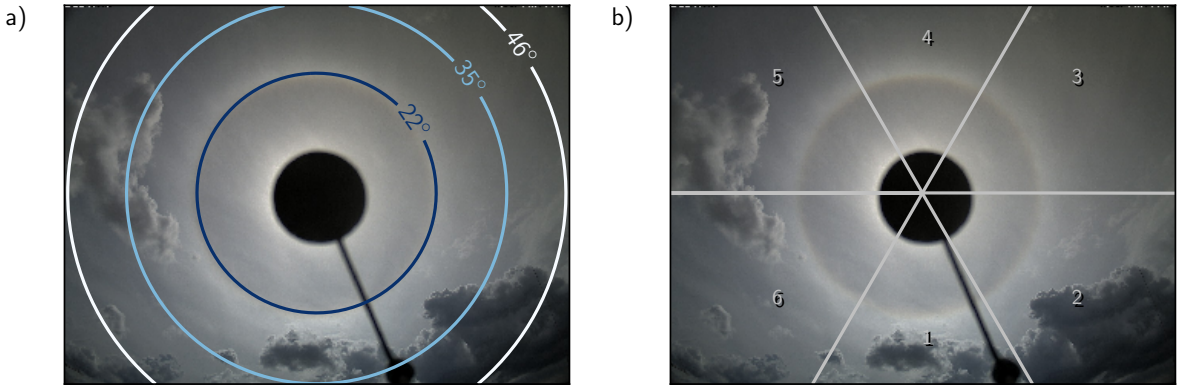

Figure 3.23: *(a) HaloCam$_{\mathrm{JPG}}$ image from 12 May 2014, 13:52 UTC. The corresponding scattering angle (ϑ) grid is displayed with representative contour lines at $\vartheta = 22°$, 35° and 46°. (b) Relative azimuth angle (φ) grid with numbered labels for the 6 image segments.*

For analysis of halo displays on the HaloCam images the pixel location on the sensor must be mapped to the spherical world coordinates. This is achieved by a geometric calibration of the camera. Furthermore, if the measured pixel intensities are to be compared with radiative transfer simulations, a radiometric calibration is required to convert the measured intensities to radiance values. The geometric calibration is performed for both cameras of the HaloCam system, whereas the radiometric calibration is applied only for HaloCam$_{\mathrm{RAW}}$.

3.5.2 Geometric calibration

Halo displays are single scattering phenomena and thus are directly linked to the optical properties of the ice crystals producing them. The ice crystal phase function predicts the scattering angle Θ of the 22° halo relative to the sun. Thus, the analysis of HaloCam images can be simplified significantly by mapping the image pixels to scattering angles. This means the camera has to be calibrated in order to determine the parameters for mapping the camera pixels to the real world spherical coordinate system. For this mapping the intrinsic camera parameters have to be determined, which are the focal lengths f_x, f_y and image center coordinates c_x, c_y, as well as the distortion coefficients of the camera lens.

Different methods exist for the geometric calibration. Here, the method described by Zhang (2000) is used, which is based on Heikkilä and Silvén (1997), to estimate the intrinsic camera parameters as well as the radial and tangential distortion parameters of the lens. This method requires several pictures of a planar pattern, for example a chessboard pattern with known dimensions, taken at different orientations. The calibration method using a chessboard pattern was implemented in OpenCV by Itseez (2015) and is described in detail by Bradski and Kaehler (2008). Using the distortion coefficients and intrinsic parameters, the camera pixels can be undistorted and mapped to the world coordinate system. Thereby, a zenith (ϑ) and azimuth angle (φ) can be assigned to each pixel relative to the center of the sun. In this case the relative zenith angle ϑ corresponds to the scattering angle Θ.

An overlay of the scattering angle grid onto a HaloCam$_{\mathrm{JPG}}$ picture is shown in Fig. 3.23a with representative contour lines at $\vartheta = 22°$, 35° and 46°. From the scattering angle grid the horizontal and vertical FOV can be calculated to ∼93° and ∼70°, respectively. HaloCam$_{\mathrm{JPG}}$ images are recorded with a resolution of 1280×960 quadratic pixels which results in an angular resolution of ∼0.07° for both the horizontal and the vertical direction. Figure 3.23b shows the

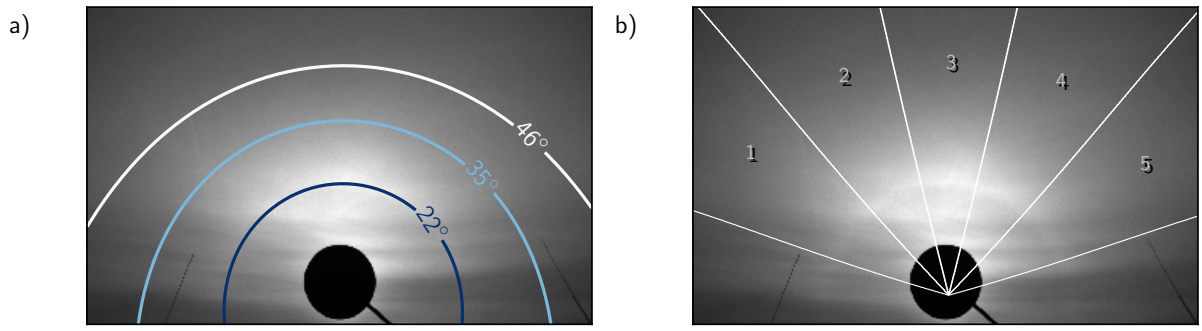

Figure 3.24: *(a) HaloCam$_{\mathrm{RAW}}$ image (red channel) from 2 February 2016, 9:42 UTC with corresponding scattering angle (ϑ) grid and representative contour lines at 22°, 35° and 46°. (b) Relative azimuth angle (φ) grid with numbered labels for the 5 image segments.*

relative azimuth angle grid which is chosen such that the image is separated into 6 segments.

For HaloCam$_{\mathrm{RAW}}$ the geometric calibration was performed with the same method but for the raw image (see Fig. 3.22). The relative zenith (ϑ) and azimuth (φ) for the HaloCam$_{\mathrm{RAW}}$ red channel (R-channel) are displayed in Fig. 3.24. Both the 22° and 46° halo are close to the image center when the elevation of the camera is tilted upward by 26°, as shown in Fig. 3.24a, in contrast to HaloCam$_{\mathrm{JPG}}$ where the sun is at the center of the image. This setup allows observation of the upper part of the 22° and 46° halo, which is more suitable for a quantitative analysis. The lower part of the halo is often obstructed by the horizon (during sunrise and sunset) and usually less pronounced than the upper part due to increased multiple scattering (cf. Fig. 3.13). The horizontal and vertical FOV of HaloCam$_{\mathrm{RAW}}$ can be estimated from the calculated scattering angle grid to ∼87° and ∼65°, respectively. With a resolution of 608×968 quadratic pixels the angular resolution of each of the 4 color channels amounts to about 0.1°. As for HaloCam$_{\mathrm{JPG}}$, the HaloCam$_{\mathrm{RAW}}$ image is separated into segments using the relative azimuth angle φ. Figure 3.24b indicates the 5 azimuth segments defined to obtain a detailed sampling of the 22° halo. For further analysis and feature extraction each of these segments is averaged in direction of the relative azimuth angle φ.

3.5.3 Radiometric characterization

Each sensor pixel is a semiconductive device which converts light into electrical charge and can be treated as an independent radiometric sensor. The charge collected on a pixel is converted to a voltage and then to a digital value by the A/D converters, which introduces noise at each step. The signal measured by the sensor can be expressed as

$$S = S_0 + S_\mathrm{d} + \mathcal{N} \tag{3.28}$$

with S_d the dark signal, S_0 the radiometric signal, and the measurement noise $\mathcal{N}$, as presented in Ewald et al. (2015). The measurement noise $\mathcal{N}$ is the sum of the radiometric signal noise $\mathcal{N}_0$ and the dark signal noise $\mathcal{N}_\mathrm{d}$

$$\mathcal{N} = \mathcal{N}_0 + \mathcal{N}_\mathrm{d}\,. \tag{3.29}$$

In the following sections the components of the measured signal S will be characterized and their sensitivity on the camera settings and ambient conditions will be investigated. The dark

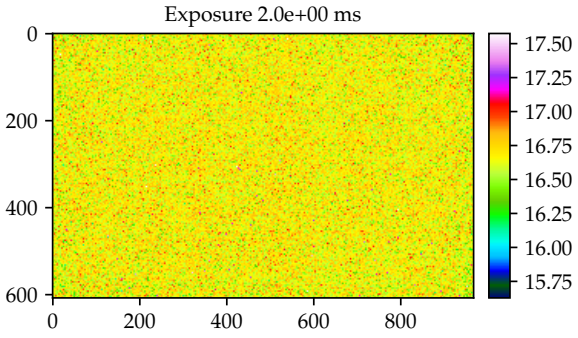

Figure 3.25: *HaloCam$_{\mathrm{RAW}}$ dark signal of the R-channel, averaged over 100 images. An exposure time of $t_{\mathrm{expos}} = 2.0\,\mathrm{ms}$ was chosen and a temperature of 45 °C was measured inside the camera.*

signal measurements were performed in the optics laboratory of the Meteorological Institute at LMU on 16 July 2015. The measurements at the Large Integrating Sphere (LIS) and the spectral characterization of the sensor were performed at the Calibration Home Base (CHB) (Gege et al., 2009) of the Remote Sensing Technology Institute at the German Aerospace Center in Oberpfaffenhofen on 28 June 2016 in close cooperation with A. Baumgartner. In the subsequent sections, temporally averaged values are indicated by angle brackets while spatial averages are denoted by an overbar. If not stated explicitly all variables are defined pixel-wise.

Dark response

The dark signal $\mathrm{S_d}$ is defined as the signal which can be measured when no light is entering the camera, i.e. the shutter is closed. This implies $S_0 = 0$ and Eq. (3.28) becomes

$$S = S_{\mathrm{d}} + \mathcal{N}_{\mathrm{d}}\,. \tag{3.30}$$

For an averaged dark image $\langle S \rangle$ the remaining noise approaches zero $\langle \mathcal{N}_{\mathrm{d}} \rangle \to 0$ and the dark signal S_{d} can directly be measured. The dark signal consists of the dark current s_{dc}, which is caused by thermally generated electrons and holes within the semiconductor material of the sensor, and the read-out offset of the A/D converters S_{read}. The dark current s_{dc} depends on the temperature T and the exposure time t_{expos}

$$S_{\mathrm{d}}(T) = s_{\mathrm{dc}}(T)\, t_{\mathrm{expos}} + S_{\mathrm{read}}\,. \tag{3.31}$$

Thermal electrons are generated randomly over time with an increasing rate as the temperature rises. Furthermore, the dark signal has a spatial component which is called fixed pattern noise (FPN). Since HaloCam$_{\mathrm{RAW}}$ has no external shutter, the dark signal during operation has to be estimated from the laboratory characterization. The following experiments were performed in a dark room and the camera lens was covered with an opaque cloth.

Figure 3.25 displays the dark signal $\langle S_{\mathrm{d}} \rangle$ averaged over 100 images for an exposure time of $t_{\mathrm{expos}} = 2.0\,\mathrm{ms}$ and a device temperature of 45 °C for the R-channel. The temporally and spatially averaged dark signal amounts to about $\overline{\langle S_{\mathrm{d}} \rangle} = (16.7 \pm 0.2)\,\mathrm{DN}$. For this number of averaged images, the dark signal in Fig. 3.25 does not show a significant spatial pattern. The same is true for the G1-, G2-, and B-channel. Thus, it can be assumed that the FPN is smaller than the dark signal noise of 0.02 DN or 0.1 % and is considered negligible for the following

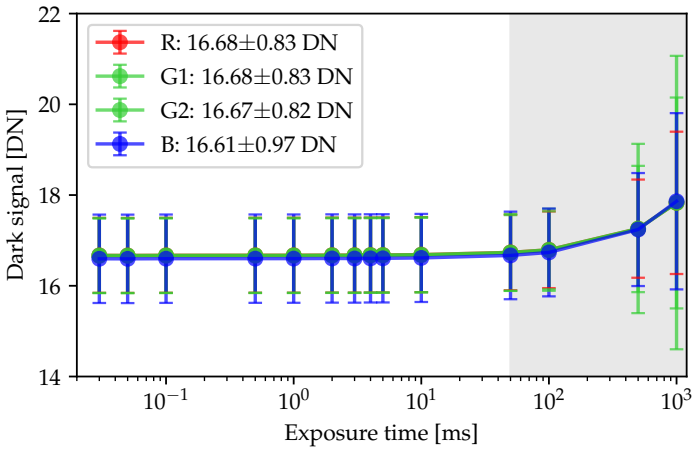

Figure 3.26: *HaloCam$_{\mathrm{RAW}}$ dark signal and dark signal noise of all 4 channels (R, G1, G2, B) for different exposure times ranging from* 0.03 ms *to* 1000 ms*. The camera's internal temperature was constant at* 45 °C*. The dark signal average and the standard deviation were evaluated over 100 images for each exposure time.*

analysis and later image processing. Figure 3.26 shows the dependency of the dark signal on exposure time for a constant temperature inside the camera of about 45 °C. In operational mode and under daylight conditions typical exposure times of 1 to 3 ms are used. For exposure times up to 50 ms the mean dark signal amounts to about 16.7 DN with a standard deviation of 0.8 DN for the R-channel. The variability of the mean dark signal for exposure times smaller than 50 ms is less than 0.02 DN (0.1 %). As observed by Urquhart et al. (2015) and Ewald et al. (2015) (VNIR camera of specMACS), the dark signal appears to be independent of the exposure time. For larger exposure times, which are shaded in gray in Fig. 3.26, a significant increase of the dark signal as well as the dark signal noise occurs. This behavior is most likely a combination of the increasing dark current signal due to a longer exposure time and an increase of the read noise signal S_{read} caused by the A/D converters. To investigate the temperature sensitivity of the dark signal, measurements were performed with the camera set up inside a climate chamber (Weiss[5], SB11/160/40) in a dark room and with the camera lens covered. The temperature inside the climate chamber can be adjusted between −40 °C to 180 °C with increments of 0.1 °C. The estimated accuracy is about 0.05 K. The temperature was controlled using the software described in Grob (2015), which is part of the runMACS software suite. For the dark measurements with HaloCam$_{\mathrm{RAW}}$ the temperature was varied between 10 °C and 50 °C in steps of 5 °C. Within this temperature range the averaged dark signal varied less than 0.5 DN. To obtain an estimate for the temporal drift of the dark signal, the standard deviation was calculated using all recorded dark images for the different camera temperatures and exposure times and results to about 2.2 DN for the 4 channels. For the dark signal correction of the HaloCam$_{\mathrm{RAW}}$ data, for each of the 4 channels the respective mean values from Fig. 3.26 are used: 16.68 DN, 16.68 DN, 16.67 DN, and 16.61 DN for the R-, G1-, G2-, and B-channel, respectively.

Sensor photoresponse non-uniformity correction

The radiometric signal S_0 differs from pixel to pixel due to different gains of each photodetector, called photoresponse non-uniformity (PRNU). Furthermore, the wide-angle lens of HaloCam$_{\mathrm{RAW}}$ causes a decreasing brightness on the sensor for raypaths further away from the optical axis of the

[5]Weiss Klimatechnik GmbH, Greizer Straße 41-49, D-35447 Reiskirchen-Lindenstruth

lens. This illumination falloff towards the edges of the sensor is called vignetting. Two different types of vignetting occur:

1. Optical vignetting occurs when the ray bundle, which forms the image, is truncated by two or more physical structures in different planes (Bass et al., 2010). Typically, one is the nominal aperture and another is the edge of a (multiple element) lens. This kind of vignetting naturally occurs in all lenses and typically affects peripheral light rays, far off the optical axis.

2. Natural vignetting describes the effect that for off-axis image points the illumination is usually lower than for the image point on the optical axis (Bass et al., 2010).

Optical vignetting can be diminished by reducing the entrance pupil, i.e. the aperture by increasing the f-number. According to Bass et al. (2010) the f-number is defined by

$$f\text{-number} = \frac{\text{focal length}}{\text{entrance pupil diameter}}\,. \tag{3.32}$$

For the Kowa lens of HaloCam$_{\mathrm{RAW}}$ the f-number can be adjusted mechanically between 1.8 and 11 by a screw. A fixed value of f-number = 8 was chosen for all measurements and the calibration. For the observation of halo displays close to the sun this represents a good trade-off between a small aperture and short exposure times.
To obtain a model for the non-uniformity of the sensor response as a function of the pixel location, flat-field measurements were performed at the LIS at CHB. Several measurements were performed with the same exposure time. To minimize the impact of inhomogeneities in the brightness of the integrating sphere, images were recorded at 6 different orientations by rotating the camera around its own axis, i.e. with the center of the camera roughly pointing to the center of the sphere. For each orientation 40 images were recorded, dark signal corrected and averaged. The measurements, which were averaged over the rotation angles of the camera relative to the sphere, are shown in Fig. 3.27a with the signal normalized to 1. The spherical patches visible in the figure are due to a hole in the sphere, which allows for injecting a laser as light source for specific experiments. The hole appears at different locations on the image due to the different rotation angles of the camera. Owing to the large field of view of the camera, the edge of the two hemispheric components of the LIS is visible. In order to fit a model to the flat-field measurements, these two regions were masked out as displayed in Fig. 3.27b. The flat-field model correcting for the PRNU was determined by fitting a 2-dimensional (2D) second order polynomial to the averaged and masked measurements.

$$F = a \cdot r^2 + b \cdot r + c\,, \tag{3.33}$$

where $r^2 = |\mathbf{x} - \mathbf{x_0}|^2$ is the distance of the pixel location $\mathbf{x}$ from the image center $\mathbf{x_0}$. The result is depicted in Fig. 3.27c for the R-channel with the following parameterization:

$$F = -1.23 \times 10^{-6} \cdot r^2 + -4.31 \times 10^{-6} \cdot r + 0.99\,, \tag{3.34}$$

with $y_0 = 297.2$ and $x_0 = 473.8$. Finally, Fig. 3.27d shows the relative difference between the flat-field model and the measurements in percent. The fluctuations of the signal difference are due to inhomogeneities of the integrating sphere (and the FPN of the camera sensor). However, these inhomogeneities are negligible for the image processing procedure since the flat-field model is used to correct the camera measurements. The average difference between model and measurement amounts to $(0.0 \pm 0.5)\,\%$ for the R-channel with similar values for the remaining channels. The PRNU correction is applied to the dark signal corrected red, green and blue channel separately.

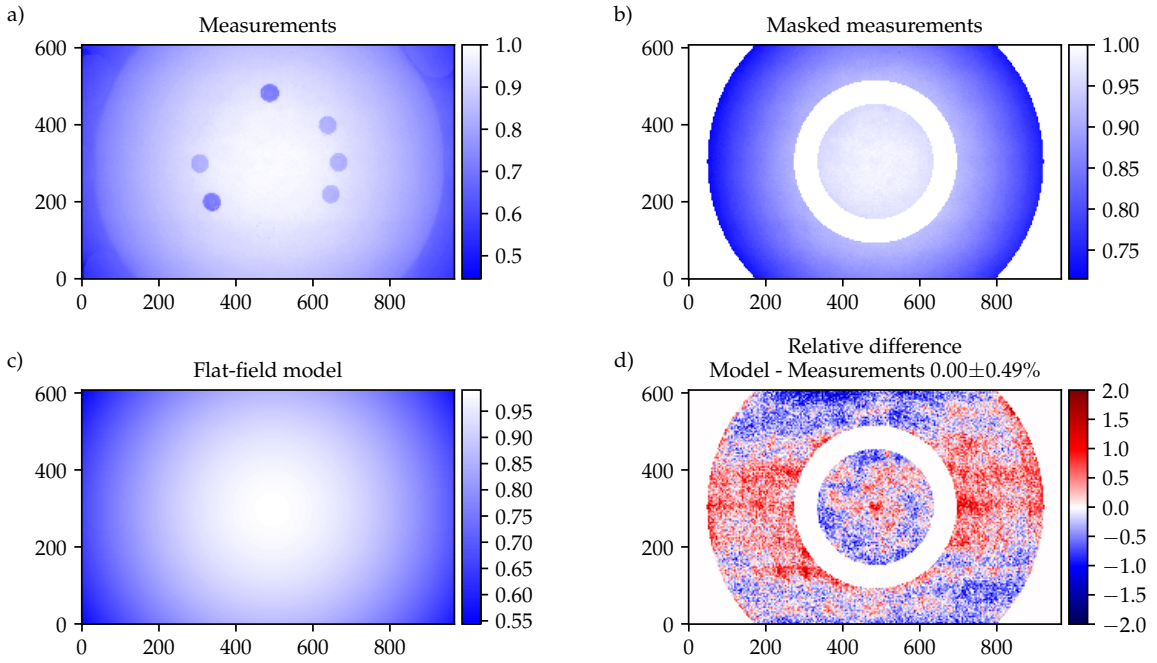

Figure 3.27: *(a) HaloCam$_{\mathrm{RAW}}$ dark signal corrected measurements S_0 (R-channel), which are normalized to 1, of the large integrating sphere (LIS) averaged over 6 different camera orientations. (b) S_0, normalized to 1, as in (a) with a mask applied to the areas where the holes and the edge of the LIS are visible. (c) Flat-field model for HaloCam$_{\mathrm{RAW}}$ R-channel fitted against the measurements with a 2-dimensional 2nd order polynomial. (d) Relative difference between flat-field model and measurements.*

Correcting for the PRNU the flat-field corrected signal S_{F} is defined by

$$S_{\mathrm{F}} = S_0 / F \,, \tag{3.35}$$

with the radiometric signal S_0 and the flat-field correction F.

Linearity of radiometric response

Similar to Ewald et al. (2015) the linearity of the CMOS sensor of HaloCam$_{\mathrm{RAW}}$ was investigated by measuring a temporally stable light source using different exposure times. This experiment was performed at the Large Integrating Sphere (LIS) at CHB. Baumgartner (2013) characterized the output stability of the LIS to better than $\sigma = 0.02\%$ over a time range of 330 s. For a perfectly linear sensor with response R, the photoelectric signal $\widetilde{S_0}$ should increase linearly with exposure time t_{expos} and radiance L

$$\widetilde{S_0} = R\, L\, t_{\mathrm{expos}} = s_{\mathrm{n}}\, t_{\mathrm{expos}} \,, \tag{3.36}$$

with the normalized signal s_{n} defined by

$$s_{\mathrm{n}} = R\, L \,. \tag{3.37}$$

The deviation of the actually observed signal S_0 from the linear relationship of $\widetilde{S_0}$ is called photo response non-linearity. The acutally observed signal S_0 can be written as

$$S_0 = F\, s_{\mathrm{n}}\, t_{\mathrm{expos}} = F\, R\, L\, t_{\mathrm{expos}} \,, \tag{3.38}$$

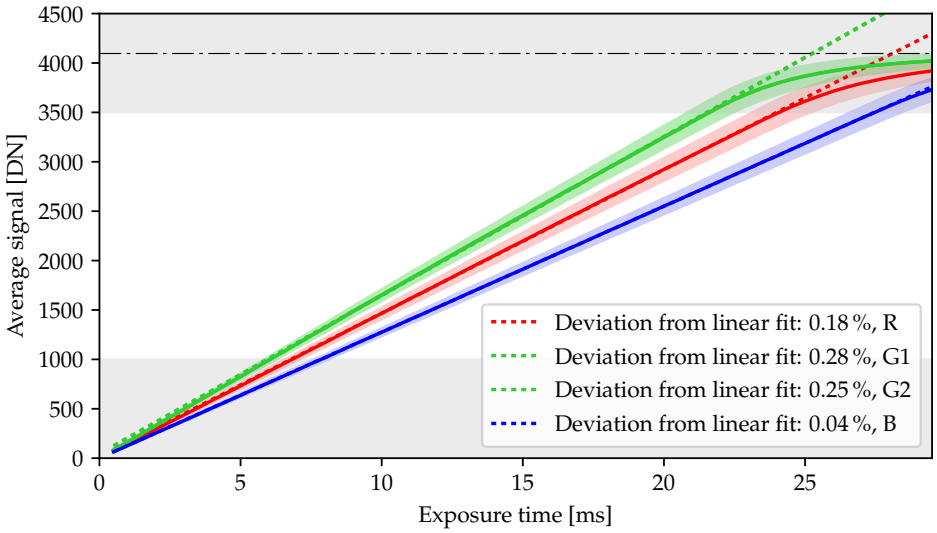

Figure 3.28: *HaloCam$_{\mathrm{RAW}}$ average radiometric signal S_0 as a function of exposure time t_{expos} for the 4 channels. In operational mode the automatic exposure settings ensure that the measured signal ranges between 1000 and 3500 DN, where the averaged signal deviates from a linear behavior between 0.04% for the B-channel and 0.28% for the G1-channel. Signals below and above this range are shaded in gray. For signals close to saturation (4096 DN, black dashed line) the signal deviates clearly from a linear behavior.*

with the flat-field correction F and it follows that the normalized signal can be obtained by

$$s_{\mathrm{n}} = S_0/(F\, t_{\mathrm{expos}})\,. \tag{3.39}$$

Figure 3.28 shows the measured radiometric signal S_0 for exposure times t_{expos} ranging from 0.5 ms to 29.5 ms, averaged over 5 images for each exposure time. The measured signal ranges between 100 and 4037 DN for the G1 and G2 channels. For the data analysis of the HaloCam$_{\mathrm{RAW}}$ images, the measured signals range between 1000 and 3500 DN, where the mean deviation from a perfectly linear sensor amounts to 0.18%, 0.28%, 0.25%, and 0.04% for the R-, G1-, G2-, and B-channel, respectively. For signals close to saturation (4096 DN) the sensor becomes strongly non-linear. Thus, signals $S_0 > 3500$ DN are excluded from the analysis.

Spectral response

The spectral response of HaloCam$_{\mathrm{RAW}}$ was characterized in a similar way as described in Gege et al. (2009) and Baumgartner et al. (2012) using a collimated beam of the monochromator (Oriel MS257) at CHB. The monochromator has an absolute uncertainty of ± 0.1 nm for $\lambda \leq 1000$ nm and ± 0.25 nm for $\lambda > 1000$ nm with a spectral bandwidth of 0.65 nm and 1.3 nm, respectively. To keep the duration of the calibration procedure short, only a small region of 8×8 pixels (per channel) on the camera sensor was illuminated by the monochromator via a parabolic mirror. Measurements were performed over a wavelength range of 350 nm to 900 nm with steps of 5 nm together with the window of the camera casing shown in Fig. 3.21. Figure 3.29 displays the result of the spectral calibration for the red, blue and the two green channels. To obtain the spectral sensitivity curves, the raw images were averaged over the illuminated pixel region and over a set of 10 images per wavelength. Subsequently, the dark signal was subtracted and the spectral response for each channel was normalized to 1.

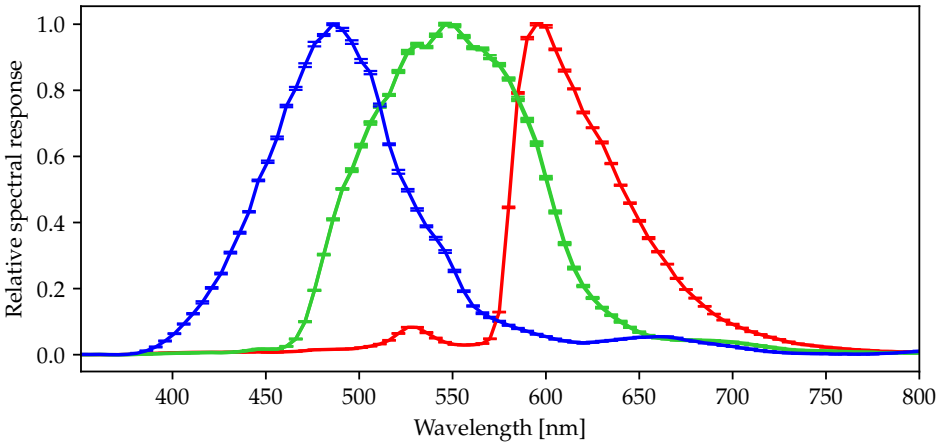

Figure 3.29: *HaloCam$_{\mathrm{RAW}}$ relative spectral response for the R-, G1-, G2-, and the B-channel.*

Absolute radiometric response

To obtain an estimate for the absolute radiometric response of HaloCam$_{\mathrm{RAW}}$ the images recorded on 22 September 2015 were cross-calibrated against simultaneous specMACS measurements. For 7 different specMACS scans the HaloCam$_{\mathrm{RAW}}$ image recorded closest to the time of the specMACS scan was selected. The absolute radiometric response of HaloCam$_{\mathrm{RAW}}$ can be determined by dividing the normalized and flat-field corrected signal s_{n} in [DN/ms] by radiance values L in [mW m^{-2} nm^{-1} sr^{-1}].

$$R = s_{\mathrm{n}}/L \tag{3.40}$$

Here, one radiometric response R for all sensor pixels is determined under the assumption that the PRNU is already accounted for by the flat-field correction. Figure 3.30a shows the calibration factor C [DN mW^{-1} m^2 nm sr], which is calculated by the HaloCam$_{\mathrm{RAW}}$ radiometric signal S_0

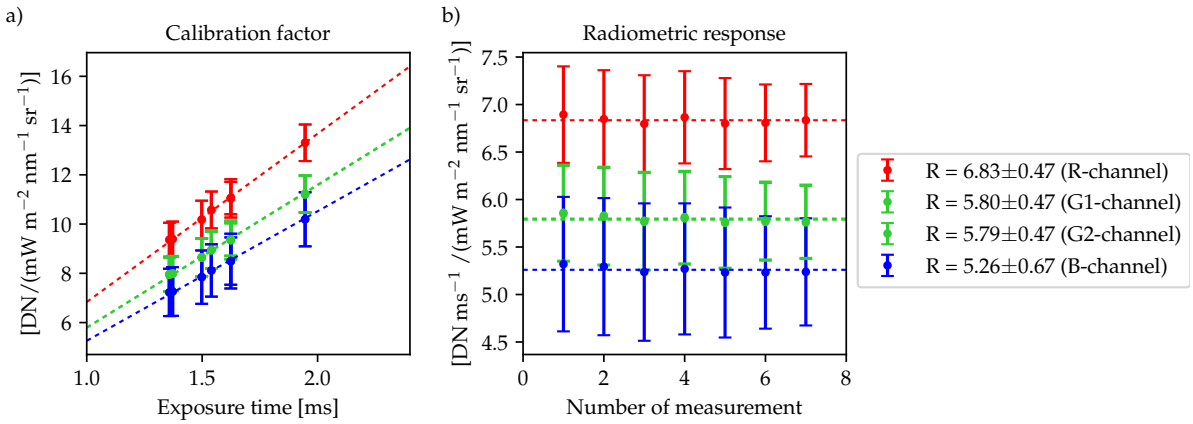

Figure 3.30: *Calibration factors (a) and radiometric response (b) for the 4 HaloCam$_{\mathrm{RAW}}$ channels. The values are derived from cross-calibration of HaloCam$_{\mathrm{RAW}}$ against specMACS for 7 different scenes measured simultaneously on 22 September 2015. The legend on the right provides the absolute radiometric response for HaloCam$_{\mathrm{RAW}}$ with 1σ uncertainty evaluated over the 7 measurements.*

divided by the specMACS radiance L and scales linearly with the exposure time t_{expos}

$$C = S_0/(L\,F) = s_{\mathrm{n}}/(L\,F) \cdot t_{\mathrm{expos}}\,. \tag{3.41}$$

The errors are provided within a 1σ confidence interval and represent the sum of the specMACS measurement error, which is calculated for each pixel as described in Section 3.4, and the standard deviation of the calibration factor calculated over all considered pixels. It should be noted that the measurement error of specMACS of about 5% is responsible for a large portion of the uncertainty of the estimated radiometric response. A large part of the uncertainty is introduced by the inhomogeneity of the observed scene. The exposure times range between 1.2 ms and 2.0 ms, which are typical values for $\mathrm{HaloCam_{RAW}}$ measurements of thin cirrus clouds in the vicinity of the sun. Figure 3.30b shows the radiometric response R [DN $\mathrm{ms^{-1}\,mW^{-1}\,m^2\,nm\,sr}$] as defined in Ewald et al. (2015) for the 7 evaluated scenes. The radiometric response is independent of the exposure time t_{expos}. The resulting radiometric response for the R-, G1-, G2-, and B-channel is provided in the legend of Fig. 3.30. These values were derived using the upper part of the specMACS scan above the sun. An additional test using the middle part of the specMACS scan to both sides of the sun revealed very similar values for the response with slightly larger uncertainties: 6.83 ± 0.56, 5.81 ± 0.56, 5.79 ± 0.56, and 5.28 ± 0.78 DN $\mathrm{ms^{-1}/(mW\,m^{-2}\,nm^{-1}\,sr^{-1})}$. The larger uncertainty of the response in the second evaluation is due to larger variabilities in the scenes used for the evaluation. Since the mean values of both evaluations are very similar, it can be argued that the results shown in Fig. 3.30 are a better estimate of the true response values. Therefore, the results shown in Fig. 3.30 will be used in the following.

Signal noise

The measurements at the LIS can also be used to estimate the noise $\mathcal{N}$ of the measured signal as described in Ewald et al. (2015). The noise consists of the dark noise $\mathcal{N}_{\mathrm{d}}$ and the photon shot noise $\mathcal{N}_{\mathrm{shot}}$. Thus, the standard deviation of the signal noise can be calculated by

$$\sigma_{\mathcal{N}} = \sqrt{\sigma^2_{\mathrm{shot}} + \sigma^2_{\mathrm{d}} + \sigma_{\mathrm{read}}}\,. \tag{3.42}$$

As argued by Ewald et al. (2015), the number of photons N detected over a time interval t_{expos} can be estimated by a Poisson distribution. A Poisson distribution with expectation value N has a standard deviation of $\sigma_{\mathrm{N}} \propto \sqrt{N}$. Thus, the variance of the photon shot noise σ^2_{shot} should scale linearly with the number of detected photoelectrons N and the squared conversion gain k^2 [$\mathrm{DN^2}$] and $\sigma_{\mathcal{N}}$ can be written as

$$\sigma_{\mathcal{N}} = \sqrt{k^2 N + \sigma^2_{\mathrm{d}}}\,. \tag{3.43}$$

Figure 3.31 shows a histogram of the variance $\sigma^2_{\mathcal{N}}$ (a) and the standard deviation $\sigma_{\mathcal{N}}$ (b) of the measured signal of each sensor pixel, evaluated over 5 images, for all exposure times (0.5 to 9.5 ms). The results are shown for the R-channel here, but are very similar for the other 3 channels. According to Eq. (3.43), the variance of the signal measured by each pixel should scale linearly with the signal itself (Fig. 3.31a), whereas the standard deviation should scale with the square root of the signal (Fig. 3.31b). The signal noise ranges from about 10 DN for signals of about 100 DN to about 40 DN for signals of about 1500 DN, typical for operational measurements.

$\mathrm{HaloCam_{RAW}}$ total radiometric uncertainty

The total radiometric uncertainty of $\mathrm{HaloCam_{RAW}}$ was estimated by applying Gaussian error propagation to the equations describing the measured signal with the respective errors. Similar

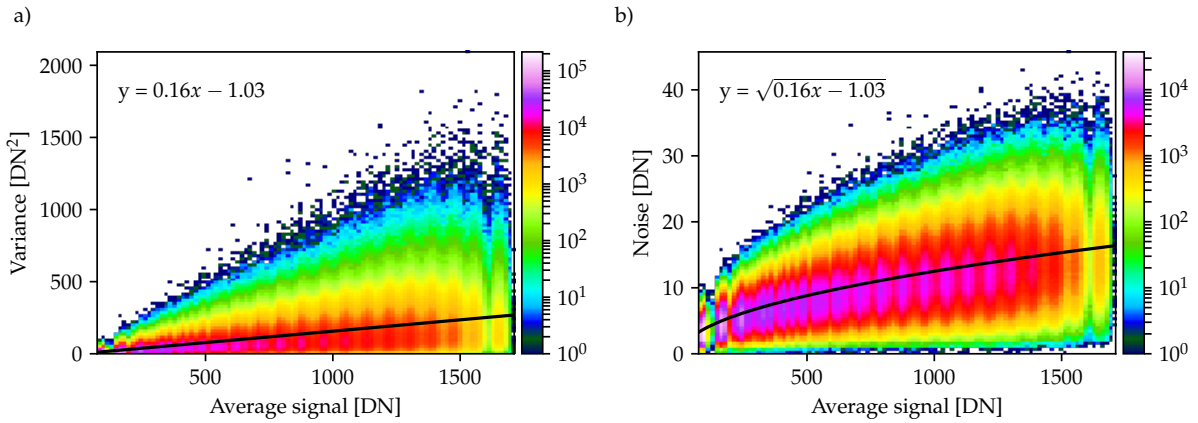

Figure 3.31: *2-dimensional histograms of the variance [DN²] (a) and the noise [DN] (b) of the measured signal as a function of the averaged signal of the R-channel.*

to the description in Ewald et al. (2015), the calculation of the total radiometric uncertainty will be outlined in the following. According to Eq. (3.28) the error of the radiometric signal S_0 is computed by combining the absolute errors of the dark signal $\sigma_\mathrm{d}(t_\mathrm{expos}, T)$ and the instantaneous noise $\sigma_\mathcal{N}(S_0)$

$$2\sigma_{S_0} = \sqrt{(2\sigma_\mathrm{d}(t_\mathrm{expos}, T))^2 + (2\sigma_\mathcal{N}(S_0))^2}\,. \tag{3.44}$$

As defined by Eq. (3.39) the uncertainty of the normalized signal s_n consists of the relative error of the photoelectric signal σ_{S_0}, the relative error of the flat-field calibration σ_F, and the non-linearity error σ_nonlin according to

$$\frac{2\sigma_{s_\mathrm{n}}}{s_\mathrm{n}} = \sqrt{\left(\frac{2\sigma_{S_0}}{S_0}\right)^2 + \left(\frac{2\sigma_\mathrm{F}}{F}\right)^2 + \left(\frac{2\sigma_\mathrm{nonlin}}{s_\mathrm{n}}\right)^2}\,. \tag{3.45}$$

Uncertainties due to polarization of light by components of the camera or the casing were not determined for HaloCam$_\mathrm{RAW}$. However, according to Ewald et al. (2015), the largest part of the polarization sensitivity of specMACS is introduced by the transmission grating which adds the spectral dimension to the measurements. Since HaloCam$_\mathrm{RAW}$ is not equipped with a grating, it is assumed that its polarization sensitivity is significantly lower than for specMACS. According to Hansen and Travis (1974) direct sunlight is unpolarized and the degree of polarization is increasing towards larger scattering angles. Thus, it can be argued that the degree of polarization for transmitted light in region of the 22° halo is lower than for observations of reflected light from cloud sides, especially in the rainbow scattering region, which is the focus of Ewald (2016).
Finally, the radiometric calibration accounts for the error of the sensor response σ_R, which was estimated from cross-calibration between HaloCam$_\mathrm{RAW}$ and specMACS

$$\frac{2\sigma_\mathrm{L}}{L} = \sqrt{\left(\frac{2\sigma_{s_\mathrm{n}}}{s_\mathrm{n}}\right)^2 + \left(\frac{2\sigma_\mathrm{R}}{R}\right)^2}\,. \tag{3.46}$$

Table 3.2 provides the total relative and absolute radiometric uncertainties for the 4 channels of HaloCam$_\mathrm{RAW}$ for two typical signals of 1000 DN and 3000 DN. The relative radiometric uncertainty is the error of the normalized signal s_n (Eq. (3.45)) which is smaller than 3% for all channels. For larger signals the relative 2σ error is smaller since the absolute error is divided by a larger value (cf. Eq. (3.46)). This uncertainty is valid for signal ratios which are independent of

Table 3.2: *HaloCam$_{\mathrm{RAW}}$ total radiometric uncertainty with a 2σ confidence interval.*

		Signal S	R-channel	G1-channel	G2-channel	B-channel
Relative radiometric uncertainty	$\frac{2\sigma_{\mathrm{s_n}}}{s_{\mathrm{n}}}100\,\%$	1000 DN	2.8 %	2.3 %	2.3 %	3.3 %
		3000 DN	1.8 %	1.6 %	1.6 %	2.1 %
Absolute radiometric uncertainty	$\frac{2\sigma_{\mathrm{L}}}{L}100\,\%$	1000 DN	14.0 %	16.4 %	16.4 %	25.6 %
		3000 DN	13.9 %	16.3 %	16.3 %	25.5 %

the sensor response R. For spectral radiance measurements, however, the uncertainty increases significantly due to the contribution of the uncertainty of the estimated sensor response σ_{R}. For the R-channel the total absolute uncertainty amounts to about 14% and about 16% for the two green channels. The uncertainty is largest for the B-channel with about 25.5%.

Since the radiometric response of HaloCam$_{\mathrm{RAW}}$ was cross-calibrated against specMACS, the relative radiometric uncertainty has to be combined with the measurement uncertainty of specMACS. This method has some implications which potentially add to the uncertainty of the estimated radiometric response. First, the HaloCam$_{\mathrm{RAW}}$ images are recorded every 10 s, so the average temporal offset between the specMACS and HaloCam$_{\mathrm{RAW}}$ measurements amount to 5 s. Second, a slight misalignment between the specMACS and HaloCam$_{\mathrm{RAW}}$ images exists, since an exact overlap is impossible due to the temporal offset. Third, to compare the measurements, the specMACS observations have to be convolved with the spectral response of the 4 channels of HaloCam$_{\mathrm{RAW}}$. For wavelengths at the edge of the spectral sensitivity of the specMACS sensor, the measurement uncertainty increases strongly introducing additional uncertainty in the estimated radiometric response for the HaloCam$_{\mathrm{RAW}}$ measurements. This effect is responsible for the large uncertainty of the blue channel, which has a spectral response centered at much shorter wavelengths where specMACS has a larger measurement uncertainty compared to the red and green channels.

3.6 HaloForest – an automated halo detection algorithm

3.6.1 Image processing and feature extraction

For processing the HaloCam images, they are decomposed into their red, green, and blue color channels. The brightness I of each pixel, provided in digital numbers [DN], can then be represented as an array of 1280×960 elements. As an example the HaloCam$_{\mathrm{JPG}}$ image of Fig. 3.23 is used to demonstrate the image processing in case of a 22° halo. Figure 3.32 depicts the brightness distributions of the red, green and blue channel as a function of the scattering angle, averaged azimuthally over the uppermost image segment (no. 4 in Fig. 3.23b). The shaded areas in Fig. 3.32 represent twice the standard deviation of the averaged image region.

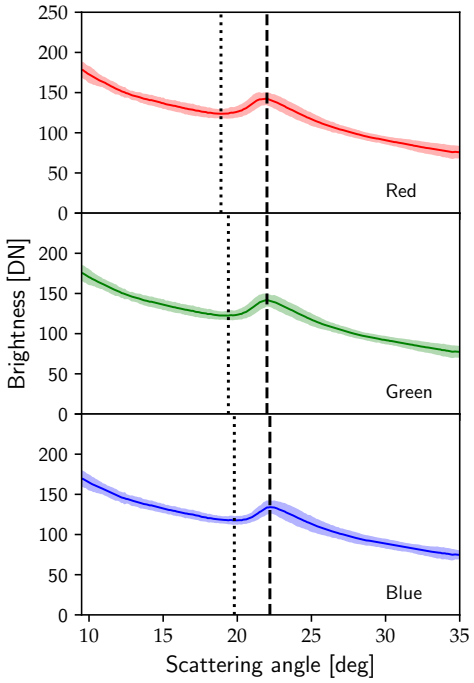

Figure 3.32: *HaloCam$_{\mathrm{JPG}}$ image processing demonstrated for the image shown in Fig. 3.23, segment no. 4. The three panels show the brightness distributions (in digital numbers [DN]) for the red, green and blue image channel as a function of the scattering angle. The solid lines represent the brightness averaged azimuthally over the image segment, whereas the shading indicates the 2σ confidence interval. Vertical lines pinpoint the scattering angles of the 22° halo minimum (dotted) and maximum (dashed) for the RGB channels.*

By analyzing the HaloCam observations several features can be extracted from the brightness distribution across the 22° halo, which will be explained in the following. The scattering angle of the brightness maximum and minimum are indicated in Fig. 3.32 by vertical dashed and dotted lines, respectively. The angular position of the 22° halo maximum ($\vartheta_{\mathrm{halo,\,max}}$) is found by searching for the maximum brightness in the interval (21.0°, 23.5°). Then, the angular position of the halo minimum ($\vartheta_{\mathrm{halo,\,min}}$) is determined by looking for the minimum brightness in the interval (18.0°, $\vartheta_{\mathrm{halo,\,max}}$). Another important feature is the brightness contrast of the halo. In analogy to the definition in Section 3.3.1, the HR in this section is defined as the brightness I at the scattering angle of the halo maximum $\vartheta_{\mathrm{halo,\,max}}$ divided by the brightness at the scattering angle of the minimum $\vartheta_{\mathrm{halo,\,min}}$:

$$\mathrm{HR} = I(\vartheta_{\mathrm{halo,\,max}})/I(\vartheta_{\mathrm{halo,\,min}})\,. \tag{3.47}$$

As an example, the values for $I(\vartheta_{\mathrm{halo,\,max}})$ and $I(\vartheta_{\mathrm{halo,\,min}})$ are indicated in Fig. 3.34 by the blue

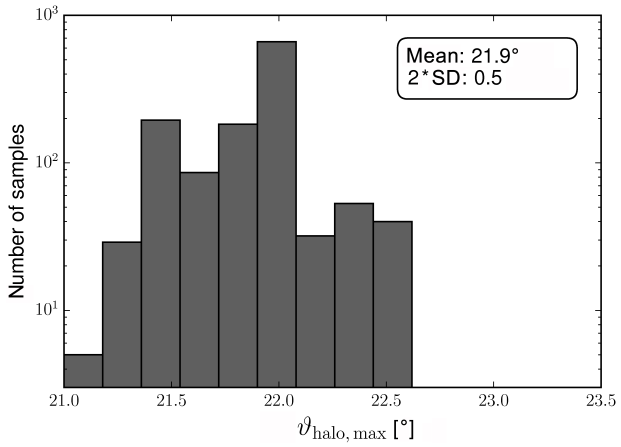

Figure 3.33: *Distribution of the scattering angles of the 22° halo brightness maximum $\vartheta_{\mathrm{halo,\,max}}$ for 1289 randomly chosen and visually classified images using the uppermost image segment (no. 4). The mean value amounts to 21.9° with a 2σ confidence interval of $\pm 0.5°$. Note the logarithmic scale of the y-axis.*

triangles pointing up (max) and down (min), respectively. For clearsky conditions and homogeneous cloud cover the brightness distribution decreases from the sun towards larger scattering angles, as shown in the example in Figs. Fig. 3.32 and Fig. 3.34. If HR < 1 the brightness at the scattering angle of the halo maximum ($I(\vartheta_{\mathrm{halo,\,max}})$) is smaller than for the minimum ($I(\vartheta_{\mathrm{halo,\,min}})$) which is representative for a monotonically decreasing, featureless curve in this scattering angle region. This is the case for clearsky conditions or homogeneous cloud cover without halo. For HR $= 1$ the brightnesses at the halo maximum and minimum are the same, causing a slight plateau in the brightness distribution. A distinct halo peak occurs for HR > 1. Thus, HR $= 1$ is assumed as a lower threshold for the visibility of a halo. For the image of Fig. 3.32 the 22° halo

Table 3.3: *22° halo features from 12 May 2014 13:52 UTC (Fig. 3.32). The relative zenith angle (which corresponds to the scattering angle) for the minimum $\vartheta_{\mathrm{halo,\,min}}$ and maximum $\vartheta_{\mathrm{halo,\,max}}$ brightness of the 22° halo together with the brightness contrast, i.e. the halo ratio (HR) for the red, green and blue image channel.*

	$\vartheta_{\mathrm{halo,\,min}}$	$\vartheta_{\mathrm{halo,\,max}}$	HR
Red	18.9°	22.0°	1.15
Green	19.4°	22.0°	1.16
Blue	19.8°	22.2°	1.14

features for the uppermost image segment are compiled in Table 3.3. The scattering angle of the halo minimum ($\vartheta_{\mathrm{halo,\,min}}$) is smallest for the red channel and largest for the blue channel which is responsible for the reddish inner edge and the slightly blueish outer edge of the 22° halo visible in Fig. 3.23. It should be noted that in many cases the 22° halo appears rather white apart from a slightly reddish inner edge (Minnaert, 1937, Vollmer, 2006). The differences between scattering angles for the three colors are smaller for $\vartheta_{\mathrm{halo,\,max}}$ compared to $\vartheta_{\mathrm{halo,\,min}}$ with a slightly larger value for the blue channel. The halo ratio amounts to about 1.15 averaged over all three channels and is largest for the green and smallest for the blue channel.
The angular position of the 22° halo brightness peak ($\vartheta_{\mathrm{halo,\,max}}$) can also be used to estimate the positioning accuracy of the HaloCam camera system relative to the sun. Figure 3.33 shows a histogram of $\vartheta_{\mathrm{halo,\,max}}$ for 1289 randomly selected HaloCam$_{\mathrm{JPG}}$ pictures showing a 22° halo in the uppermost image segment. This segment was chosen since it contains the most pronounced halos.

For a faint halo the peak in the brightness distribution is rather flat, causing a larger uncertainty in the determination of its the angular position. The mean value of $\vartheta_{\text{halo, max}}$ amounts to 21.9° with a 2σ uncertainty of 0.5°, which is a rough estimate of HaloCam's pointing accuracy. The angular interval, which is used to determine $\vartheta_{\text{halo, max}}$ and $\vartheta_{\text{halo, min}}$, is chosen sufficiently large to account for the pointing accuracy of ±0.5°.

3.6.2 Setup and training of HaloForest

The HaloCam$_{\text{JPG}}$ long-term dataset from January 2014 until June 2016 was evaluated by applying a machine learning algorithm for the automated detection of halos. The algorithm was trained using features extracted from the HaloCam$_{\text{JPG}}$ images. Some of these features (e.g., HR, $\vartheta_{\text{halo, max}}$, $\vartheta_{\text{halo, min}}$) were already described in the previous section. The detection algorithm is presented here for the case of the 22° halo but it is possible to extend it to other halo types as well. The detection is performed by a classification algorithm which is trained to predict whether a HaloCam$_{\text{JPG}}$ picture belongs to the class "22° halo" or "no 22° halo". For such a binary classification a decision tree can be used to create a model which predicts the class of a data sample. Details on decision trees are explained in Appendix A.1.1. One major issue of decision trees is their tendency to overfit by growing arbitrarily complex trees depending on the complexity of the data. In this study the random forest classifier was used as described by Breiman (2001), which improves the issue of overfitting significantly by growing an ensemble of decision trees. A description of the random forest classifier used in this study is provided in Appendix A.1.2. In principle, other classification algorithms could be used like artificial neural networks. The random forest classifier was chosen for the following reasons. Apart from being robust against overfitting it does not require much preprocessing of the input data like scaling or normalizing. During the training of the individual trees the out-of-bag (OOB) samples (i.e., the samples which were not in the training subsets) are used as test data and classification error estimates (e.g. out-of-bag error) can be calculated simultaneously (Breiman, 2001). In contrast to artificial neural networks, the basic structure and the internal threshold tests of decision trees are simple to understand and can be explained by boolean logic. Henceforward, the algorithm applied to the classification of 22° halos will be called HaloForest.

The features used here for the classification are the 22° halo ratio, the scattering angle position of the halo minimum and maximum, and the scattering angle confining the halo peak $\vartheta_{\text{halo, end}}$, which are shown in Fig. 3.34 together with the slope of the regression line in black (solid). The halo peak is confined by $\vartheta_{\text{halo, end}}$ (dash-dotted line) which represents the scattering angle with the same brightness level as $\vartheta_{\text{halo, min}}$ in the scattering angle interval ($\vartheta_{\text{halo, max}}$, 35°]. This feature is used to ensure that the brightness for angles larger than $\vartheta_{\text{halo, max}}$ is decreasing again. The slope of the regression line serves as an estimate for the brightness gradient around the sun. For clearsky images this gradient is steeper than for overcast cases. As a measure of the separation of color in the halo, the scattering angle difference between the blue and red channel for the halo minimum ($\Delta\vartheta_{\text{halo, min}}$) and maximum ($\Delta\vartheta_{\text{halo, max}}$) are calculated, which are defined as

$$\begin{aligned} \Delta\vartheta_{\text{halo, max}} &= \vartheta_{\text{halo, max, blue}} - \vartheta_{\text{halo, max, red}} \,, \\ \Delta\vartheta_{\text{halo, min}} &= \vartheta_{\text{halo, min, blue}} - \vartheta_{\text{halo, min, red}} \,. \end{aligned} \tag{3.48}$$

Furthermore, the standard deviation of the brightness averaged over the image segment is used as a proxy for the inhomogeneity of the scene. These eight features are calculated for each of the six image segments separately. In order to get an impression of typical values of the training features for the two classes, Fig. 3.35a – c shows 2D scatter plots of selected feature pairs for the upper image segment (no. 4). Features, which belong to the class "22° halo", are displayed in blue

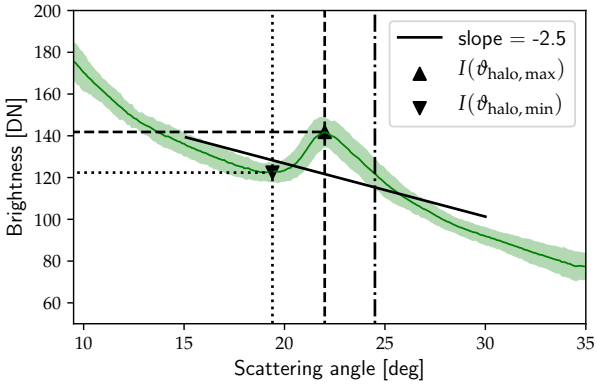

Figure 3.34: *As Fig. 3.32 showing the first minimum $\vartheta_{\mathrm{halo,\,min}}$ (dotted) and the maximum $\vartheta_{\mathrm{halo,\,max}}$ (dashed) of the 22° halo for the green channel. In addition, $\vartheta_{\mathrm{halo,\,end}}$ is indicated (dash-dot line) which represents the scattering angle of the same brightness as $\vartheta_{\mathrm{halo,\,min}}$ and confines the halo peak. In this example $\vartheta_{\mathrm{halo,\,end}}$ is located at about 24.5°. The corresponding brightness $I(\vartheta_{\mathrm{halo,\,min}})$ and $I(\vartheta_{\mathrm{halo,\,max}})$ used to calculate the HR are marked with the blue triangles pointing down (min) and up (max). The regression line of the averaged brightness distribution (solid black), which is evaluated between scattering angles of 15° and 30°, has a slope of −2.5 for this example.*

whereas the features of the class "no 22° halo" are represented by gray scatter points. Figure 3.35a shows the distribution of the scattering angle of the halo maximum vs. minimum. The scattering angles of the halo maximum $\vartheta_{\mathrm{halo,\,max}}$ are confined to a smaller interval for "22° halo" compared with "no 22° halo". However, the two classes share many data points in this projection so more features are needed to generate decision boundaries in a higher, here 8-dimensional space. Figure 3.35b depicts the scattering angle difference between the blue minus the red channel for the halo maximum ($\Delta\vartheta_{\mathrm{halo,\,max}}$) versus minimum ($\Delta\vartheta_{\mathrm{halo,\,max}}$), which is positive for the "22° halo" class since the inner edge (smaller ϑ) of the 22° halo is slightly red. The HR, which is shown in Fig. 3.35c, takes values between 1 and ∼1.3 for the class "22° halos". Images with a low mean standard deviation of the image segment indicate rather homogeneous scenes which are present most of the time when a 22° halo is visible. Figure 3.35a – c visualizes that the two classes "22° halo" and "no 22° halo" can not be separated easily since the values of the features overlap. The lower panels of Fig. 3.35d – f display the regions which are detected as "22° halo" (blue) and "no 22° halo" (gray) by the trained algorithm.

For each of the six image segments an individual classifier was trained using a dataset of visually classified $\mathrm{HaloCam_{JPG}}$ images which were chosen randomly from the dataset. The performance of the classifiers was tested using a random selection of 30% of the dataset which was excluded from training. This procedure was repeated 100 times to get statistically significant results for the performance of the classifier. Table 3.4 shows the confusion matrix for the classifier of the segments directly above (no. 4) and below the sun (no. 1) which represent the two extreme cases of the performance of the six different classifiers: the upper part of the 22° halo has a higher brightness contrast compared to the lower part which is often obstructed by the horizon. For the training of HaloForest 1289 samples with a 22° halo and 5181 samples without 22° halo were used for the uppermost segment (no. 4). The lowermost segment (no. 1) was trained with 296 and 3370 samples of the classes 22° halo and no 22° halo, respectively. The rows of the confusion matrix indicate the true class labels of the samples ("22° halo" and "no 22° halo"), whereas the columns contain the predicted class labels. The number of true positive and negative (in bold) as well as false positive and negative classifications are evaluated and provided with a 2σ confidence interval. The correct classification of "22° halo" is maximum for the uppermost image segment

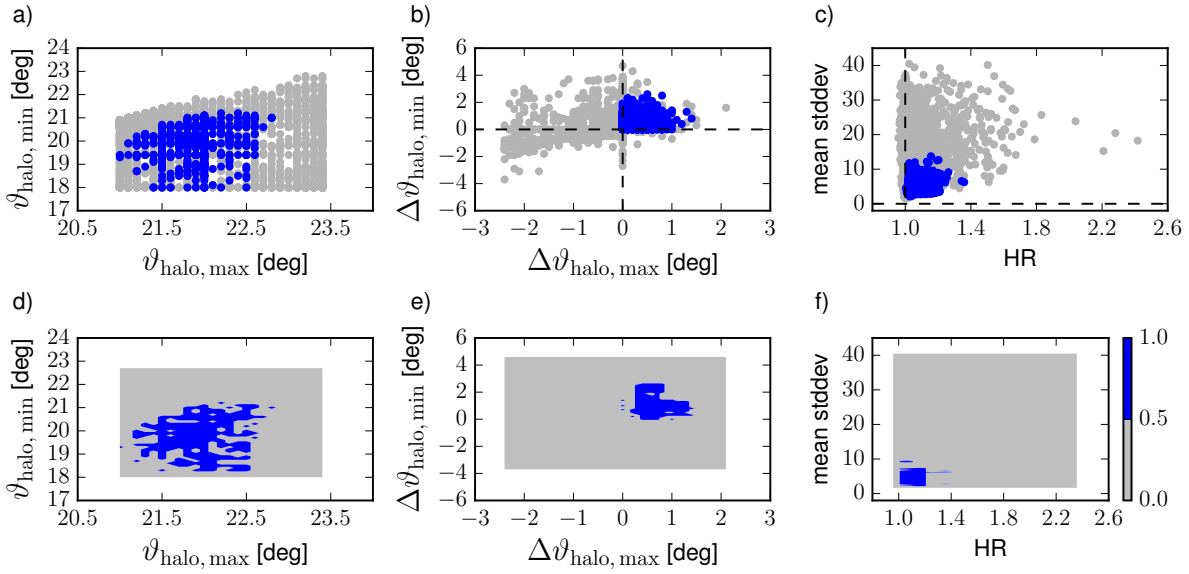

Figure 3.35: *Panels (a) – (c): scatter plots of selected pairs of the 8 features used for training HaloForest. Training samples with(out) 22° halos are represented in blue (gray). Panels (d) – (f): decision boundaries of the random forest classifier for the respective feature pair. The predicted probability used for separating the classes "22° halo"* ($p > 0.5$) *and "no 22° halo"* ($p \leq 0.5$) *is displayed in blue and gray, respectively.*

Table 3.4: *Confusion matrix for HaloForest for the uppermost (no. 4) and lowermost (no. 1) image segments. The label "Predicted" refers to the class which was predicted by HaloForest whereas "True" labels the visually identified class. The true positives (correctly classified "22° halo") are printed in bold font. False positives ("no 22° halo" classified as "22° halo") and false negatives are listed on the other diagonal. The results are provided with a 2σ confidence interval.*

		Predicted	
	Segment 4:	22° halo	no 22° halo
True	22° halo	**(97.3 ± 1.9) %**	(0.4 ± 0.3) %
	no 22° halo	(2.7 ± 0.9) %	**(99.6 ± 0.2) %**
	Segment 1:	22° halo	no 22° halo
True	22° halo	**(88.5 ± 7.1) %**	(0.5 ± 0.5) %
	no 22° halo	(11.5 ± 3.5) %	**(99.5 ± 0.2) %**

(no. 4) with about 98% and minimum for the lowermost segment with about 89%. The correct classification of "no 22° halo" is overall higher than 99%, so the HaloForest algorithm seems to be able to separate the two classes well. The performance of the other four segments ranges between the results of the upper and lowermost segments.

3.7 RICO – Retrieval of ice crystal properties

The preceding section presented the halo detection algorithm HaloForest which can be used to automatically evaluate the large HaloCam dataset for the frequency of 22° halos. Cirrus clouds featuring a halo display contain at least a certain amount of smooth hexagonal ice crystals. The frequency of these cirrus clouds, which will be referred to as "halo-producing" cirrus in the following, provides therefore a first estimate of the minimum fraction of smooth hexagonal ice crystals in cirrus clouds.

More detailed information about ice crystal properties can be obtained by analyzing the brightness contrast and angular width of the 22° halo as discussed in Section 3.3. The slope of the radiance distribution around the 22° halo contains information about the cirrus optical thickness (COT) and ice crystal effective radius. To obtain the maximum information content of the 22° halo regarding the ice crystal optical and microphysical properties, all parameters have to be considered simultaneously. This can be achieved by comparing radiance measurements of the 22° halo with radiative transfer simulations. To determine the optical and microphysical properties which best match the observations, a look-up table (LUT) was compiled by performing radiative transfer simulations with DISORT. The LUT comprises different ice crystal habits, surface roughness values, effective radii, COTs, and AOTs. Furthermore, the LUT is calculated for different SZAs and observation geometries. For the surface albedo, aerosol type, atmospheric profile and cloud height, fixed parameters were used for the LUT. Then, the LUT elements are compared with the radiance measurements to find the best match. LUT and observations have to be compared on the same angular grid. Maximizing the scattering angle range, which is used for this comparison, provides more information. On the other hand, for a too large angular region inhomogeneities in the cirrus optical and microphysical properties become relevant. To optimize this trade-off, a scattering angle range between $16° \leq \Theta \leq 33°$ was chosen. Measurements and LUT are compared via the averaged root mean squared error (RMSE), which is calculated by

$$\mathrm{RMSE}^2 = \overline{L_{\mathrm{meas}} - L_{\mathrm{LUT}}}\,. \tag{3.49}$$

Taking the measurement error into account, all LUT elements with a mean RMSE within the 2σ confidence interval are considered solutions for the cirrus optical and microphysical properties

$$\mathrm{RMSE} \leq 2\sigma_{\mathrm{L,meas}}\,. \tag{3.50}$$

The LUT element with the minimum RMSE is considered the best match. In the following this retrieval method will be referred to by the acronym RICO, which stands for "Retrieval of Ice Crystal prOperties".

3.7.1 Ice crystal shape and roughness models

For the RICO retrieval three different models of ice crystal optical properties are used. Following the findings of Schmitt and Heymsfield (2014), atmospheric ice crystals can be separated into simple and complex particles. The 3 models used in this work have in common that the optical properties of a specific ice crystal shape are mixed using smooth and rough ice crystals.

- YANG: optical properties based on Yang et al. (2013) for 9 different habits: droxtals, solid columns, hollow columns, plates, 8-element columns, 5-element plates, 10-element plates, solid bullet rosettes, and hollow bullet rosettes. Since this parameterization provides only three different roughness levels (smooth, moderately roughened, and severely roughened), the optical properties of smooth and severely roughened ice crystals were mixed linearly

to achieve a continuous distribution of roughness levels. Different fractions of smooth and rough ice crystals were mixed via their extinction coefficient in the radiative transfer simulations. The smooth crystal fraction (SCF) ranges between $0 \leq \mathrm{SCF} \leq 1$, resulting in a rough crystal fraction of $\mathrm{RCF} = 1 - \mathrm{SCF}$. This approach is inspired by the findings of Schmitt and Heymsfield (2014) and Liu et al. (2014) who suggest to separate ice crystals into simple and complex particles.

- $\mathrm{YANG_{RND}}$: optical properties based on a random mixture of the Yang et al. (2013) optical properties. All 9 habits were considered, each with a smooth and a severely roughened version. The SCF was chosen randomly between 0% and 100% in steps of 5% for each combination of a smooth and rough habit. Likewise, the effective radius was chosen randomly for each habit between 5 and 90 µm with steps of 5 µm. The random sampling was performed similar to Wang et al. (2014) and the optical properties were mixed by their extinction coefficients as for YANG.

- GO: optical properties were calculated with the geometric optics raytracing code (Macke et al., 1996) using the corrected version and the Weibull roughness parameterization as described in Section 3.2.2. Solid hexagonal ice crystals were assumed with aspect ratios ranging from 0.02 (thin plates) to 50 (long columns). Ice crystal roughness was parameterized by a Weibull distribution taking values between $0 \leq \sigma_{\mathrm{rough}} \leq 0.3$. As for the YANG optical properties, the different SCFs were achieved here by mixing the optical properties for smooth ($\sigma_{\mathrm{rough}} = 0$) and rough crystals ($\sigma_{\mathrm{rough}} = 0.3$) via their extinction coefficients.

While the GO optical properties allow the definition of different ice crystal aspect ratios and surface roughness levels, they do not account for the physical optics effects responsible for the increasing power spillover index for a decreasing ice crystal size (cf. Section 3.3.1). The YANG and $\mathrm{YANG_{RND}}$ optical properties, in contrast, are also suitable for small ice crystals, but their aspect ratios are coupled with the ice crystal size. In Chapter 4 both parameterizations will be applied to measured radiance distributions of the 22° halo and their suitability to represent optical properties of realistic ice clouds will be investigated.

3.7.2 Sensitivity studies

In the following the sensitivity of RICO on the retrieved smooth crystal fraction (SCF) is tested for different scenarios using the YANG model for the ice crystal optical properties. LUTs assuming slightly different atmospheric or ice cloud parameters are matched against synthetic measurements simulated with DISORT. The tests are performed for the ice crystal habit, AOT, the aerosol type, surface albedo, and atmospheric profile. The synthetic measurements were simulated for a wavelength of 500 nm and a solar zenith angle of 45° in the almucantar plane. The SCF is varied between 0 and 1 in steps of 0.05, whereas the cirrus optical thickness ranges between 0.1 and 3. The effective radius, which is related to the width of the 22° halo, was demonstrated to be independent from multiple scattering effects. Thus, the sensitivity studies presented in this section focus on the SCF with the effective radius treated as a free parameter, ranging from 10 µm to 90 µm in steps of 10 µm. Unless otherwise stated, ice clouds with different mixtures of smooth and severely roughened solid columns with an aerosol-free atmosphere assuming the U.S. standard atmospheric profile (Anderson et al., 1986) were used for the radiative transfer simulations.

First, the retrieval error is estimated by applying the retrieval to simulated test cases using LUTs with slight deviations in the assumed atmospheric condition, e. g. surface albedo, AOT,

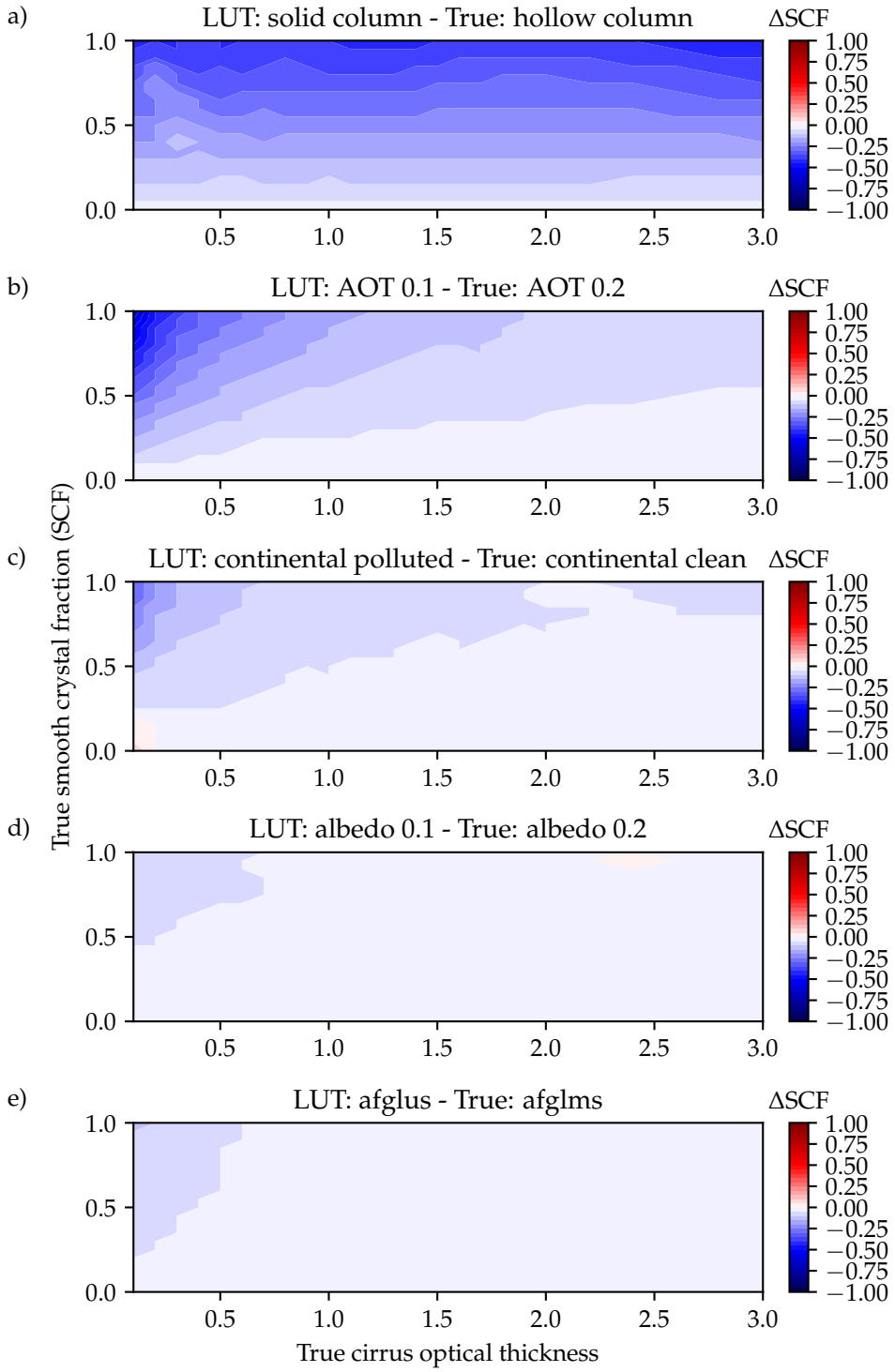

Figure 3.36: *Sensitivity of RICO regarding 5 different LUT parameters: (a) ice crystal habit, (b) AOT, (c) aerosol type, (d) surface albedo, and (e) atmospheric profile. A LUT was matched against synthetic measurements simulated with DISORT at a wavelength of* 500 nm *and an SZA of* 45° *in the almucantar plane. Synthetic measurements for different COTs and SCFs were calculated and are considered as "truth". The LUTs were calculated for slightly different parameter values or parameterizations for the different tests (a–e) while all other LUT parameters were correct. Panels (a) – (e) show contour plots of the difference between the true and retrieved smooth crystal fraction* $\Delta\mathrm{SCF} = \mathrm{SCF}_{\mathrm{Retrieved}} - \mathrm{SCF}_{\mathrm{True}}$*. Blue indicates an underestimation* ($\mathrm{SCF}_{\mathrm{Retrieved}} < \mathrm{SCF}_{\mathrm{True}}$) *and red an overestimation* ($\mathrm{SCF}_{\mathrm{Retrieved}} > \mathrm{SCF}_{\mathrm{True}}$) *of the true SCF.*

aerosol type. In order to investigate the stability of the retrieval for different ice clouds, simulations were performed for a range of COTs and SCFs for one ice crystal habit population. The retrieval error is evaluated for the difference between the true and retrieved SCF defined by

$$\Delta\mathrm{SCF} = \mathrm{SCF}_{\mathrm{Retrieved}} - \mathrm{SCF}_{\mathrm{True}} \,. \tag{3.51}$$

Figure 3.36a demonstrates the effect of assuming a wrong ice crystal shape. All other LUT parameters are correct. The surface albedo is zero and an aerosol free atmosphere is assumed. The difference of the retrieved smooth crystal fraction is denoted by ΔSCF. Blue colors indicate an underestimation of the true SCF ($\mathrm{SCF}_{\mathrm{Retrieved}} < \mathrm{SCF}_{\mathrm{True}}$) and red colors represent an overestimation of the true SCF ($\mathrm{SCF}_{\mathrm{Retrieved}} > \mathrm{SCF}_{\mathrm{True}}$). Calculating the LUT for solid columns and applying it to a cirrus cloud consisting of hollow columns causes a tendency to underestimate the retrieved fraction of smooth ice crystals. This is due to the fact that solid columns produce a brighter halo than hollow columns. Therefore, a smaller fraction of smooth ice crystals is needed in case of the solid columns to produce an equally bright halo. The error of the retrieved fraction of smooth ice crystals is almost independent of the COT but increases with SCF. A maximum error of $\Delta\mathrm{SCF} = -0.45$ occurs for $\mathrm{COT} = 2.8$ and $\mathrm{SCF} = 0.8$.

In Fig. 3.36b the sensitivity of the retrieved smooth crystal fraction is tested for an error in the assumed AOT. For this test the surface albedo is set to zero and the "continental clean" aerosol mixture from the OPAC library was chosen. Underestimating the AOT leads to an underestimation of the SCF, especially for very small COTs. The 22° halo in the LUT is brighter than in the true data due to the lower AOT, especially for low COTs for which the aerosol scattering features dominate over the halo features. Therefore, a smaller SCF is sufficient to obtain a 22° halo of the same brightness contrast as the true halo. When the COT becomes larger than the AOT the retrieval error tends to decrease. For this test the largest error of the retrieved SCF amounts to $\Delta\mathrm{SCF} = -0.65$ for $\mathrm{COT} = 0.1$ and $\mathrm{SCF} = 0.9$.

A similar but much less pronounced effect occurs for errors in the assumed aerosol type, demonstrated in Fig. 3.36c. For the LUT the "continental polluted" OPAC aerosol optical properties were used whereas the truth is "continental clean" with a constant AOT of 0.2 and surface albedo zero. In this case the SCF is overestimated for very small COTs. The maximum difference between retrieved and true smooth crystal fraction amounts to $\Delta\mathrm{SCF} = -0.3$ for $\mathrm{COT} = 0.1$ and $\mathrm{SCF} = 0.7$. The results of these two sensitivity studies demonstrate that especially for ground-based remote sensing it is crucial to have an accurate representation of aerosol type and optical thickness in the model setup in order to retrieve information about ice cloud optical properties. An error in the assumed surface albedo of 0.1 (Fig. 3.36d) has a significantly weaker effect on the retrieved smooth crystal fraction with a maximum error of $\Delta\mathrm{SCF} = -0.05$ for $\mathrm{COT} = 0.1$ and $\mathrm{SCF} = 0.1$. For these simulations an aerosol free atmosphere was assumed.

The last sensitivity study shown in Fig. 3.36e investigates the effect of a different atmospheric profile. This results in a slightly different humidity profile which in turn affects the aerosol optical properties. For this experiment the LUT assumes the U.S. standard atmospheric profile whereas the true profile is the mid-latitude summer atmosphere with higher relative humidity values in the lower layers (Anderson et al., 1986). The results show that for very thin cirrus there is a small difference between true and retrieved smooth crystal fraction of $\Delta\mathrm{SCF} = -0.1$ for $\mathrm{COT} = 0.1$ and $\mathrm{SCF} = 0.8$. In general the introduced error is negligible compared to the errors caused by a wrong representation of the aerosol optical properties.

Figure 3.37 shows the same sensitivity studies as Fig. 3.36 but assuming measurements with unknown radiometric response (cf. Eq. (3.13)). To retrieve the best match in the LUT, the radiometric response of the measured radiance is a free parameter. The sensitivity test of assuming a wrong ice crystal shape, shown in Fig. 3.37a, yields almost the same results as the study with

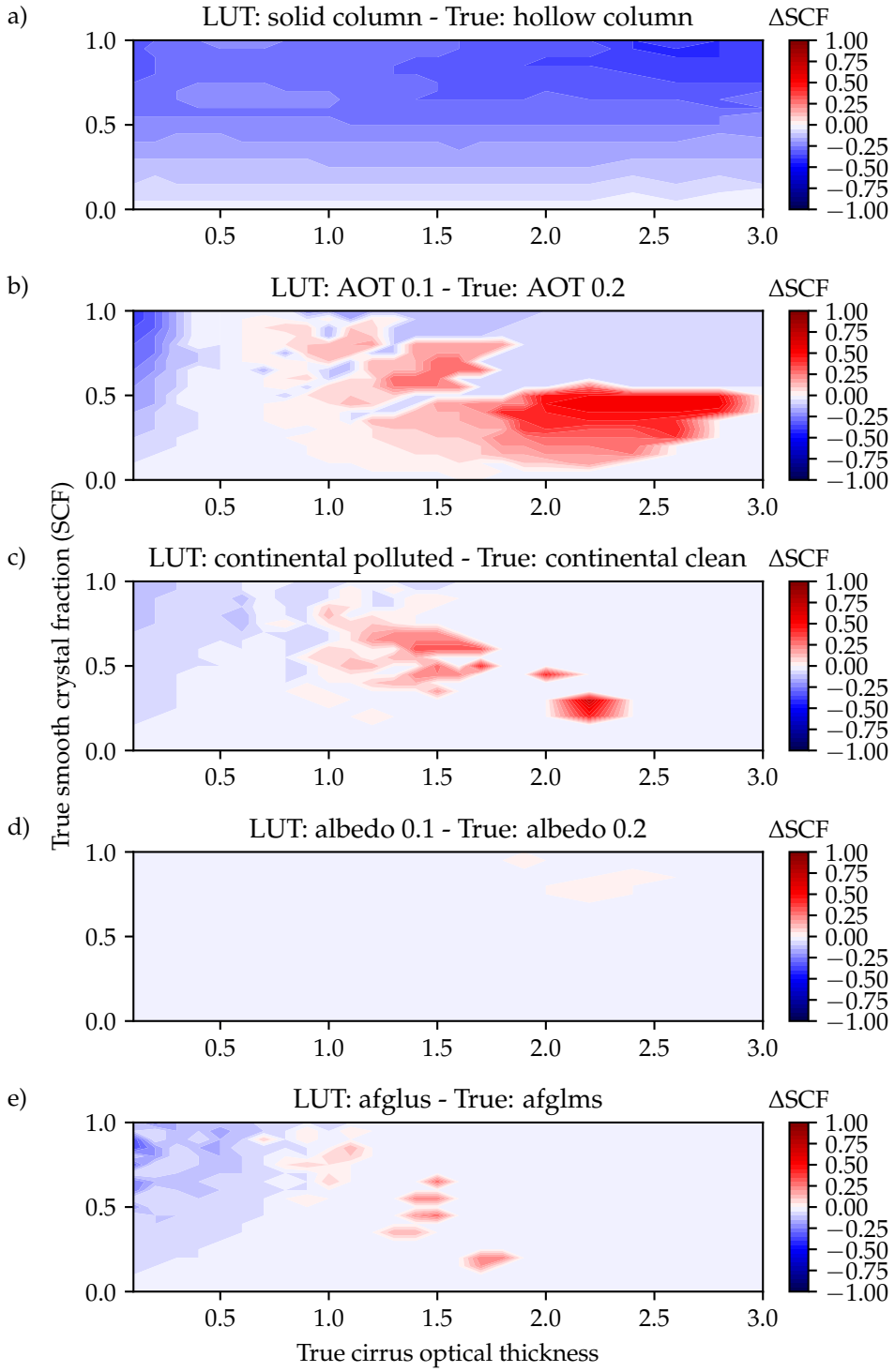

Figure 3.37: *Sensitivity studies for RICO as in Fig. 3.36 assuming uncalibrated measurements by treating the radiometric response as a free scaling parameter in the retrieval.*

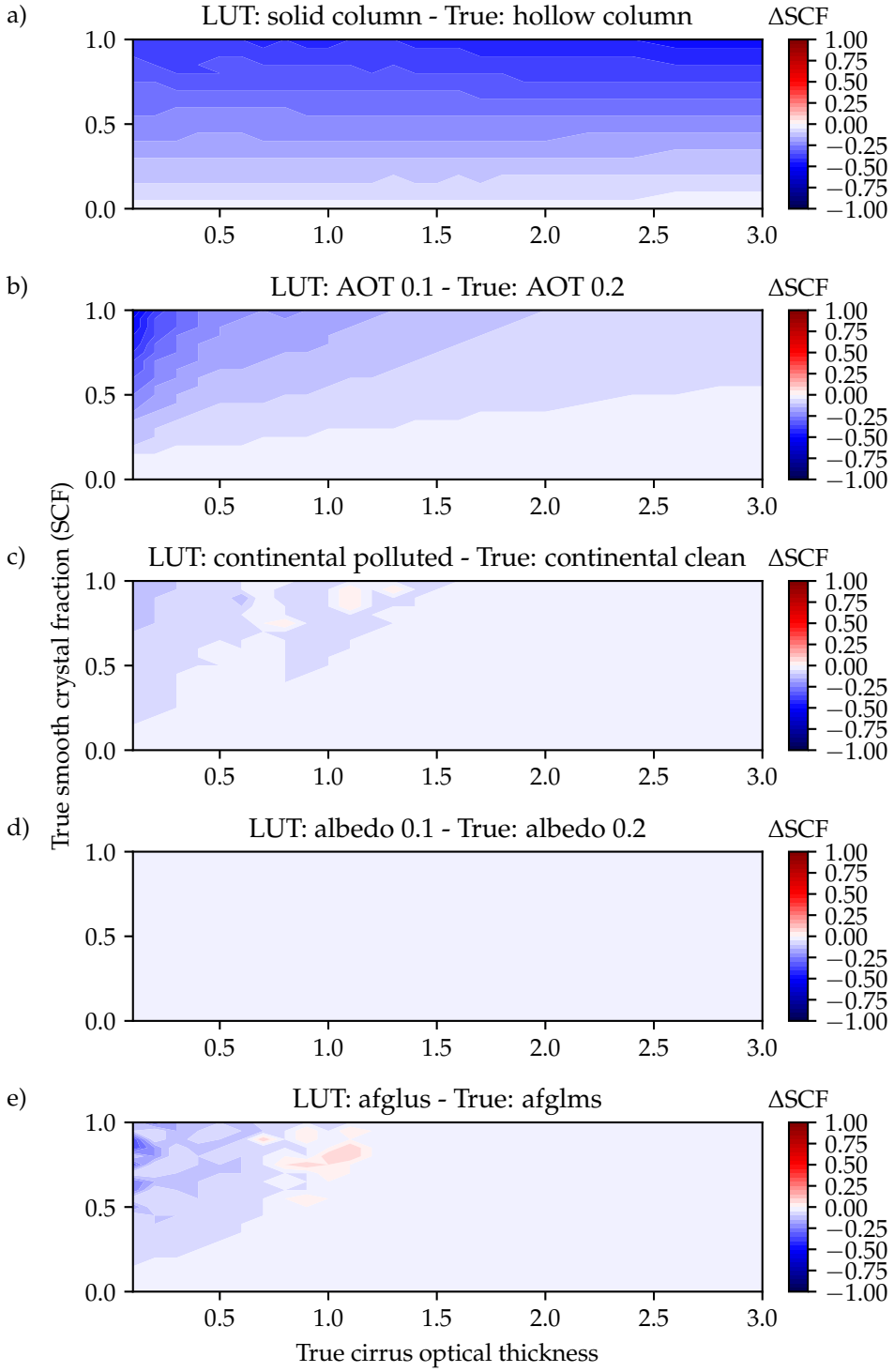

Figure 3.38: *Sensitivity studies for RICO as in Fig. 3.36 assuming a radiometric calibration error of 15%. This is achieved by using the radiometric response as free scaling parameter within the boundaries of ±15%, i.e. $R \in [0.85, 1.15]$ for the synthetic measurements simulated with DISORT.*

the calibrated measurements. The underestimation of the SCF is larger for a brighter halo if solid columns are assumed instead of hollow columns with a maximum error of the retrieved SCF of $\Delta\text{SCF} = -0.4$ for $\text{COT} = 2.2$ and $\text{SCF} = 0.85$. Figure 3.37b shows that uncalibrated measurements can lead to large errors of the SCF ranging from an underestimation of $\Delta\text{SCF} = -0.4$ for small COTs to an overestimation up to $\Delta\text{SCF} = 0.55$ for $\text{COT} > 1$ for an error in the assumed AOT of 0.1. A similar behavior can be observed for the sensitivity test of the aerosol type in Fig. 3.37c which results in a maximum underestimation of the SCF of $\Delta\text{SCF} = -0.15$ for small COTs and an overestimation of the SCF up to $\Delta\text{SCF} = 0.7$ for $\text{COT} = 1.5$ and $\text{SCF} = 0.5$. The tendency to underestimate the retrieved SCF for small COTs and a high SCF remains almost the same as for calibrated measurements. The sensitivity studies of the retrieval on wrong assumptions of the surface albedo (Fig. 3.37d) is almost negligible with a maximum error of $\Delta\text{SCF} = 0.05$ in the retrieved SCF. An error in the assumed atmospheric profile (Fig. 3.37e) results in a maximum error of the retrieved SCF between $\Delta\text{SCF} = -0.35$ and $\Delta\text{SCF} = 0.3$ at a COT of 0.1 and 0.9, respectively. This study demonstrates that for uncalibrated measurements the retrieval uncertainties can deviate up to 70% in the retrieved SCF from the errors of the calibrated measurements.

Another test was performed for calibrated measurements with an error of the radiometric response of 15%, which corresponds to the error of $\text{HaloCam}_{\text{RAW}}$'s R-channel (cf. Section 3.5.3). Figure 3.38 shows the results for the same sensitivity studies as in the previous cases (Figs. 3.36 and 3.37). The results of the ice crystal habit and AOT test in Fig. 3.38a and Fig. 3.38b are very similar to the calibrated measurements assuming no error for the radiometric response (cf. Fig. 3.36a and Fig. 3.36b). A slight overestimation of the retrieved SCF occurs for the aerosol type and atmospheric profile test (Fig. 3.38c and Fig. 3.38e) compared to the sensitivity of the calibrated measurements assuming no error for the radiometric response. For the aerosol type test (Fig. 3.38c) the error of the retrieved SCF ranges between $\Delta\text{SCF} = -0.15$ and $\Delta\text{SCF} = 0.15$, whereas for the atmospheric profile test (Fig. 3.38e) ΔSCF varies between $[-0.35, 0.15]$. The error of the retrieved SCF for the albedo test (Fig. 3.38d) is negligible which occurs most likely since errors in the assumed LUT parameters are transferred to the radiometric calibration factor to some extent.

These sensitivity studies demonstrate that the largest retrieval errors occur for wrong assumptions of the ice crystal habit and the AOT. Thus, for the compiled LUTs all available ice crystal habits for the YANG optical properties are considered. Under the assumption that the optical properties represent the variability of ice crystals in natural cirrus clouds, the retrieval error for the ice crystal habit is negligible. The AOT is varied in the LUT assuming typical values for Munich. For the remaining LUT parameters, i.e. aerosol type, surface albedo, and atmospheric profile, "best guess" fixed values or parameters are chosen. The procedure how the LUT parameters are selected will be presented in the following sections.

Depending on the temperature regime of the cirrus and its evolutionary stage, the cloud can contain supercooled water droplets alongside the ice crystals. Hu et al. (2010) investigated the occurrence frequency, liquid water content, liquid water path, and temperature dependence of supercooled water droplets using global depolarization and backscatter intensity measurements from CALIOP. These observations were combined with temperature information from co-located infrared imaging radiometer (IIR) and MODIS measurements to derive cloud water paths. This study considers clouds with an optical thickness greater than 0.4. Hu et al. (2010) confirmed the findings of Hogan et al. (2004) who state that supercooled water clouds are rarely found below −35 °C. According to Hu et al. (2010) the probability of water phase occurring in a cloud is almost 0% for $T \leq -35\,^{\circ}\text{C}$ and increases rapidly to almost 100% at about −10 °C.

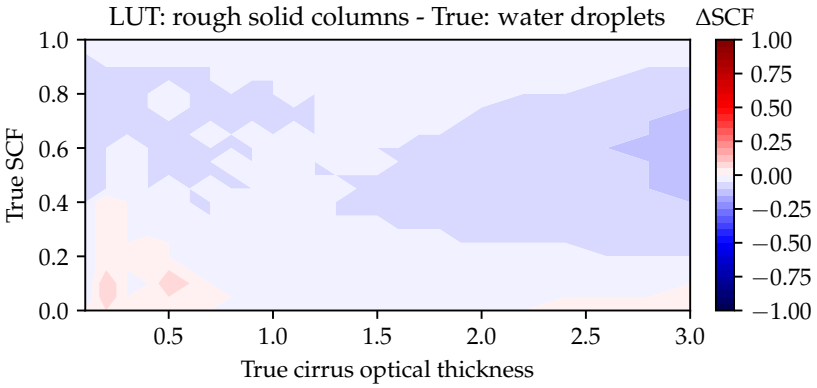

Figure 3.39: *Sensitivity studies for RICO as in Fig. 3.36 for measurements assuming mixtures of smooth ice crystal columns with supercooled water droplets.*

Since water droplets cannot form halo displays due to their spherical shape, they have in principle a similar smoothing effect on halo displays as rough ice crystals. Water droplets may therefore not be distinguishable from rough ice crystals by passive ground-based observations in the visible spectral range. To investigate the effect of supercooled water droplets on the retrieved smooth crystal fraction, synthetic measurements were simulated with DISORT for different mixtures of smooth ice crystal columns and water droplets. Similar as for the two-habit LUTs, the fraction of water droplets was increased from 0 for a cloud consisting entirely of smooth solid ice crystal columns to 1 for a pure water cloud. The water cloud optical properties were calculated with the Mie tool described in Wiscombe (1980). A gamma size distribution $N(r)$ was assumed

$$N(r) = N_0 r^{\alpha} exp\left(-\frac{r}{r_{\text{eff}}\ \nu_{\text{eff}}}\right), \tag{3.52}$$

with the droplet radius r, the normalization constant N_0, and $\alpha = 7$, which corresponds to an effective variance of $\nu_{\text{eff}} = 1/(\alpha + 3) = 0.1$, as described in Emde et al. (2016). It is assumed that all cloud particles (water droplets and ice crystals) have the same effective radius which was varied between 10 and 90 µm in steps of 10 µm. A LUT assuming different mixtures of smooth and rough ice crystal columns was matched against these synthetic measurements. The retrieved SCF is displayed in Fig. 3.39. The error of the retrieved SCF ranges in the interval $\Delta\text{SCF} \in [-0.1, 0.1]$. This means that water droplets indeed have a very similar effect on the 22° halo as rough ice crystals and introduce an error of the retrieved smooth crystal fraction of $\Delta\text{SCF} = \pm 0.1$.

The sensitivity of the cloud height and thickness as well as the atmospheric profile on the 22° halo radiance distribution was tested. The tests were performed for the $\text{HaloCam}_{\text{RAW}}$ R-, G-, and B-channel. Varying the cloud base height between 6 km and 10 km, both with a geometrical thickness of 1 km resulted in differences of $\ll 1\,\%$. Similar results were obtained for the depth of the cloud which was varied between 1 km and 4 km. Also the choice of the atmospheric profile is negligible in this spectral range: the difference between a simulations using the U.S. standard atmosphere and the mid-latitude summer atmosphere was $\ll 1\,\%$. Both atmospheric profiles are defined in Anderson et al. (1986). Unless otherwise stated the LUT simulations were performed using the U.S. standard atmospheric profile and a cirrus cloud between 10 km to 11 km height.

Furthermore, it was tested whether it is sufficient to perform radiative transfer simulations for a representative wavelength rather than integrating over the full spectral sensitivity curves of $\text{HaloCam}_{\text{RAW}}$. Figure 3.40 shows the results of radiative transfer simulations using *libRadtran*

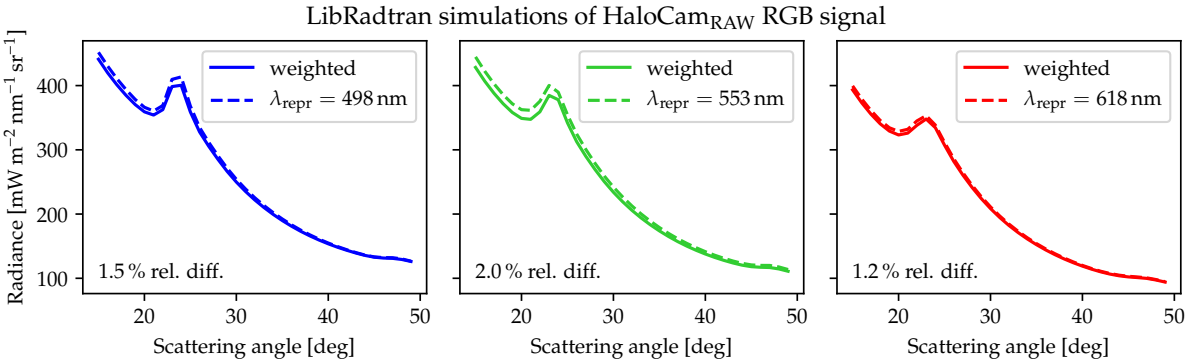

Figure 3.40: *Radiative transfer simulations performed with libRadtran for the HaloCam$_{RAW}$ red, green and blue channel in the principal plane above the sun with* SZA = 45°. *A cirrus cloud with* COT = 1 *(at a wavelength* 550 nm*),* r_{eff} = 20 µm *and a mixture of 25% smooth and 75% severely roughened solid columns was assumed. The continental average aerosol mixture from OPAC was chosen with* AOT = 0.1 *at* 550 nm.

for realistic conditions including a cirrus cloud with 25% smooth crystals and a typical AOT of 0.1. The geometry was chosen in the principal plane above the sun (SZA = 45°) for scattering angles between 10° and 50°. The solid lines represent spectral simulations integrated over the spectral sensitivity functions for the red, green and blue channel of HaloCam$_{RAW}$. The dashed lines display the same simulations but for only one wavelength which is equal to the weighted average of the respective camera channels. The averaged relative differences are overall smaller than 2%. Considering the large uncertainties of the unknown aerosol type let alone the variability of the ice crystal shape, this uncertainty is considered small enough to allow for monochromatic radiative transfer simulations using the representative wavelengths of each camera channel. The representative wavelengths for HaloCam$_{RAW}$ were determined by the weighted average over the spectral response of each channel (cf. Fig. 3.29) resulting in 618 nm for the red, 553 nm for the green, and 498 nm for the blue channel.

3.7.3 Ancillary data

The sensitivity studies in the previous section revealed that the RICO retrieval is influenced by additional parameters. Besides the ice crystal shape itself, the cirrus optical thickness has the strongest impact on the retrieval followed by the aerosol optical thickness and the surface albedo. The subsequent sections present ancillary data which are used to constrain these additional parameters in the retrieval and explains the methods which are used to determine these parameters.

Aerosol optical thickness

The aerosol optical thickness was derived from the AERONET AOT product (Holben et al., 1998) for the observation site on the MIM rooftop platform. The AOT during the time when the cirrus cloud was observed can be estimated from clearsky periods before or after. According to the study of Schnell (2014) typical AOT values for Munich during the period from 2007 to 2010 amount to 0.269 ± 0.014 based on AERONET data for a wavelength of 500 nm and ranged between 0.12 – 0.17 at 532 nm for measurements with MULIS (Multichannel Lidar System) (Freudenthaler et al., 2009). Analyzing the AERONET aerosol optical thickness values (version 2, level 1.5) between September 2015 and April 2017 the mean AOT at a wavelength of 500 nm amounts to 0.19 as displayed in Fig. 3.41. 3% of the values range between $0.7 \leq$ AOT ≤ 3, which are most likely thin,

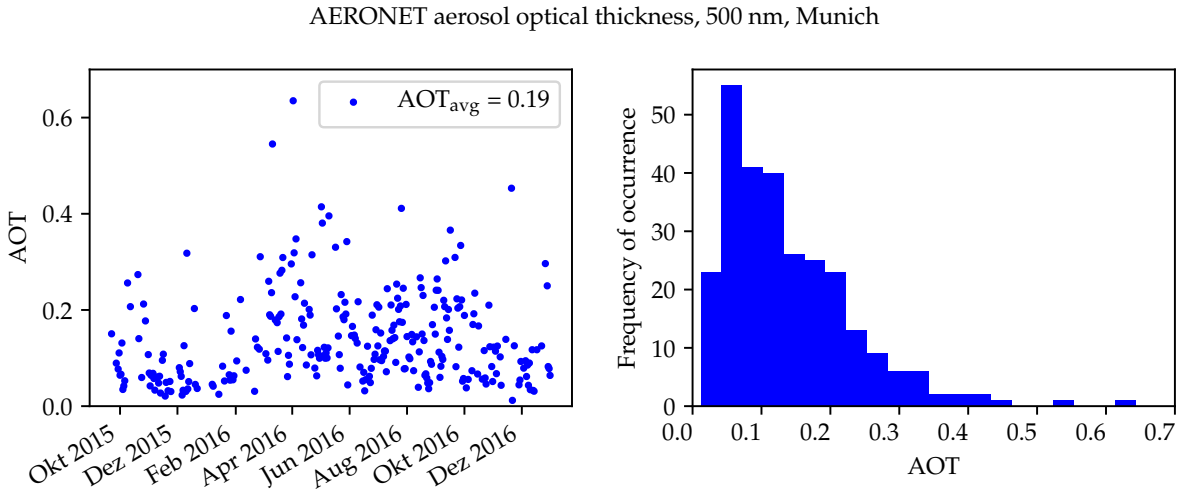

Figure 3.41: *AERONET aerosol optical thickness (AOT) at* 500 nm *wavelength for the time range between September 2015 and December 2016 for which the LUTs are calculated. The average AOT during this time range amounts to about 0.19 (left panel). The histogram in the right panel displays the AOT up to 0.7 and shows that the most frequent AOTs range between 0 and 0.5. 3% of the values range between* $0.7 \leq \mathrm{AOT} \leq 3$. *These are most likely thin, homogeneous cloud layers which are not filtered out by the AERONET cloud-screening algorithm.*

homogeneous cloud layers which are not filtered out by the AERONET cloud-screening algorithm. To cover the most frequently observed values for Munich, which are displayed in Fig. 3.41b, the LUTs were calculated for AOTs ranging between 0.0 and 0.5 in steps of 0.05. Schnell (2014) also studied the typical aerosol type over Munich using CALIPSO data. Evaluated in geometrical layer depth, the dominant aerosol type was smoke, followed by polluted dust. In autumn the continental clean aerosol type was the second largest fraction. Other observed aerosol types were dust and continental polluted aerosol. Unless otherwise stated, the LUT simulations were performed using the "continental average" mixture which is part of the OPAC database and described in Hess et al. (1998). To constrain the AOT in the retrieval, the daily mean value from AERONET was used within a 2σ confidence interval.

Cirrus optical thickness

The cirrus optical thickness (COT) has a strong influence on the brightness contrast of the 22° halo and has to be constrained as much as possible to retrieve ice crystal shape and roughness. For this retrieval the COT is derived from sun photometer measurements using the SSARA instrument (Toledano et al., 2009, 2011). The SSARA instrument provides direct sun measurements with a temporal resolution of 2 s which is much more suitable for the observation of the highly variable cirrus clouds than the AERONET data which has a temporal resolution of 15 min (Holben et al., 1998). The COT is derived by calculating the total optical thickness from the SSARA direct sun measurements. The previously estimated AOT is then subtracted and a correction parameter is applied to account for the diffuse radiation measured additionally due to the increased forward scattering of the large ice crystals. Similar to the procedure presented in Reinhardt et al. (2014) the concept of the apparent optical thickness is used as in Shiobara and Asano (1994), Guerrero-Rascado et al. (2013), and Segal-Rosenheimer et al. (2013).

According to Bouguer-Lambert-Beer's law (cf. Eq. (2.24)), the solar radiance L transmitted

by the atmosphere with a slant path optical thickness τ_s can be denoted as

$$L = L_0 \exp(-\tau_s)\,,$$

where L_0 is the solar radiance at the top of the atmosphere. Any detector with a finite FOV which is pointing towards the sun will measure both the direct solar radiance and the diffuse radiance produced by scattering particles and molecules in the atmosphere. The total radiance entering the instrument FOV can be considered as an apparent radiance L' representing the direct and the diffuse part together. The apparent radiance is defined as

$$L' = L_0 \exp(-\tau_{app}) = L_0 \exp(-k\,\tau_s)\,, \tag{3.53}$$

with the apparent optical thickness τ_{app}. The apparent optical thickness can be related with the slant-path optical thickness τ_s by introducing the correction factor k

$$\tau_{app} = k\,\tau_s\,, \tag{3.54}$$

which accounts for the difference between direct and apparent radiance due to the additional diffuse part and takes values $k \in [0, 1]$. Using Eq. (3.54) the slant-path optical thickness τ_s can be calculated by

$$\tau_s = \ln\left(\frac{L_0}{L'}\right)/k\,. \tag{3.55}$$

As discussed in Reinhardt et al. (2014), for $\tau_s < 3$ the correction factor k is most sensitive to the detector FOV, the effective particle radius and shape but is almost independent of τ_s itself. For the RICO retrieval the k-factors were calculated according to this procedure for the SSARA FOV of 1.2° (Toledano et al., 2009) assuming a COT of 1.5 as proposed by Reinhardt et al. (2014). The k-factors were calculated for all ice crystal habits, surface roughness values, and effective radii used in the LUT. The COTs derived from the SSARA direct sun measurements using the presented method, are used as an additional constraint in the retrieval.

Surface albedo

The surface albedo is another parameter which affects the transmission measured at the ground. With increasing surface albedo more radiation is reflected by the ground which is scattered again by the clouds. However, for an error of 0.1 in the assumed surface albedo the errors in the retrieved SCF are significantly smaller ($|\Delta\text{SCF}| \leq 0.05$) than for a wrong assumption of the aerosol type ($|\Delta\text{SCF}| \leq 0.3$) or AOT ($|\Delta\text{SCF}| \leq 0.65$) (cf. Fig. 3.36). To estimate the surface albedo during the time of the measurements, the MODIS white-sky albedo product MCD43B3 (Strahler et al., 1999) was used. The MODIS white sky albedo product is available for 7 wavelength bands centered at 469, 555, 645, 858, 1240, 1640 and 2130 nm. Figure 3.42 shows the MODIS white-sky albedo for the 555 nm wavelength band. For orientation, a few locations are indicated in Fig. 3.42 by red dots. The MIM (Meteorological Institute of the LMU) in Munich is represented by the northernmost red dot and the DLR (German Aerospace Center) in Oberpfaffenhofen is marked by the red dot south-west of Munich. The displayed geographic region was selected to cover the coordinates of the projected 22° halo between sunrise and sunset throughout the year. Details on the calculation of the coordinates of the projected 22° halo are described in Appendix A.2. At a wavelength of 555 nm albedo values range between about 0.015 and 0.12 with the lowest values for lakes (e.g. south of Starnberg) and forests (e.g. east of DLR). To obtain spectrally continuous data, the ASTER spectral library (Baldridge et al., 2009) is applied to interpolate the MODIS albedo data similar to the procedure described in Hausmann (2012). A linear combination of the

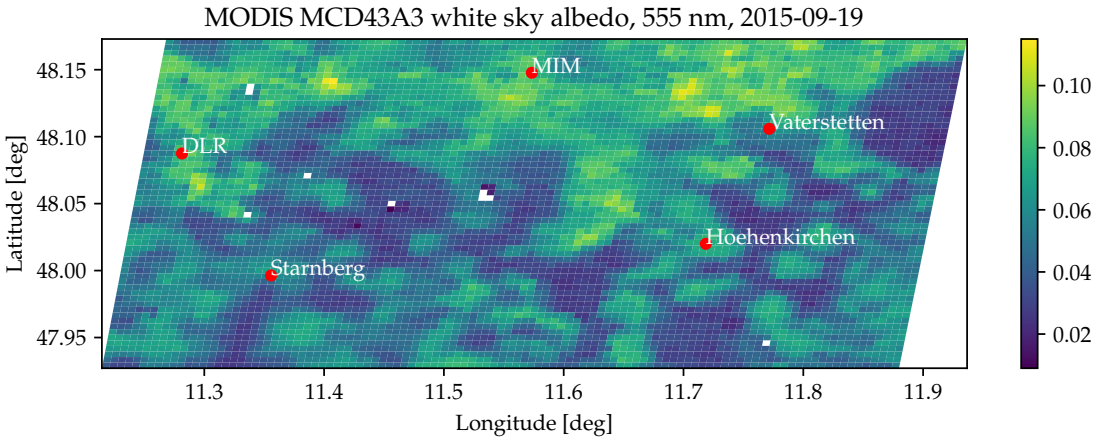

Figure 3.42: *MODIS MCD43A3 white sky albedo from 19 September 2015 at a wavelength of* 555 nm *displayed for the geographic region which is covered by the projected* 22° *halo between sunrise and sunset throughout the year. The Meteorological Institute of LMU in Munich is marked by a red dot and labeled with "MIM". Some more locations, e.g. the DLR in Oberpfaffenhofen, are marked for orientation.*

spectral albedo of deciduous and conifer trees, grass, shingle and concrete is used to represent the MODIS white sky albedo. Figure 3.43 shows the MODIS white sky albedo measured at the seven wavelengths with black dots. The black line represents the linear combination of the single ASTER spectral albedos which provides the best match of the MODIS measurements. The single spectral albedos with the corresponding weighting coefficients are depicted in different colors. To obtain the albedo measured e.g. by $\text{HaloCam}_{\text{RAW}}$, the fitted spectral albedo from the ASTER library (cf. black line in Fig. 3.43) is integrated over the spectral sensitivity of the respective camera channel. In the case of $\text{HaloCam}_{\text{RAW}}$, integrating the spectral albedo over the red, green,

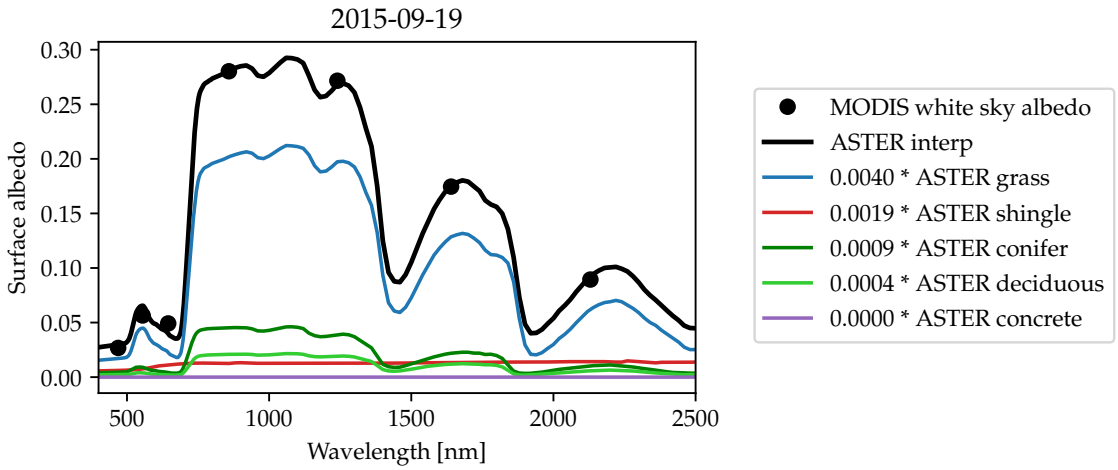

Figure 3.43: *Spectral albedo data from the ASTER library provided with a resolution of* 2 nm *for grass (blue), shingle (red), conifer (dark green) and deciduous trees (green) as well as concrete (purple). A linear combination for the different ASTER albedo types is determined which represents best the averaged MODIS data from Fig. 3.42 by applying the least-squares method. The weighting factors for 19 September 2015 are provided in the legend of the figure. The resulting mixture of ASTER albedo data is then used to obtain an approximation of the MODIS albedo product for high spectral resolution, which is represented by the black solid line.*

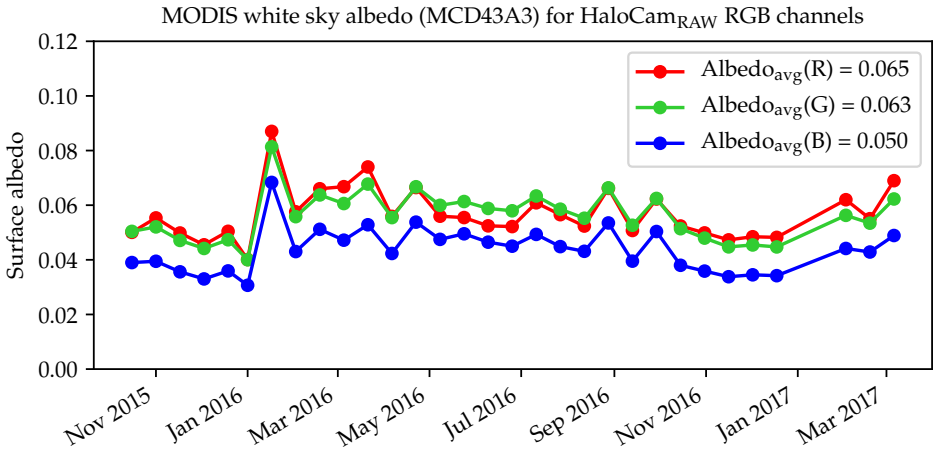

Figure 3.44: *Surface albedo between October 2015 and March 2017 for the HaloCam$_{RAW}$ RGB channels. The data are obtained by weighting the spectral high-resolution parameterization of the MODIS albedo data (cf. Fig. 3.43 black curve) with the spectral response of the RGB channels (cf. Fig. 3.29). The surface albedo for the HaloCam$_{RAW}$ channels averaged over this period amounts to 0.065 (R), 0.063 (G), and 0.050 (B).*

and blue channel yields the albedo values displayed in Fig. 3.44 with the respective line color. For this figure the MODIS white sky albedo values were evaluated between October 2015 and March 2017. Values larger than 0.1 were excluded since it is likely that they are affected by snow. Averaging over the whole period yields mean albedo values for the red, green, and blue channel of 0.065, 0.063, and 0.050 respectively. The red and green channels show higher values than the blue channel since the surface South of Munich is dominated by green grass and trees. Comparing the red and the green channel, a slight difference between winter and summer is noticeable which is very likely due to the vegetation period. During summer the deciduous trees increase the albedo in the part of the spectrum covered mostly by the green channel, whereas in winter the albedo measured by the green channel is slightly lower than the red channel.

3.8 CrystalTrace – a raytracing algorithm for oriented ice crystals

For radiative transfer simulations it is usually assumed that the scattering particles are randomly oriented within the cloud or the atmosphere. This allows for a simplified parameterization of the scattering process. The scattering phase function depends only on the scattering angle and the relative azimuth angle of the incident and outgoing light can be selected randomly. In most cases the assumption of randomly oriented particles is realistic, but in case of cirrus clouds oriented ice crystals have frequently been observed by space-borne and ground-based observations. Noel and Sassen (2005) studied the orientation of ice crystals in cirrus and mid-level clouds using scanning polarization lidar observations. Chepfer et al. (1999) and Noel and Chepfer (2004) observed oriented ice crystals in more than 40% of ice clouds by analyzing POLDER bidirectional polarized radiances for specular reflection above optically thick ice clouds. Noel and Chepfer (2010) analyzed CALIOP backscatter and depolarization ratios for thin ice clouds and found oriented crystals in about 6% of all ice cloud layers. Zhou et al. (2012) retrieved the frequency of oriented ice crystals by simulating the CALIOP backscatter and depolarization ratio with help of a 3D Monte Carlo model and found a maximum fraction of oriented plates between 0.5% in cold ice clouds and 6% in optically thick mixed-phase clouds.
Furthermore, certain halo displays such as sundogs and upper tangent arcs can only be explained by the presence of oriented ice crystals (e.g. Wegener (1925), Tricker (1970), Tape (1994), Tape and Moilanen (2006)). One objective of this work is to investigate the effect of ice crystal orientation on halo displays and to explore possibilities to infer the fraction of oriented ice crystals from their brightness contrast. When ice crystals are oriented the single-scattering properties are not only a function of the scattering angle but depend also on the azimuth of the scattering plane (Liou and Yang, 2016). For radiative transfer simulations of oriented ice crystals, their optical properties have to be stored for the different incident and scattered directions which implies an increase of the required memory space by a factor 360 for a resolution of 1°. This can be avoided by using the geometric raytracing method to calculate the radiance field caused by the refraction and reflection of sunlight by ice crystals.

The raytracing method was first developed by Wendling et al. (1979) for hexagonal ice crystal columns and plates. Several authors advanced the method by using more complex particles and including absorption and polarization: Pattloch and Tränkle (1984), Muinonen et al. (1989), Takano and Liou (1990) and later Macke (1994), Takano and Liou (1995), Hess (1996), Macke et al. (1996), Yang and Liou (1998), and Prigarin (2009). This work focuses on the visible spectral range (400 nm to 700 nm), where the wavelength is much smaller than the crystal size resulting in size parameters of the order of 100. For large size parameters the geometric optics approach can be used as an asymptotic approximation of fundamental electromagnetic theory (Liou and Yang, 2016). As another advantage geometric raytracing can be simulated using the Monte Carlo method and can thus be easily implemented in the existing MYSTIC code of *libRadtran*. The raytracing method developed in this work and its implementation in MYSTIC will be explained in the following.

For large size parameters the incident light can be considered as a bundle of parallel rays that undergo reflection and refraction outside and inside the ice crystal with propagation directions determined by Snell's law (cf. Eq. (2.47)) at the surface. Starting with the direction of the incident ray $\mathbf{x_0}$, the crystal's orientation is calculated by randomly choosing three Euler angles α_{Euler} (angle of crystal c-axis), β_{Euler} and γ_{Euler}. The Euler rotations around these three angles are illustrated in Fig. 3.45. Three different configurations are usually distinguished for the choice of the Euler angles:

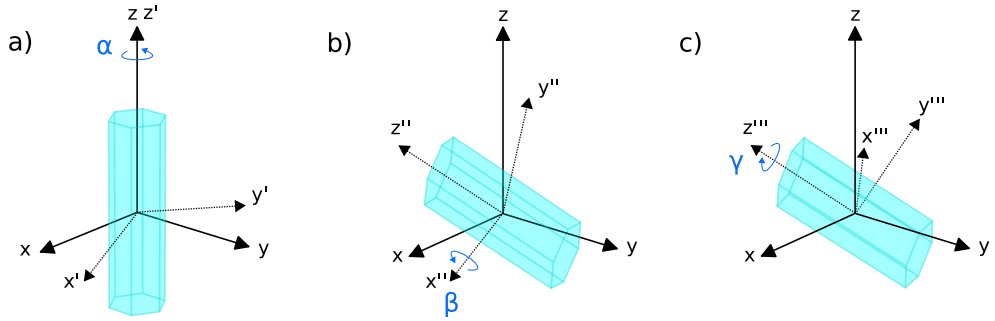

Figure 3.45: *Ice crystal geometry and definition of Euler angles as used for CrystalTrace. The reference coordinate system is represented by the x, y, and z-axes. (a) Original geometry of the ice crystal rotated by the Euler angle α_{Euler} around its z-axis. The axes of the updated coordinate system are denoted by x', y', and z'. The second rotation by β_{Euler} around the x'-axis results in the crystal orientation shown in (b) with the updated coordinate system denoted by x'', y'', and z''. (c) Third rotation around the z''-axis by γ_{Euler}.*

1. Randomly oriented ice crystals: for randomly oriented crystals the new orientation is determined by drawing a random number ϱ between $[0, 1)$

$$\alpha_{\text{Euler}} = 2\pi\,\varrho\,, \tag{3.56}$$
$$\beta_{\text{Euler}} = \arccos(1 - 2\varrho)\,, \tag{3.57}$$
$$\gamma_{\text{Euler}} = 2\pi\,\varrho\,. \tag{3.58}$$

   Randomly oriented crystals cause the 22° and 46° halo.

2. Singly oriented ice crystals: for the parameterization of ice crystal orientation along their c-axis, a Gaussian distribution is used with mean value $\mu_{\beta,\text{Euler}}$ and standard deviation $\sigma_{\beta,\text{Euler}}$

$$\beta_{\text{Euler}} = \frac{1}{\sqrt{2\,\sigma^2_{\beta,\text{Euler}}\,\pi}} \exp\left(-\frac{(\varrho - \mu_{\beta,\text{Euler}})^2}{2\,\sigma^2_{\beta,\text{Euler}}}\right)\,. \tag{3.59}$$

   The standard deviation of the Gaussian orientation distribution will be referred to as *orientation parameter* in the following. Ice crystal plates orient with their c-axis vertically which implies $\mu_{\beta,\text{Euler}} = 0°$. Ice crystal columns instead have aerodynamically stable orientations with their c-axis horizontal and thus $\mu_{\beta,\text{Euler}} = 90°$. This configuration is referred to as singly oriented since only one crystal axis is oriented and the other two Euler angles α_{Euler} and γ_{Euler} are chosen randomly as in (1). Singly oriented ice crystals cause the upper and lower tangent arcs in case of columns and sundogs in case of plates.

3. Parry oriented ice crystals: in rare cases horizontally oriented ice crystal columns can also be oriented in their rotation around z''' (cf. Fig. 3.45c). This means that both β_{Euler} and γ_{Euler} are parameterized by a Gaussian distribution in analogy to Eq. (3.59). Only α_{Euler} is sampled from a uniform distribution between 0 and 2π. These oriented ice crystal columns form the rare Parry arc which is visible above the upper tangent arc in Fig. 2.10.

Using the rotated ice crystal coordinates, an intersection between the direction of the incident ray $\mathbf{x_0}$ and the plane of a crystal face is determined at a randomly chosen point. This procedure is illustrated in Fig. 3.46: a circle is defined in the plane perpendicular to $\mathbf{x_0}$ and centered around the geometric center of the ice crystal $\mathbf{s}$. The radius is determined by the maximum diameter D of the ice crystal. Within this circle a point is chosen by drawing random numbers for the zenith

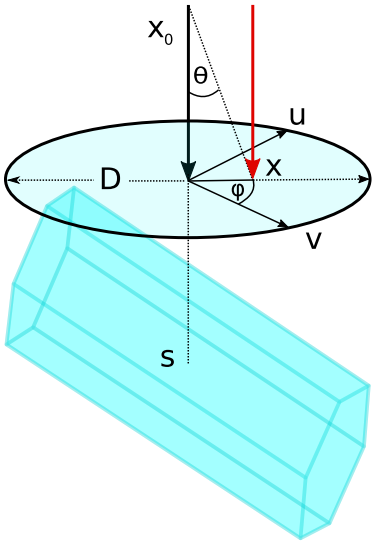

Figure 3.46: *Method to determine the initial point* $\mathbf{x}$ *of the incident ray* $\mathbf{x_0}$*. The red arrow denotes the incident direction of the ray with starting point* $\mathbf{x}$*. The intersection point with the ice crystal* $\mathbf{x}$ *is determined by drawing random angles* θ *and* ϕ *in a circle centered around the barycenter* s *with diameter* D*, the maximum dimension of the ice crystal. The vectors* $\mathbf{u}$ *and* $\mathbf{v}$ *are auxiliary vectors which are perpendicular to* $\mathbf{x}$ *and to each other.*

(θ) and azimuth angle (ϕ). The resulting vector of the incident ray is denoted by a red arrow in Fig. 3.46 and is calculated by

$$\mathbf{x} = \mathbf{s} - \mathbf{x_0} \cdot D/2 + (\cos\phi\,\mathbf{u} + \sin\phi\,\mathbf{v})\,\sqrt{\theta} \cdot D/2\,. \tag{3.60}$$

Random points are repeatedly selected until an intersection is found between the plane of an ice crystal face and the vector of the incident ray $\mathbf{x}$. Once an intersection is found, the photon ray is traced through the ice crystal by refraction and reflection using the Monte Carlo method. The direction of the reflected and transmitted rays can be calculated using Snell's law (Eq. (2.51)) and their intensity with the Fresnel reflection coefficient $\mathcal{R} = (r_\parallel^2 + r_\perp^2)/2$ using Eqs. (2.48) and (2.49). The photon is reflected if the chosen random number is $\varrho < \mathcal{R}$, otherwise it is transmitted. Total reflection occurs if the angle of refraction is $\theta_\mathrm{t} > \arcsin(1/n_\mathrm{Re})$. This procedure is repeated until the photon escapes from the crystal.

This raytracing method allows performing radiative transfer simulations without explicit knowledge of the scattering phase function. Furthermore, the raytracing technique is computationally fast compared to other methods like T-matrix or Discrete-Dipole Approximation (Draine and Flatau, 1994, Flatau and Draine, 2014) which is an important advantage for the use of radiative transfer simulations. However, the raytracing method is based on the laws of geometric optics which can be applied to particle sizes much larger than the wavelength, i.e. $\chi \gg 1$. As stated by Liou and Yang (2016), this allows for the assumption that rays can be localized. Furthermore, it has to be assumed that the energy attenuated by the scatterer may be decomposed into equal extinction from diffraction and from Fresnel rays. The raytracing method developed for this study is called CrystalTrace and allows radiative transfer simulations of mixtures of different ice crystal shapes with selected degrees of orientation. The current implementation does not account for the polarization state of the photon, diffraction, ice absorption and ice crystal roughness which could be incorporated in the future. To study ice crystal orientation and its effect on the brightness of halo displays in the visible spectral range, this is considered a suitable tool for basic sensitivity studies. CrystalTrace was validated by comparing the scattering phase functions for ice crystals

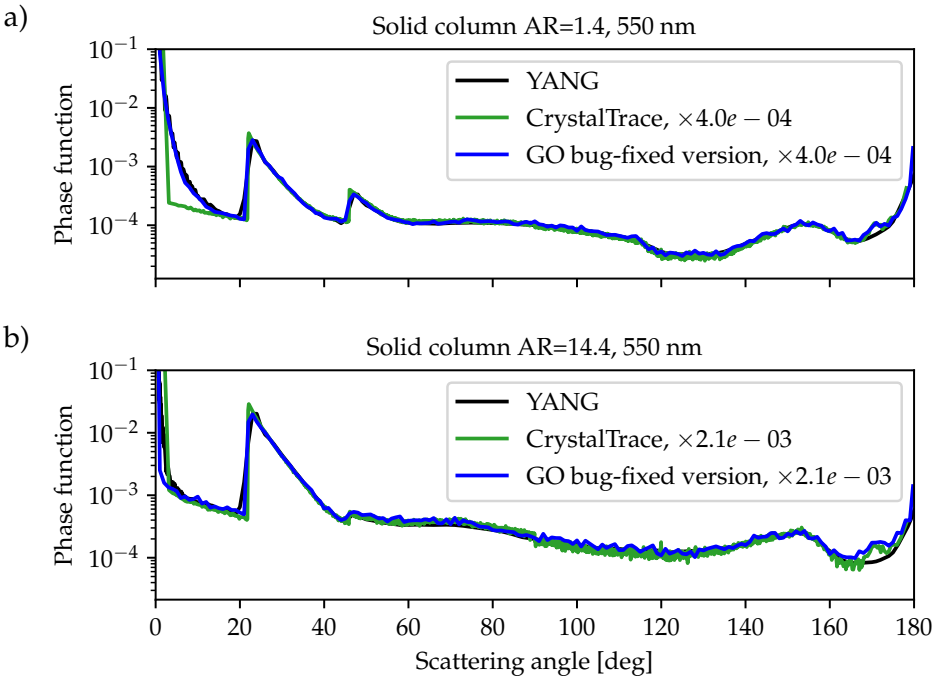

Figure 3.47: *Comparison of the scattering phase functions calculated with YANG (black), CrystalTrace (green) and the bug-fixed version of GO (blue) at wavelength of* 550 nm. *(a) Scattering phase functions for a solid ice crystal column with* AR = 1.4 *and maximum dimension* $D = 65\,\mu\text{m}$ *and (b) for* AR = 14.4 *with* $D = 1 \times 10^4\,\mu\text{m}$. *Both the GO and CrystalTrace phase functions were scaled to allow for a comparison of the results for scattering angles excluding the forward scattering peak. The results compare well apart from the forward scattering region for the smaller ice crystal (a) due to diffraction which is not accounted for by CrystalTrace.*

with different aspect ratios with the GO raytracing code (cf. Section 3.2.2). Figure 3.47 compares the phase functions calculated with CrystalTrace (green) and the GO raytracing code (blue) for ice crystals columns with aspect ratio 1.4 (a) and long solid columns with aspect ratio 14.4 (b) at a wavelength of 550 nm. The corresponding phase function of the YANG database (black) is shown as a reference. The results compare well apart from the forward scattering region where CrystalTrace shows smaller values than GO and YANG. This is due to diffraction which is not accounted for by CrystalTrace. Due the coarser scattering angle resolution in the case of the GO phase functions the peaks of the 22° and 46° halos are not as pronounced as for CrystalTrace.

To perform simulations of realistic ice clouds with multiple scattering in combination with molecules and aerosol particles, CrystalTrace is implemented in *libRadtran*'s MYSTIC solver. MYSTIC solves the radiative transfer equation by using the Monte Carlo method to trace single photons through the atmosphere as described in Section 3.1.1. This is a perfectly suited framework for implementing CrystalTrace. When a scattering process takes place at an ice crystal, the photon is traced through the ice crystal and the new direction is directly calculated by CrystalTrace instead of using the stored scattering phase functions. Furthermore, no delta-scaling is needed since photons refracted by two parallel crystal faces escape the crystal and are traced further through the atmosphere, i.e. are treated as unscattered. To account for the varying projected ice crystal area for different orientations in the CrystalTrace extension implemented in MYSTIC, the photons can be assigned with a weight. The simulations shown in this work were performed with a version of MYSTIC and CrystalTrace, which does not yet account for this effect. However, the simulations with MYSTIC and CrystalTrace are only used for qualitative analyses throughout this work. Furthermore, the ice crystal aspect ratios used here are 2.5 for solid columns and

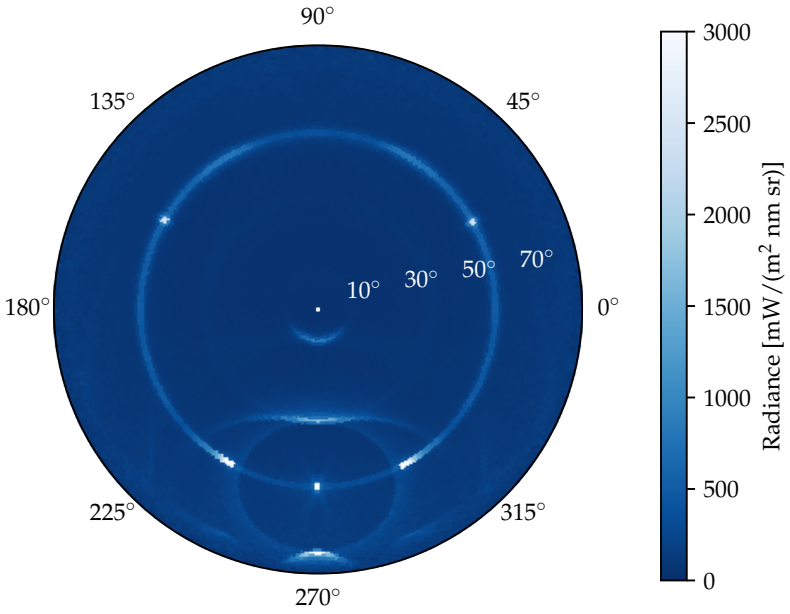

Figure 3.48: *Raytracing simulation with MYSTIC and CrystalTrace showing the radiance distribution in a polar projection for the upper hemisphere using* 1×10^7 *photons. The zenith angle* θ *ranges from* $0°$ *to* $90°$ *at the horizon, whereas the azimuth angle* ϕ *ranges from* $0°$ *to* $360°$*. The sun is located at an SZA of* $60°$ *and an azimuth angle of* $\phi_0 = 270°$*. The simulation was performed for a wavelength of* 550 nm *and an ice cloud of optical thickness of 0.8. The cirrus cloud contains 40% oriented ice crystal columns (c-axis horizontal), 40% oriented ice crystal plates (c-axis vertical), and 20% randomly oriented ice crystal columns. For both oriented crystal populations an orientation parameter of* $\sigma_{\beta,\mathrm{Euler}} = 1°$ *was chosen.*

0.5 for plates, which is compact enough for this effect to be insignificant. Figure 3.48 shows the radiance distribution simulated with MYSTIC and CrystalTrace for a cirrus with optical thickness 0.8 in an aerosol-free atmosphere with non-reflective surface. A solar zenith angle of 60° and an azimuth angle of 270° were chosen. The cirrus cloud contains 40% oriented ice crystal columns (c-axis horizontal), 40% oriented ice crystal plates (c-axis vertical), and 20% randomly oriented ice crystal columns. For both oriented crystal populations an orientation parameter of $\sigma_{\beta,\mathrm{Euler}} = 1°$ was chosen. The oriented plates are responsible for the sundogs (22° parhelia) visible on each side of the sun, the 120° parhelia, and the circumzenithal arc, which is visible at $\theta \approx 10°$. All parhelia are located on the parhelic circle which forms at the zenith angle of the sun $\theta = \theta_0$ and is produced by reflection at vertical crystal faces of both oriented plates and columns. The oriented hexagonal columns produce the upper and lower tangent arcs visible above and below the sun in Fig. 3.48 and the 22° halo forms due to the presence of randomly oriented hexagons. This simulation was performed using 1×10^7 photons. For the implementation of CrystalTrace MYSTIC has to be used in the "forward mode" (cf. Section 3.1.1 and Fig. 3.2a), which has a similar computational time as the backward mode if both hemispheres are simulated. The runtime for 1×10^5 photons amounts to about 12 s for a setup as in Fig. 3.48 using an Intel Xeon E5-2650 processor with 2 GHz clock frequency.

Chapter 4

Results

Section 4.1 was partly published in Forster et al. (2017):
Forster, L., M. Seefeldner, M. Wiegner, and B. Mayer, 2017: Ice crystal characterization in cirrus clouds: a sun-tracking camera system and automated detection algorithm for halo displays. *Atmospheric Measurement Techniques*, **10 (7)**, 2499–2516, 10.5194/amt-10-2499-2017.

4.1 Halo display statistics

HaloCam has been operated at MIM in Munich (Germany) since Sept 2013 where it provides continuous measurements including contributions to the ML-CIRRUS campaign in March and April 2014 (Voigt et al., 2017). Only during the ACCEPT campaign (Analysis of the Composition of Clouds with Extended Polarization Techniques, Myagkov et al. (2016)) in October and November 2014 it was installed in Cabauw (The Netherlands). In the following sections the HaloCam datasets collected during the ACCEPT campaign and in Munich will be evaluated regarding the frequency of halo displays and halo-producing cirrus clouds.

4.1.1 Halo display statistics during ACCEPT

A first visual evaluation of the halo display frequency during the ACCEPT campaign (10 October until 14 November 2014) was performed. The results are displayed in Fig. 4.1 as Venn diagram (Venn, 1880). The occurrence of each different halo type is visualized by a circle. The radius of each circle scales with the total observation time for the respective halo type. Cross sections between the circles indicate instances where two or three halo displays were visible at the same time. The observation time is given in hours. The total time of HaloCam observations, which were collected during daytime only, amounts to about 344 h. With about 30 h, halo displays were observed in almost 9% of the time. The presence of cirrus clouds within the HaloCam field of view was evaluated visually and amounts to about 110 h. Thus, about 27% of the cirrus clouds produced a visible halo display. The 22° halo (complete or partial) occurred in 16.2%, the sundogs in 19% and the upper tangent arcs in 7.8% of the time when cirrus clouds were present. Circumscribed halos were not observed during the campaign due to the low solar elevations. As illustrated in Fig. 4.1, sundogs were observed more often than 22° halos with about 21 h vs. 18 h. Thus, sundogs occurred in 70% and 22° halos in 60% of the total halo observation time (30 h). Upper tangent arcs occurred in total for about 9 h (30%) and were most of the time accompanied by 22° halos and sundogs. Thus, the majority of the halo displays were produced by oriented ice crystals (cf. Section 2.3).

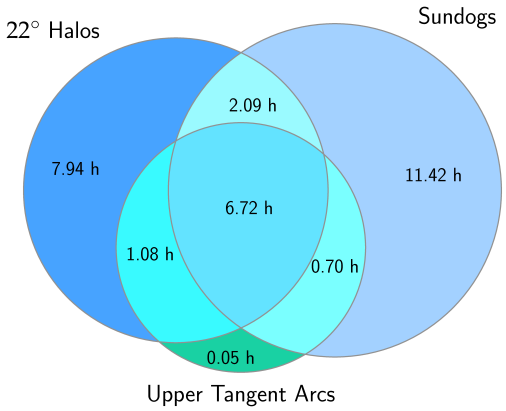

Figure 4.1: *Halo display statistics from HaloCam observations during the ACCEPT campaign 10 October until 14 November 2014. The observation times of 22° halo, sundogs and upper tangent arc are provided in hours and are represented by the radii of the three circles. Cross sections of circles indicate time periods when two or three halo displays were visible simultaneously. The total observation time amounts to* 344 h.

Compared to the findings of Sassen et al. (2003b) the relative fraction of 22° halos is roughly similar with 50%, but sundogs with 12%, and upper/lower tangent arcs with about 15% were far less frequent than observed during ACCEPT with 60%, 70%, and 30%, respectively. AKM observed 22° halos 36% of the time, upper and lower tangent arcs 11% and left and right sundogs with a relative frequency of 18% each. Although the frequency of simultaneous occurrence of the left and right sundog is unknown (from the AKM database), one can deduce that the relative frequency of both sundogs ranges between 18% and 36%, which is larger than the 12% of Sassen et al. (2003b). Overall, Sassen et al. (2003b) and AKM found a much higher frequency for 22° halos compared to sundogs and tangent arcs, which is in contrast to the HaloCam observations during the ACCEPT campaign. An overview of the complete halo display statistics evaluated from HaloCam observations is provided in Table 4.2 (Section 4.1.2). The reasons for the differences in the observed halo frequencies could be manifold: one main reason might be that a statistical evaluation over six weeks is compared to a database of 10 (Sassen et al., 2003b) and 30 years (AKM). It is possible that the observation time during ACCEPT was not long enough to yield representative results for the frequency of the different halo displays. Another factor could be the observation site. The mountains in the east of Salt Lake City, the observation site of Sassen et al. (2003b), could obscure the sun during periods with low solar elevation which are favorable for the formation of sundogs. It is possible that on average fewer sundogs could have been observed in Salt Lake City than in Cabauw which is surrounded by a rather flat landscape. Also differences in the dominating weather patterns forming cirrus clouds in Salt Lake City and Cabauw could have an impact on halo formation as discussed in Sassen et al. (2003b). For the AKM and the HaloCam dataset, information about dominating weather patterns for different halo displays is not available. Furthermore, the observation period during the ACCEPT campaign from October until mid-November was dominated by low solar elevations which implies a higher chance for observing sundogs. Long-term observations have to be evaluated to obtain representative results for the frequency of the individual halo types.

4.1.2 Long-term halo statistics in Munich

In Munich HaloCam has collected data over more than 2 years between January 2014 and June 2016. This long-term dataset was evaluated automatically with the halo detection algorithm HaloForest (cf. Section 3.6.2). HaloForest is based on a random forest classifier and a separate classifier is trained for each of the 6 image segments shown in Fig. 3.23b. To ensure a high classification accuracy, only the classifiers for the upper image segments (3, 4, and 5) were used (cf. Table 3.4). A HaloCam image is assigned to the class "22° halo" if at least one of the image segments 3, 4, or 5 predicts a 22° halo. Applying a probability threshold of $p > 0.5$, 22° halos were detected in 152 h of the 7345 h total observation time during daylight. Hence, 22° halos occurred in about 2.1% of the time.

As an additional test, the classification accuracy of HaloForest was checked for 470 randomly chosen HaloCam images for the "22° halo" and "no 22° halo" class within this long-term observation period in Munich. The confusion matrix for this test is provided in Table 4.1 for the image segments no. 3, 4, and 5 together. More than 88% of the 22° halos are classified correctly

Table 4.1: *Confusion matrix similar to Table 3.4 for 470 randomly selected HaloCam images between January 2014 and June 2016, evaluated for segments 3, 4, and 5.*

		Predicted	
		22° halo	no 22° halo
True	22° halo	**88.8 %**	2.8 %
	no 22° halo	11.2 %	**97.2 %**

and less than 12% are classified incorrectly as 22° halos. Images were incorrectly classified as 22° halo predominantly due to small bright clouds or contrails in a blue sky or structures in overcast conditions which happen to cause a peak in the averaged brightness distribution at a scattering angle of 22°.

In addition, the fraction of cirrus clouds which produced a 22° halo during this time period was investigated. The total frequency of occurrence of cirrus clouds was determined by independent data of co-located CHM15kx ceilometer observations (Wiegner and Geiß, 2012). To guarantee consistent observational conditions, only ceilometer measurements in the absence of low-level clouds were considered. Proprietary software of the ceilometer automatically provides up to three cloud base heights with a temporal resolution of 15 s. The detection is based on the fact that the backscatter signals of clouds are significantly larger than the background noise. The sensitivity of the ceilometer is sufficient to even detect clouds near the tropopause during daytime. Since ceilometers, however, do not provide depolarization information, the discrimination between water and ice clouds was made by means of the cloud base temperature T_{base}. Sassen and Campbell (2001) state that cirrus cloud base temperatures ranged between −30 °C and −40 °C during the 10-year observation period at the FARS observation site. As a temperature threshold is not an unambiguous criterion for the existence of ice clouds, the frequency of occurrence for three different temperatures was calculated: −20 °C, −30 °C, and −40 °C. If T_{base} is lower than the given temperature threshold, the cloud is considered a "cirrus cloud". The temperature profiles were obtained from routine radiosonde ascents of the German Weather Service at Oberschleißheim (WMO station code 10868)[1], which is located about 13 km north of the HaloCam site. During the time period from January 2014 until June 2016 a fraction of 5.6% cirrus clouds was detected for

[1]The radiosonde data were downloaded from http://weather.uwyo.edu/upperair/sounding.html of the University of Wyoming, College of Engineering, Department of Atmospheric Science.

a cloud base temperature of $T_{base} < -20\,°C$. Towards lower cloud base temperatures the amount of detected cirrus clouds decreases to 3.5% for $T_{base} < -30\,°C$ and 1.9% for $T_{base} < -40\,°C$.

Due to the different pointing directions of the ceilometer (towards zenith) and HaloCam (towards sun), the instruments observe different regions of the sky. This is accounted for by prescreening the data for 1 h time intervals when the ceilometer detected a cirrus cloud. The prescreening is subject to data availability for both instruments. The subsequent analysis of cirrus fraction and halo frequency of occurrence is based on the full temporal resolution of 15 s and 10 s, respectively. Relative to the amount of detected cirrus clouds about 25% occurred together with a 22° halo for the image segments 3, 4, and 5. This fraction does not change much for the different cloud base temperatures (26.4% for $T_{base} < -20\,°C$ and 24.5% for $T_{base} < -40\,°C$) since the fraction of detected clouds decreases together with the detected halos for lower temperatures. According to the confusion matrix in Table 4.1, 88.8% of the detected "22° halos" are real halos, while 2.8% of the "no 22° halos" are actually "22° halos". Correcting the result for the estimated false classifications, the fraction of halo-producing cirrus clouds amounts to about $25\% \cdot 88.8\% + 75\% \cdot 2.8\% \approx 24\%$. The comparison of ceilometer and HaloCam data implies that about 25% of the cirrus clouds contain some fraction of smooth, hexagonal ice crystals. Sassen et al. (2003b) observed a fraction of 37.3% cirrus clouds which produced a 22° halo within 1 h time intervals. The results most likely differ because the observations originate from different locations which might be dominated by different mechanisms for cirrus formation and a different topography. It has to be noted however, that the evaluation method is very sensitive to the sampling strategy of the observations: the fraction of halo-producing cirrus clouds increases to more than 50%, if the HaloCam observations are binned to 1 h intervals, which are counted as containing a halo regardless of their duration. This might also be a reason for the larger fraction of halo-producing cirrus clouds observed by Sassen et al. (2003b). For comparison, the fraction of cirrus clouds producing a halo display was evaluated visually for the HaloCam observations during the ACCEPT campaign with a temporal resolution of 10 s and amounts to about 27% including 22° halos, sundogs and upper/lower tangent arcs (cf. Section 4.1.1). This value is also lower than the result provided by Sassen et al. (2003b) who observed any of the three halo types in about 54% of the 1 h periods with cirrus. An overview of the frequency of halo displays (cf. Section 4.1.1) and halo-producing cirrus clouds evaluated with HaloCam observations is provided in Table 4.2.

The current version of HaloForest discriminates only between the two classes "22° halo" and "no 22° halo". Thus, interference with other halo types as sundogs or upper/lower tangent arcs and circumscribed halos might occur at certain solar elevations. The position of sundogs relative to the sun depends on the solar zenith angle (SZA) and can be calculated analytically as described in Wegener (1925), Tricker (1970), Minnaert (1993) and Liou and Yang (2016). The sundogs are located at scattering angles close to the 22° halo for large SZAs and occur at larger scattering angles for small SZAs, i.e. high solar elevations (cf. Fig. 2.16). Figure 4.2 shows the same HaloCam image with the azimuth segments as Fig. 3.23b. The minimum scattering angle of the sundogs are calculated as a function of the SZA and represented by the red and green squares. The SZAs range between 90° and 35° with a resolution of 1°. The two white circles centered around the sun at scattering angles of 21.0° and 23.5° indicate the mask which is used to find the scattering angle of the 22° halo peak. For SZA $\leq 67°$ the sundog positions are located outside this mask and cannot be misclassified as 22° halo (green squares). The red squares represent sundog positions which are located within this mask and might therefore be misclassified. This is the case for SZAs between 90° and 67°. To obtain an estimate of the fraction of sundogs which are misclassified as 22° halo, 1000 randomly selected HaloCam images were counter-checked visually. This revealed that only 6 images showing sundogs without 22° halo in the segments (3–5) were

Table 4.2: *Summarized results of the frequency of halo displays derived from HaloCam observations from Sections 4.1.1 and 4.1.2.*

Dataset	HaloCam MIM	HaloCam ACCEPT	Sassen et al. (2003b) FARS	AKM
Location	Munich	The Netherlands	Salt Lake City, U. S.	Europe
Observation	2014 – 2016	Oct – Nov 2014	1986 – 1996	since 1986
period	2.5 years	6 weeks	∼10 years	∼30 years
Relative frequency of halo displays (cf. Section 4.1.1)				
22° halo	–	60%	50%	36%
Sundogs	–	70%	12%	18%
Upper/lower tangent arcs	–	30%	15%	11%
Frequency of halo-producing cirrus clouds				
22° halo	24%	16%	37%	–
Sundogs	–	19%	9%	–
Upper/lower tangent arcs	–	8%	9%	–
Total	24%	27%	54%	–

misclassified as 22° halo, which is $< 1\%$. Upper tangent arcs could be detected by the uppermost image segment (no. 4) and might therefore be misclassified as 22° halo. For very small SZAs (high solar elevations) the tangent arcs merge to form the circumscribed halo which could be detected in the segments 3 and 5 as well. The same procedure was repeated for these halo types: 1000 randomly selected images were checked for the presence of tangent arcs and circumscribed halos without 22° halo yielding 28 images or 2.8%. However, if only a fragment of a halo is visible in the uppermost segment, it is generally difficult to discriminate between an upper tangent arc and circumscribed halo and a 22° halo.

The halo classification algorithm was presented for 22° halos, but it is possible to include training data for other halo types as well. With the current version of HaloForest and the co-located ceilometer observations the fraction of cirrus clouds producing a halo display was estimated to about 25% for Munich between January 2014 and September 2016. Extending HaloForest for the detection of other halo types, such as sundogs, may easily result in a larger fraction. It can be argued that these halo-producing cirrus clouds contain a certain amount of smooth, hexagonal ice crystals. By analyzing ice crystal single scattering properties, van Diedenhoven (2014) showed that a minimum fraction of 10% smooth hexagonal ice crystal columns is sufficient to produce a 22° halo. For a 22° halo produced by ice crystal plates the minimum fraction of smooth crystals amounts to 40%. Thus, if the exact ice crystal habits of the cirrus cloud are unknown, the minimum amount of smooth ice crystals probably ranges between 10% and 40%. This implies that even for a large fraction of irregular or small ice crystals a 22° halo might still be visible. A larger fraction of smooth ice crystals, however, could well be possible for 22° halos with larger halo ratio, i.e. increased brightness contrast. Multiple scattering of the cirrus cloud or atmosphere was not considered by van Diedenhoven (2014). If accounted for, the minimum fraction of smooth crystals in halo-producing cirrus clouds could be much larger (cf. Section 3.3.2). A more detailed analysis of the actual fraction of smooth ice crystals in

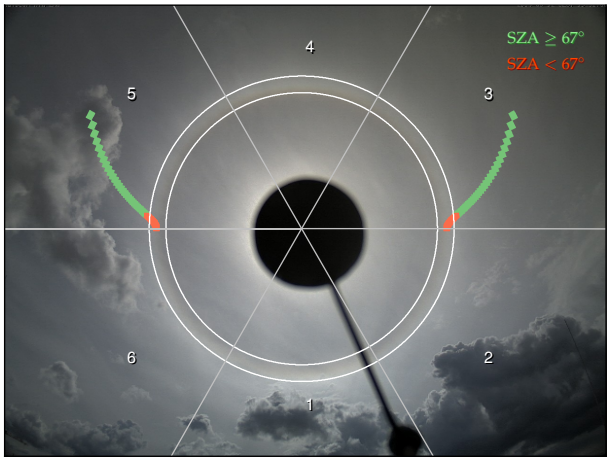

Figure 4.2: *HaloCam image as in Fig. 3.23b. The red and green squares indicate the minimum scattering angle of the sundogs as a function of the solar zenith angle (SZA). The SZA ranges between 90° and 35° with 1° resolution. The mask used to search for the 22° halo peak is displayed by the two white circles and covers scattering angles between 21.0° and 23.5°. Sundog positions located within this mask might be misclassified as 22° halo and are marked as red. These positions correspond with SZAs between 90° and 67°. For smaller SZAs (higher solar elevations) the sundogs are located outside the mask and cannot be misclassified as 22° halo by the algorithm.*

halo-producing cirrus clouds will be presented in the following sections. For this analysis the halo observations are complemented by radiative transfer simulations and additional measurements of aerosol and cirrus optical thickness and surface albedo.

4.2 Retrieval of ice crystal properties

To retrieve more detailed information about ice crystal properties in halo-producing cirrus clouds, the RICO retrieval (cf. Section 3.7) was applied to calibrated radiance observations from specMACS and HaloCam$_{\mathrm{RAW}}$. Both the relative and absolute radiometric calibration of specMACS were performed in the laboratory and the absolute radiometric uncertainty was estimated to about 5% (Ewald et al., 2015). The absolute radiometric calibration of HaloCam$_{\mathrm{RAW}}$ however had to be performed using specMACS as a reference which results in a much higher uncertainty of about 15%. Thus, to investigate the potential and the limitations of the RICO retrieval, it was first applied to two case studies with specMACS measurements on 24 March and 22 September 2015 at the Meteorological Institute, Munich. Additional observations are available measured operationally by a MIRA-35 cloud radar (Görsdorf et al., 2015), a CHM15kx ceilometer (Wiegner et al., 2014) and a sun photometer, which is part of the AERONET (Aerosol Robotic Network) network (Holben et al., 1998), as well as with the institute's own sun photometer SSARA (Sun–Sky Automatic Radiometer, Toledano et al. (2009, 2011)).

4.2.1 Case study of 24 March 2015

On 24 March 2015 cirrus clouds formed in an airmass between a ridge and a trough at the 500 hPa pressure level. Cirrus clouds were present between 11:00 UTC until 15:30 UTC with clearsky conditions in the morning and afternoon. Figure 4.3 shows an overview of the co-located ceilometer and cloud radar (top), HaloCam (center) and sun photometer (bottom) observations. When comparing the data it should be kept in mind that both the radar and the ceilometer are pointing to the zenith, whereas HaloCam and the sun photometer are following the sun. Thus, the observed regions of the sky are not the same, unless the sun is at the zenith. The presence of a

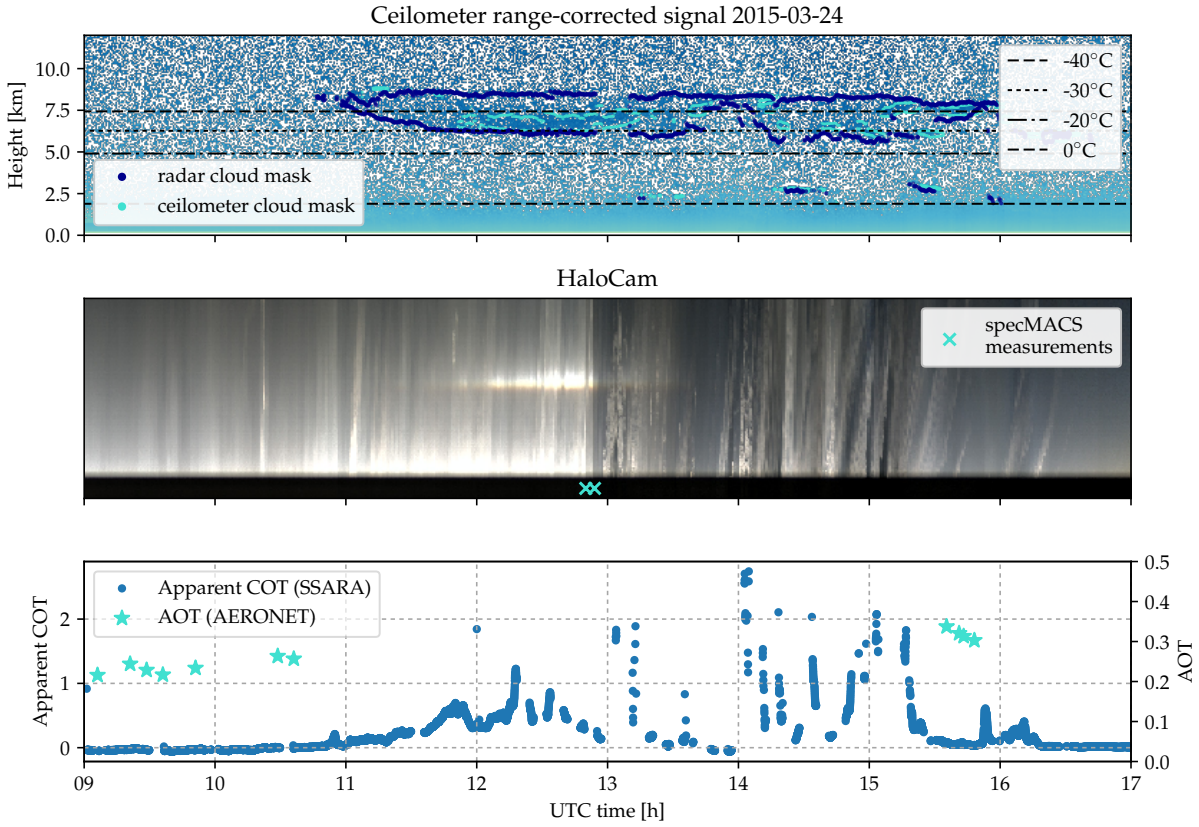

Figure 4.3: *Overview of observations on 24 March 2015. Top: cloud base and top height from ceilometer range-corrected signal (turquoise dots) and cloud radar reflectivity (dark blue dots). The gap in the radar reflectivity at around 13 UTC is due to a scan. Temperature contour lines at* 0 °C *(dashed),* −20 °C *(dash-dotted),* −30 °C *(dotted), and* −40 °C *(dashed) are interpolated from radiosonde data. Center: time line of HaloCam*$_{\mathrm{JPG}}$ *pixel slices above the sun extending from the center of the black circular sun shade to the top of the image. The upper part of the 22° halo or upper tangent arc is visible as a bright line in the center of the panel. The times of the specMACS measurements are indicated by the turquoise crosses around noontime. Bottom: AERONET AOT (turquoise stars) and apparent COT derived from SSARA direct-sun measurements (blue) interpolated to a wavelength of* 550 nm.

complete 22° halo requires relatively homogeneous cloud cover which allows a comparison between the data with a time shift. In a westerly flow, which is typical for the observation site in Munich, the sun-tracking instruments detect the clouds in their field of view later (earlier) than the zenith-pointing instruments in the morning (evening). Cloud radar and ceilometer measurements are used to estimate cloud top and base height.

Figure 4.3 (top) shows the range-corrected ceilometer signal and the detected cloud base and top height as turquoise dots. The ceilometer detected the cloud base height at 6.5 km and cloud top height at 7.5 km between 12 – 13 UTC. The cloud base and top height, which is derived from the equivalent radar reflectivity factor (Ze) of hydrometeors at the boundaries of the cloud, is represented by the dark blue dots. The gap in the radar reflectivity at around 13 UTC is due to a scan, which was excluded from the analysis. The cloud base height estimated from the radar observations is similar to the cloud height derived from the ceilometer measurements. Large differences, however, are visible for the estimated cloud top height, which is significantly larger for the radar data with about 9 km. This effect is due to attenuation of the ceilometer signal which is more sensitive to the particle number concentration. The radar signal is able to reach

Table 4.3: *Cloud and aerosol properties during the specMACS scans on 24 March 2015.*

specMACS scan time	cloud top (base) height	cloud top (base) temperature	AOT daily average	apparent COT
12:50 UTC 12:54 UTC	9 km (6 km)	−54 °C (−28 °C)	0.27 ± 0.06	0.13 to 1.37

the cloud top and is more sensitive to the size of the particles. To obtain the best estimate of the cloud base and top height, the observations of both instruments are combined using the largest height for cloud top and the smallest height for cloud base.

This work focuses on cirrus clouds, which have a cloud base height at temperatures below the freezing point (Section 2.1.1). Thus, only height levels with temperatures of 0 °C and below are indicated in Fig. 4.3 (top). The temperature profile is obtained from radiosonde ascents at Oberschleißheim. In addition, the temperature levels at −20 °C, −30 °C and −40 °C are indicated by dash-dot, dotted, and dashed lines, respectively. At cloud base (6 km) the temperature ranged between −24 °C and −28 °C, whereas at cloud top (9 km) the temperature amounts to about −54 °C.

To obtain a temporal overview, the HaloCam data (Fig. 4.3 center) is visualized by a time series of pixel lines, which are extracted from each image (every 10 s) in the principal plane above the sun, i.e. extending from the center of the circular sun shade to the image top. The image slices are stitched together along the time axis showing the upper part of a 22° halo, upper tangent arc or circumscribed halo as a line approximately in the center of the panel. The trace of the halo features appears slightly reddish at the lower (inner) edge. The abrupt change in the HaloCam image brightness shortly before 13 UTC was due to a restart of the camera system which was necessary due to an earlier power outage. The power outage caused a reset in the automatic exposure settings of the camera which is the reason for the overexposed pixels in the halo region between 12 – 13 UTC. The HaloCam observations show a 22° halo together with an upper and lower tangent arc from 11 UTC until around 14 UTC with faint sundogs between 13 and 14 UTC. Note that sundogs and lower tangent arcs are not visible in the representation of the HaloCam data in Fig. 4.3 center. The 22° halo and the bright upper and lower tangent arcs indicate the presence of smooth hexagonal columns which were partly oriented. The sundogs are produced by smooth ice crystal plates which are oriented with their c-axis horizontal. Low-level water clouds started to form at around 13 UTC which obstructed the visibility of the halos at times.

The sun photometer observations are displayed in bottom panel of Fig. 4.3. The turquoise stars represent the aerosol optical thickness (AOT) from AERONET version 2, level 2.0 (cloud screened) interpolated to 550 nm. Clearsky conditions until 10:30 UTC and in the afternoon starting from about 15:30 UTC allowed to estimate the AOT with a daily mean of 0.27 ± 0.06 within a 2σ confidence interval. The apparent cirrus optical thickness (COT) is derived from SSARA sun photometer measurements as explained in Section 3.7.3. While AERONET performs measurements every 15 min, the SSARA measurements are available every 2 s. During the time when the halo displays were observed the apparent COT ranged between 0.1 and 0.4. A time interval of ±10 min was chosen to estimate the apparent COT during the specMACS measurements, taking into account the different pointing directions of the direct sun and the 22° halo measurements. Table 4.3 shows the estimated values for cloud top and base height, apparent COT and average AOT which are used to define the parameter range at the time of the specMACS measurements.

Figure 4.4 shows specMACS measurements at 12:50 and 12:54 UTC at a wavelength of 550 nm and the retrieved ice crystal properties using the YANG optical properties. The left panel displays

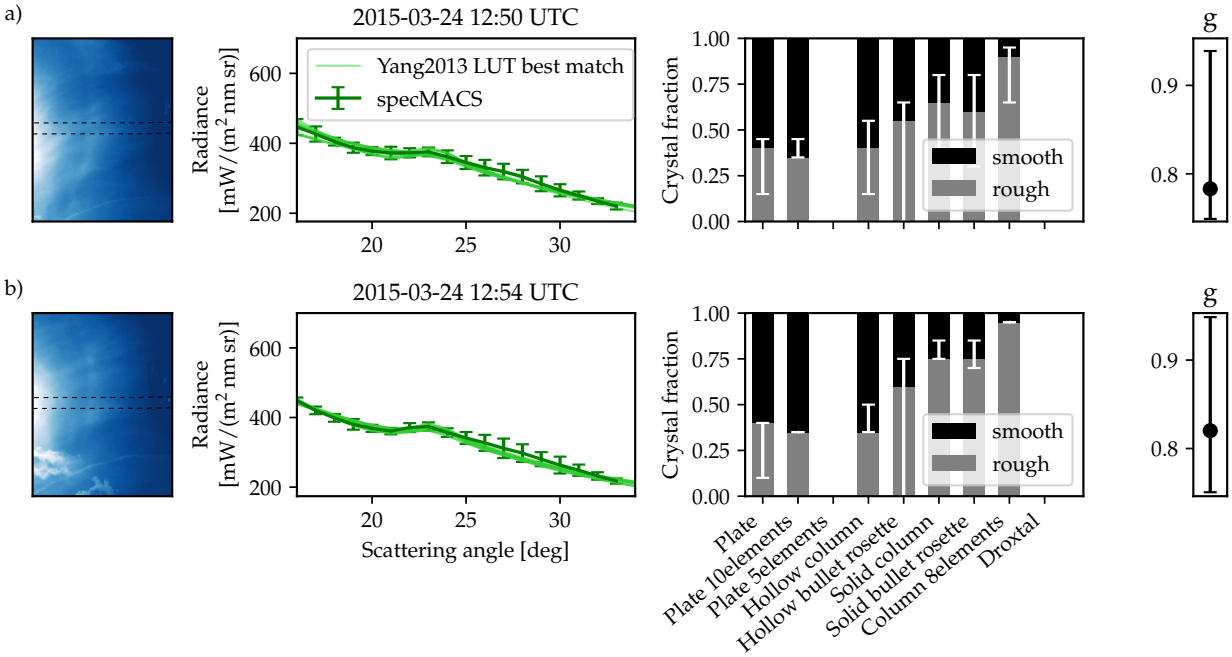

Figure 4.4: *Retrieval of specMACS observations on 24 March 2015 at (a) 12:50 UTC and (b) 12:54 UTC using the YANG optical properties. The first panel displays the specMACS scan across the right side of a 22° halo at a wavelength of 550 nm. The black dashed lines indicate the region used to extract the radiance distribution shown in the second panel (dark green) as a function of the scattering angle. The light green lines in the second panel represent matching LUT radiance distributions with the minimum and maximum SCF for each habit. The third panel shows the fraction of smooth (black) and rough (gray) crystals for all 9 habits. The white error bars, which are centered around the SCF of the best match LUT element, indicate the spread of all possible solutions. The fourth panel shows the asymmetry factor (g) of the best match (black dot) and the error bars indicate the minimum and maximum value for all matching LUT elements of all 9 habits.*

the specMACS scan across the 22° halo on the right side of the sun with the azimuth angle on the x- and elevation angle on the y-axis. The dashed black lines indicate the region in the almucantar plane which is used for the retrieval to avoid interference with the upper tangent arc above the sun. Since the YANG optical properties assume randomly oriented ice crystals, applying the RICO retrieval to halo displays formed by oriented crystals (e.g. upper tangent arc or sundogs) would yield wrong results. Sundogs were not present during the time of the specMACS scans. The specMACS measurements in the second panel (green) are obtained by averaging the radiance over the masked region indicated by the black dashed lines which range between SZA $\pm\,1°$. The error bars of the specMACS measurements in the second panel represent the total measurement uncertainty, which was calculated as explained in Section 3.4, within a 2σ confidence interval.

LUTs were calculated for both measurement times separately and for all 9 ice crystal habits of the YANG parameterization for different fractions of smooth and severely roughened crystals (cf. Section 3.7.1). For the aerosol optical properties the OPAC "continental average" mixture was chosen (cf. Section 3.2.1). A surface albedo of 0.073 at 550 nm was determined from the MODIS white sky albedo product as explained in Section 3.7.3. For this case study an ice cloud base height of 6 km and top height of 9 km was chosen according to the radar and ceilometer observations (cf. Table 4.3). The range and resolution of the remaining LUT parameters, which comprise smooth crystal fraction (SCF), effective radius (r_{eff}), cirrus optical thickness (COT), and aerosol optical thickness (AOT), are provided in Table 4.4.

Table 4.4: *LUT parameters for 24 March 2015: minimum, maximum and resolution for smooth crystal fraction (SCF), effective radius (r_{eff}), cirrus optical thickness (COT), and aerosol optical thickness (AOT).*

LUT parameter	min	max	resolution
SCF	0%	100%	5%
r_{eff}	5 µm	90 µm	5 µm
COT	0.1	2.0	0.05
	2.1	3.0	0.1
	3.2	4.0	0.2
	4.5	6.0	0.5
AOT	0.05	0.5	0.05

Retrieval based on YANG optical properties

As explained in Section 3.7, the simulated radiance distributions of the LUT and the specMACS almucantar measurements are compared by calculating the mean RMSE between the curves. A match is found if the condition RMSE $\leq 2\sigma_{L,specMACS}$ is fulfilled. The best match corresponds to the minimum RMSE. The light green curves in the second column of Fig. 4.4 represent matching LUT elements for the maximum and minimum retrieved SCF of each habit. The third column of Fig. 4.4 shows a bar chart of the smooth (black) and rough (gray) ice crystal fraction for each habit corresponding to the best match, i.e. the minimum RMSE between LUT and measurement. White error bars indicate the range between the minimum and maximum retrieved SCF for each habit. The fourth column of Fig. 4.4 shows the retrieved asymmetry factors with the best match represented by a black dot and error bars indicating the retrieved minimum and maximum values. The y-axis ranges between 0.747 and 0.951, which corresponds to the minimum and maximum asymmetry factor for all habits, smooth crystal fractions and effective radii in the LUT. In this first retrieval step no additional measurements are used to constrain the LUT parameters, so the results shown in Fig. 4.4 are only based on a comparison of measured and simulated radiances for AOTs, COTs, and effective radii which can take any value available in the LUT.

At 12:50 UTC (Fig. 4.4a) and 12:54 UTC (Fig. 4.4b) the specMACS measurements are evaluated in the almucantar plane on the right side of the sun. A faint 22° halo is visible in the specMACS data, which is caused by a thin cirrus cloud. The specMACS radiance distributions in the second column exhibit larger error bars in the scattering angle range from 25° to 30° which is due to spatial inhomogeneity of the cirrus. All habits except for 5-element plates and droxtals match the measurements with different smooth crystal fractions. However, for column-like crystals a smaller fraction of smooth crystals was retrieved on average compared to plate-like crystals. This is due to the different aspect ratios of columns and plates, which causes a much brighter halo in the case of columns compared to plates (cf. Section 3.3.1). Therefore, a much higher fraction of smooth crystals is needed in the case of plate-like habits to produce the same halo brightness as for columns. The best match for both 12:50 UTC and 12:54 UTC are solid columns. At 12:50 UTC the best match SCF amounts to 35% with an effective radius of 10 µm and 25% with an effective radius of 20 µm at 12:54 UTC. The best match asymmetry factor results in 0.780 (12:50 UTC) and 0.785 (12:54 UTC). For both specMACS scans the 22° halo is not pronounced enough to constrain the ice crystal properties without additional information.

The retrieval was repeated with additional constraints on the LUT using the daily mean AOT from AERONET and the apparent COT derived from the SSARA direct sun measurements. Both optical thicknesses were interpolated to 550 nm. The actual COT was derived from the apparent

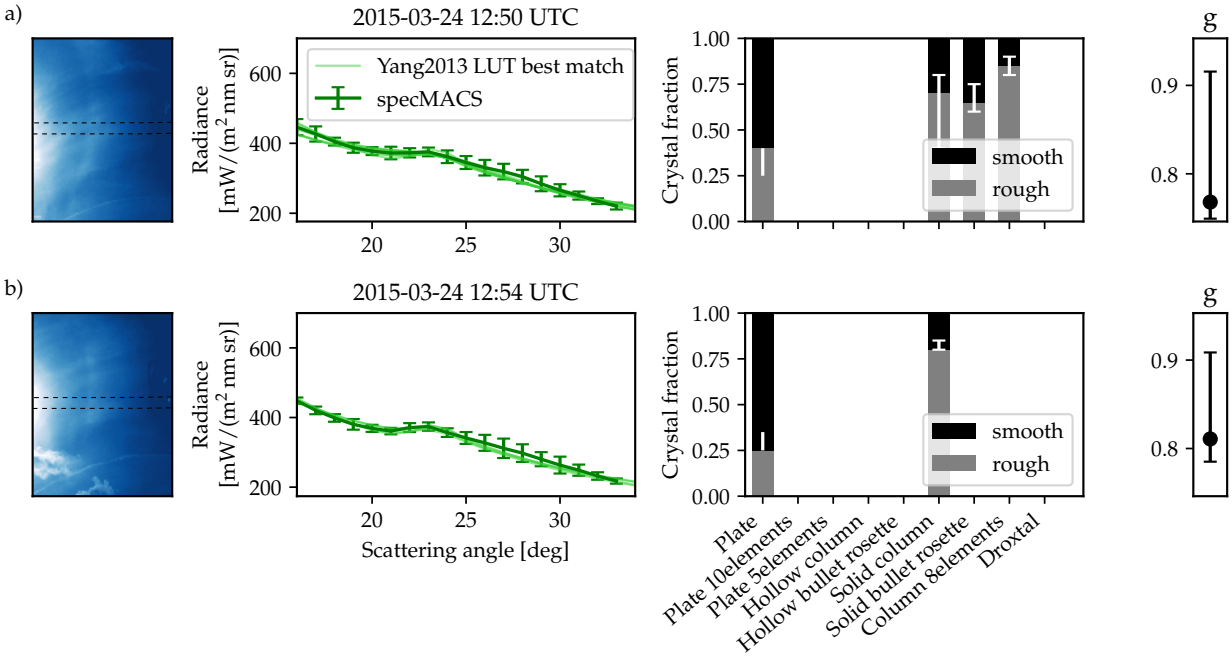

Figure 4.5: *As Fig. 4.4 but using constrained aerosol and cirrus optical thickness from sun photometer observations.*

COT according to Eq. (3.54) by using the k-factors for the respective ice crystal habit. For each habit the k-factors were calculated for all effective radii and SCFs available in the LUT. The minimum and maximum k-factors for each habit were used to estimate the lower and upper boundary of the true COT. Since the k-factors strongly depend on the ice crystal effective radius, the retrieval was performed iteratively: the retrieved effective radii from the first run are used to constrain the k-factors in the second run using the mean effective radius with a 2σ uncertainty. The LUT was constrained using the observed COT within the 10 min time interval. The minimum observed COT within this time interval was used as lower limit and the mean value plus 2 standard deviations as upper limit. The AOT in the LUT was constrained using the daily average within a 2σ confidence interval. Figure 4.5 shows the retrieval results for the same measurements and LUTs as in Fig. 4.4 but with additional constraints on the possible AOT and COT values in the LUT. In this case only few ice crystal habits match the observations. At 12:50 UTC plates, solid columns, solid bullet rosettes, and 8-element columns match the observations, whereas at 12:54 UTC only plates and solid columns are retrieved. The best matching habits are still the solid columns with the same asymmetry factors as in Fig. 4.4 but with a SCF of 30% (12:50) and 20% (12:54) and an effective radius of 10 µm (12:50) and 20 µm (12:54). The best matching results of the constrained retrieval are provided in Table 4.5. Confining the aerosol and cirrus optical thickness helps constrain the ice crystal habit, but an ambiguity between plate and column-shaped crystals remains. Although the results confirm that plate-like crystals with larger SCF

Table 4.5: *Best match cloud properties retrieved for the specMACS scans on 24 March 2015 using constrained cirrus optical thickness (COT) and aerosol optical thickness (AOT).*

specMACS scan time	habit	SCF	effective radius	asymmetry factor	COT	AOT
12:50 UTC	solid column	30%	10 µm	0.780	0.80	0.25
12:54 UTC	solid column	20%	20 µm	0.785	0.70	0.25

can produce an equally bright 22° halo as columnar crystals with smaller SCF, their asymmetry factors are quite different (cf. Fig. 3.11). Thus, as long as both plate-like and columnar crystals match the observations, the asymmetry factor can not be significantly constrained.

Retrieval based on YANG$_{\mathrm{RND}}$ optical properties

As a test, the retrieval was performed for the 12:54 UTC case using the YANG$_{\mathrm{RND}}$ optical property parameterization which consists of random habit mixtures (cf. Section 3.7.1). The best match phase function consists of 50% smooth and 35% rough 10-element plates, 8% smooth droxtals, and 5% rough solid columns. The remaining habits sum up to 2%. The mean effective radius of the corresponding radiance distribution amounts to 70 µm with an asymmetry factor of 0.855 at a wavelength of 550 nm. However, several different mixtures of ice crystal habits match the observations. Allowing for arbitrary mixtures of multiple ice crystal habits, surface roughness, and size might yield a mixture which better represents the observations than using a single habit with smooth and rough crystal fraction. However the retrieved habit mixtures are "radiatively equivalent effective shapes", as stated by McFarlane and Marchand (2008) and Cole et al. (2013). Retrieving ice cloud properties from halo displays using ground-based remote sensing is a complex task which is not well constrained. Thus, allowing more freedom for arbitrary mixtures of ice crystal properties does not necessarily increase the information gain. The YANG parameterization, assuming single habits with varying fraction of smooth and rough crystals, is the most simple parameterization which is apparently sufficient to represent observations of the 22° halo and is therefore the preferred choice.

Retrieval based on GO optical properties

Figure 4.6 presents results of the retrieval applied to the same specMACS measurements as in Fig. 4.4 using optical properties of the GO database for different ice crystal aspect ratios ranging from 0.02 (thin plate) over 1 (compact crystal) to 50 (long column). The LUT for this retrieval was generated assuming a mixture of smooth and rough crystals as for the YANG database. Here, roughness parameters of $\sigma = 0$ and $\sigma = 0.3$ were chosen for the smooth and rough crystals respectively. The results show that the LUT contains combinations of AR and SCF which yield a matching radiance distribution for all ARs. The best match between specMACS measurements and simulations at 12:50 UTC was achieved for ice crystal columns with AR = 3.5, a SCF of 10% and an asymmetry factor (g) of 0.848. For the specMACS observations from 12:54 UTC the best match was found for ice crystal plates with AR = 0.3, a SCF of 75% and an asymmetry factor of 0.928. However, for both times several combinations of AR and SCF exist which match the observations within the measurement uncertainty. Columnar crystals as best match for the 12:50 UTC measurements is in agreement with the YANG parameterization. The smaller SCF in the case of the GO parameterization is due to the larger AR indicating long columns compared to the 10 µm column retrieved for YANG which corresponds to more compact crystals (cf. Fig. 3.7). At 12:54 UTC GO retrieves plate-like crystals, whereas YANG retrieves solid columns as best match with an effective radius of 20 µm. Plate-like crystals are also a possible solution for the YANG parameterization with a SCF of about 75% which is comparable to GO.

Compared to the YANG ice crystal model, the GO model allows varying the ice crystal AR independently from ice crystal size. This is an advantage for investigating 22° halos since the halo ratio, i.e. the brightness contrast of the 22° halo, is mainly determined by ice crystal aspect ratio and surface roughness (cf. Fig. 3.10). However, the conventional geometric optics method to calculate ice crystal optical properties has several shortcomings for smaller pristine ice crystals with random orientation which form the 22° halo (Bi and Yang, 2014, Yang et al., 2015, Um et al.,

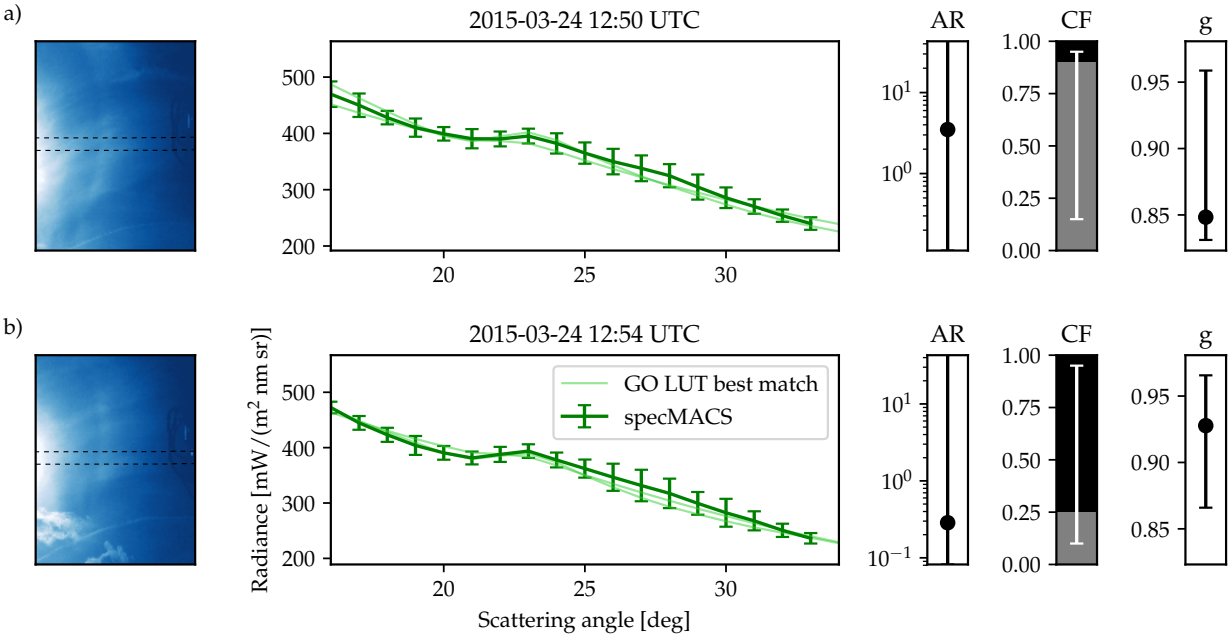

Figure 4.6: *Retrieval results for 24 March 2015 at (a) 12:50 UTC and (b) 12:54 UTC using GO optical properties. The first panel displays the specMACS scan across the right side of a 22° halo at a wavelength of 550 nm. The black dashed lines indicate the region used to extract the radiance distribution shown in the second panel (dark green) as a function of the scattering angle. The light green lines in the second panel represent matching LUT radiance distributions with the minimum and maximum SCF for each ice crystal aspect ratio (AR). The results of all matching ARs, crystal fractions (CF) and asymmetry factors (g) are displayed as error bars in the last three panels. Note the logarithmic y-scale of the AR panel. For the AR and asymmetry factor the best match values are represented by a black dot. The best matching CF is displayed by a bar plot with black representing the smooth and gray the rough crystal fraction.*

2015). Um et al. (2015) calculated optical properties of ice crystals with different aspect ratios with the Amsterdam Discrete Dipole Approximation (ADDA), which provides exact numerical solutions of Maxwell's equations, and the conventional Geometric Optics Method (GOM), which is also used for the GO parameterization (Macke et al., 1996). The authors found that the minimum size parameter χ (cf. Eq. (2.30)) required to produce a visible 22° halo strongly depends on the AR of the ice crystal and amounts to $\chi = 45$ (68; 91) for AR $= 1$ (0.5; 2), corresponding to compact (plate-like; column-like) crystals. For these size parameters the asymmetry factors calculated with the GOM and ADDA method differ by up to 5% and the extinction efficiency up to 30%. As stated by Um et al. (2015) the differences in the phase functions can be much larger. Thus, for the following analyses the YANG optical properties will be used and each ice crystal habit will be treated separately.

4.2.2 Case study of 22 September 2015

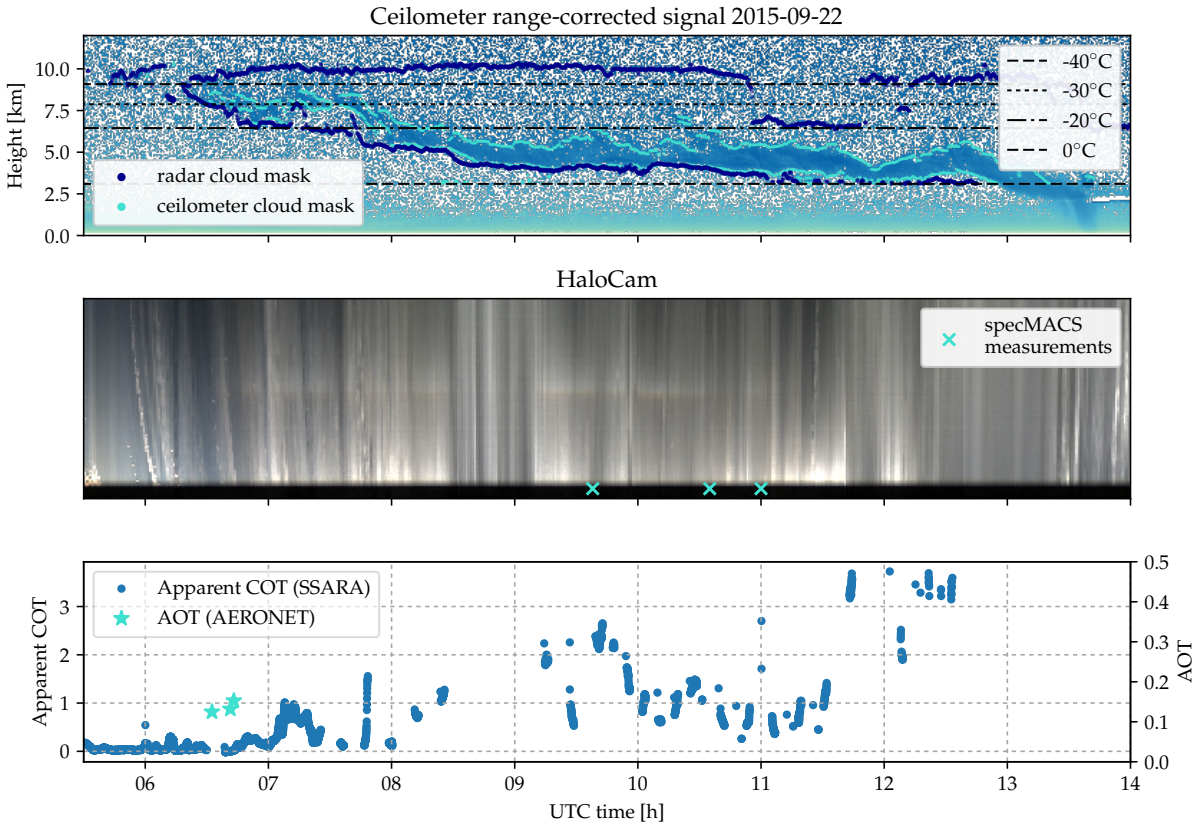

Figure 4.7: *Overview of observations on 22 September 2015. For a detailed description see Fig. 4.3.*

On 22 September 2015 cirrus clouds formed on the leading edge of a warm front approaching from the west. After clearsky conditions in the early morning the first cirrus clouds formed around 7:00 UTC. Figure 4.7 shows an overview of the ceilometer and cloud radar observations (top), HaloCam (center), and sun photometer (bottom) observations between 5:30 and 14:00 UTC. As explained in the previous section it is important to keep in mind that the zenith-pointing instruments (radar and ceilometer) observe different regions of the sky than the sun-tracking instruments (HaloCam and sun photometer). For a homogeneous cloud cover the data can be compared with a time shift. The height of the cirrus cloud base and top can be derived from ceilometer (lidar) and radar measurements. Figure 4.7 (top) shows the range-corrected ceilometer signal. As in Fig. 4.3 the detected cloud base and top height derived from the ceilometer measurements are represented by turquoise dots whereas the cloud base and top height from the radar measurements are marked with dark blue dots. Similar to Fig. 4.3 (top) the cloud top height derived from the radar measurements is significantly larger than for the ceilometer measurements. As already discussed in the previous section, the best estimate for cloud base and top height is achieved by combining both observations using the cloud base height from the ceilometer and the cloud top height from the radar measurements. This results in a cloud top height which is almost constant at 10 km between 6:30 and 11:00 UTC. Between 11:00 and 12:00 UTC the cloud top height drops to about 7 km. The cloud base height decreases in the course of the day from about 8 km at 6:30 UTC to about 4 km around 10:00 UTC where it remains until the onset of rain, which is visible in the backscatter signal of the ceilometer at around 13:30 UTC. As in Fig. 4.3

Table 4.6: *Cloud and aerosol properties during the specMACS scans on 22 September 2015.*

specMACS scan time	cloud top (base) height	cloud top (base) temperature	AOT daily average	apparent COT
09:38 UTC				0.53 to 3.47
10:35 UTC	10 km (4.5 km)	−48 °C (−10.5 °C)	0.14 ± 0.02	0.53 to 2.10
11:00 UTC				0.26 to 1.14

the temperature levels at 0 °C, −20 °C, −30 °C and −40 °C, which are derived from radiosonde measurements at Oberschleißheim, are indicated by dashed, dash-dotted, dotted, and dashed lines, respectively. Cloud top temperatures amount to about −48 °C during the observed period, whereas the cloud base temperature increases to −5 °C and 0 °C. As in Fig. 4.3 the HaloCam data (Fig. 4.7 center) is represented by a time series of pixel lines in the principal plane above the sun with a temporal resolution of 10 s. The 22° halo observed between 7:00 to 11:00 UTC with interruptions is visible as a line approximately in the middle of the figure which appears slightly reddish at the lower (inner) edge.

The sun photometer observations in Fig. 4.7 (bottom) display the AERONET AOT version 2, level 2.0 (cloud screened) with turquoise stars interpolated to 550 nm. Clearsky conditions in the early morning around 6:30 UTC allowed to estimate the AOT with a daily mean of 0.14 ± 0.02 within a 2σ confidence interval. The apparent COT is derived from SSARA sun photometer measurements as explained in Section 3.7.3. During the time when the halo display was observed a maximum apparent COT of about 2.8 was measured. As in Section 4.2.1 a time interval of ±10 min was chosen to estimate the apparent COT during the specMACS measurements taking into account the different pointing directions of the direct sun and the 22° halo measurements. The LUT was constrained using the averaged COT over this 10 min time interval. The minimum observed COT within this time interval was used as lower limit and the mean value plus 2 standard deviations as upper limit. Table 4.6 shows the estimated values for cloud top and base height, apparent COT and average AOT which are used to define the range of the LUT parameters at the time of the specMACS measurements.

Figure 4.8 shows the specMACS measurements at 9:38, and 10:35 UTC on the left side of the sun and at 11:00 UTC on the right side of the sun at a wavelength of 550 nm. As in the previous case study the almucantar plane is used for the retrieval to avoid interference with the upper tangent arc which contains light scattered by oriented ice crystals. Sundogs were not observed. The specMACS data are displayed in green with error bars consisting of the standard deviation of the averaged radiance and the propagated measurement uncertainty, as explained in Section 3.4. The LUT is calculated for the same parameters as for the case study of 24 March 2015 (cf. Table 4.4) for the respective solar zenith angle of each measurement. The simulated radiance distributions in the LUT and the specMACS almucantar measurements are compared by calculating the mean RMSE between the curves. A match is found if the condition $\mathrm{RMSE} \leq 2\sigma_{\mathrm{L,specMACS}}$ is fulfilled. The light green curves in the second column of Fig. 4.8 represent matching LUT elements for the maximum and minimum retrieved SCF of each habit. The 3rd column of Fig. 4.8 shows a bar chart of the smooth (black) and rough (gray) ice crystal fraction for each habit corresponding to the best match between LUT and measurement with error bars spreading between the retrieved minimum and maximum values for each habit. The 4th column of Fig. 4.8 shows the retrieved asymmetry factors as an error bar with a black dot at the value corresponding to the best match and ranging between retrieved minimum and maximum value. The y-axis ranges between 0.747 and 0.951, which are the minimum and maximum value for the asymmetry factor if all habits, SCFs and effective radii are considered.

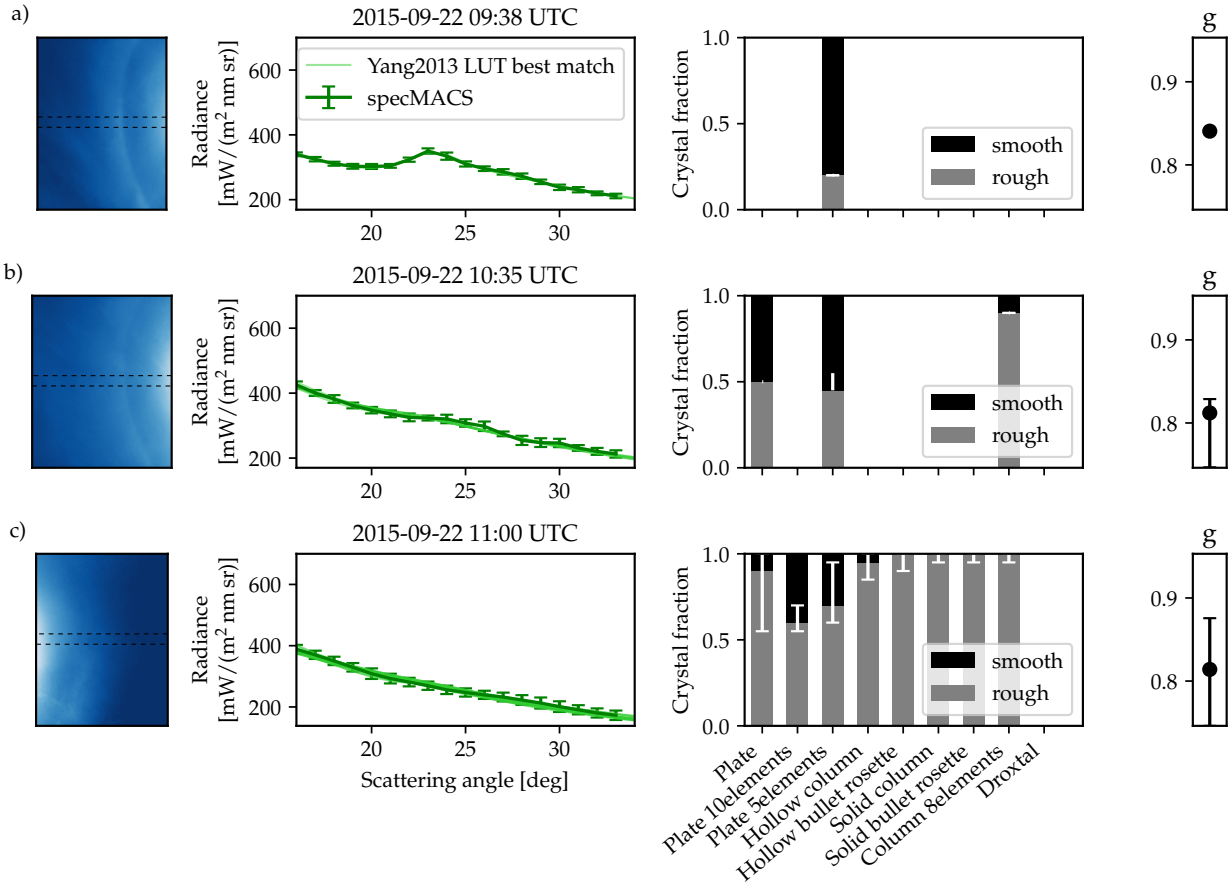

Figure 4.8: *Retrieval applied to specMACS observations of 22 September 2015 using the YANG optical properties. Aerosol and cirrus optical thickness of the LUT were constrained using sun photometer observations as displayed in Table 4.6. For a detailed description see Fig. 4.4.*

At 9:38 UTC (Fig. 4.8a) a pronounced 22° halo is visible which constrained the LUT parameters to 5-element plates as the only matching habit. The SCF is constrained to 80%, the effective radius to 10 µm with an asymmetry factor of about 0.841 at 550 nm. The retrieved COT varies between 1.3 and 1.35 and the retrieved AOT amounts to 0.15. The 22° halo at 10:35 UTC is less pronounced but helps constrain possible combinations of ice crystal habit and surface roughness. Matching habits are plates, 5-element plates and 8-element columns. For the plates the SCF amounts to 50%, for 5-element plates the SCF ranges between 45% and 55% and for the 8-element columns a SCF of 10% was retrieved. The retrieved effective radius was 5 µm for all habits. For the 10:35 UTC case, the asymmetry factor can be constrained to values smaller than 0.83. The best match is represented by the 5-element plates with a SCF of 55% and an asymmetry factor of 0.829 with a COT of 1.15 and an AOT of 0.15. The third measurement at 11:00 UTC was taken just after the 22° halo disappeared (cf. Fig. 4.7, center) showing a featureless curve. All habits except droxtals match the measurements with different amounts of smooth ice crystals. In this case the SCF is very low as expected and rough ice crystals are dominating with an average SCF of about 10% over all habits. The asymmetry factor could be slightly constrained to values lower than 0.88. Again, the 5-element plates are the best matching habits with a SCF of 30%, an effective radius of 5 µm and an asymmetry factor of 0.819 with a COT of 0.6 and an AOT of 0.15. An overview of the retrieval best match for the three specMACS scans is provided in Table 4.7.

The two case studies showed that the 22° halo contains information about ice crystal habit, smooth crystal fraction, effective radius and asymmetry factor. The more pronounced the 22° halo

Table 4.7: *Best match cloud properties retrieved for the specMACS scans on 22 September 2015 using constrained cirrus optical thickness (COT) and aerosol optical thickness (AOT).*

specMACS scan time	habit	SCF	effective radius	asymmetry factor	COT	AOT
09:38 UTC	5-element plate	80%	10 µm	0.841	1.30	0.15
10:35 UTC	5-element plate	55%	5 µm	0.829	1.15	0.15
11:00 UTC	5-element plate	30%	5 µm	0.819	0.60	0.15

the better constrained are the retrieval results. In most cases an ambiguity exists as plate-like crystals with a larger SCF can produce an equally bright 22° halo as columnar crystals with a smaller SCF. This is in agreement with the findings from analysis of single scattering properties which showed that roughened columns exhibit the same 22° halo ratio as smooth plates (cf. Fig. 3.10). Since the asymmetry factor, however, differs between plates and columns as shown in Fig. 3.11, it can only be constrained if the ambiguity between plates and columns is resolved. Constraining AOT and COT from sun photometer measurements helps constrain possible solutions. Using the YANG parameterization, the retrieved best match habit seems to be consistent over the time period of the specMACS scans, with solid columns with SCFs between 20% and 30% for 24 March and 5-element plates with SCFs between 55% and 80% for 22 September 2015. Comparing the formation and temporal evolution of the cirrus clouds using the cloud radar and ceilometer information of Figs. 4.3 and 4.7, the cloud top temperature is less than −40 °C in both cases whereas the cloud base temperature on 22 September is much higher with −10.5 °C than on 24 March with −28 °C. Thus, the colder and thinner cirrus on 24 March is better represented by columnar crystals, whereas aggregates of plates better represent the ice crystal properties of the deeper cirrus on 22 September with a warmer cloud base. Applying the RICO retrieval with the GO parameterization to the observations a certain SCF can be found for almost all aspect ratios which is able to reproduce the specMACS measurements within the measurement error. The best match, however, are columns at 12:50 UTC and plates at 12:54 UTC which disagrees with the retrieval results using YANG. Um et al. (2015) report that larger differences exist between scattering phase functions calculated with exact methods and the geometric optics approximation for ice crystals which are just large enough to produce a 22° halo. The effective radii which were retrieved using the YANG parameterization were rather small and ranged between 5 µm and 20 µm. For these reasons only the YANG parameterization will be used in the following.

4.2.3 Application to long-term HaloCam observations

To obtain representative results for ice crystal properties of halo-producing cirrus clouds, long-term observations are required. However, specMACS measurements can not be performed operationally since the instrument is not water-proof. Therefore, the weather-proof automatic camera $\text{HaloCam}_{\text{RAW}}$ was installed in September 2015 on the rooftop platform of MIM. Between 22 September 2015 and 31 December 2016 $\text{HaloCam}_{\text{RAW}}$ recorded scenes with a 22° halo on 52 days with a temporal resolution of 10 s. The automated halo detection algorithm HaloForest, described in Section 3.6.2, was used to filter the $\text{HaloCam}_{\text{RAW}}$ images for 22° halos. Additional sun photometer measurements are used to constrain aerosol optical thickness (AOT) and cirrus optical thickness (COT). As demonstrated in Section 4.2.1, the better these two parameters can be constrained the more information about the ice crystal microphysical properties can be gained from the observations. As described in Section 3.7.3, the AOT is obtained from the AERONET database and the mean and standard deviation over the whole day are used as an estimate for the AOT during the halo event. The apparent COT is derived from the SSARA sun photometer measurements with a temporal resolution of 2 s. The retrieval is applied to the R-channel of $\text{HaloCam}_{\text{RAW}}$ with a central wavelength of 618 nm (cf. Fig. 3.40) to minimize the relative contribution of Rayleigh and aerosol scattering compared to the scattering by ice crystals.

Table 4.8: *$\text{HaloCam}_{\text{RAW}}$ 22° halo days between 22 September 2015 and 31 December 2016.*

Date	Start time	End time	Number of images
2015-09-22	6:38 UTC	11:14 UTC	1054
2015-11-08	10:00 UTC	10:37 UTC	198
2015-11-10	9:00 UTC	10:23 UTC	88
2016-01-20	9:36 UTC	11:37 UTC	544
2016-02-02	8:00 UTC	14:00 UTC	1029
2016-02-06	12:00 UTC	15:20 UTC	724
2016-04-21	11:34 UTC	13:52 UTC	770
2016-11-04	10:27 UTC	10:40 UTC	78

Simultaneous measurements of the SSARA and the Cimel (AERONET) sun photometer together with $\text{HaloCam}_{\text{RAW}}$ observations are available for only 8 of the 52 days listed in Table 4.8. Figure 4.9 shows an example of the AOT and apparent COT derived from sun photometer measurements on 21 April 2016. The AOT is obtained from the AERONET dataset and is represented by turquoise stars. The daily average AOT amounts to about 0.08 ± 0.04 at 618 nm. The blue dots in Fig. 4.9 indicate the apparent COT derived from SSARA direct sun measurements, which are available from about 11:30 UTC. The lower panel of Fig. 4.9 shows slices of the HaloCam images along the principal plane above the sun. 22° halos and upper tangent arcs appear as a bright line in the center of the panel with a reddish inner, i.e. lower, edge from about 11:30 until 14:00 UTC.

The $\text{HaloCam}_{\text{RAW}}$ observations were geometrically and radiometrically calibrated as described in Sections 3.5.2 and 3.5.3. For applying the RICO retrieval to the $\text{HaloCam}_{\text{RAW}}$ data the LUT was calculated for a wavelength of 618 nm with a surface albedo of 0.065 and a cloud base and top height of 10 km and 11 km, respectively. For details on the choice of these LUT parameters see Section 3.7.3. The remaining LUT parameters are provided in Table 4.9. To use as much information as possible from the $\text{HaloCam}_{\text{RAW}}$ images for the retrieval, the radiative transfer simulations for the LUT were performed for the viewing angles of all 5 image segments. The file size of the LUT and observations was then reduced by averaging both simulated and measured

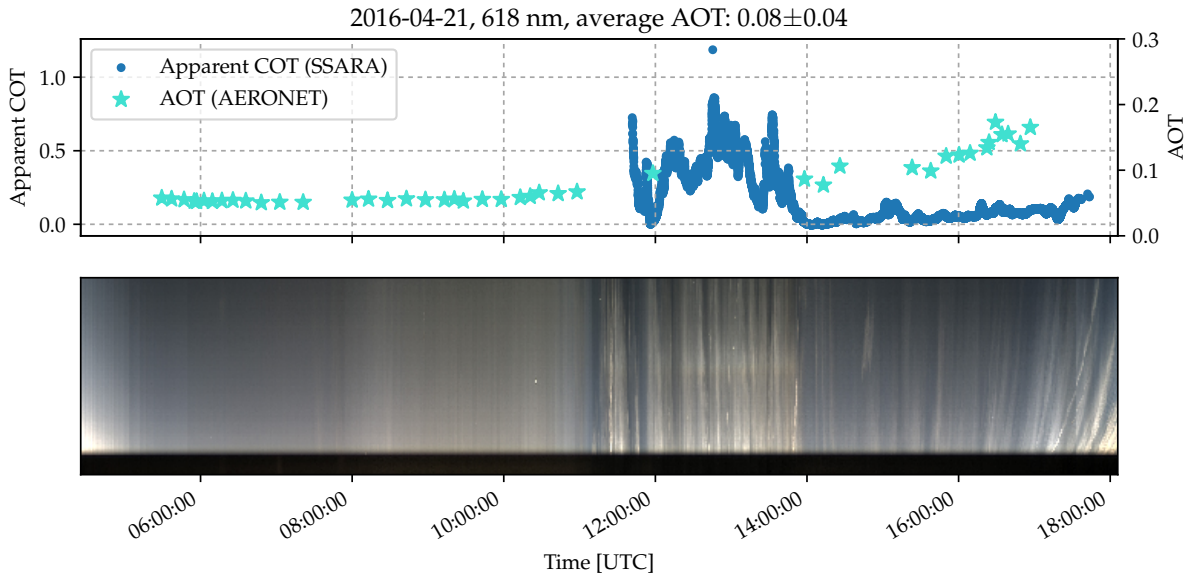

Figure 4.9: *Top: AERONET aerosol optical thickness (AOT, turquoise stars) and apparent cirrus optical thickness (COT) derived from SSARA measurements (blue dots) for a wavelength of* 618 nm. *Bottom: time line of HaloCam$_{\mathrm{JPG}}$ pixel slices above the sun as described in Fig. 4.3.*

images over the 5 segments in the direction of the relative azimuth angle φ (cf. Fig. 3.24b). Thus, a separate LUT was compiled for each of the 5 HaloCam$_{\mathrm{RAW}}$ image segments which are evaluated separately.

The RICO retrieval (Section 3.7) was performed as follows: for each HaloCam$_{\mathrm{RAW}}$ image the LUT was interpolated to the respective SZA and constrained to the previously determined AOT within a 2σ confidence interval. To constrain the COT of the applied LUT, a 10 min time interval centered at the time of the HaloCam$_{\mathrm{RAW}}$ image was chosen to account for the slightly different pointing directions $\Theta = 0°$ (sun photometer) and $\Theta = 22°$ (halo display) in combination with the unknown wind direction. The corresponding COT was obtained by correcting the apparent COT with the k-factors of the respective ice crystal habit in the LUT according to Eq. (3.54). Then, each of the 5 averaged radiance distributions measured with HaloCam$_{\mathrm{RAW}}$ was compared to the LUT elements with the respective geometry. The scattering angle grid was optimized for the retrieval to account for the vicinity of the 22° halo in addition to its peak while keeping the angular region as small as possible to avoid inhomogeneities of the cirrus optical and microphysical properties. The case studies presented in Sections 4.2.1 and 4.2.2 showed that cirrus cloud inhomogeneities were present in some cases for scattering angles larger than about 25°. Thus, for HaloCam$_{\mathrm{RAW}}$'s long-term dataset, measurements and LUT were compared on a scattering angle grid between 18° and 25° with an angular resolution of 0.5°. The previous case studies (Sections 4.2.1 and 4.2.2) demonstrated that multiple configurations of ice crystal habit, SCF, effective radius, COT and AOT matched the specMACS radiance observations within the measurement error. Here, the goal is to investigate which ice crystal habit and SCF best matches the observed radiance distributions across 22° halos. Sampling over many scenes should provide a good estimate of the average ice crystal properties of halo-producing cirrus clouds. For each image segment the best matching radiance distribution of the LUT was determined separately. Only results are considered which agree with the measurements within the measurement uncertainty RMSE $\leq 2\sigma_{\mathrm{L}}$. In addition, the results were filtered for HR > 1 to ensure that only samples with 22° halo are considered. The uppermost segment (no. 3 in Fig. 3.24) might contain signatures of the upper tangent arc. Although the results did not significantly change, the upper image

Table 4.9: *LUT parameters: minimum, maximum value and resolution for smooth crystal fraction (SCF), effective radius (r_{eff}), cirrus optical thickness (COT), aerosol optical thickness (AOT), and solar zenith angle (SZA). COT and AOT are defined at a wavelength of* 550 nm.

LUT parameter	min	max	resolution
SCF	0%	100%	5%
r_{eff}	5 µm	90 µm	5 µm
COT	0.1	2.0	0.05
	2.1	3.0	0.1
	3.2	4.0	0.2
AOT	0.00	0.50	0.05
SZA	25°	30°	5°
	40°	70°	10°

segment was excluded for the presented retrieval results. Sundogs appear in the left and right image segments (no. 1 and 5) only for SZA $< 45°$ at scattering angles of $\Theta > 29°$ which does not interfere with the 22° halo (cf. Fig. 4.2).

Figure 4.10 displays the retrieval results for the 3080 samples (4 segments per image) of a 22° halo observed on 21 April 2016, assuming solid columns (a), hollow columns (b), and plates (c) as dominating ice crystal habit. The retrieved values for the SCF, effective radius, and asymmetry factor (g) are provided as histograms with parameter boundaries and bins as defined in the LUT. The cirrus and aerosol optical thickness are provided for the sake of completeness but it is important to note that the retrieval is not optimized to retrieve these parameters. The RMSE between LUT and measurement is provided in the rightmost panels of Figure 4.10. For solid columns (Fig. 4.10a) the SCF peaks below 50% with a mean value of 33.4%, which implies that the 22° halo on the $\text{HaloCam}_{\text{RAW}}$ images is represented best by a larger fraction of rough solid columns. The ice crystal effective radii peak at 15 µm with a mean value of 23.0 µm and a mean asymmetry factor of 0.788. Although the distribution of retrieved effective radii is strongly skewed towards small values, the mean value and standard deviation are provided to allow for comparison with other studies. The majority of COT values are below 1 with a mean value of 0.53, whereas the AOT is constrained between 0.05 and 0.15 with a mean value of 0.10. In the case of hollow columns (Fig. 4.10b), the retrieved SCF ranges around 50% with effective radii of 18.5 µm on average and a mean asymmetry factor of about 0.81. The COT values are slightly smaller than for the solid columns with a mean value of about 0.4. For ice crystal plates (Fig. 4.10c) larger SCFs with a mean value of 75.1% are required to match the brightness contrast of the 22° halo measured with $\text{HaloCam}_{\text{RAW}}$. The mean effective radius with 16.4 µm is slightly smaller than for the solid columns. Assuming plates as dominating ice crystal habit causes a larger asymmetry factor on average with 0.867. The average COT amounts to 1.07 with a few values larger than 2. In contrast to the AOT values, the COTs of the best match radiance distributions are significantly larger for plates than for solid columns. This is due to the large asymmetry factors and thus increased forward scattering of plates. This in turn causes smaller k-factors to correct for the larger difference between true and apparent COT (cf. Section 3.7.3). Compared with solid and hollow columns the plate habit shows the smallest RMSE values for this dataset.

Figure 4.11 shows the results of the retrieval applied to the 8 days of 22° halo observations with $\text{HaloCam}_{\text{RAW}}$. The upper panel presents the retrieved SCF for each day and for the 8 habits: plates (turquoise), 10-element plates (blue), 5-element plates (dark blue), hollow columns (pink),

Table 4.10: *RICO retrieval results evaluated for all 8 days. Mean value and standard deviation are provided for the smooth crystal fraction (SCF), effective radius, and asymmetry factor, sorted by increasing mean RMSE.*

Habit	RMSE	SCF [%]	Effective radius [µm]	Asymmetry factor
plate	3.81	80 ± 10	20.7 ± 10.9	0.876 ± 0.021
solid column	4.08	40 ± 20	21.7 ± 13.2	0.787 ± 0.008
8-element column	4.19	30 ± 20	21.4 ± 16.4	0.752 ± 0.001
5-element plate	4.29	70 ± 10	16.2 ± 10.1	0.838 ± 0.005
10-element plate	4.25	80 ± 10	13.5 ± 11.5	0.876 ± 0.004
solid bullet rosette	4.55	30 ± 10	18.7 ± 12.2	0.779 ± 0.013
hollow column	4.63	50 ± 10	19.9 ± 09.6	0.811 ± 0.005
hollow bullet rosette	5.16	50 ± 20	19.1 ± 12.7	0.829 ± 0.007

hollow bullet rosettes (purple), solid columns (light green), solid bullet rosettes (green) and 8-element columns (dark green). Droxtals were not considered for the retrieval since they do not produce a 22° halo and did not reproduce the specMACS observations within the measurement error (cf. Sections 4.2.1 and 4.2.2). By grouping the ice crystal habits into columnar (green), hollow (pink), and plate-shaped (blue) crystals, the average SCF clusters at ∼30%, ∼60%, and ∼80%, respectively. A similar clustering results for the asymmetry factor, which is smallest for columnar crystals and largest for plate-like crystals. In contrast to the differences of the retrieved mean SCFs and asymmetry factors among the habits, the retrieved mean effective radii, shown in the third panel of Fig. 4.11, seem to be almost independent of ice crystal habit and roughness. This confirms that the width of the 22° halo is primarily determined by ice crystal size, while shape and surface roughness play a minor role, as discussed in Section 3.3.2. The mean effective radius amounts to about 20 µm. Due to the skewed distribution of the retrieved effective radii (cf. Fig. 4.10), more than 90% of the results are smaller than 40 µm.

Figure 4.12 (upper panel) shows the cloud top (circles) and base (dots) height represented by the mean value and standard deviation, which were derived from co-located cloud radar measurements. On 4 November 2016 cirrus clouds formed only in the south and south-east during the 22° halo event (cf. Table 4.8). Thus, the zenith-pointing cloud radar did not detect the cirrus cloud observed by $\text{HaloCam}_{\text{RAW}}$ and therefore no cloud height could be provided. In the other cases the cirrus clouds were more extended and the 22° halo was visible over a longer time period. The cloud top height varied around 10 km except for 20 January 2016 with 6 km. The cloud base height yields a larger variability between 5 km and 10 km. The corresponding temperatures at cloud top (circles) and cloud base (dots), indicated by mean value and standard deviation, are displayed in the lower panel of Fig. 4.12. The threshold temperature for homogeneous nucleation is represented by the blue dashed line at −38 °C. For all 7 cases the cloud top temperature is equal or colder than −38 °C while the cloud base temperature varies between −10 °C and −50 °C on average. It is interesting to note that the coldest and thinnest cirrus on 10 November 2015 with a cloud base temperature of about −50 °C coincides with the smallest retrieved effective radii in Fig. 4.11. This is in agreement with in situ observations which found the smallest ice crystals close to cloud top and for the coldest temperatures in case of synoptic cirrus (e.g. Bailey and Hallett (2009), Baran (2012)).

Table 4.10 presents the retrieved SCF, effective radius and asymmetry factor for all evaluated days, sorted by increasing mean RMSE. The RICO retrieval revealed that ice crystal plates have the overall smallest mean RMSE and thus seem to match the $\text{HaloCam}_{\text{RAW}}$ observations better than the other 7 habits of the YANG database. The best matching LUT elements of ice crystal

Table 4.11: *Best match habit for the RICO retrieval applied to HaloCam$_{\mathrm{RAW}}$ daily observations for the default retrieval (first column) and considering the spectral response (second column), followed by the continental clean, polluted, and urban aerosol type. Columns 7 and 8 show the retrieved best matching habit assuming the upper and lower boundaries of radiometric response within a 1σ confidence interval. The habits vary between plates (plate), 5-element plates (5-plate), 10-element plates (10-plate), 8-element columns (8-col), solid columns (sCol), hollow columns (hCol), and solid bullet rosettes (sbRos).*

Date	Default	Sensitivity tests					
		Spectral response	Aerosol type			Radiometric response	
			contin. clean	contin. polluted	urban	$R+\sigma_{\mathrm{R}}$	$R-\sigma_{\mathrm{R}}$
2015-09-22	8-col	8-col	8-col	sCol	sCol	8-col	sCol
2015-11-08	plate	5-plate	plate	plate	plate	plate	10-plate
2015-11-10	sCol	hCol	hCol	sCol	sbRos	8-col	sCol
2016-01-20	plate	plate	plate	plate	plate	plate	plate
2016-02-02	sCol	sCol	sCol	sbRos	sbRos	sCol	sCol
2016-02-06	plate	plate	plate	plate	plate	plate	plate
2016-04-21	plate	plate	plate	plate	plate	plate	plate
2016-11-04	plate	plate	5-plate	plate	plate	5-plate	plate

plates have a SCF of (80 ± 10) %, an effective radius of (20.7 ± 10.9) µm and an asymmetry factor of 0.876 ± 0.021. With increasing RMSE, the plates are followed by solid columns and 8-element columns. Hollow columns and bullet rosettes have the largest mean RMSE.

Using the representative wavelength of the camera channel instead of accounting for the spectral response of the channel, introduces a small bias of less than 2% for the R-channel (cf. Fig. 3.40). Since the LUT was calculated for the OPAC continental average aerosol type, the retrieval results might be biased if the actual aerosol type differs. To obtain a rough estimate of the sensitivity of the retrieval, it was repeated with a modified LUT to model the effect of these approximations. The LUT was modified by multiplication with a slope which is representative for the amount and the sign of the bias introduced by the approximations. Table 4.11 shows the results of the best matching habit for each day retrieved with the modified LUT. The last two columns of Table 4.11, present the results of testing the sensitivity of the retrieval on the uncertainty of the radiometric response within a 1σ confidence interval. A 1σ interval was considered since a large part of the uncertainty is probably due to inhomogeneities in the cirrus clouds used for the calibration (cf. Section 3.5.3). For this test the default LUT was used and applied to HaloCam$_{\mathrm{RAW}}$ measurements which were calibrated with $R+\sigma_{\mathrm{R}}$ and $R-\sigma_{\mathrm{R}}$, respectively. The best matching habit slightly changed for the different modifications of the LUT but only within the plate-like or column-like crystal groups. The ice crystal plates remain the overall best-matching habit. Another uncertainty might be the presence of supercooled water droplets as discussed in Section 3.7.2 for cloud base temperatures warmer than $-35\,^{\circ}\mathrm{C}$. However, Fig. 3.39 showed that the presence of water droplets has a small effect on the retrieved SCF since spherical water droplets act like rough ice crystals in diminishing the 22° halo.

To test how representative the retrieved LUT parameters are for the whole scene, the averaged HaloCam$_{\mathrm{RAW}}$ images were compared with DISORT simulations for the same viewing geometry and resolution as the image. Figure 4.13 shows the averaged HaloCam$_{\mathrm{RAW}}$ images for 6 of the 8 evaluated days (left) in comparison with DISORT simulations (center). The right panels display the relative difference between observations and simulations. Interestingly, none of the

$\text{HaloCam}_{\text{RAW}}$ images (Fig. 4.13 left panels) shows a 46° halo. Except for the 8 November 2015, the observation periods are long enough that cloud inhomogeneities almost disappear after averaging. This is clearly visible in the relative difference between observation and DISORT simulation in the right image panels. If ice crystals in the cirrus cloud were able to form a 46° halo, it should appear in the averaged image. Figure 4.13a displays the comparison with DISORT simulations using ice crystal plates, which were found to best match the observations in the region of the 22° halo (cf. Table 4.10). However, the optical properties of plates produce a pronounced 46° halo in addition to the 22° halo for all evaluated days, which is presented here for 22 September 2015 as an example. Comparing the retrieval results for all 8 habits revealed that 8-element columns best match the whole scene of the $\text{HaloCam}_{\text{RAW}}$ images, taking into account the region of the 46° halo. The results in Fig. 4.13b are displayed for 6 of the 8 days. In contrast to Fig. 4.13a, the DISORT simulations using 8-element columns do not show a 46° halo in the center panels. The faint signatures in the region of the 46° halo of the relative difference between the $\text{HaloCam}_{\text{RAW}}$ images and the DISORT simulations for 22 September 2015 and 21 April 2016 are exaggerated in this representation due to subtracting small radiance values.

Thus, the absence of the 46° halo can be used to further constrain the ice crystal microphysical properties. The retrieval was repeated for the individual $\text{HaloCam}_{\text{RAW}}$ images excluding all LUT elements with a 46° halo. The results of the SCF, effective radius and asymmetry factor, averaged over all habits, did not change significantly. In this case, the best matching habit (with the overall smallest RMSE) in the scattering angle region between $18° \leq \Theta \leq 25°$ is the solid column followed by the 8-element column. For the whole scene of the $\text{HaloCam}_{\text{RAW}}$ images, 8-element columns revealed to slightly better represent the observations than solid columns. It revealed that ice crystal plates match the observations only for larger effective radii of about 50 µm on average. This can be explained with the relationship between ice crystal aspect ratio and size for the Yang et al. (2013) optical properties: small ice crystal plates have aspect ratios of $\text{AR} \approx 1$ (cf. Fig. 3.7) which are effective for the formation of 46° halos, as shown in Fig. 3.10. Since the overall mean effective radius for all habits except for plates did not change significantly compared to the results in Fig. 4.11, it seems that the size-AR parameterization of the plate habit does not represent well the observations. Although the sundogs visible on 8 November 2015 and 6 February 2016 are a clear indication for the presence of oriented ice crystal plates, they are obviously too large in these cases to be randomly oriented.

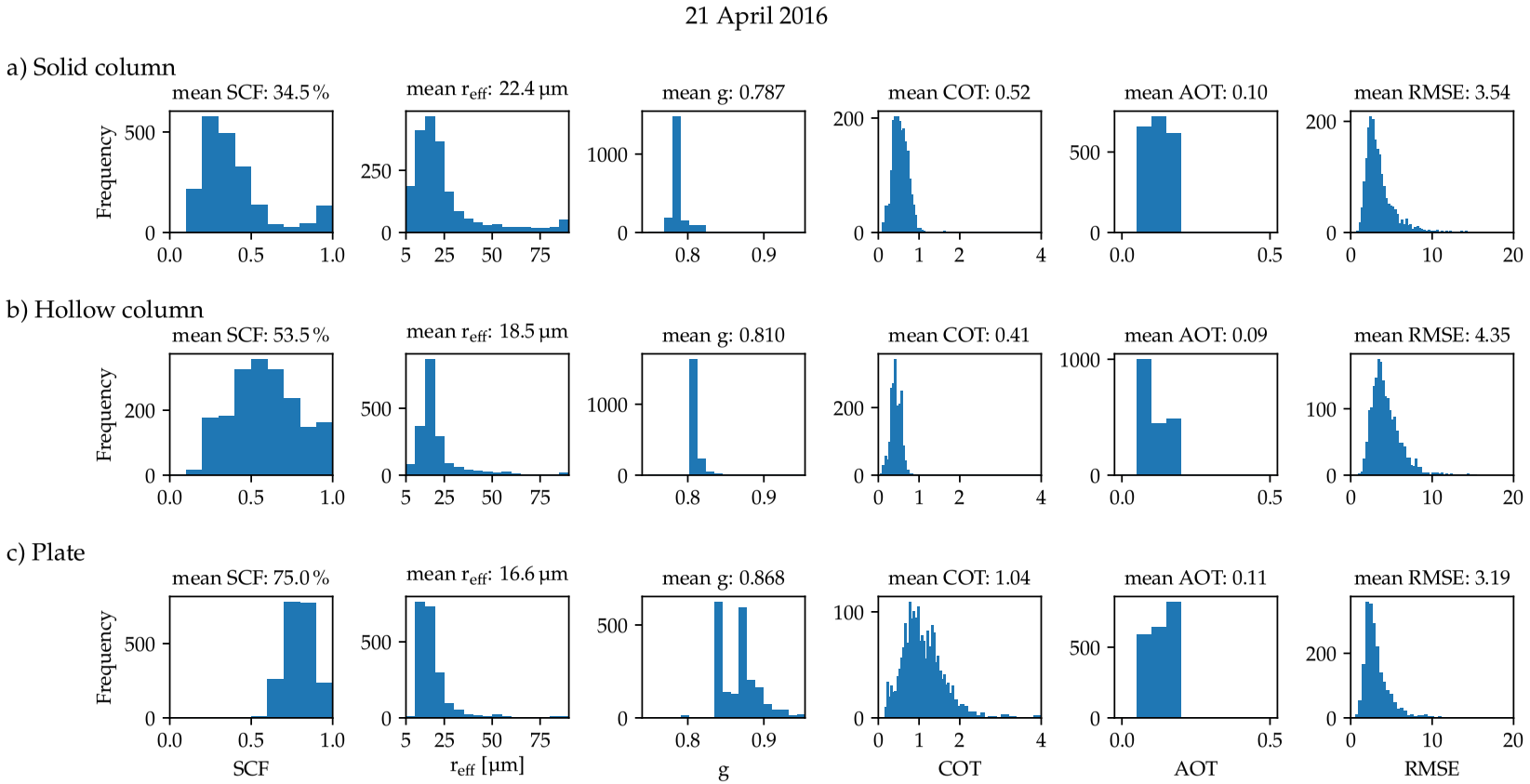

Figure 4.10: *Results of the RICO retrieval applied to the R-channel of the HaloCam$_{\mathrm{RAW}}$ images for 21 April 2016 using the YANG optical properties for (a) solid columns, (b) hollow columns, and (c) plates. The different panels show the frequency of occurrence for the LUT parameters as histograms for the smooth crystal fraction (SCF), effective radius (r_{eff}), asymmetry factor (g), cirrus optical thickness (COT), aerosol optical thickness (AOT), and the RMSE between LUT and measurement (from left to right). The results were filtered for* HR > 1 *to ensure that only image slices with* $22°$ *halo were analyzed and the uppermost image segment was excluded from the analysis to avoid applying the retrieval to upper tangent arcs.*

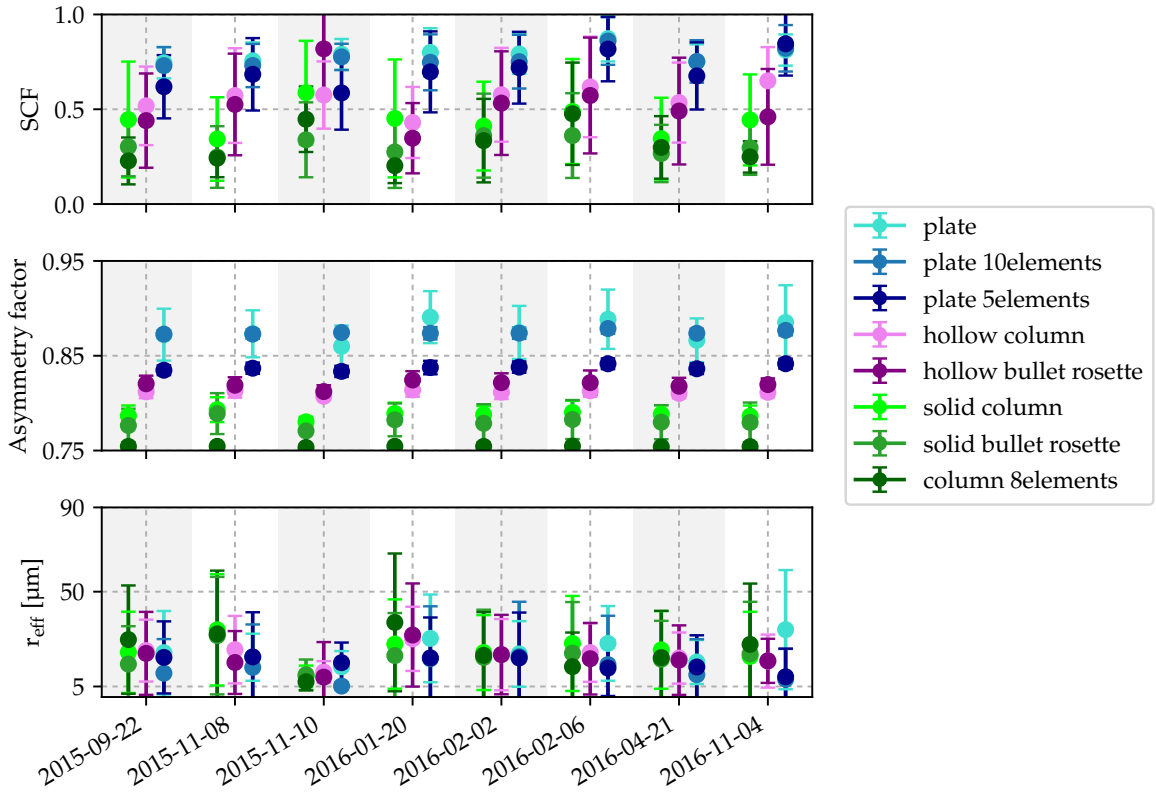

Figure 4.11: *Retrieval results for all 8 days listed in Table 4.8 and 8 habits of the YANG optical property database. Results are shown for the SCF (top), asymmetry factor (center), and effective radius (bottom) using the mean value within a 1σ confidence interval. Note that the underlying distributions might be asymmetric as depicted in Fig. 4.10. The colors are grouped into blue, pink and green to highlight the plate-like, hollow, and columnar ice crystals, respectively. Darker colors refer to more complex crystals.*

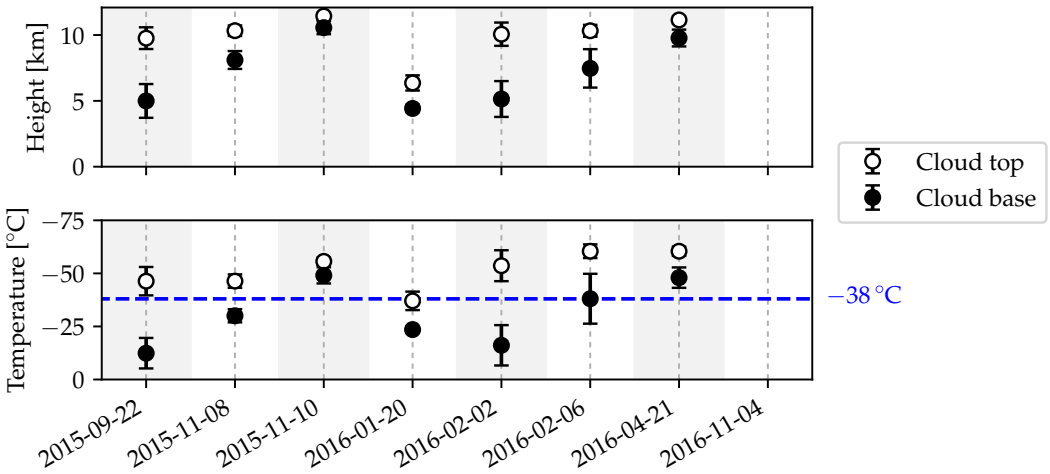

Figure 4.12: *Top: cloud top (circles) and base (dots) height was derived from cloud radar observations. Bottom: the corresponding temperature was estimated from radiosonde profiles launched at Oberschleißheim. The dashed blue line indicates the threshold for homogeneous nucleation at a temperature of −38 °C. The results are provided by the mean values within a 1σ confidence interval over the time periods with a visible 22° halo.*

(a) Plate

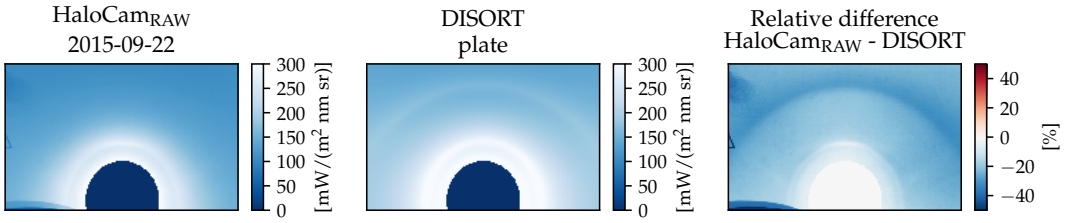

(b) 8-element column

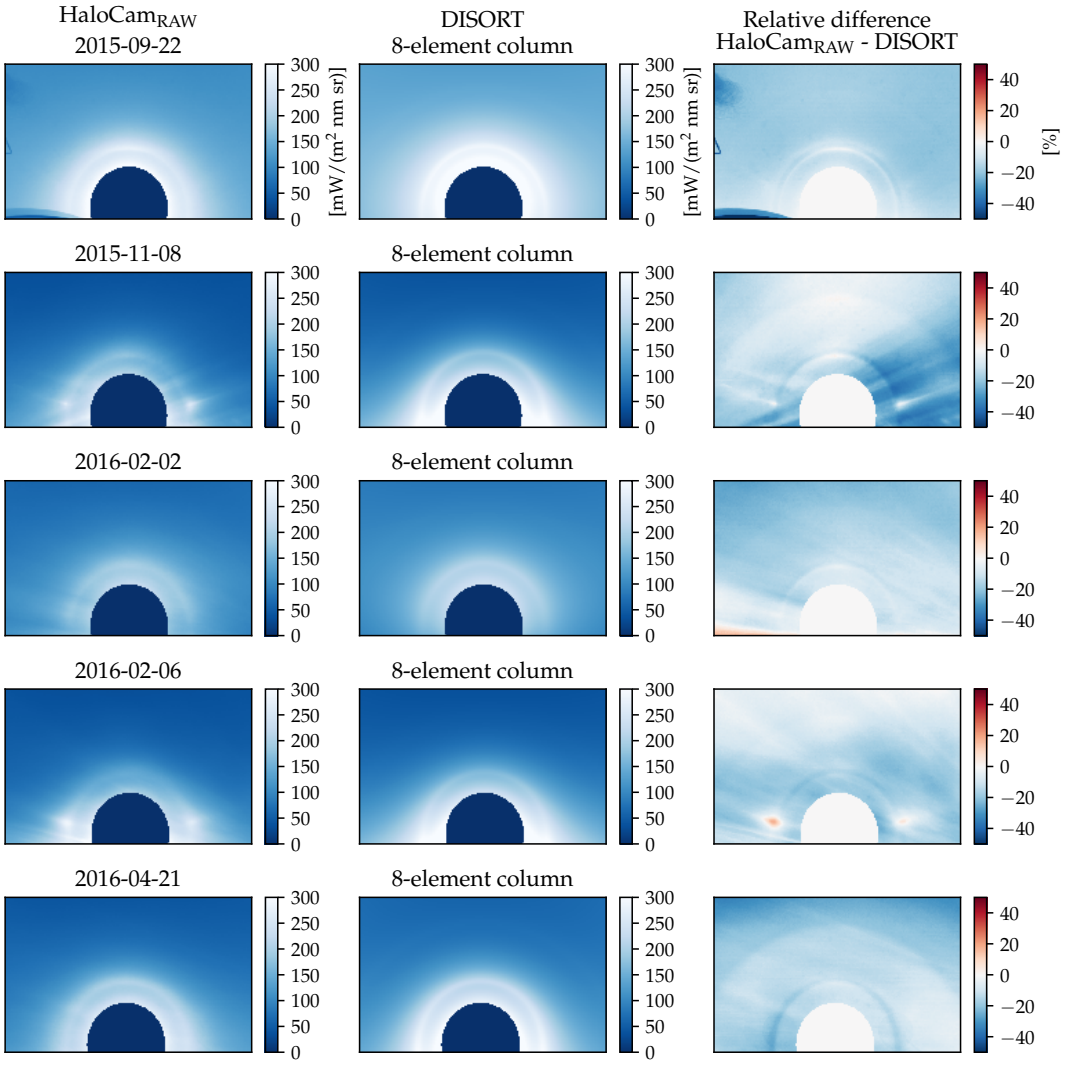

Figure 4.13: *Left: HaloCam$_{RAW}$ radiance of the R-channel averaged over all images containing a 22° halo for the respective day. Center: DISORT simulations using the retrieved best match ice crystal habit for the 22° halo region (a) and the best match habit for the whole scene (b). Right: relative difference between HaloCam$_{RAW}$ observations and the DISORT simulation.*

4.3 Considerations on ice crystal orientation

A significant fraction of cirrus clouds contains oriented ice crystals (Noel and Sassen, 2005, Noel and Chepfer, 2010, Zhou et al., 2012). The statistics of halo displays during the ACCEPT campaign (Section 4.1.1) revealed that the majority of halo displays was caused by oriented ice crystals. Sundogs and upper tangent arcs, which are formed by oriented plates and columns, were observed in 70% and 30% of the total observation time, respectively. 22° halos, which are produced by randomly oriented hexagonal crystals, were observed 60% of the time. Furthermore, 22° halos, sundogs, and upper tangent arcs often occurred simultaneously with a frequency of about 22% relative to the total observation time. This section presents first results of the observations during the ML-CIRRUS campaign (Voigt et al., 2017) with halo displays formed by oriented ice crystals. Using CrystalTrace, a method is proposed to derive the fraction of oriented ice crystal plates and columns from simultaneous observations of 22° halos and sundogs or upper tangent arcs.

4.3.1 Observation of oriented ice crystals during ML-CIRRUS

During the ML-CIRRUS campaign (Voigt et al., 2017) between March and April 2014 the novel High Altitude and Long Range Research Aircraft (HALO) was probing cirrus clouds in Europe with a unique set of instruments to characterize microphysical, optical, and radiative properties of the cirrus clouds and the atmospheric conditions. Based at and flying out of the German Aerospace Center (DLR) in Oberpfaffenhofen, southern Germany, several overpasses of the HALO research aircraft were performed over the Meteorological Institute of the LMU in Munich. During the campaign continuous measurements were performed with several instruments on the MIM rooftop platform. At this time HaloCam was operated with $\text{HaloCam}_{\text{JPG}}$ and a Canon Powershot G12 to record images in the uncompressed and unprocessed "raw" format. Additional measurements were performed with the specMACS imaging spectrometer. Continuous observations of the MIRA cloud radar are available both for zenith pointing measurements and scans. Moreover, lidar measurements were performed with the Portable Lidar System (POLIS, Heese et al. (2004)) and continuous sun photometer measurements are available both from the AERONET Cimel and the SSARA instruments.

On 1 April 2014 halo displays formed in a very homogeneous cirrus layer over Munich showing a 22° halo simultaneously with an upper tangent arc and sundogs which lasted for about 4 h. These halo displays were accompanied with a high aerosol concentrations due to transported Saharan dust (Voigt et al., 2017). Figure 4.14 (left) shows the recorded $\text{HaloCam}_{\text{JPG}}$ image from 8:25 UTC on 1 April 2014. The right side of Fig. 4.14 displays the same image filtered with an unsharp mask to highlight the optical features in the image. Besides the 22° halo and the upper tangent arc, the concave Parry arc on top of the tangent arc is clearly visible and was present for some minutes. This halo display is very rare and is formed by Parry oriented ice crystal columns. As explained in Sections 2.3 and 3.8, these ice crystal columns have a horizontal orientation, but in addition with a fixed orientation around their *c*-axis. Thus, they are only randomly oriented around their vertical axis. CrystalTrace was used to perform a radiative transfer simulation of the scene in Fig. 4.14 for the corresponding SZA of 57° at a wavelength of 500 nm which is shown in Fig. 4.15. As an estimate of the AOT, the daily average provided by AERONET was assumed which amounts to 0.48 at a wavelength of 500 nm. The desert aerosol type from the OPAC database was chosen (Hess et al., 1998). The simulation was performed for a COT of 1 and an ice crystal mixture of 45% randomly oriented columns which form the 22° halo, 10% oriented plates which cause the sundogs, 35% oriented columns which are responsible for the upper and lower tangent arcs, and 10% Parry oriented columns which form the upper Parry arc. The different ice crystal components were estimated to qualitatively reproduce the different halo displays visible in

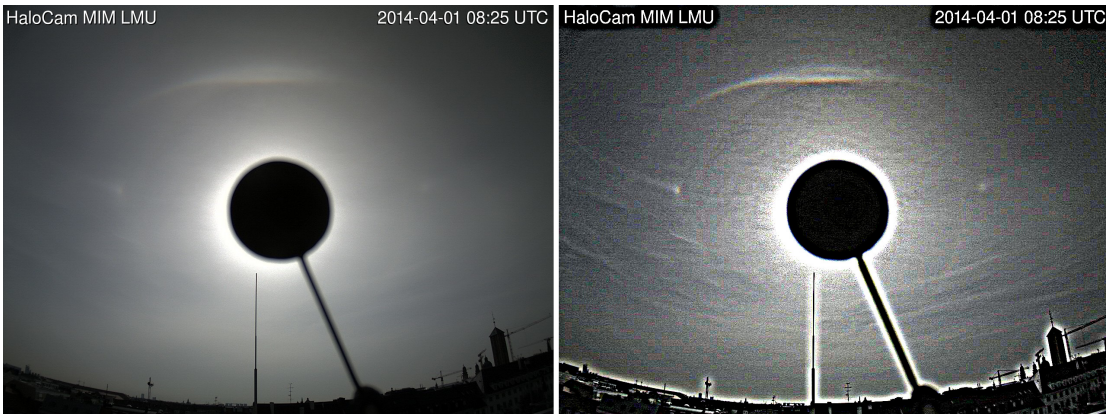

Figure 4.14: *HaloCam$_{\mathrm{JPG}}$ image from 1 April 2014 during the ML-CIRRUS campaign. Left: original HaloCam$_{\mathrm{JPG}}$ image with a faint 22° halo, both sundogs, an upper tangent arc and a concave Parry arc on top. Right: same image with an unsharp mask filter applied to better highlight the optical features. On the right image the Parry arc is clearly visible and even a faint circumhorizontal arc can be noticed which extends outwards from the left sundog.*

Fig. 4.14. As in Fig. 4.14, the Parry arc below the sun in Fig. 4.15 is not visible due to the large AOT and the long path through the atmosphere due to the low viewing zenith angles. Compared to Fig. 3.48, which was simulated for an aerosol-free atmosphere, Fig. 4.15 shows a strong forward scattering signal in the solar aureole region and the brightness of the halo displays is significantly reduced.

On 1 April 2014 the HALO research aircraft probed the cirrus clouds above MIM in Munich and flew two legs at different heights crossing the cirrus clouds exactly where the halo displays were visible from MIM. The flight path of the HALO aircraft is depicted in blue in Fig. 4.16 with light blue representing the flight path inside the cirrus cloud layer. The MIM in Munich is indicated by the green pin and the 22° halo, visible from MIM and projected on the cirrus layer, is indicated by the yellow ellipse (cf. Appendix A.2 for details on the calculation of the projection). Figure 4.16 shows the two overpasses of HALO over the institute inside the cirrus cloud passing through the cloud volume where the 22° halo should be visible. The first overpass crosses the 22° halo between 10:03 UTC and 10:05 UTC and the second overpass between 10:16 UTC and 10:18 UTC. The measurements of the Small Ice Detector Mark 3 (SID-3) were performed and evaluated by Martin Schnaiter and Emma Järvinen from KIT Karlsruhe (personal communication). The SID-3 instrument is described in Ulanowski et al. (2014) and is able to detect ice crystals in a size range of 5 to 50 µm. SID-3 allows to resolve single particle light scattering patterns which can be used to derive ice crystal complexity (Schnaiter et al., 2016). The SID-3 measurements during the first and lower leg (10:04 UTC) contained 83 well-exposed images. These images showed a halo feature in 16.9% and signatures of hexagonal crystals together with a halo feature in 3.6% of the images. In the second and higher leg 59 images were well-exposed and a halo feature was detected in 27.1% of the cases whereas 8.5% showed signatures of hexagonal crystals together with a halo feature. Only about 4% to 8% of the crystals showed signatures of a hexagonal structure in addition to a halo feature, corresponding to pristine hexagonal crystals with smooth crystal faces. Nevertheless, between about 17% and 27% of the in situ collected ice crystals were able to produce a 22° halo although their hexagonal structure was not as pronounced. Since the SID-3 data were collected simultaneously to the visible halo display, these results are another indication that already a small fraction of halo-producing ice crystals is sufficient to produce a visible halo display. For a future study it would be very interesting to compare these results with the ice crystal properties retrieved via remote sensing. However, before a quantitative retrieval of the

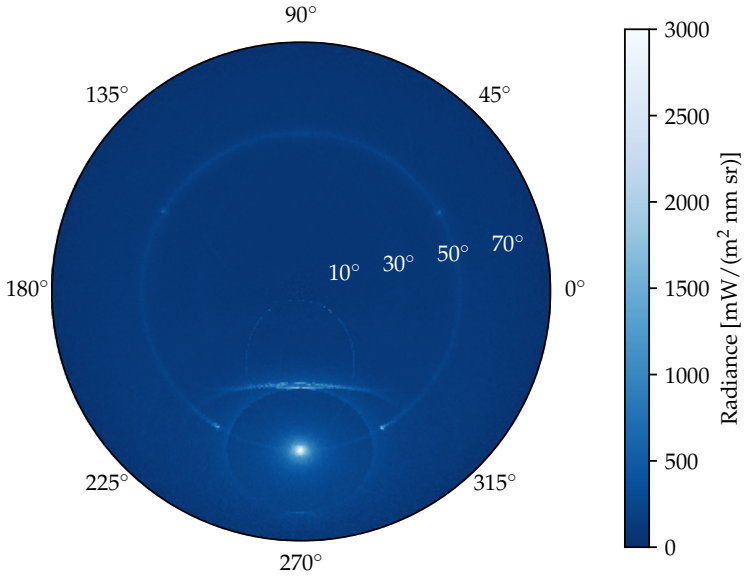

Figure 4.15: *CrystalTrace simulation of 1 April 2014 8:25 UTC at an SZA of* 57° *and a wavelength of* 500 nm. *The simulation was performed for 45% randomly oriented columns which form the* 22° *halo, 10% oriented plates which cause the sundogs, 35% oriented columns which are responsible for the upper and lower tangent arcs, and 10% Parry-oriented columns which form the upper Parry arc. A cirrus optical thickness of 1 was chosen and the aerosol was parameterized by the OPAC desert dust mixture with an AOT of 0.48 at* 500 nm, *which is the daily mean provided by AERONET.*

ice crystal optical and microphysical properties and orientation is possible, CrystalTrace needs to be extended with a parameterization of diffraction and ice crystal roughness. Furthermore, a parameterization of ice crystal optical properties has to be developed which allows to compare the ice crystal roughness retrieved via remote sensing with the ice crystal complexity derived from the SID-3 measurements.

To investigate whether and how the fraction of oriented ice crystals can be derived from observations of halo displays, simulations were performed using the CrystalTrace algorithm. The presented method assumes the presence of a 22° halo as a reference since it is formed only by randomly oriented ice crystals. Then, the fraction of oriented plates can be derived by comparing the brightness of the sundogs with the brightness of the 22° halo. An estimate of the fraction of oriented columns can be retrieved by comparing the brightness contrast, i.e. the halo ratio, of the upper tangent arc with the 22° halo. The fraction of oriented plates can be estimated by comparing the halo ratio of the sundogs with the halo ratio of the 22° halo. This method will be explained in more detail in the following sections.

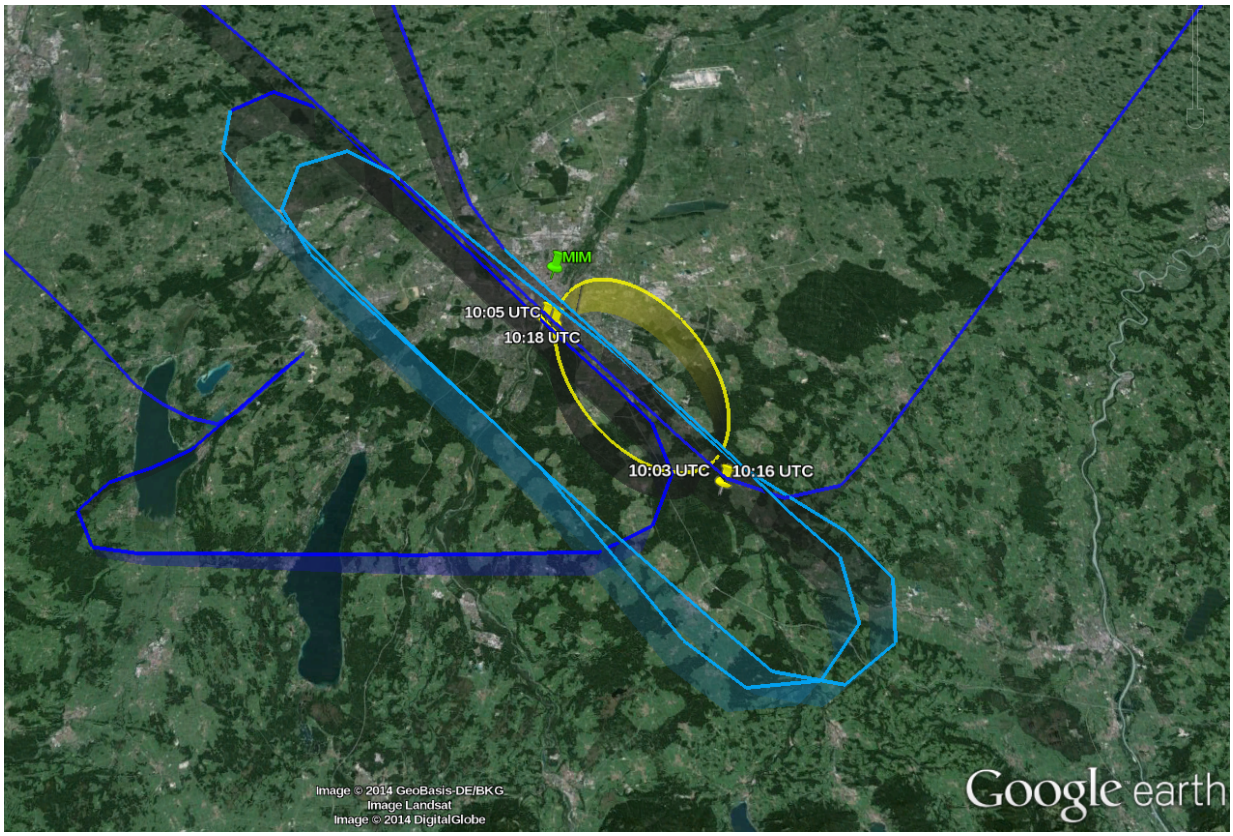

Figure 4.16: *Flight path of the HALO research aircraft on 1 April 2014 during the ML-CIRRUS campaign displayed in blue. The Meteorological Institute in Munich (MIM) is indicated by a green pin. The 22° halo visible from MIM is represented by the yellow ellipse, which was calculated using the equations described in Appendix A.2. The coordinates of the 22° halo were calculated for the respective position of the sun and the height of the cirrus cloud base, which was derived from radar measurements. The light blue sections of the HALO flight path indicate the location of the aircraft within the cirrus cloud with two overpasses over MIM at around 10:04 UTC and 10:17 UTC.*

4.3.2 Information content of sundogs

Sundogs together with a 22° halo were simulated with CrystalTrace for different fractions of randomly and oriented ice crystal plates with an aspect ratio of 0.5. The oriented ice crystal plates have a vertical *c*-axis and are oscillating with a standard deviation of 1° (cf. Section 3.8). To focus only on the effect of ice crystal orientation, an aerosol-free atmosphere was assumed. The simulations were performed for a wavelength of 550 nm, a solar zenith angle of 60° and a cirrus optical thickness of 0.8. Figure 4.17 displays the CrystalTrace simulations as polar plots for the upper hemisphere with the sun at a solar azimuth angle of 270° for an increasing fraction of oriented ice crystals. The cirrus cloud in Fig. 4.17a contains only randomly oriented plates which produce a 22° and a 46° halo. A fraction of oriented columns of 20% already shows both sundogs, the parhelic circle with the 120° parhelia and the circumzenithal arc above the sun. As the fraction of oriented crystals increases, the sundogs and other scattering features produced by the oriented crystals intensify. Simultaneously, the brightness of the 22° and 46° halo is decreasing. In this representation the 46° halo disappears at a fraction of 60% oriented plates while the 22° halo disappears at a fraction of 100% oriented ice crystal plates.

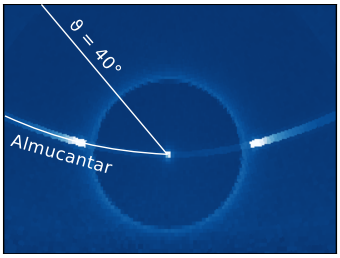

Figure 4.18: *CrystalTrace simulation for plates with an orientation fraction of 40% (cf. Fig. 4.17c) in image projection. The white lines indicate the almucantar plane and the relative azimuth angle $\vartheta = 40°$.*

The smooth crystal fraction can be estimated using the 22° halo ratio. To obtain an estimate of the fraction of oriented ice crystal plates, the ratio between the 22° halo ratio and the halo ratio of the sundogs can be compared, which will be denoted by $\mathrm{HR}_{\mathrm{random}}$ and $\mathrm{HR}_{\mathrm{oriented}}$, respectively. As illustrated in Fig. 4.18, the halo ratio of the sundogs is calculated in the almucantar plane whereas the 22° halo ratio is determined in the plane at a relative azimuth angle of $\vartheta = 40°$. Note that evaluating ratios of measured radiances does not require an absolute radiometric calibration of the camera (cf. Section 3.5.3). The radiance distributions in the almucantar plane and at $\vartheta = 40°$ are shown in Fig. 4.19a and Fig. 4.19b, respectively. Black lines represent the location of the halo minimum (dashed) and maximum (solid), which are used to calculate the halo ratio. The radiance distribution across the sundog and the brightness of the halo peak is increasing for a larger fraction of oriented plates. Figure 4.19b shows the radiance distribution across the 22° halo which is evaluated at a relative azimuth angle of $\vartheta = 40°$. The radiance distribution across the 22° halo and the brightness of the halo peak are both decreasing for a larger fraction of oriented plates. Figure 4.20 shows the halo ratio of the sundog ($\mathrm{HR}_{\mathrm{oriented}}$) in the almucantar plane (a), the halo ratio of the 22° halo ($\mathrm{HR}_{\mathrm{random}}$) at a relative azimuth angle of $\vartheta = 40°$ (b) and the HR factor (c), which is defined by $\mathrm{HR}_{\mathrm{oriented}}/\mathrm{HR}_{\mathrm{random}}$. The $\mathrm{HR}_{\mathrm{oriented}}$ of the sundog (a) is increasing for a larger fraction of oriented crystals while the $\mathrm{HR}_{\mathrm{random}}$ of the 22° halo is decreasing (b). The HR factor represents the factor by which the $\mathrm{HR}_{\mathrm{random}}$ is increased due to the presence of oriented crystals. Thus, the fraction of oriented ice crystal plates could be retrieved by calculating this factor from the measurement and comparing it to a look-up table of pre-calculated factors. Besides the fraction of oriented crystals, the enhancement factor depends on the orientation parameter, the ice crystal roughness, and the solar zenith angle.

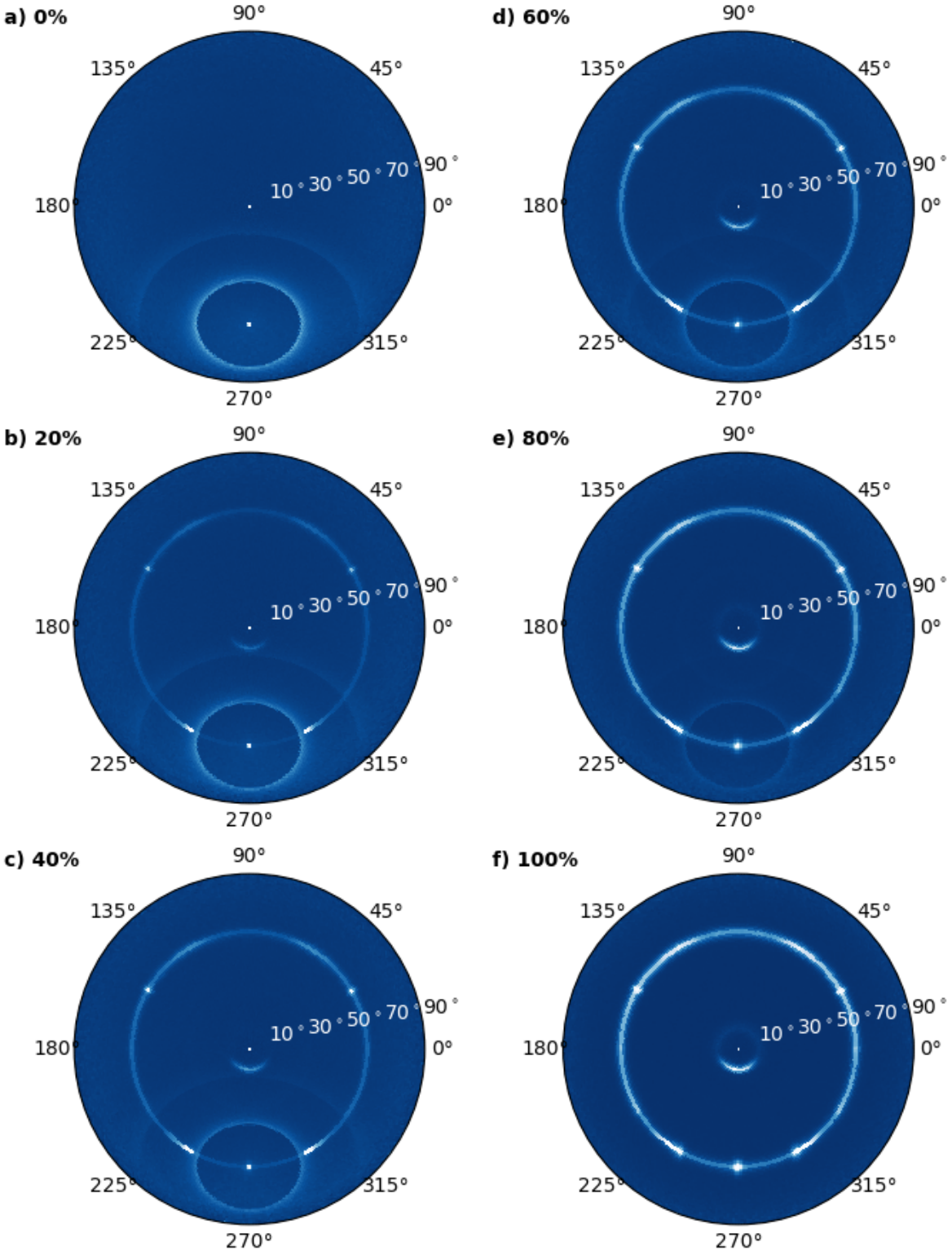

Figure 4.17: *Radiative transfer simulations of a cirrus cloud containing ice crystal plates using libRadtran's MYSTIC solver combined with CrystalTrace for 10^7 photons. An SZA of 60° and an azimuth angle of 270° were chosen. A cirrus optical thickness of 0.8 and an aspect ratio of 0.5 were chosen for the ice crystal plates. The simulations were performed for different fractions of randomly oriented ice crystals and ice crystals oriented with a vertical c-axis with a distortion parameter of 1°. The fraction of oriented crystals increases from 0% in (a) to 100% in (f).*

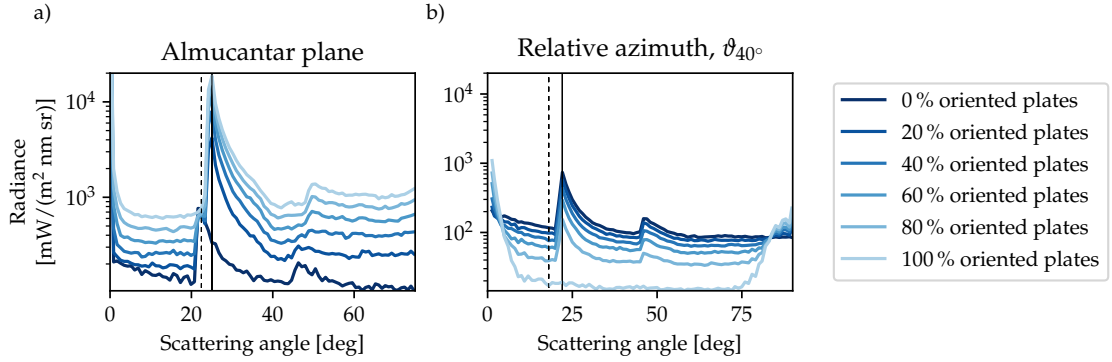

Figure 4.19: *Radiance distributions extracted from Fig. 4.17 (a) in the almucantar plane and (b) between the almucantar and principal plane at $\vartheta = 40°$ for an increasing fraction of oriented ice crystal plates (AR = 0.5) at a wavelength of 550 nm. The radiance distribution in (a) shows the cross section of the 22° halo and the right sundog, which occurs at a scattering angle of about 25°. (b) Radiance distribution across the 22° and 46° halo. Black lines indicate the maximum (solid) and minimum (dashed) of each halo display in the vicinity of the 22° halo.*

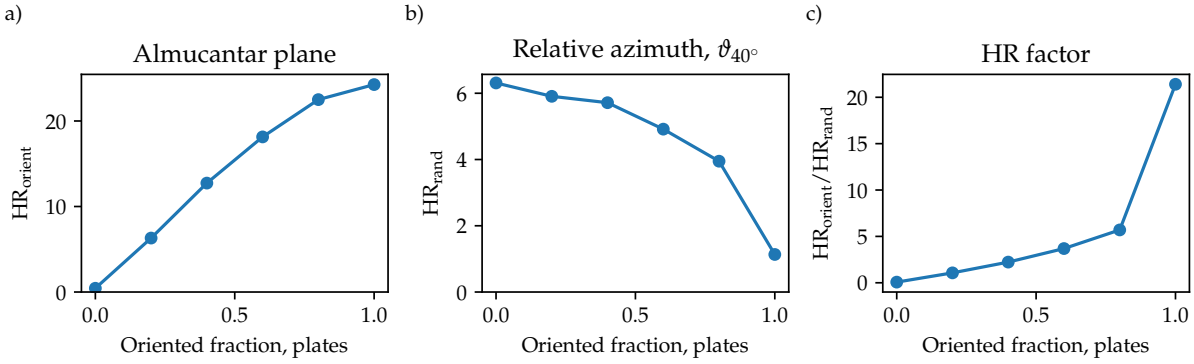

Figure 4.20: *Halo ratios calculated using the maximum and minimum radiance values of the halo peak cross section indicated by the black lines in Fig. 4.19 as a function of the oriented crystal fraction. (a) Halo ratio of the sundogs in the almucantar plane as a measure of the fraction of oriented ice crystal plates, denoted by $HR_{oriented}$. (b) Halo ratio of the 22° halo at $\vartheta = 40°$ as a measure of the randomly oriented crystal fraction, labeled with HR_{random}. (c) Halo ratio enhancement factor, calculated by $HR_{oriented}/HR_{random}$.*

4.3.3 Information content of upper tangent arcs

A 22° halo together with an upper tangent arc were simulated with CrystalTrace for different fractions of randomly and oriented ice crystal columns with an aspect ratio of 2.5. The oriented ice crystal columns have a horizontal c-axis and are oscillating with a standard deviation of 1°. The simulations were performed for a wavelength of 550 nm, a solar zenith angle of 60° and a cirrus optical thickness of 0.8 similar to Fig. 4.17. Figure 4.21 shows polar plots of the upper hemisphere with the sun at a solar azimuth angle of 270° for an increasing fraction of oriented ice crystals. The cirrus cloud in Fig. 4.21a contains only randomly oriented columns which produce a 22° halo and a faint 46° halo. A fraction of oriented crystals of 20% already shows the upper and lower tangent arc. As the fraction of oriented columns increases, the brightness of the upper and lower tangent arc increases and the wings of the arcs become more pronounced. Starting from an oriented crystal fraction of 40% the circumhorizontal arc is visible in this representation.

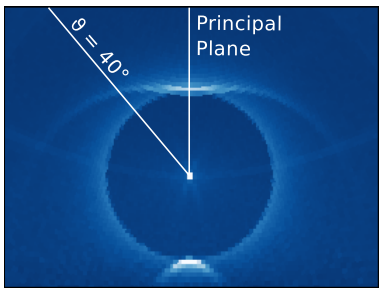

Figure 4.22: *CrystalTrace simulation for solid columns with an orientation fraction of 40% (cf. Fig. 4.21c) in image projection. The white lines indicate the principal plane and the relative azimuth angle $\vartheta = 40°$.*

Similar to Fig. 4.17 the 22° halo is still visible for 80% oriented columns and the upper and lower tangent arc are visible already for a fraction of 20% oriented crystals in this representation.

The smooth crystal fraction can be estimated using the 22° halo ratio. Then, the fraction of oriented ice crystal columns can be estimated by comparing the halo ratio of the upper tangent arc in the principal plane, i.e. at $\phi = \phi_0$, with the halo ratio of the 22° halo at a relative azimuth angle of $\vartheta = 40°$, as depicted in Fig. 4.22. Figure 4.23a shows the radiance distribution across the upper tangent arc in the principal plane, whereas Fig. 4.23b displays the radiance distribution across the 22° halo at a relative azimuth angle of $\vartheta = 40°$. The corresponding halo ratios are presented in Fig. 4.24a for the upper tangent arc ($HR_{oriented}$) and in Fig. 4.24b for the 22° halo (HR_{random}). For the upper tangent arc an enhancement factor of the halo ratio can be calculated from the fraction of $HR_{oriented}/HR_{random}$ as shown in Fig. 4.24c. Similar to the case of oriented plates, the halo ratio of the upper tangent arc increases with larger fractions of oriented crystals and the HR of the 22° halo decreases. Since the halo ratio of the oriented crystals $HR_{oriented}$ is much larger than HR_{random}, the enhancement factor is increasing.

This approach assumes that the ice crystals forming the 22° halo and the upper tangent arc or sundogs have the same shape and aspect ratio. This is not necessarily the case. When sundogs and a 22° halo are visible simultaneously they might be produced by the same ice crystals, one part of the ice crystal population being oriented and the other part randomly oriented. This might occur due to localized turbulence in the air. However, it is more likely that the ice crystals, which are responsible for the sundogs and tangent arcs, are oriented since they are larger and have more extreme aspect ratios compared to the crystals forming the 22° halo. To account for this, LUTs have to be compiled for the enhancement factor assuming mixtures of different ice crystal populations.

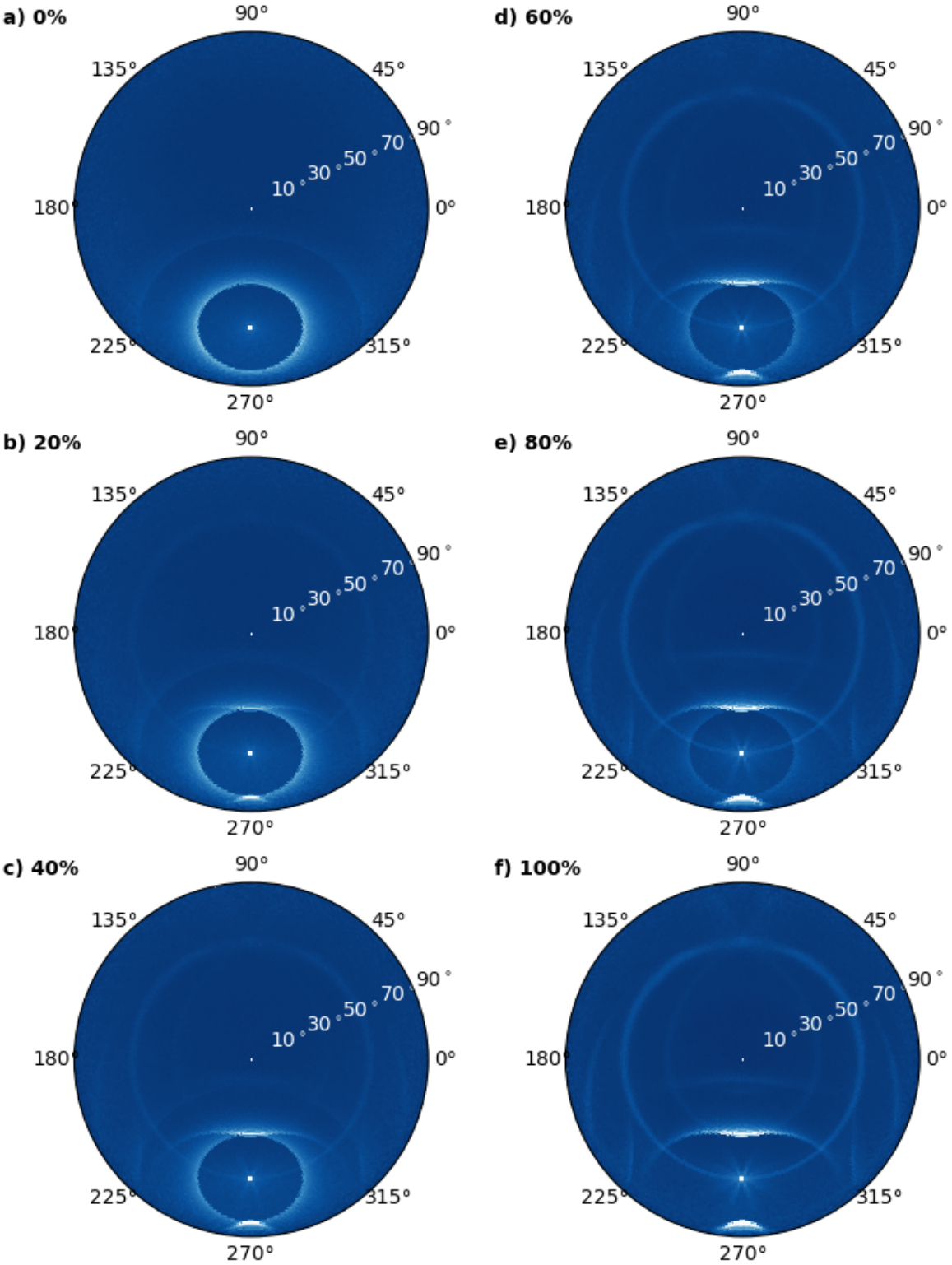

Figure 4.21: *As Fig. 4.17 but for ice crystal columns with an aspect ratio of 2.5. Randomly oriented columns were mixed with columns oriented with a horizontal c-axis and a distortion parameter of 1°. The fraction of oriented crystals increases from 0% in (a) to 100% in (f).*

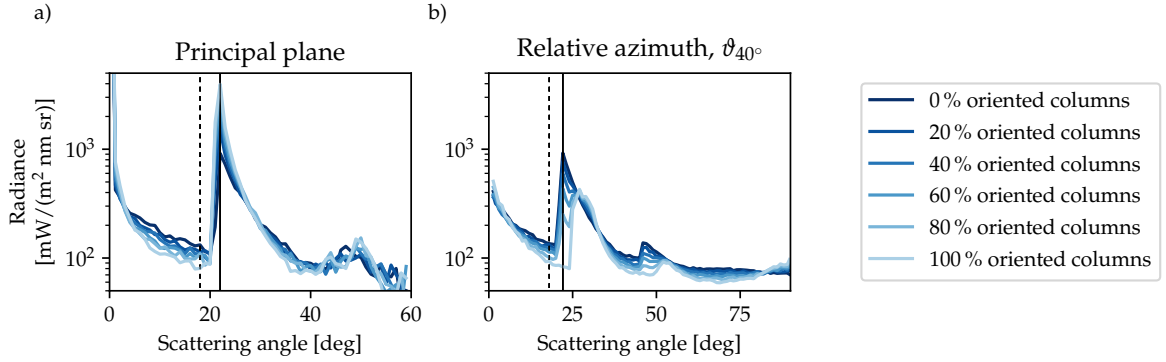

Figure 4.23: *Radiance distributions extracted from Fig. 4.17 (a) in the principal plane and (b) between the almucantar and principal plane at $\vartheta = 40°$ for an increasing fraction of oriented ice crystal columns (AR = 2.5) at a wavelength of 550 nm. The radiance distribution in (a) shows the cross section of the upper tangent arc, which occurs at the same scattering angle as the 22° halo. (b) Radiance distribution across the 22° and 46° halo. Black lines indicate the maximum (solid) and minimum (dashed) of each halo display in the vicinity of the 22° halo.*

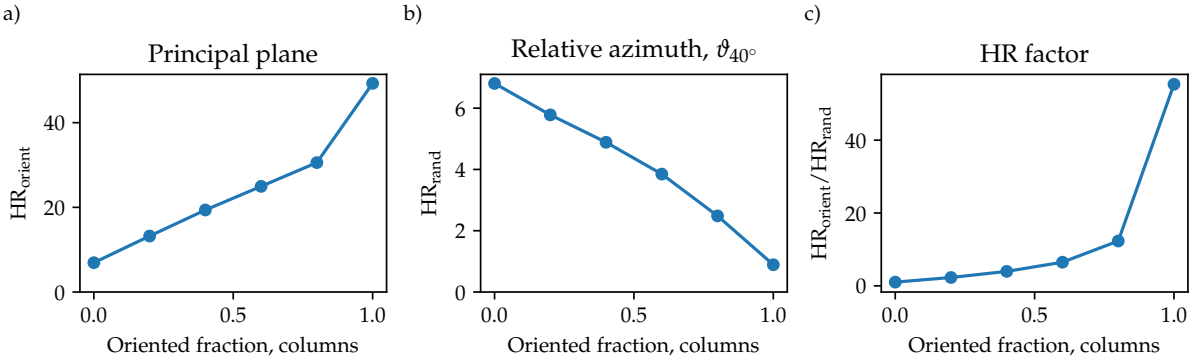

Figure 4.24: *Halo ratios calculated using the maximum and minimum radiance values of the halo peak cross section indicated by the black lines in Fig. 4.23 as a function of the oriented crystal fraction. (a) Halo ratio of the upper tangent arc in the principal plane as a measure of the fraction of oriented ice crystal columns, denoted as HR_{orient}. (b) Halo ratio of the 22° halo at $\vartheta = 40°$ as a measure of the randomly oriented crystal fraction, labeled with HR_{rand}. (c) Halo ratio enhancement factor, calculated by HR_{orient}/HR_{rand}.*

Chapter 5

Discussion

In the following the results of this study results will be further discussed and compared with the literature. Previous studies retrieved information about ice crystal shape and surface roughness, to the author's knowledge, only using space-borne remote sensing. Passive remote sensing from space of optically thin clouds over land is challenging since the measured reflectances are very sensitive to the surface albedo. While the BRDF of the ocean is well-known, it is highly variable over land surfaces. Thus, over land the majority of ice crystal shape and roughness retrievals based on passive remote sensing techniques focuses on optically thicker ice clouds. Moreover, space-borne observations of ice clouds might also include the ice phase of (deep) convection, e.g. anvils of thunderstorms. Ground-based remote sensing of halo displays focuses on rather thin cirrus clouds instead with a cirrus optical thickness (COT) smaller than about 5 (Gedzelman and Vollmer, 2008). It should also be kept in mind that the results of this study were obtained from local measurements in Munich in contrast to the space-borne observations which have a global coverage.

Ice crystal roughness

Long-term HaloCam observations in Munich revealed that about 25% of the cirrus clouds produced a 22° halo. This fraction might be slightly larger when considering other halo types, such as sundogs and upper tangent arcs as well. A visual evaluation of the 6-week HaloCam dataset during the ACCEPT campaign resulted in about 27% halo-producing cirrus clouds, accounting for all three halo types. Thus, the majority (∼73%) of cirrus clouds most likely contains predominantly rough or complex ice crystals which do not produce a visible halo.

These findings are in agreement with the results of several studies based on satellite retrievals. Using multi-angle reflectance measurements, Baran et al. (1998, 1999) and McFarlane and Marchand (2008) found polycrystals and complex crystals to better represent the observations than pristine single crystals. Studies based on multi-angular polarized reflectances from POLDER (Polarization and Directionality of Earth Reflectance) also report that featureless phase functions, which correspond to roughened or complex crystals, better represent the measurements than phase functions of a single ice crystal habit (Descloitres et al., 1998, Chepfer et al., 2001, Baran et al., 2001, Baran and Labonnote, 2006, Sun et al., 2006). Holz et al. (2016) and Wang et al. (2014) confirmed that rough and complex crystals better match the observations than smooth single crystals for optically thin clouds (COT < 3) using retrievals based on lidar observations and reflectances in the infrared spectrum.

Ice crystal shape

This study revealed that the overall best matching ice crystal habits are solid columns and 8-element columns with a smooth crystal fraction (SCF) of $(40 \pm 20)\,\%$ and $(30 \pm 20)\,\%$ and asymmetry factors at 618 nm between 0.75 and 0.79, respectively. Although plates best match the $\text{HaloCam}_{\text{RAW}}$ observations in the region of the 22° halo, they produce a pronounced 46° halo for the retrieved effective radii with a mean value of 20 µm, which was not visible in the evaluated $\text{HaloCam}_{\text{RAW}}$ scenes.

Ice crystal columns and aggregates of columns were also found by Holz et al. (2016), however without any smooth crystals, resulting in an asymmetry factor of about 0.75 in the mid-visible spectrum. Also Wang et al. (2014) retrieved a mixture with a dominating fraction of columnar crystals to best match the MODIS and CALIPSO observations over ocean with a SCF of 10% and an asymmetry factor of 0.778 at a wavelength of 0.65 µm. These retrievals were performed for COT < 3 which is comparable to the optical thickness range observed in this work. It is interesting to note that the 8-element column, which is the overall best matching ice crystal habit in this work, is the same as for the MODIS Collection 6 data product used for the operational retrieval of ice cloud optical thickness and effective radius (Platnick et al., 2017).

Several other studies found plate-like or compact ice crystals to better represent the observations than columns, for example McFarlane and Marchand (2008), van Diedenhoven et al. (2012, 2013), Cole et al. (2014). However, these studies focus on optically thick cirrus, in particular anvil cirrus, with potentially very different formation mechanisms compared to thin halo-producing cirrus clouds. Um et al. (2015) studied aspect ratios of natural ice crystals, which were collected during field campaigns by a cloud particle imager, for temperatures between 0 °C and −87 °C and found that synoptic cirrus is dominated by columnar crystals, while anvil cirrus contains a larger fraction of plate-like crystals. All evaluated $\text{HaloCam}_{\text{RAW}}$ observations showed synoptic cirrus or contrail cirrus and did not contain any anvil cirrus. Columnar ice crystals were found to best match these $\text{HaloCam}_{\text{RAW}}$ observations, which is in agreement with the findings of Um et al. (2015).

Ice crystal plates of the Yang et al. (2013) database produce a pronounced 46° halo for the retrieved effective radii which was not visible in the $\text{HaloCam}_{\text{RAW}}$ observations. A possible explanation could be that the parameterization of aspect ratio and size for ice crystal plates used in Yang et al. (2013) does not represent the shapes of the observed ice crystals which produced a 22° halo without a 46° halo.

Ice crystal size

The retrieved effective radii in this study are, to the author's knowledge, the first observational results for 22° halos and yield similar results for all 8 ice crystal habits with 90% of the raii being smaller than 40 µm and with a mean value of 20 µm. Several studies (e.g. Mishchenko and Macke (1999), Fraser (1979), Garrett et al. (2007)) investigated the size range in which ice crystals actually produce a 22° halo based on theoretical and analytical considerations for single crystals. A lower boundary for ice crystal maximum dimensions of about 10 µm was found based on an analysis of the 22° and 46° halo in scattering phase functions of Yang and Liou (1996) and Yang et al. (2000). This lower boundary is in agreement with the results from the laboratory studies of Sassen and Liou (1979). Another criterion for the formation of a 22° and 46° halo is random orientation. This occurs for compact ice crystals with maximum dimensions smaller than about 100 µm. Ambiguities might occur since aggregated ice crystals such as bullet rosettes can be oriented while their components are randomly oriented relative to each other (Fraser, 1979, Sassen et al., 1994, Tape, 1994). Another indication for this upper size limit are the findings of

Mishchenko and Macke (1997) who report that air bubbles develop in larger ice crystals, which cause the 22° halo to fade. Furthermore, Bailey and Hallett (2002) state that pristine shapes are mostly found in the laboratory for maximum dimensions smaller than about 100 µm. Um and McFarquhar (2015)[1] determined minimum size parameters for the formation of 22° halos as a function of the aspect ratio (AR) resulting in $\chi = 45$ for compact particles (AR = 1), $\chi = 103$ for plates with AR = 0.1, and $\chi = 182$ for columns with AR = 4. The 46° halo forms starting from size parameters of $\chi = 68$ for plates (AR = 0.5), $\chi = 45$ for compact crystals, and $\chi = 223$ for columns (AR = 2). Unfortunately, these results are difficult to compare since the effective radius is defined for an ensemble of crystals accounting for different shapes, whereas ice crystal maximum dimension and size parameter are defined for single particles. However, global observations of ice cloud effective radii are available from the MODIS Collection 6 (Yi et al., 2017), which range between 30 µm to 35 µm over land in the northern mid-latitudes. These values are slightly larger than the mean effective radius retrieved for ice crystals producing a 22° halo with about 20 µm.

[1]It should be noted that the term "circumscribed halo" was used in Um and McFarquhar (2015) as a collective term for the 22° and 46° halo. However, it is the correct term for the halo which is formed by horizontally oriented ice crystal columns at high solar elevations, when upper and lower tangent arcs merge. This halo type is very different from the investigated 22° and 46° halo which are formed by randomly oriented crystals.

Chapter 6

Summary and Conclusions

The overarching aim of this thesis was to investigate the information content of halo displays regarding ice crystal properties. The main focus lies on the 22° halo which is formed by randomly oriented hexagonal ice crystals. It can be concluded that the brightness contrast and width of the 22° halo contains valuable information on ice crystal size, shape, and surface roughness.

Using optical properties calculated with an improved version of the raytracing code described in Macke et al. (1996) (GO), it was demonstrated that the brightness contrast of 22° halo, i.e. the halo ratio, is monotonically increasing from thin plates (AR $<$ 1) over compact particles (AR $=$ 1) to long columns (AR $>$ 1). It could be confirmed that the 22° and 46° halo ratio is determined by the ice crystal aspect ratio and surface roughness as shown in van Diedenhoven (2014). Analysis of the 22° halo ratio further revealed that the relationship between the ice crystal AR and the 22° halo ratio is ambiguous in the sense that smooth plates can produce an equally bright 22° halo as roughened columns.

Based on the optical properties of the Yang et al. (2013) database (YANG), it was demonstrated that the width of the 22° halo is related to the size of the ice crystals as suggested by Flatau and Draine (2014). Two different parameters were investigated: the power spillover index, which is a measure of the amount of light scattered into the region inside the 22° halo, and the full width at half maximum (FWHM) as a measure of the angular width of the halo peak. While the power spillover index proved to be a useful estimate of ice crystal size for scattering phase functions, it is very sensitive to the cirrus optical thickness under multiple scattering conditions. However, the sensitivity of the FWHM on the optical thickness revealed to be negligible.

With help of radiative transfer simulations it was demonstrated that the 22° halo ratio depends on the cirrus and aerosol optical thickness and to a minor degree on the surface albedo. Besides the ambiguity between columns and plates, the cirrus optical thickness (COT) introduces another ambiguity to the halo ratio. The halo ratio reaches a maximum when the cirrus optical thickness is larger than the background, i.e. Rayleigh and aerosol optical thickness (AOT).

The novel sun-tracking camera system HaloCam allows an automated observation of halo displays and collection of a long-term database of halo observations. The HaloCam system is weather-proof and consists of two cameras on a sun-tracking mount which ensures that the halo displays stay centered relative to the camera. The most frequent halo displays are formed by either randomly oriented or oriented plates and columns and therefore contain the most important information about ice crystal properties. Thus, the camera setup was optimized for observing 22° halos, sundogs and upper/lower tangent arcs with high spatial and temporal resolution without loosing relevant information. The HaloCam camera system was installed in September 2013 on the rooftop platform of the Meteorological Institute in Munich, first operating $\text{HaloCam}_{\text{JPG}}$ only, followed by $\text{HaloCam}_{\text{RAW}}$ in September 2015.

In a first analysis the frequency of the 22° halo produced by cirrus clouds over Munich was in-

vestigated using more than 2.5 years of $\text{HaloCam}_{\text{JPG}}$ data. For evaluating the long-term HaloCam observations in Munich an automated halo detection algorithm, called HaloForest, was developed. HaloForest is employed in this thesis for the detection of 22° halos but it can be extended for the detection of other halo types such as sundogs and upper/lower tangent arcs. Applied to the more than 2.5 years of data, HaloForest detected 22° halos about 2% of the total observation time during daylight.

The frequency of cirrus clouds which were accompanied by halo displays was evaluated for long-term HaloCam observations in Munich. Co-located ceilometer measurements were used to evaluate the fraction of cirrus clouds. About 25% of the detected cirrus clouds occurred together with a 22° halo. Extending HaloForest for more halo types (e.g. sundogs) would increase the fraction of "halo-producing" cirrus clouds above 25%. During the 6-week ACCEPT campaign the frequency of halo displays was evaluated visually and revealed that sundogs occurred in 70%, 22° halos in 60%, and upper tangent arcs in 30% of the total halo observation time. The fraction of halo-producing cirrus clouds amounts to about 27% for this dataset.

To estimate the ice crystal optical and microphysical properties, the RICO (Retrieval of Ice Crystal prOperties) retrieval was developed. This retrieval compares measured radiance distributions across the 22° halo with look-up tables of radiative transfer simulations, which were calculated for a range of ice crystal optical and microphysical properties. Additional sun photometer measurements are used to constrain COT and AOT. To achieve continuous roughness levels, the optical properties of smooth and severely roughened ice crystals of a specific habit were mixed with smooth crystal fractions (SCFs) ranging from 0% to 100%. Sensitivity tests showed that if the retrieval is applied to uncalibrated measurements with unknown radiometric response, the retrieved SCF can deviate up to 70% from the true value. If the uncertainty of the radiometric response is smaller than 15%, the error in the retrieved SCF is smaller than about 15%. A reasonable absolute calibration is therefore required to retrieve quantitative results of the ice crystal properties.

The RICO retrieval was tested using specMACS calibrated radiance measurements of a 22° halo for two case studies on 24 March and 22 September 2015. The total measurement uncertainty of specMACS was estimated to less than 5% (Ewald et al., 2015). By applying the retrieval to these well characterized observations, the potential of the retrieval to constrain the variability of ice crystal properties was assessed. It was found that several ice crystal habits and SCFs match the observations within the measurement error. Plate-like crystals with a large SCF and columnar crystals with a small SCF could reproduce the same 22° halo within the measurement uncertainty. This result confirms the findings from the analysis of the single scattering properties. Furthermore, the results indicate that the more pronounced the 22° halo, the better constrained the retrieved ice crystal properties. If no 22° halo was visible, the retrieved SCF was smaller than about 40% for plate-like crystals and smaller than about 10% for columnar crystals. The droxtal habit did not match the observations for any of the case studies. The best matching habits were solid columns on 24 March and 5-element plates on 22 September 2015 with effective radii of 5 µm and 20 µm.

In addition to the YANG optical properties the GO optical properties were tested for the case study on 24 March 2015, which are based on the geometric optics approximation. It revealed that for each aspect ratio a corresponding SCF could be found to represent the observations within the measurement uncertainty. A best match was retrieved for columnar crystals with AR = 3.5 and a SCF of 10% at 12:50 UTC and plate-like crystals with AR = 0.3 and a SCF of 75% at 12:54 UTC. These results differ from the ice crystal habits retrieved with YANG. The conventional geometric optics method has several shortcomings for small ice crystals. Um et al. (2015) showed that phase functions calculated with geometric optics methods significantly differ

from phase functions calculated with exact methods even if ice crystal sizes are large enough to produce a 22° halo.

Another test was performed using radiative transfer simulations of ice crystal mixtures of different habits, SCFs, and effective radii. The best match consists of 50% smooth and 35% rough 10-element plates, 8% smooth droxtals, and 5% rough solid columns. The remaining ice crystal habits sum up to 2%. This test demonstrated that arbitrary mixtures of multiple ice crystal habits, surface roughness, and size might yield a better representation than a single habit with smooth and rough crystal fraction. However, the retrieved habit mixtures are "radiatively equivalent effective shapes", as stated by McFarlane and Marchand (2008) and Cole et al. (2013). Thus, allowing for arbitrary mixtures of ice crystal properties does not necessarily increase the information gain.

As specMACS is not weather-proof, long-term observations of ice crystal optical and microphysical properties were performed using $\text{HaloCam}_{\text{RAW}}$. This camera provides the "raw" signal directly from the sensor and was geometrically and radiometrically calibrated. For the retrieval the red channel was used with an absolute radiometric uncertainty of less than 15%. HaloForest was used to select HaloCam images with a 22° halo. For 8 days in total, 22° halo observations with simultaneous sun photometer measurements were available which are necessary to constrain both AOT and COT. The retrieval was applied to a total of about 4400 $\text{HaloCam}_{\text{RAW}}$ images and the best matching ice crystal microphysical and optical properties were analyzed. The results showed that the average SCF for columnar, hollow, and plate-shaped crystals amounts to about ∼30%, ∼60%, and ∼80%, which is about 20% (solid columns) to 40% (plates) larger than the minimum SCF estimated from single scattering properties (van Diedenhoven, 2014). The variation of the retrieved effective radii between the ice crystal habits is much smaller than for the SCF and yields an overall mean of about 20 µm. The underlying distribution of the retrieved effective radii is skewed towards smaller values with more than 90% of the radii being smaller than 40 µm. Comparing the retrieved ice crystal effective radii with the temperature of cloud base and top revealed that the smallest crystals were retrieved for the coldest cloud base temperature. This is in agreement with in-situ observations which found the smallest crystals at the coldest temperatures close to cloud top (Baran, 2012). Although ice crystal plates with a SCF of (80 ± 10) % best match the observations in the angular region of the 22° halo, the YANG optical properties would produce a pronounced 46° halo for effective radii smaller than about 50 µm, which is not visible in the evaluated HaloCam images. Filtering the LUT for elements without a 46° halo yields solid columns and 8-element columns as best matching ice crystal habits with an average SCF of (40 ± 20) %, an average effective radius of (23.8 ± 13.4) µm and an asymmetry factor of 0.788 ± 0.008. This result is in agreement with satellite-based retrievals for optically thin cirrus which find aggregates of columns as best matching ice crystal habit (Wang et al., 2014, Holz et al., 2016).

During the ML-CIRRUS campaign HaloCam observations on 1 April 2014 showed complex halo displays lasting for several hours with a rare Parry arc visible for a few minutes. Additional measurements during this campaign were performed with the MIRA-35 cloud radar, the POLIS lidar, the CHM15kx ceilometer and the Cimel and SSARA sun photometers, as well as with the hyperspectral imaging spectrometer specMACS. A unique dataset could be collected which is complemented by in situ observations during two overpasses of the HALO research aircraft. The halo displays on 1 April indicate the presence oriented ice crystals. To allow for radiative transfer simulations of oriented ice crystals the Monte Carlo radiative transfer model MYSTIC was extended by the raytracing algorithm CrystalTrace. A method was suggested to retrieve the fraction of oriented ice crystal plates (columns) from simultaneous observation of the 22° halo and sundogs (upper tangent arc). While the halo ratio of the 22° halo serves as a reference for

the fraction of halo-producing crystals, the halo ratio of the sundogs or upper tangent arc relative to the halo ratio of the 22° halo should contain information about the fraction of oriented ice crystals.

This work demonstrates that halo displays contain valuable information about ice crystal properties such as ice crystal shape, surface roughness, size and orientation. With the new automated camera system HaloCam and the halo detection algorithm HaloForest this study provides, for the first time to the author's knowledge, a framework for consistent and automated observations of halo displays. By applying the RICO retrieval to long-term observations of calibrated radiances, HaloCam allows for the first time to systematically investigate typical ice crystal properties of halo-producing cirrus clouds. These observations contribute to an improved understanding of ice crystal optical and microphysical properties. Implemented on different sites, HaloCam in combination with the HaloForest detection algorithm can provide a consistent dataset for climatological studies of ice crystal properties representing typical cirrus clouds. Representative ice crystal optical properties are required for remote sensing of cirrus clouds as well as climate modeling. To the author's knowledge, this thesis presents the first ground-based retrieval of ice crystal shape and surface roughness using passive remote sensing. Since ground-based observations provide information about the forward scattering part of the ice crystal optical properties, the results of this work ideally complement the results of satellite-based studies.

Chapter 7

Outlook

This study demonstrates the potential of remote sensing of halo displays to provide information about ice crystal shape, roughness, size and orientation. New aspects and further interesting questions occurred in the course of this work which will be briefly mentioned in the following. The results of this study showed that the parameterization of ice crystal size and aspect ratio of the Yang et al. (2013) optical properties does not always reproduce the observations, especially for small to medium-sized plates which show both a 22° and a 46° halo. The raytracing code of Macke et al. (1996) allows to calculate optical properties with the aspect ratio as free parameter. However, these optical properties are only valid in the geometric optics approximation which do not represent well the optical properties of smaller ice crystals. Thus, for studying 22° halos, optical properties calculated with improved geometric optics methods as in Yang et al. (2013) would be necessary, which provide ice crystal size and aspect ratio as independent parameters.

In this study a monodisperse size distribution following a gamma distribution with $\mu = 1$ (cf. Eqs. (2.10) and (3.4)) was used to calculate the bulk optical properties. The shape of cirrus particle size distributions is often bi-modal as reported by Heymsfield and Miloshevich (1995), Ivanova et al. (2001), Field et al. (2005) and Zhao et al. (2011). Investigating different size distributions for halo-producing cirrus clouds may reveal that the smooth ice crystals which produce the halo displays follow a different size distribution than the rough ice crystals.

For ground-based measurements the information content of the 22° halo depends on many parameters such as the optical thickness of the cirrus and aerosol, the aerosol type, the surface albedo and of course the ice crystal shape, surface roughness, and particle size. To minimize the influence of the aerosol, the retrieval was applied to the red channel of HaloCam. Additionally, the HaloCam measurements could be performed on top of a mountain, for example at the observation platform on mount Zugspitze, which is located above the boundary layer.

The HaloCam system consists of two low-cost off the shelf cameras and a sun-tracking mount which can easily be set up and installed at multiple locations. To constrain cirrus and aerosol optical thickness, additional sun photometer measurements are required for the quantitative retrieval of ice crystal properties. Thus, HaloCam could be installed alongside the AERONET instruments. The automated halo detection algorithm HaloForest could also be used to filter out events of homogeneous cirrus clouds in the AERONET dataset. Most 22° halos form in thin, homogeneous cirrus clouds which are difficult to filter from the sun photometer data (Smirnov et al., 2000) and are often causing a bias in the retrieved AOT (e.g. Chew et al. (2011)). HaloCam in combination with the RICO retrieval could also be used operationally to complement other ground-based remote sensing methods by constraining ice crystal size, habit and surface roughness and thus reducing uncertainties of the retrieved cirrus optical thickness (Eichler et al., 2009, Zinner et al., 2016).

Furthermore, HaloForest could be extended for the detection of sundogs and upper tangent

arcs for a long-term statistic of halo displays formed by oriented ice crystals. With help of radiative transfer simulations with MYSTIC and CrystalTrace a method was proposed to retrieve the fraction of oriented ice crystals from the simultaneous observation of the 22° halo and sundogs or the upper tangent arc. CrystalTrace needs to be extended to account for ice crystal surface roughness and diffraction. Then, the information content of halo displays produced by oriented crystals could be further investigated by sensitivity studies. Besides the ice crystal shape and surface roughness, the brightness of these halo displays depends also on the fraction of oriented crystals and the distortion width of the orientation. It should be noted that the simultaneous observation of different halo displays does not necessarily constrain ice crystal shapes: although the presence of sundogs indicates ice crystal plates, other ice crystal shapes could still occur in the same cirrus cloud and a simultaneous 22° halo could be formed by randomly oriented ice crystal plates, columns or other hexagonal crystals.

The ML-CIRRUS observations of 1 April 2014 provide a unique dataset of co-located airborne in-situ and ground-based remote sensing observations of different instruments. This dataset contains observations of complex halo displays which were observed over several hours in very homogeneous conditions. Accompanied by transported Saharan dust, the evaluation of these observations is challenging but using synergies between the different available datasets it can provide valuable insights on oriented ice crystals from a remote sensing as well as an in-situ perspective.

Figure 7.1: *HaloCam picture from 28 January 2017 showing left and right sundog which are formed by contrails and contrail cirrus.*

Besides cirrus clouds, the HaloCam observations also contain halo displays formed by contrails and contrail cirrus as shown in Fig. 7.1. Evaluating the HaloCam observations regarding the formation of halo displays by contrails could provide further information of the ice crystal properties of these clouds which have an important impact on the global radiation budget (e.g. Schumann (2005), Forster et al. (2012)).

This study focused on observations of halo displays during daytime only. However, halo displays can also be observed during nighttime with the moon as light source (Lynch and Schwartz, 1985, Sassen et al., 2003a). Sassen et al. (2003a) stated that halo observations during nighttime showed different cirrus properties than daytime observations. This could be investigated with HaloCam by using a moon-tracking algorithm in addition to the sun-tracking algorithm.

Appendix A

Appendix

A.1 Decision trees and random forest classifier

The subsequent sections provide more details on decision trees and the random forest classifier presented in Section 3.6.

A.1.1 Decision trees

The following description is based on Alpaydin (2010) and Raschka (2015). Decision trees start with a root node followed by internal decision nodes, branches and terminal nodes, called leaves. A typical example of a single decision tree, as used for HaloForest, is shown in Fig. A.1. For a

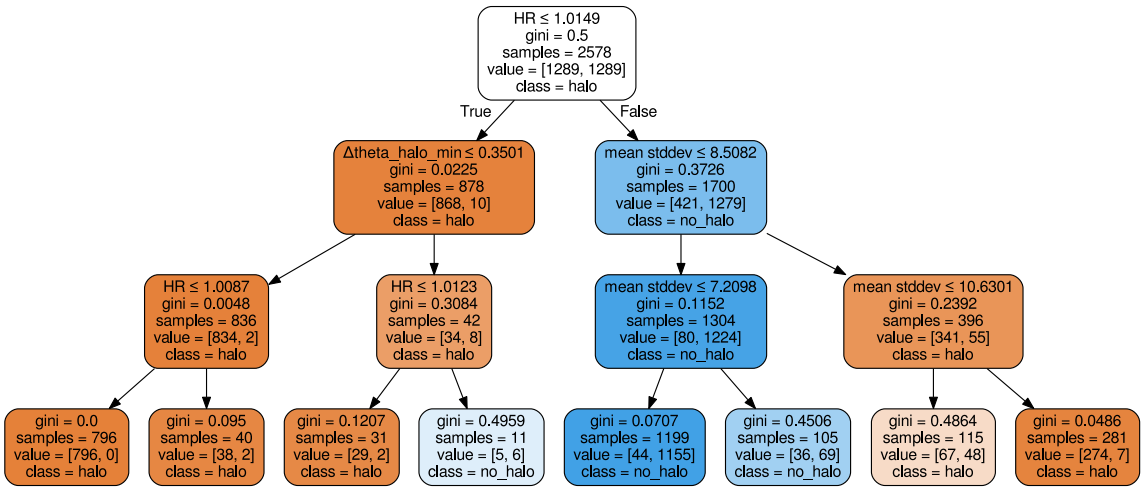

Figure A.1: *Example for a decision tree for a selection of three HaloCam image features confined to a maximum depth of three layers. The two classes, "halo" and "no halo" are depicted by red and blue color. The transparency of the color represents the impurity of the class.*

better visualization, the tree is grown using only three of the eight features and is pruned to a depth of three layers. The explanation provided here focuses on the structure of tree rather than the exact numbers of the threshold tests which differ from the ones used by HaloForest. The halo ratio (HR), the mean standard deviation, and $\Delta\vartheta_{\mathrm{halo,\,min}}$ are used as features in this case, which are displayed in the first line of each node box with the respective threshold test. At each decision node a threshold test is applied to one element of the n-dimensional feature vector (here,

$n = 3$) which best splits the set of samples. The metric to determine the best split in this study is the Gini impurity index, which is defined by Raschka (2015) as

$$I_G(t) = 1 - \sum_{i=1}^{c} p(i|t)^2 \,, \tag{A.1}$$

with c the number of classes and $p(i|t)$ the fraction of samples which belongs to class i at node t. The Gini index takes a minimum value for the maximum information gain (all the samples at node t belong to one class) and the index is maximum for a uniform distribution. The discrete result (here, True or False) of the threshold test decides which of the following branches is chosen. The node boxes are connected by arrows representing the branches of the tree. They are colored depending on the dominating class in the samples which is noted at the bottom of each box: red for "22° halo" and blue for "no 22° halo". The more transparent the color the higher the impurity of the classes and the larger the Gini impurity index. This splitting process is repeated recursively at each child node until a leaf node is reached. A leaf node is hit when all the samples in the subset belong to the same class, or when splitting does not add more information. By repeating this recursive decision process the n-dimensional feature space is subdivided into the pre-defined classes on a path following from the root down. Figure 3.35 shows examples of the resulting decision boundaries as 2-dimensional projections for a selection of feature pairs. The decision tree is trained using a set of labeled training samples. During training the tree grows by adding branches and leaves depending on the complexity of the data, which can lead to over-fitting. By growing an ensemble of decision trees this issue can be improved, which is the idea of random forest classifiers.

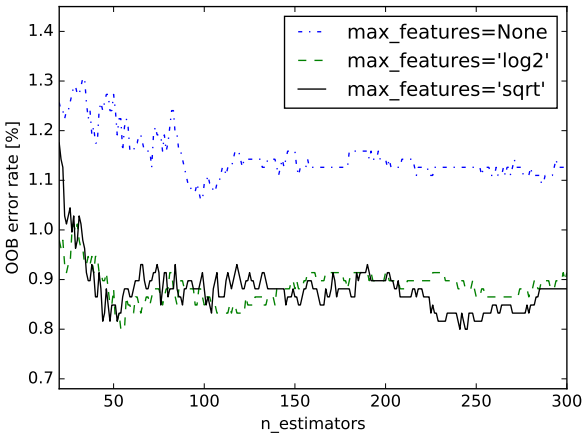

Figure A.2: *Out-of-bag (OOB) error rate for different values of n_estimators (number of trees) for three different realizations of the random forest classifier by changing the number of features considered at each split.*

A.1.2 Random forest classifier implementation

In this study the random forest classifier was used, which is described by Breiman (2001) and implemented in the python module scikit-learn (Pedregosa et al. (2011), version 0.18.1). The trees are trained by applying the bootstrap aggregation (bagging) method (Breiman, 1996), i.e. by using a subset of the training samples which is chosen randomly with replacement and has the same size as the original input samples. This implementation predicts the class of a sample by averaging the probabilistic prediction of all individual decision trees instead of using the majority

vote among the trees. The function call allows to define a number of parameters: the number of trees is set to 100 and a maximum number of 3 features ($\log_2(n)$ with n features) is considered for searching the best split. These parameters are chosen to minimize the out-of-bag (OOB) error, as shown in Fig. A.2. For an increasing number of estimators (trees) the OOB error stabilizes at around 100 trees and is in general smaller for a confined number of features considered at each split.

A.2 Projection of the 22° halo

This section outlines the calculation of the geographic coordinates of the 22° halo projected on a cirrus cloud layer, which is used in Sections 3.7.3 and 4.3.1. Viewing the 22° halo from the ground defines a cone with an opening angle of $\theta = 22°$ centered around the sun, as illustrated in Fig. A.3. The cross-section of this cone with a plane-parallel cirrus cloud, represented by a plane at height z, describes an ellipse with the sun in the focal point. Let the plane be located at $z = 0$. The coordinates of the position of the sun are

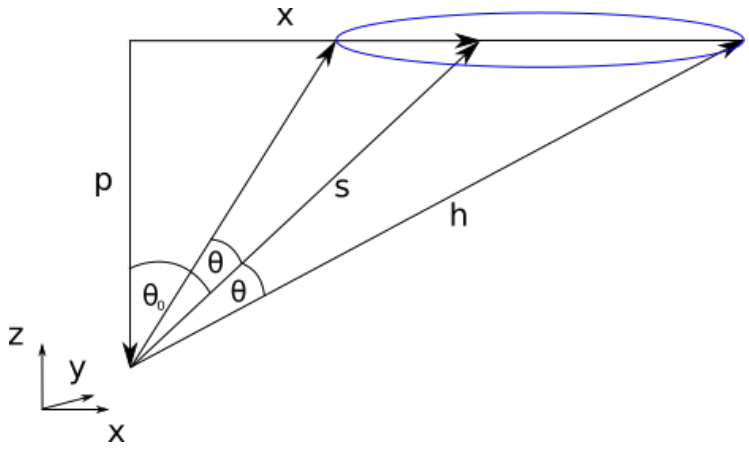

Figure A.3: *Geometry of the 22° halo projected onto a cloud in the x-y-plane at height $z = 0$. The projected 22° halo has the shape of an ellipse with the sun in the focal point. The position of the sun is denoted with the solar zenith angle θ_0. The observer is located at point $\vec{p}$ with $\vec{s}$ pointing into the sun and with $\vec{h}$ pointing at the 22° halo. The elliptic shape of the projected 22° halo is the result of the intersection of a cone with opening angle θ and the x-y-plane. In case of the 22° halo $\theta = 22°$ and in case of the 46° halo $\theta = 46°$, accordingly.*

$$\vec{s} = (\sin\theta_0,\, 0,\, \cos\theta_0) = (\sin\theta_0,\, 0,\, \mu_0)\,, \tag{A.2}$$

with the solar zenith angle θ_0. The observer is located at point $\vec{p}$

$$\vec{p} = (0,\, 0,\, -p_3)\,. \tag{A.3}$$

Let $\vec{h}$ describe the points on the 22° halo projected on the plane at $z = 0$. Then the following conditions must be fulfilled:

$$\vec{h} \cdot \vec{s} = \cos\theta = \mu\,, \tag{A.4}$$

and

$$|\vec{h}| = 1\,, \tag{A.5}$$

assuming $\overrightarrow{s}$ is already normalized. The points of the projected 22° halo x relative to the point p can then be found by a linear combination of p and h

$$\overrightarrow{x} = \overrightarrow{p} + \alpha \cdot \overrightarrow{h} \,. \tag{A.6}$$

where $\overrightarrow{x} = (x_1, x_2, x_3)$. With $x_3 = 0$ $\overrightarrow{x} = 0$ it follows that $\alpha = \overrightarrow{p}/\overrightarrow{h} = p_3/h_3 \equiv p/h$. Then

$$\overrightarrow{h} = \overrightarrow{x}/\alpha = \overrightarrow{x}/(\overrightarrow{p}/\overrightarrow{h}) \,. \tag{A.7}$$

To fulfill $|\overrightarrow{h}| = 1$

$$|\overrightarrow{x}/(\overrightarrow{p}/\overrightarrow{h})| = 1 \,, \tag{A.8}$$

which can be expressed by the vector components

$$h^2 \frac{x_1^2}{p^2} + h^2 \frac{x_2^2}{p^2} + h^2 = 1 \,, \tag{A.9}$$

or

$$\frac{x_1^2}{p^2} + \frac{x_2^2}{p^2} + 1 = \frac{1}{h^2} \,. \tag{A.10}$$

The condition $\overrightarrow{h} \cdot \overrightarrow{s} = \mu$ can also be written as

$$h_1 \sin\theta_0 + h_3 \cos\theta_0 = \mu \,, \tag{A.11}$$

which yields

$$\frac{1}{h^2} = (\frac{x_1}{p} \sin\theta_0 + \cos\theta_0)^2/\mu^2 \,. \tag{A.12}$$

Using Eq. (A.10) the vector $\overrightarrow{x}$ can be calculated by

$$x_1^2 + x_2^2 = (\frac{1}{h^2} - 1)\, p^2 \,, \tag{A.13}$$

with

$$h = \mu/(\frac{x_1}{p} \sin\theta_0 + \cos\theta_0) \,. \tag{A.14}$$

Bibliography

Allied Vision Technologies GmbH, 2015: *Manta Technical Manual*. Accessed: 2017-07-10, `https://www.alliedvision.com/en/products/machine-vision-cameras/detail/Manta/G-235/action/pdf.html`.

Alpaydin, E., 2010: *Introduction to Machine Learning*. 2d ed., Adaptive computation and machine learning, MIT Press, Cambridge.

Anderson, G., S. Clough, F. Kneizys, J. Chetwynd, and E. Shettle, 1986: AFGL Atmospheric Constituent Profiles (0–120 km). Tech. Rep. AFGL-TR-86-0110, AFGL (OPI), Hanscom AFB, MA 01736.

Arnott, W. P., Y. Y. Dong, J. Hallett, and M. R. Poellot, 1994: Role of small ice crystals in radiative properties of cirrus: A case study, FIRE II, November 22, 1991. *Journal of Geophysical Research*, **99 (D1)**, 1371–1381, doi:10.1029/93JD02781.

Auer, A. H. and D. L. Veal, 1970: The dimension of ice crystals in natural clouds. *J. Atmos. Sci.*, **27 (6)**, 919–926, doi:10.1175/1520-0469(1970)027⟨0919:TDOICI⟩2.0.CO;2.

Bailey, M. and J. Hallett, 2002: Nucleation effects on the habit of vapour grown ice crystals from −18 to −42°C. *Quarterly Journal of the Royal Meteorological Society*, **128 (583)**, 1461–1483, doi:10.1002/qj.200212858304.

Bailey, M. and J. Hallett, 2004: Growth rates and habits of ice crystals between −20 and −70°C. *J. Atmos. Sci.*, **61 (5)**, 514–544, doi:10.1175/1520-0469(2004)061⟨0514:GRAHOI⟩2.0.CO;2.

Bailey, M. and J. Hallett, 2012: Ice Crystal Linear Growth Rates from −20 to −70°C: Confirmation from Wave Cloud Studies. *J. Atmos. Sci.*, **69 (1)**, 390–402, doi:10.1175/JAS-D-11-035.1.

Bailey, M. P. and J. Hallett, 2009: A Comprehensive Habit Diagram for Atmospheric Ice Crystals: Confirmation from the Laboratory, AIRS II, and Other Field Studies. *J. Atmos. Sci.*, **66 (9)**, 2888–2899, doi:10.1175/2009JAS2883.1.

Baldridge, A., S. Hook, C. Grove, and G. Rivera, 2009: The ASTER spectral library version 2.0. *Remote Sensing of Environment*, **113 (4)**, 711–715, doi:10.1016/j.rse.2008.11.007.

Baran, A., P. Francis, S. Havemann, and P. Yang, 2001: A study of the absorption and extinction properties of hexagonal ice columns and plates in random and preferred orientation, using T-Matrix theory and aircraft observations of cirrus. *J. Quant. Spectrosc. Radiat. Transfer*, **70**, 505–518, doi:10.1016/S0022-4073(01)00025-5.

Baran, A., P. Watts, and P. Francis, 1999: Testing the coherence of cirrus microphysical and bulk properties retrieved from dual-viewing multispectral satellite radiance measurements. *Journal of Geophysical Research*, **104 (D24)**, 31 673–31 683, doi:10.1029/1999JD900842.

Baran, A. J., 2012: From the single-scattering properties of ice crystals to climate prediction: A way forward. *Atmospheric Research*, **112**, 45–69, doi:10.1016/j.atmosres.2012.04.010.

Baran, A. J. and L. C. Labonnote, 2006: On the reflection and polarisation properties of ice cloud. *J. Quant. Spectrosc. Radiat. Transfer*, **100 (1)**, 41–54, doi:10.1016/j.jqsrt.2005.11.062, VIII Conference on Electromagnetic and Light Scattering by Nonspherical Particles.

Baran, A. J., P. D. Watts, and J. S. Foot, 1998: Potential retrieval of dominating crystal habit and size using radiance data from a dual-view and multiwavelength instrument: A tropical cirrus anvil case. *Journal of Geophysical Research*, **103 (D6)**, 6075–6082, doi:10.1029/97JD03122.

Bass, M., C. DeCusatis, J. Enoch, V. Lakshminarayanan, G. Li, C. Macdonald, V. Mahajan, and E. Van Stryland, 2010: *Handbook of Optics, Third Edition Volume I: Geometrical and Physical Optics, Polarized Light, Components and Instruments*. 3d ed., McGraw-Hill, Inc., New York, NY, USA.

Baumgarten, G., J. Fiedler, F.-J. Lübken, and G. von Cossart, 2008: Particle properties and water content of noctilucent clouds and their interannual variation. *Journal of Geophysical Research*, **113 (D6)**, D06 203, doi:10.1029/2007JD008884.

Baumgartner, A., 2013: Characterization of Integrating Sphere Homogeneity with an Uncalibrated Imaging Spectrometer. Proc. WHISPERS 2013, 1–4, URL `http://elib.dlr.de/83300`, 25.-28. Jun. 2013, Gainsville, Florida, USA.

Baumgartner, A., P. Gege, C. Köhler, K. Lenhard, and T. Schwarzmaier, 2012: Characterisation methods for the hyperspectral sensor HySpex at DLR's calibration home base. *Proc. SPIE*, **8533**, 8533–8533–8, doi:10.1117/12.974664.

Bayer, B., 1975: Color imaging array. US Patent 3,971,065.

Bergeron, T., 1935: On the Physics of Clouds and Precipitation. International Geodetic Geophys. Union, Vol. 2, 156–175, 5th General Assembly, Sept. 1933, Lisbon.

Bi, L. and P. Yang, 2014: Accurate simulation of the optical properties of atmospheric ice crystals with the invariant imbedding T-matrix method. *J. Quant. Spectrosc. Radiat. Transfer*, **138**, 17–35, doi:10.1016/j.jqsrt.2014.01.013.

Bradski, D. G. R. and A. Kaehler, 2008: *Learning OpenCV, 1st Edition*. 1st ed., O'Reilly Media, Inc., Sebastopol, CA.

Breiman, L., 1996: Bagging Predictors. *Machine Learning*, **24 (2)**, 123–140, doi:10.1023/A:1018054314350.

Breiman, L., 2001: Random Forests. *Machine Learning*, **45 (1)**, 5–32, doi:10.1023/A:1010933404324.

Buras, R., T. Dowling, and C. Emde, 2011: New secondary-scattering correction in DISORT with increased efficiency for forward scattering. *J. Quant. Spectrosc. Radiat. Transfer*, **112 (12)**, 2028–2034, doi:10.1016/j.jqsrt.2011.03.019.

Chandrasekhar, S., 1960: *Radiative Transfer*. Dover Publications, New York.

Chepfer, H., G. Brogniez, P. Goloub, F. M. Bréon, and P. H. Flamant, 1999: Observations of horizontally oriented ice crystals in cirrus clouds with POLDER-1/ADEOS-1. *J. Quant. Spectrosc. Radiat. Transfer*, **63 (2)**, 521–543, doi:10.1016/S0022-4073(99)00036-9.

Chepfer, H., P. Goloub, J. Riedi, J. F. De Haan, J. Hovenier, and P. Flamant, 2001: Ice crystal shapes in cirrus clouds derived from POLDER/ADEOS-1. *Journal of Geophysical Research*, **106**, 7955–7966, doi:10.1029/2000JD900285.

Chew, B. N., J. R. Campbell, J. S. Reid, D. M. Giles, E. J. Welton, S. V. Salinas, and S. C. Liew, 2011: Tropical cirrus cloud contamination in sun photometer data. *Atmospheric Environment*, **45 (37)**, 6724–6731, doi:10.1016/j.atmosenv.2011.08.017.

CIE, 1986: Standard on Colorimetric Observers. *Commission Internationale de l'Eclairage CIE*.

Cole, B. H., P. Yang, B. A. Baum, J. Riedi, and L. C.-Labonnote, 2014: Ice particle habit and surface roughness derived from PARASOL polarization measurements. *Atmos. Chem. Phys.*, **14 (7)**, 3739–3750, doi:10.5194/acp-14-3739-2014.

Cole, B. H., P. Yang, B. A. Baum, J. Riedi, L. C.-Labonnote, F. Thieuleux, and S. Platnick, 2013: Comparison of PARASOL Observations with Polarized Reflectances Simulated Using Different Ice Habit Mixtures. *Journal of Applied Meteorology and Climatology*, **52 (1)**, 186–196, doi:10.1175/JAMC-D-12-097.1.

Cox, C. and W. Munk, 1954: Measurement of the roughness of the sea surface from photographs of the sun's glitter. *Journal of the Optical Society of America*, **44 (11)**, 838–850, doi:10.1364/JOSA.44.000838.

Davis, J., T. McKee, and S. Cox, 1985: Application of the Monte Carlo method to problems in visibility using a local estimate: an investigation. *Applied Optics*, **24 (19)**, 3193–3205, doi:10.1364/AO.24.003193.

Descloitres, J., J.-C. Buriez, F. Parol, and Y. Fouquart, 1998: POLDER observations of cloud bidirectional reflectances compared to a plane-parallel model using the International Satellite Cloud Climatology Project cloud phase functions. *Journal of Geophysical Research*, **103 (D10)**, 11 411–11 418, doi:10.1029/98JD00592.

Draine, B. T. and P. J. Flatau, 1994: Discrete-Dipole Approximation For Scattering Calculations. *J. Opt. Soc. Am. A*, **11 (4)**, 1491–1499, doi:10.1364/JOSAA.11.001491.

Eichler, H., A. Ehrlich, M. Wendisch, G. Mioche, J.-F. Gayet, M. Wirth, C. Emde, and A. Minikin, 2009: Influence of ice crystal shape on retrieval of cirrus optical thickness and effective radius: A case study. *Journal of Geophysical Research*, **114 (D19)**, D19 203, doi:10.1029/2009JD012215.

Emde, C., R. Buras, and B. Mayer, 2011: ALIS: An efficient method to compute high spectral resolution polarized solar radiances using the Monte Carlo approach. *J. Quant. Spectrosc. Radiat. Transfer*, **112 (10)**, 1622–1631, doi:10.1016/j.jqsrt.2011.03.018.

Emde, C. and B. Mayer, 2007: Simulation of solar radiation during a total solar eclipse: A challenge for radiative transfer. *Atmos. Chem. Phys.*, **7**, 2259–2270, doi:10.5194/acp-7-2259-2007.

Emde, C., et al., 2016: The libRadtran software package for radiative transfer calculations (version 2.0.1). **9 (5)**, 1647–1672, doi:10.5194/gmd-9-1647-2016.

Ewald, F., 2016: Retrieval of vertical profiles of cloud droplet effective radius using solar reflectance from cloud sides. Ph.D. thesis, Ludwig-Maximilians-Universität München, `http://nbn-resolving.de/urn:nbn:de:bvb:19-205322`.

Ewald, F., C. Winkler, and T. Zinner, 2015: Reconstruction of cloud geometry using a scanning cloud radar. *Atmos. Meas. Tech.*, **8 (6)**, 2491–2508, doi:10.5194/amt-8-2491-2015.

Feister, U. and R. Grewe, 1995: Spectral albedo measurements in the UV and visible region over different types of surfaces. *Photochemistry and Photobiology*, **62**, 736–744, doi:10.1111/j.1751-1097.1995.tb08723.x.

Field, P. R., R. J. Hogan, P. R. A. Brown, A. J. Illingworth, T. W. Choularton, and R. J. Cotton, 2005: Parametrization of ice-particle size distributions for mid-latitude stratiform cloud. *Quarterly Journal of the Royal Meteorological Society*, **131 (609)**, 1997–2017, doi:10.1256/qj.04.134.

Findeisen, W., 1938: Die kolloidmeteorologischen Vorgänge bei der Niederschlagsbildung. *Meteor. Z.*, **55**, 121–133.

Flatau, P. J. and B. T. Draine, 2014: Light scattering by hexagonal columns in the discrete dipole approximation. *Opt. Express*, **22 (18)**, 21 834–21 846, doi:10.1364/OE.22.021834.

Forster, L., C. Emde, S. Unterstrasser, and B. Mayer, 2012: Effects of Three-Dimensional Photon Transport on the Radiative Forcing of Realistic Contrails. *J. Atmos. Sci.*, **69 (7)**, 2243–2255, doi:10.1175/JAS-D-11-0206.1.

Forster, L., M. Seefeldner, M. Wiegner, and B. Mayer, 2017: Ice crystal characterization in cirrus clouds: a sun-tracking camera system and automated detection algorithm for halo displays. *Atmos. Meas. Tech.*, **10 (7)**, 2499–2516, doi:10.5194/amt-10-2499-2017.

Fraser, A. B., 1979: What size of ice crystals causes the halos? *J. Opt. Soc. Am.*, **69 (8)**, 1112–1118, doi:10.1364/JOSA.69.001112.

Freudenthaler, V., et al., 2009: Depolarization ratio profiling at several wavelengths in pure Saharan dust during SAMUM 2006. *Tellus B*, **61 (1)**, 165–179, doi:10.1111/j.1600-0889.2008.00396.x.

Garrett, T. J., M. B. Kimball, G. G. Mace, and D. G. Baumgardner, 2007: Observing cirrus halos to constrain in-situ measurements of ice crystal size. *Atmos. Chem. Phys. Discuss.*, **7**, 1295–1325, doi:10.5194/acpd-7-1295-2007.

Gayet, J., O. Crepel, J. Fournol, and S. Oshchepkov, 1997: A new airborne polar Nephelometer from the measurements of optical and microphysical cloud properties. Part I: Theoretical design. *Ann. Geophysicae*, **15 (4)**, 451–459, doi:10.1007/s00585-997-0451-1.

Gayet, J.-F., G. Mioche, V. Shcherbakov, C. Gourbeyre, R. Busen, and A. Minikin, 2011: Optical properties of pristine ice crystals in mid-latitude cirrus clouds: a case study during CIRCLE-2 experiment. *Atmos. Chem. Phys.*, **11 (6)**, 2537–2544, doi:10.5194/acp-11-2537-2011.

Gayet, J.-F., et al., 1998: In situ measurements of the scattering phase function of stratocumulus, contrails and cirrus. *Geophys. Res. Lett.*, **25 (7)**, 971–974, doi:10.1029/98GL00541.

Gedzelman, S. D., 2008: Simulating halos and coronas in their atmospheric environment. *Appl. Opt.*, **47 (34)**, H157–H166, doi:10.1364/AO.47.00H157.

Gedzelman, S. D. and M. Vollmer, 2008: Atmospheric Optical Phenomena and Radiative Transfer. *Bull. Amer. Meteor. Soc.*, **89 (4)**, 471–485, doi:10.1175/BAMS-89-4-471.

Gege, P., et al., 2009: A new laboratory for the characterisation of hyperspectral airborne sensors. `http://elib.dlr.de/58527/`.

Geogdzhayev, I. and B. van Diedenhoven, 2016: The effect of roughness model on scattering properties of ice crystals. *J. Quant. Spectrosc. Radiat. Transfer*, **178**, 134–141, doi:10.1016/j.jqsrt.2016.03.001, electromagnetic and light scattering by nonspherical particles XV: Celebrating 150 years of Maxwell's electromagnetics.

Görsdorf, U., V. Lehmann, M. Bauer-Pfundstein, G. Peters, D. Vavriv, V. Vinogradov, and V. Volkov, 2015: A 35-GHz Polarimetric Doppler Radar for Long-Term Observations of Cloud Parameters – Description of System and Data Processing. *Journal of Atmospheric and Oceanic Technology*, **32 (4)**, 675–690, doi:10.1175/JTECH-D-14-00066.1.

Greenler, R., 1980: *Rainbows, Halos and Glories*. Cambridge University Press, Cambridge.

Grob, H., 2015: Characterisation and Calibration of an IR imaging spectrometer for cloud observation. M.S. thesis, Ludwig-Maximilians-Universität München.

Guerrero-Rascado, J. L., M. J. Costa, A. M. Silva, and F. J. Olmo, 2013: Retrieval and variability analysis of optically thin cloud optical depths from a Cimel sun-photometer. *Atmospheric research*, **127**, 210–220.

Guignard, A., C. J. Stubenrauch, A. J. Baran, and R. Armante, 2012: Bulk microphysical properties of semi-transparent cirrus from AIRS: a six year global climatology and statistical analysis in synergy with geometrical profiling data from CloudSat-CALIPSO. *Atmos. Chem. Phys.*, **12 (1)**, 503–525, doi:10.5194/acp-12-503-2012.

Hansen, J. and L. Travis, 1974: Light scattering in planetary atmospheres. *Space Sci. Rev.*, **16**, 527–610, doi:10.1007/BF00168069.

Hausmann, P., 2012: Ground-based remote sensing of optically thin ice clouds. M.S. thesis, Ludwig-Maximilians-Universität München.

Heese, B., V. Freudenthaler, M. Kosmale, M. Seefeldner, and M. Wiegner, 2004: First Results from the Portable LIDAR System Polis. *22nd Internation Laser Radar Conference (ILRC 2004)*, G. Pappalardo and A. Amodeo, Eds., ESA Special Publication, Vol. 561, 79.

Heikkilä, J. and O. Silvén, 1997: A four-step camera calibration procedure with implicit image correction. *Proceedings of IEEE Computer Society Conference on Computer Vision and Pattern Recognition*, Washington, DC, USA, 1106–1112, doi:10.1109/CVPR.1997.609468.

Hess, M., 1996: Modellierung und Messung optischer Eigenschaften von Cirren. Ph.D. thesis, Ludwig-Maximilians-Universität München.

Hess, M., P. Koepke, and I. Schult, 1998: Optical properties of aerosols and clouds: the software package OPAC. *Bull. Amer. Meteor. Soc.*, **79 (5)**, 831–844.

Heymsfield, A., 1972: Ice crystal terminal velocities. *J. Atmos. Sci.*, **29 (7)**, 1348–1357, doi:10.1175/1520-0469(1972)029⟨1348:ICTV⟩2.0.CO;2.

Heymsfield, A. and L. Miloshevich, 2003: Parameterizations for the cross-sectional area and extinction of cirrus and stratiform ice cloud particles. *J. Atmos. Sci.*, **60 (7)**, 936–956, doi:10.1175/1520-0469(2003)060⟨0936:PFTCSA⟩2.0.CO;2.

Heymsfield, A. and C. Platt, 1984: A parameterization of the particle size spectrum of ice clouds in terms of the ambient temperature and the ice water content. *J. Atmos. Sci.*, **41 (5)**, 846–855, doi:10.1175/1520-0469(1984)041⟨0846:APOTPS⟩2.0.CO;2.

Heymsfield, A. J. and L. M. Miloshevich, 1995: Relative Humidity and Temperature Influences on Cirrus Formation and Evolution: Observations from Wave Clouds and FIRE II. *J. Atmos. Sci.*, **52 (23)**, 4302–4326, doi:10.1175/1520-0469(1995)052⟨4302:RHATIO⟩2.0.CO;2.

Heymsfield, A. J., C. Schmitt, and A. Bansemer, 2013: Ice Cloud Particle Size Distributions and Pressure-Dependent Terminal Velocities from In Situ Observations at Temperatures from 0° to -86°C. *J. Atmos. Sci.*, **70 (12)**, 4123–4154, doi:10.1175/JAS-D-12-0124.1.

Hogan, R., M. Behera, E. O'Connor, and A. Illingworth, 2004: Estimate of the global distribution of stratiform supercooled liquid water clouds using the LITE radar. *Geophys. Res. Lett.*, **31 (5)**, L05 106, doi:10.1029/2003GL018977.

Holben, B., et al., 1998: AERONET - A Federated Instrument Network and Data Archive for Aerosol Characterization. *Remote Sens. of Environ.*, **66 (1)**, 1–16, doi:10.1016/S0034-4257(98)00031-5.

Holz, R. E., et al., 2016: Resolving ice cloud optical thickness biases between CALIOP and MODIS using infrared retrievals. *Atmos. Chem. Phys.*, **16 (8)**, 5075–5090, doi:10.5194/acp-16-5075-2016.

Hu, Y., S. Rodier, K. Xu, W. Sun, J. Huang, B. Lin, P. Zhai, and D. Josset, 2010: Occurrence, liquid water content, and fraction of supercooled water clouds from combined CALIOP/IIR/MODIS measurements. *Journal of Geophysical Research*, **115 (D4)**, D00H34, doi:10.1029/2009JD012384.

Itseez, 2015: *Open Source Computer Vision Library*. Accessed: 2017-07-10, `https://github.com/itseez/opencv`.

Ivanova, D., D. L. Mitchell, W. Arnott, and M. Poellot, 2001: A GCM parameterization for bimodal size spectra and ice mass removal rates in mid-latitude cirrus clouds. *Atmospheric Research*, **59**, 89–113, doi:10.1016/S0169-8095(01)00111-9.

Jayaweera, K. and B. Mason, 1965: The behaviour of freely falling cylinders and cones in a viscous fluid. *Journal of Fluid Mechanics*, **22 (04)**, 709–720, doi:10.1017/S002211206500109X.

Key, J., P. Yang, B. Baum, and S. Nasiri, 2002: Parameterization of shortwave ice cloud optical properties for various particle habits. *Journal of Geophysical Research*, **107 (D13)**, 10.1029/2001JD000 742.

Kokhanovsky, A., 2008: The contrast and brightness of halos in crystalline clouds. *Atmos. Res.*, **89 (1-2)**, 110–112, doi:10.1016/j.atmosres.2007.12.006.

Konoshonkin, A. V., N. V. Kustova, A. G. Borovoi, Y. Grynko, and J. Förstner, 2016: Light scattering by ice crystals of cirrus clouds: comparison of the physical optics methods. *J. Quant. Spectrosc. Radiat. Transfer*, **182**, 12–23, doi:10.1016/j.jqsrt.2016.05.006.

Kunkel, K. and J. Weinman, 1976: Monte Carlo Analysis of multiply scattered lidar returns. *J. Atmos. Sci.*, **33 (9)**, 1772–1781, doi:10.1175/1520-0469(1976)033⟨1772:MCAOMS⟩2.0.CO;2.

Kurucz, R., 1992: Synthetic infrared spectra. *Proceedings of the 154th Symposium of the International Astronomical Union (IAU); Tucson, Arizona, March 2-6, 1992*, Kluwer, Acad., Norwell, MA.

Lamb, D. and J. Verlinde, 2011: *Physics and chemistry of clouds*. Cambridge University Press.

Liou, K.-N., 1986: Influence of cirrus clouds on weather and climate processes: A global perspective. *Monthly Weather Review*, **114 (6)**, 1167–1199, doi:10.1175/1520-0493(1986)114⟨1167:IOCCOW⟩2.0.CO;2.

Liou, K.-N. and P. Yang, 2016: *Light Scattering by Ice Crystals: Fundamentals and Applications*. Cambridge University Press, Cambridge.

Liu, C., P. Yang, P. Minnis, N. Loeb, S. Kato, A. Heymsfield, and C. Schmitt, 2014: A two-habit model for the microphysical and optical properties of ice clouds. *Atmos. Chem. Phys.*, **14 (24)**, 13 719–13 737, doi:10.5194/acp-14-13719-2014.

Lynch, D., K. Sassen, D. Starr, and G. Stephens, (Eds.) , 2002: *Cirrus*. Oxford University Press.

Lynch, D. K. and P. Schwartz, 1985: Intensity profile of the 22° halo. *J. Opt. Soc. Am. A*, **2 (4)**, 584–589, doi:10.1364/JOSAA.2.000584.

Macke, A., 1994: Modellierung der optischen Eigenschaften von Cirruswolken. Ph.D. thesis, Universität Hamburg.

Macke, A., J. Mueller, and E. Raschke, 1996: Single scattering properties of atmospheric ice crystals. *J. Atmos. Sci.*, **53 (19)**, 2813–2825, doi:10.1175/1520-0469(1996)053⟨2813:SSPOAI⟩2.0.CO;2.

Magono, C. and C. W. Lee, 1966: Meteorological classification of natural snow crystals. *J. Fac. Sci.*, **2**, 321–335.

Mayer, B., 2009: Radiative transfer in the cloudy atmosphere. *European Physical Journal Conferences*, **1**, 75–99, doi:10.1140/epjconf/e2009-00912-1.

Mayer, B. and A. Kylling, 2005: Technical Note: The libRadtran software package for radiative transfer calculations: Description and examples of use. *Atmos. Chem. Phys.*, **5**, 1855–1877, doi:10.5194/acp-5-1855-2005.

McFarlane, S. A. and R. T. Marchand, 2008: Analysis of ice crystal habits derived from MISR and MODIS observations over the ARM Southern Great Plains site. *Journal of Geophysical Research: Atmospheres*, **113 (D7)**, D07 209, doi:10.1029/2007JD009191.

McFarquhar, G. and A. Heymsfield, 1998: The definition and significance of an effective radius for ice clouds. *J. Atmos. Sci.*, **55 (11)**, 2039–2052, doi:10.1175/1520-0469(1998)055⟨2039:TDASOA⟩2.0.CO;2.

Mie, G., 1908: Beiträge zur Optik trüber Medien, speziell kolloidaler Metallösungen. *Annalen der Physik, Vierte Folge*, **25 (3)**, 377–445.

Minnaert, M., 1993: *Rainbows, Halos, and Coronas*, 185–258. Springer New York, New York, NY, doi:10.1007/978-1-4612-2722-9_10.

Minnaert, M. G. J., 1937: *De natuurkunde van't vrije veld. Deel I. Licht en kleur in het landschap*. W. J. Thieme, Zutphen.

Mishchenko, M. and A. Macke, 1997: Asymmetry parameters of the phase function for isolated and densely packed spherical particles with multiple internal inclusions in the geometric optics limit. *J. Quant. Spectrosc. Radiat. Transfer*, **57 (6)**, 767–794, doi:10.1016/S0022-4073(97)00012-5.

Mishchenko, M. and A. Macke, 1999: How big should hexagonal ice crystals be to produce halos? *Applied Optics*, **38 (9)**, 1626–1629, doi:10.1364/AO.38.001626.

Mishchenko, M., W. Rossow, A. Macke, and A. Lacis, 1996: Sensitivity of cirrus cloud albedo, bidirectional reflectance and optical thickness retrieval accuracy to ice particle shape. *Journal of Geophysical Research*, **101 (D12)**, 16 973–16 985, doi:10.1029/96JD01155.

Mitchell, D. L. and W. P. Arnott, 1994: A Model Predicting the Evolution of Ice Particle Size Spectra and Radiative Properties of Cirrus Clouds. Part II: Dependence of Absorption and Extinction on Ice Crystal Morphology. *J. Atmos. Sci.*, **51 (6)**, 817–832, doi:10.1175/1520-0469(1994)051⟨0817:AMPTEO⟩2.0.CO;2.

Muinonen, K., K. Lumme, J. Peltoniemi, and W. M. Irvine, 1989: Light scattering by randomly oriented crystals. *Applied Optics*, **28 (15)**, 3051–3060, doi:10.1364/AO.28.003051.

Myagkov, A., P. Seifert, U. Wandinger, J. Bühl, and R. Engelmann, 2016: Relationship between temperature and apparent shape of pristine ice crystals derived from polarimetric cloud radar observations during the ACCEPT campaign. *Atmos. Meas. Tech.*, **9 (8)**, 3739–3754, doi:10.5194/amt-9-3739-2016.

Neshyba, S. P., B. Lowen, M. Benning, A. Lawson, and P. M. Rowe, 2013: Roughness metrics of prismatic facets of ice. *Journal of Geophysical Research: Atmospheres*, **118 (8)**, 3309–3318, doi:10.1002/jgrd.50357.

Noel, V. and H. Chepfer, 2004: Study of Ice Crystal Orientation in Cirrus Clouds Based on Satellite Polarized Radiance Measurements. *J. Atmos. Sci.*, **61 (16)**, 2073–2081, doi:10.1175/1520-0469(2004)061⟨2073:SOICOI⟩2.0.CO;2, `https://doi.org/10.1175/1520-0469(2004)061<2073:SOICOI>2.0.CO;2`.

Noel, V. and H. Chepfer, 2010: A global view of horizontally oriented crystals in ice clouds from Cloud-Aerosol Lidar and Infrared Pathfinder Satellite Observation (CALIPSO). *Journal of Geophysical Research: Atmospheres*, **115 (D4)**, D00H23, doi:10.1029/2009JD012365.

Noel, V. and K. Sassen, 2005: Study of Planar Ice Crystal Orientations in Ice Clouds from Scanning Polarization Lidar Observations. *Journal of Applied Meteorology*, **44 (5)**, 653–664, doi:10.1175/JAM2223.1, `https://doi.org/10.1175/JAM2223.1`.

Ono, A., 1969: The shape and riming properties of ice crystals in natural clouds. *J. Atmos. Sci.*, **26 (1)**, 138–147, doi:10.1175/1520-0469(1969)026⟨0138:TSARPO⟩2.0.CO;2.

Pattloch, F. and E. Tränkle, 1984: Monte Carlo simulation and analysis of halo phenomena. *J. Opt. Soc. Am. A*, **1 (5)**, 520–526, doi:10.1364/JOSAA.1.000520.

Pedregosa, F., et al., 2011: Scikit-learn: Machine Learning in Python. *Journal of Machine Learning Research*, **12**, 2825–2830.

Pekkola, M., 1991: Finnish Halo Observing Network: search for rare halo phenomena. *Applied Optics*, **30 (24)**, 3542–3544, doi:10.1364/AO.30.003542.

Pernter, J. M. and F. Exner, 1910: *Meteorologische Optik*. W. Braumüller, Wien.

Petty, G. W., 2006: *A first course in atmospheric radiation*. Sundog Publishing, Madison, Wisconsin.

Platnick, S., et al., 2017: The MODIS Cloud Optical and Microphysical Products: Collection 6 Updates and Examples From Terra and Aqua. *IEEE Transactions on Geoscience and Remote Sensing*, **55**, 502–525, doi:10.1109/TGRS.2016.2610522.

Platt, C., 1978: Lidar backscatter from horizontal ice crystal plates. *J. Appl. Meteorol.*, **17 (4)**, 482–488, doi:10.1175/1520-0450(1978)017⟨0482:LBFHIC⟩2.0.CO;2.

Prigarin, S. M., 2009: Numerical simulation of halos in crystal clouds by Monte Carlo method. *Russ. J. Numer. Anal. Math. Modelling*, **24 (5)**, 481–493, doi:10.1515/RJNAMM.2009.031.

Raschka, S., 2015: *Python Machine Learning*. Community experience distilled, Packt Publishing, Birmingham, UK.

Reinhardt, B., R. Buras, L. Bugliaro, S. Wilbert, and B. Mayer, 2014: Determination of circumsolar radiation from Meteosat Second Generation. *Atmos. Meas. Tech.*, **7 (3)**, 823–838, doi:10.5194/amt-7-823-2014.

Rogers, R. R. and M. K. Yau, 1996: *A short course in cloud physics*. Elsevier, Burlington, MA.

Sassen, K. and J. R. Campbell, 2001: A Midlatitude Cirrus Cloud Climatology from the Facility for Atmospheric Remote Sensing. Part I: Macrophysical and Synoptic Properties. *J. Atmos. Sci.*, **58 (5)**, 481–496, doi:10.1175/1520-0469(2001)058⟨0481:AMCCCF⟩2.0.CO;2.

Sassen, K., N. C. Knight, Y. Takano, and A. J. Heymsfield, 1994: Effects of ice-crystal structure on halo formation: cirrus cloud experimental and ray-tracing modeling studies. *Applied Optics*, **33 (21)**, 4590–4601, doi:10.1364/AO.33.004590.

Sassen, K. and K.-N. Liou, 1979: Scattering of polarized laser light by water droplet, mixed-phase and ice crystal clouds. Part I: Angular scattering patterns. *J. Atmos. Sci.*, **36 (5)**, 838–851, doi:10.1175/1520-0469(1979)036⟨0838:SOPLLB⟩2.0.CO;2.

Sassen, K., Z. Wang, C. Platt, and J. Comstock, 2003a: Parameterization of infrared absorption in midlatitude cirrus clouds. *J. Atmos. Sci.*, **60 (2)**, 428–433, doi:10.1175/1520-0469(2003)060⟨0428:POIAIM⟩2.0.CO;2.

Sassen, K., J. Zhu, and S. Benson, 2003b: Midlatitude cirrus cloud climatology from the Facility for Atmospheric Remote Sensing. IV. Optical displays. *Applied Optics*, **42 (3)**, 332–341, doi:10.1364/AO.42.000332.

Schmitt, C. G. and A. J. Heymsfield, 2007: On the Occurrence of Hollow Bullet Rosette– and Column-Shaped Ice Crystals in Midlatitude Cirrus. *J. Atmos. Sci.*, **64 (12)**, 4514–4519, doi:10.1175/2007JAS2317.1.

Schmitt, C. G. and A. J. Heymsfield, 2014: Observational quantification of the separation of simple and complex atmospheric ice particles. *Geophysical Research Letters*, **41 (4)**, 1301–1307, doi:10.1002/2013GL058781, 2013GL058781.

Schnaiter, M., et al., 2016: Cloud chamber experiments on the origin of ice crystal complexity in cirrus clouds. *Atmos. Chem. Phys.*, **16 (8)**, 5091–5110, doi:10.5194/acp-16-5091-2016.

Schnell, F. I. J., 2014: Aerosol distribution above Munich using remote sensing techniques. Ph.D. thesis, Ludwig-Maximilians-Universität München, `http://nbn-resolving.de/urn:nbn:de:bvb:19-173683`.

Schumann, U., 2005: Formation, properties and climatic effects of contrails. *Comptes Rendus Physique*, **6**, 549–565.

Seefeldner, M., A. Oppenrieder, D. Rabus, J. Reuder, M. Schreier, P. Hoeppe, and P. Koepke, 2004: A Two-Axis Tracking System with Datalogger. *Journal of Atmospheric and Oceanic Technology*, **21 (6)**, 975–979, doi:10.1175/1520-0426(2004)021⟨0975:ATTSWD⟩2.0.CO;2.

Segal-Rosenheimer, M., P. B. Russell, J. M. Livingston, S. Ramachandran, J. Redemann, and B. A. Baum, 2013: Retrieval of cirrus properties by Sun photometry: A new perspective on an old issue. *Journal of Geophysical Research: Atmospheres*, **118 (10)**, 4503–4520, doi:10.1002/jgrd.50185.

Shcherbakov, V., 2013: Why the 46° halo is seen far less often than the 22° halo? *J. Quant. Spectrosc. Radiat. Transfer*, **124**, 37–44, doi:10.1016/j.jqsrt.2013.03.002.

Shiobara, M. and S. Asano, 1994: Estimation of cirrus optical thickness from sun photometer measurements. *J. Appl. Meteorol.*, **33 (6)**, 672–681, doi:10.1175/1520-0450(1994)033⟨0672:EOCOTF⟩2.0.CO;2.

Smirnov, A., B. Holben, T. Eck, O. Dubovik, and I. Slutsker, 2000: Cloud-Screening and Quality Control Algorithms for the AERONET Database. *Remote Sensing of Environment*, **73 (3)**, 337–349, doi:10.1016/S0034-4257(00)00109-7.

Sonntag, D., 1990: Important new Values of the Physical Constants of 1986, Vapour Pressure Formulations based on ITS-90, and Psychrometer Formulae. *Zeitschrift für Meteorologie*, **40 (5)**, 340–344.

Stamnes, K., S. Tsay, W. Wiscombe, and K. Jayaweera, 1988: A numerically stable algorithm for discrete-ordinate-method radiative transfer in multiple scattering and emitting layered media. *Applied Optics*, **27 (12)**, 2502–2509, doi:10.1364/AO.27.002502.

Stephens, G. L., S.-C. Tsay, P. W. S. Jr., and P. J. Flatau, 1990: The Relevance of the Microphysical and Radiative Properties of Cirrus Clouds to Climate and Climatic Feedback. *J. Atmos. Sci.*, **47 (14)**, 1742–1754, doi:10.1175/1520-0469(1990)047⟨1742:TROTMA⟩2.0.CO;2.

Strahler, A., et al., 1999: MODIS BRDF/albedo product: algorithm theoretical basis document version 5.0. *MODIS documentation.*

Strutt, J. W., 1871: LVIII. On the scattering of light by small particles. *The London, Edinburgh, and Dublin Philosophical Magazine and Journal of Science*, **41 (275)**, 447–454.

Stubenrauch, C. J., A. Chédin, G. Rädel, N. A. Scott, and S. Serrar, 2006: Cloud Properties and Their Seasonal and Diurnal Variability from TOVS Path-B. *Journal of Climate*, **19 (21)**, 5531–5553, doi:10.1175/JCLI3929.1.

Sun, W., N. G. Loeb, and P. Yang, 2006: On the retrieval of ice cloud particle shapes from POLDER measurements. *J. Quant. Spectrosc. Radiat. Transfer*, **101 (3)**, 435–447, doi:10.1016/j.jqsrt.2006.02.071.

Takano, Y. and K.-N. Liou, 1990: Halo phenomena modified by multiple scattering. *Journal of the Optical Society of America A*, **7 (5)**, 885–889, doi:10.1364/JOSAA.7.000885.

Takano, Y. and K.-N. Liou, 1995: Solar radiative transfer in cirrus clouds. Part III: Light scattering by irregular ice crystals. *J. Atmos. Sci.*, **52 (7)**, 818–837, doi:10.1175/1520-0469(1995)052⟨0818:RTICCP⟩2.0.CO;2.

Tang, G., R. L. Panetta, P. Yang, G. W. Kattawar, and P.-W. Zhai, 2017: Effects of ice crystal surface roughness and air bubble inclusions on cirrus cloud radiative properties from remote sensing perspective. *J. Quant. Spectrosc. Radiat. Transfer*, **195**, 119–131, doi:10.1016/j.jqsrt.2017.01.016.

Tape, W., 1994: *Atmospheric halos*. Antarctic Research Series, American Geophysical Union, Washington, DC.

Tape, W. and J. Moilanen, 2006: *Atmospheric Halos and the Search for Angle X*. American Geophysical Union, Washington, DC.

Thomas, G. and K. Stamnes, 1999: *Radiative transfer in the Atmosphere and Ocean*. Cambridge University Press, Cambridge, UK.

Toledano, C., M. Wiegner, M. Garhammer, M. Seefeldner, J. Gasteiger, D. Müller, and P. Koepke, 2009: Spectral aerosol optical depth characterization of desert dust during SAMUM 2006. *Tellus B*, **61 (1)**, 216–228, doi:10.1111/j.1600-0889.2008.00382.x.

Toledano, C., et al., 2011: Optical properties of aerosol mixtures derived from sun-sky radiometry during SAMUM-2. *Tellus B*, **63 (4)**, 635–648, doi:10.1111/j.1600-0889.2011.00573.x.

Tricker, R. A. R., 1970: *Introduction to Meteorological Optics*. Elsevier, New York.

Ulanowski, Z., P. H. Kaye, E. Hirst, R. S. Greenaway, R. J. Cotton, E. Hesse, and C. T. Collier, 2014: Incidence of rough and irregular atmospheric ice particles from Small Ice Detector 3 measurements. *Atmos. Chem. Phys.*, **14 (3)**, 1649–1662, doi:10.5194/acp-14-1649-2014.

Um, J. and G. M. McFarquhar, 2015: Formation of atmospheric halos and applicability of geometric optics for calculating single-scattering properties of hexagonal ice crystals: Impacts of aspect ratio and ice crystal size. *J. Quant. Spectrosc. Radiat. Transfer*, **165**, 134–152, doi:10.1016/j.jqsrt.2015.07.001.

Um, J., G. M. McFarquhar, Y. P. Hong, S.-S. Lee, C. H. Jung, R. P. Lawson, and Q. Mo, 2015: Dimensions and aspect ratios of natural ice crystals. *Atmos. Chem. Phys.*, **15 (7)**, 3933–3956, doi:10.5194/acp-15-3933-2015.

Urquhart, B., B. Kurtz, E. Dahlin, M. Ghonima, J. E. Shields, and J. Kleissl, 2015: Development of a sky imaging system for short-term solar power forecasting. *Atmos. Meas. Tech.*, **8 (2)**, 875–890, doi:10.5194/amt-8-875-2015.

van Diedenhoven, B., 2014: The prevalence of the 22° halo in cirrus clouds. *J. Quant. Spectrosc. Radiat. Transfer*, **146**, 475–479, doi:10.1016/j.jqsrt.2014.01.012.

van Diedenhoven, B., B. Cairns, A. M. Fridlind, A. S. Ackerman, and T. J. Garrett, 2013: Remote sensing of ice crystal asymmetry parameter using multi-directional polarization measurements – Part 2: Application to the Research Scanning Polarimeter. *Atmos. Chem. Phys.*, **13 (6)**, 3185–3203, doi:10.5194/acp-13-3185-2013.

van Diedenhoven, B., A. M. Fridlind, A. S. Ackerman, and B. Cairns, 2012: Evaluation of Hydrometeor Phase and Ice Properties in Cloud-Resolving Model Simulations of Tropical Deep Convection Using Radiance and Polarization Measurements. *J. Atmos. Sci.*, **69 (11)**, 3290–3314, doi:10.1175/JAS-D-11-0314.1.

Venn, J., 1880: On the employment of geometrical diagrams for the sensible representations of logical propositions. *Proceedings of the Cambridge Philosophical Society*, **4**, 47–59.

Verschure, P.-P. H., 1998: Thirty years of observing and documenting sky optical phenomena. *Appl. Opt.*, **37 (9)**, 1585–1588, doi:10.1364/AO.37.001585.

Voigt, C., et al., 2017: ML-CIRRUS - The airborne experiment on natural cirrus and contrail cirrus with the high-altitude long-range research aircraft HALO. *Bull. Amer. Meteor. Soc.*, **98**, 271–288, doi:10.1175/BAMS-D-15-00213.1.

Vollmer, M., 2006: *Lichtspiele in der Luft*. 1st ed., Spektrum Akademischer Verlag, München.

von Helmholtz, H. and A. König, 1896: *Handbuch der physiologischen Optik*. No. Bd. 1 in Handbuch der physiologischen Optik, L. Voss, Hamburg and Leipzig.

Wallace, J. and P. Hobbs, 2006: *Atmospheric Science: An Introductory Survey*. International Geophysics, Elsevier Science.

Wang, C., P. Yang, A. Dessler, B. A. Baum, and Y. Hu, 2014: Estimation of the cirrus cloud scattering phase function from satellite observations. *J. Quant. Spectrosc. Radiat. Transfer*, **138**, 36–49, doi:10.1016/j.jqsrt.2014.02.001.

Warren, S. G. and R. E. Brandt, 2008: Optical constants of ice from the ultraviolet to the microwave: A revised compilation. *Journal of Geophysical Research: Atmospheres*, **113 (D14)**, D14 220, doi:10.1029/2007JD009744.

Wegener, A., 1925: *Theorie der Haupthalos*, Vol. 43. Aus dem Archiv der Deutschen Seewarte und des Marineobservatoriums, Hamburg.

Wegener, A., 1926: *Thermodynamik der Atmosphäre*, 156–189. Springer Berlin Heidelberg, Berlin, Heidelberg, doi:10.1007/978-3-642-90779-1_3.

Weickmann, H., 1947: *Die Eisphase in der Atmosphäre*. Royal Aircraft Establishment.

Wendisch, M., P. Yang, and P. Pilewskie, 2007: Effects of ice crystal habit on thermal infrared radiative properties and forcing of cirrus. *Journal of Geophysical Research*, **112 (D8)**, D08 201, doi:10.1029/2006JD007899.

Wendling, P., R. Wendling, and H. K. Weickmann, 1979: Scattering of solar radiation by hexagonal ice crystals. *Appl. Opt.*, **18 (15)**, 2663–2671, doi:10.1364/AO.18.002663.

Wiegner, M. and A. Geiß, 2012: Aerosol profiling with the Jenoptik ceilometer CHM15kx. *Atmos. Meas. Tech.*, **5 (8)**, 1953–1964, doi:10.5194/amt-5-1953-2012.

Wiegner, M., et al., 2014: What is the benefit of ceilometers for aerosol remote sensing? An answer from EARLINET. *Atmos. Meas. Tech.*, **7 (7)**, 1979–1997, doi:10.5194/amt-7-1979-2014.

Wielicki, B., R. Cess, M. King, D. Randall, and E. Harrison, 1995: Mission to planet Earth: Role of clouds and radiation in climate. *Bull. Amer. Meteor. Soc.*, **76 (11)**, 2125–2153, doi:10.1175/1520-0477(1995)076⟨2125:MTPERO⟩2.0.CO;2.

Wiscombe, W., 1980: Improved Mie scattering algorithms. *Applied Optics*, **19 (9)**, 1505–1509, doi:10.1364/AO.19.001505.

World Meteorological Organization, (Ed.) , 2017: *International Cloud Atlas – Manual on the observation of clouds and other meteors*, Vol. 407. WMO.

Wylie, D. P. and W. P. Menzel, 1999: Eight Years of High Cloud Statistics Using HIRS. *Journal of Climate*, **12 (1)**, 170–184, doi:10.1175/1520-0442(1999)012⟨0170:EYOHCS⟩2.0.CO;2.

Yang, P., B. Baum, A. Heymsfield, Y. Hu, H.-L. Huang, S.-C. Tsay, and S. Ackerman, 2003: Single-scattering properties of droxtals. *J. Quant. Spectrosc. Radiat. Transfer*, **79-80**, 1159–1169, doi:10.1016/S0022-4073(02)00347-3.

Yang, P., L. Bi, B. A. Baum, K.-N. Liou, G. W. Kattawar, M. I. Mishchenko, and B. Cole, 2013: Spectrally Consistent Scattering, Absorption, and Polarization Properties of Atmospheric Ice Crystals at Wavelengths from 0.2 to 100 μm. *J. Atmos. Sci.*, **70 (1)**, 330–347, doi:10.1175/JAS-D-12-039.1.

Yang, P. and K.-N. Liou, 1996: Geometric-optics-integral-equation method for light scattering by nonspherical ice crystals. *Applied Optics*, **35 (33)**, 6568–6584, doi:10.1364/AO.35.006568.

Yang, P. and K.-N. Liou, 1998: Single-scattering properties of complex ice crystals in terrestrial atmosphere. *Contributions to Atmospheric Physics*, **71 (2)**, 223–248.

Yang, P., K.-N. Liou, L. Bi, C. Liu, B. Yi, and B. A. Baum, 2015: On the radiative properties of ice clouds: Light scattering, remote sensing, and radiation parameterization. *Advances in Atmospheric Sciences*, **32 (1)**, 32–63, doi:10.1007/s00376-014-0011-z.

Yang, S., P. Ricchiazzi, and C. Gautier, 2000: Modified correlated k-distribution methods for remote sensing applications. *J. Quant. Spectrosc. Radiat. Transfer*, **64 (6)**, 585–608, doi:10.1016/S0022-4073(99)00140-5.

Yi, B., A. D. Rapp, P. Yang, B. A. Baum, and M. D. King, 2017: A comparison of Aqua MODIS ice and liquid water cloud physical and optical properties between collection 6 and collection 5.1: Cloud radiative effects. *Journal of Geophysical Research*, **122 (8)**, 4550–4564, doi:10.1002/2016JD025654, 2016JD025654.

Yi, B., P. Yang, B. A. Baum, T. L'Ecuyer, L. Oreopoulos, E. J. Mlawer, A. J. Heymsfield, and K.-N. Liou, 2013: Influence of Ice Particle Surface Roughening on the Global Cloud Radiative Effect. *J. Atmos. Sci.*, **70 (9)**, 2794–2807, doi:10.1175/JAS-D-13-020.1.

Zdunkowski, W., T. Trautmann, and A. Bott, 2007: *Radiation in the Atmosphere: A Course in Theoretical Meteorology*. Cambridge University Press, New York.

Zhang, Y., W. Rossow, A. Lacis, V. Oinas, and M. Mishchenko, 2004: Calculation of radiative fluxes from the surface to top of atmosphere based on ISCCP and other global data sets: Refinements of the radiative transfer model and the input data. *Journal of Geophysical Research*, **109 (D19)**, doi:10.1029/2003JD004 457.

Zhang, Z., 2000: A flexible new technique for camera calibration. *IEEE Transactions on Pattern Analysis and Machine Intelligence*, **22 (11)**, 1330–1334.

Zhao, Y., G. G. Mace, and J. M. Comstock, 2011: The Occurrence of Particle Size Distribution Bimodality in Midlatitude Cirrus as Inferred from Ground-Based Remote Sensing Data. *J. Atmos. Sci.*, **68 (6)**, 1162–1177, doi:10.1175/2010JAS3354.1.

Zhou, C., P. Yang, A. E. Dessler, Y. Hu, and B. A. Baum, 2012: Study of Horizontally Oriented Ice Crystals with CALIPSO Observations and Comparison with Monte Carlo Radiative Transfer Simulations. *Journal of Applied Meteorology and Climatology*, **51 (7)**, 1426–1439, doi:10.1175/JAMC-D-11-0265.1.

Zinner, T., P. Hausmann, F. Ewald, L. Bugliaro, C. Emde, and B. Mayer, 2016: Ground-based imaging remote sensing of ice clouds: uncertainties caused by sensor, method and atmosphere. *Atmos. Meas. Tech.*, **9 (9)**, 4615–4632, doi:10.5194/amt-9-4615-2016.

Zinth, W. and U. Zinth, 2005: *Optik. Lichtstrahlen, Wellen, Photonen.* Oldenbourg Verlag, München.

Acknowledgements

First of all I would like to thank my supervisors Prof. Dr. Bernhard Mayer and Prof. Dr. Markus Rapp for providing me with the opportunity and the funding to work on such an interesting and challenging project. I greatly value the experiences I gained from workshops and international conferences. I thank both for supervising me and for many fruitful discussions. Especially, I would like to thank Prof. Dr. Bernhard Mayer for his continuing patient support, many insightful discussions and helpful guidance on the path from simple halo photography to a scientific observation method.

I would like to acknowledge Prof. Dr. Christiane Voigt and Prof. Dr. Ulrich Schumann for including me in the ML-CIRRUS campaign. The radar, lidar, specMACS and HaloCam measurements on the MIM rooftop platform were only possible thanks to the great support and enthusiasm of Prof. Dr. Bernhard Mayer, Dr. Volker Freudenthaler, Dr. Florian Ewald, Tobias Kölling, Hans Grob, Markus Garhammer, Dr. Carolin Klinger and Hubert Stephanblome. Special thanks go to Dr. Silke Groß (DLR) and Dr. Volker Freudenthaler for evaluating the lidar measurements as well as to Dr. Martin Schnaiter and Dr. Emma Järvinen (KIT Karlsruhe) who evaluated the SID-3 data and also gave me a tour of their facilities.

I thank Dr. Bastiaan van Diedenhoven (NASA GISS, New York City) and Prof. Dr. Brian Cairns (NASA GISS and Columbia University, New York City) for valuable discussions at several conferences.

Dr. Patric Seifert (TROPOS, Leipzig) and Prof. Dr. Stefan Russchenberg (TU Delft) gave me the opportunity to participate in the ACCEPT campaign and supported me in securing funding. The halo observations during the ACCEPT campaign were funded by the European Union Seventh Framework Program (FP7/2007-2013) under grant agreement n° 262254. I greatly appreciate the support during the campaign by Markus Garhammer, Dr. Marc Allaart (KNMI, De Bilt), Dr. Lukas Pfitzenmaier and Dr. Alexander Myagkov.

HaloCam was brought to life by Meinhard Seefeldner and Anton Lex, who constructed the sun-tracking mount and the weather-proof camera housing. I would like to thank Andreas Baumgartner and Dr. Karim Lenhard from DLR for their kind assistance with the camera calibration.

I very much appreciate the inspiring, friendly and cooperative research environment at the Meteorological Institute in Munich. I would like to thank Dr. Claudia Emde, Dr. Tobias Zinner and Dr. Christoph Knote for valuable discussions not only on radiative transfer. Dr. Matthias Wiegner provided great support in evaluating the ceilometer data and proof-reading the paper. I'd like to thank Markus Garhammer for solving administrative matters and his great support with all the campaigns. Special thanks go to my office mates Dr. Florian Ewald, Tobias Kölling and Hans Grob for so many on and off topic discussions and especially for sharing their knowledge and experience on camera calibration. Thanks to my colleagues Carolin, Andreas, Fabian, Mares, Nina, and Lucas – I will always look back fondly at our shared time at MIM.

Finally and most importantly I'd like to thank especially my friends and family who supported me during the past years and reminded me to keep work and life balanced. Most outstandingly I'd like to highlight the support of my parents Ilse and Claus and Bastian Baudisch who has been my steadfast companion since the start of our masters theses.